Effects of spin and orbital correlations on the optical spectral weights of transition-metal oxides

Inaugural - Dissertation
zur
Erlangung des Doktorgrades
der Mathematisch-Naturwissenschaftlichen Fakultät
der Universität zu Köln

vorgelegt von
Julia Christina Reul (geb. Küppersbusch)
aus Datteln

Köln, im August 2013

Berichterstatter:
Prof. Dr. Markus Grüninger
Prof. Dr. ir. Paul H. M. van Loosdrecht

Vorsitzender der Prüfungskommission:
Prof. Dr. Simon Trebst

Tag der letzten mündlichen Prüfung:
18. Oktober 2013

Contents

1 Introduction **1**

2 Electronic structure of correlated electron systems **5**
2.1 The Hubbard model 5
2.2 On-site properties 7
2.2.1 Crystal structure and crystal-field splitting 7
2.2.2 Multiplets 8
2.3 The multi-orbital Hubbard model 11
2.4 Superexchange 11
2.5 Orbital correlations due to orbital-lattice coupling 13
2.6 Mott-Hubbard excitations and their temperature dependence . . . 14
2.7 Mott-Hubbard and charge-transfer insulators 16

3 Optical Spectroscopy **19**
3.1 Linear response functions and optical constants 19
3.1.1 Linear response theory 19
3.1.2 The optical constants 21
3.1.3 The Kramers-Kronig relation 22
3.1.4 Reflection properties of electromagnetic waves 23
3.1.5 Modeling the dielectric function 26
3.2 Ellipsometry 28
3.2.1 Jones and Mueller-matrix formalism 29
3.2.2 The pseudo-dielectric function 37
3.2.3 The working principle of a rotating analyzer ellipsometer . 39
3.2.4 A brief presentation of the quantities relevant for the fitting procedure 40

4 Data acquisition and analysis **43**
4.1 Data acquisition 43
4.1.1 The experimental setup 43
4.1.2 Sample preparation 46
4.1.3 Mounting, aligning, and calibrating the sample 48
4.2 Data analysis 50
4.2.1 Surface effects 51

4.2.2 Parametric models 51
4.2.3 The spectral weight 53

5 Probing orbital fluctuations in RVO_3 ($R = Y$, rare earth ion) 55
5.1 The compounds RVO_3 ($R = Y$, rare-earth ion) 56
5.1.1 The crystal structure 56
5.1.2 Spin and orbital ordering phase diagram 58
5.1.3 Importance of orbital fluctuations 59
5.1.4 Details on YVO_3 63
5.1.5 Details on $CeVO_3$ 64
5.1.6 Details on $GdVO_3$ 66
5.1.7 Mott-Hubbard excitations in RVO_3 70
5.1.8 Probing orbital fluctuation by the use of ellipsometry . . . 71
5.2 Experimental data 76
5.2.1 Optical conductivity of YVO_3 76
5.2.2 Optical conductivity of $GdVO_3$ 85
5.2.3 Optical conductivity of $CeVO_3$ 90
5.3 Discussion 95
5.3.1 Multiplet assignment and temperature dependence 95
5.3.2 Comparison with literature 100
5.3.3 Temperature dependence of the spectral weight: strength of orbital fluctuations 102
5.4 Observation of an excitonic resonance in RVO_3 106
5.4.1 Literature on photoemission spectroscopy and band structure calculations 107
5.4.2 Exciton formation in correlated insulators 111
5.4.3 Hubbard exciton in RVO_3 112
5.5 Conclusion 116

6 Ellipsometry on $LaSrFeO_4$ 117
6.1 The compound $LaSrFeO_4$ 117
6.1.1 Motivation 117
6.1.2 Structure, spins, and orbitals 120
6.2 Experimental data 122
6.3 Discussion 127
6.3.1 Charge-transfer and Mott-Hubbard excitations 127
6.3.2 Peak assignment 130
6.3.3 Temperature dependence 132
6.4 Conclusion 137

7 Ellipsometry on cobaltates **139**
7.1 The compounds 140
7.1.1 The compounds $LaCoO_3$ and $EuCoO_3$ 140
7.1.2 The compounds $La_{2-x}Sr_xCoO_4$ and $La_{2-x}Ca_xCoO_4$ 150
7.2 Experimental data 160
7.2.1 Optical conductivity of $LaCoO_3$ and $EuCoO_3$ 161
7.2.2 Optical conductivity of $La_{2-x}Sr_xCoO_4$ (x = 0, 0.33, 0.45, 0.5, and 0.9) and $La_{1.5}Ca_{0.5}CoO_4$ 170
7.3 Discussion 190
7.3.1 Results on $LaCoO_3$ and $EuCoO_3$ 190
7.3.2 Results on $La_{2-x}Sr_xCoO_4$ (x = 0, 0.33, 0.45, 0.5, 0.9) and $La_{1.5}Ca_{0.5}CoO_4$ 196
7.4 Conclusion 212

8 Conclusion **213**

List of Figures **217**

List of Tables **223**

Bibliography **225**

1 Introduction

The Coulomb interaction between individual electrons plays an important role for many transition-metal compounds. Whereas they are expected to exhibit metallic behavior due to their partially filled d shells, many transition-metal compounds have shown to be insulating by experiment [1]. A variety of fascinating phenomena has been observed such as high-temperature superconductivity and colossal-magneto resistance [2–4]. The physical model which has proven successful in describing the remarkable properties of these so-called correlated electron systems is the Hubbard model [5, 6]. It accounts not only for the energy gain due to charge delocalization, but also adds a term which describes the on-site Coulomb repulsion between individual electrons. It follows a splitting of the valence band into a lower and an upper Hubbard band. As a consequence of charge localization, the atomic degrees of freedom, like spin, charge, and orbital, retain their meaning in these correlated insulators [7]. A competition between the individual degrees of freedom arises and complex spin, orbital, and charge ordering phase diagrams have been observed.

In the framework of this thesis a variety of transition-metal compounds is investigated by means of spectroscopic ellipsometry in the energy range from 0.75 eV to 5.5 eV for temperatures ranging from 15 K to 490 K. Ellipsometry measures the change of the polarization state of a polarized light beam which is reflected from the sample surface. The technique of ellipsometry bears two significant advantages over conventional reflection measurements. It acquires two independent parameters, which are needed to describe the state of polarization, at each wavelength. As a consequence, it yields both, the real and the imaginary part of the complex dielectric function directly without a Kramers-Kronig transformation. Furthermore, it is a self-normalizing technique and no reference measurement is required. Due to its high accuracy, ellipsometry is particularly well suited to determine the precise temperature dependence of the optical spectral weights.

The optical spectra of correlated insulators are dominated by Mott-Hubbard excitations, i.e. an electron transfer between neighboring transition-metal sites i and j, and charge-transfer excitations, i.e. an electron transfer from the ligand oxygen $2p$ band to the transition-metal $3d$ band. Depending on the relative energy cost of charge-transfer and Mott-Hubbard excitations, one distinguishes between two kinds of correlated insulators. In a Mott-Hubbard insulator the lowest

dipole-allowed excitation corresponds to a Mott-Hubbard excitation, whereas the charge-transfer excitation is the lowest dipole-allowed excitation in a so-called charge-transfer insulator. Typically, early transition-metal compounds belong to the group of Mott-Hubbard systems, while late ones are characterized as being of charge-transfer type. Due to the multiplet splitting of Mott-Hubbard and charge-transfer absorption bands in these multi-orbital systems, the optical conductivity shows a complex multi-peak structure. The spectral weight of the Mott-Hubbard excitations is very sensitive to nearest-neighbor spin-spin and orbital-orbital correlations [8, 9]. A change of spin and orbital correlations with temperature leads to a characteristic spectral-weight transfer between the individual components of the optical multiplets [10]. This has been very nicely demonstrated for the $3d^4$ systems $LaMnO_3$ and $LaSrMnO_4$ [11, 12]. Here, the orbital occupation is independent of temperature because of the large ligand-field splitting of the singly occupied e_g orbitals, thus the spectral-weight transfer of the Mott-Hubbard excitations is mainly governed by the spin-spin correlations. However, the behavior of the $3d^1$ Mott-Hubbard insulators $YTiO_3$ and $SmTiO_4$ is still not understood in this context [13]. It is the aim of this thesis to systematically study the importance of spin/orbital correlations and also excitonic effects on the temperature dependence of the optical spectra.

First, the focus lies on the $3d^2$ systems RVO_3 ($R = $ Y, rare earth ion). Undoped RVO_3 can be characterized as a Mott-Hubbard insulator with pseudocubic perovskite structure. The orbital degree of freedom plays a decisive role in RVO_3. The coupling of the orbitals to the lattice is only weak in these systems with active t_{2g} orbitals and as a consequence orbital and spin degrees of freedom are intimately related to each other. The hopping amplitude between orbitals on adjacent lattice sites determines both the size and the sign of the magnetic exchange coupling between spins. It follows a complex spin and orbital ordering phase diagram which is expected to be reflected in a pronounced anisotropy and temperature dependence of the optical spectra. It is still not clear under which circumstances the orbitals themselves may be considered as a truly low-energy degree of freedom displaying low-energy excitations, in other words, to establish compounds with strong orbital fluctuations. The typical situation in most Mott-Hubbard insulators is that the orbitals are strongly coupled to the lattice, i.e. the crystal field, opening a gap in the orbital excitations of a few 100 meV or larger. In this case, it usually is sufficient to consider rigid orbital order with no fluctuations. However, it has been claimed that orbital fluctuations may be strong in the Mott-Hubbard insulators RVO_3. For YVO_3 the observation of a one-dimensional orbital liquid, of an orbital Peierls phase, and of bi-orbitons has been reported [8, 10, 14–18]. On the other hand, other groups rule out strong orbital fluctuations in YVO_3 due to a sizable crystal-field splitting [19, 20] but support the importance of orbital fluctuations for compounds with larger R ions such as $LaVO_3$. Here, it is aimed to approach the

determination of low-energy orbital fluctuations by means of optical spectroscopy. The observed absorption bands can be described in terms of the different $3d^3$ multiplets which form the upper Hubbard band. A comparison of the experimental results for $R = \mathrm{Y}$, Gd, and Ce with a theory based on a low-energy spin-orbital superexchange Hamiltonian [8, 10] should lead to a conclusion about the character of the orbital degree of freedom. Optical data of undoped $R\mathrm{VO_3}$ ($R = \mathrm{Y}$, La) are well present in the literature [21–23]. However, different data sets strikingly disagree with each other, calling for a clarification.

Further optical investigations focus on the compound $\mathrm{LaSrFeO_4}$. The correlated insulator $\mathrm{LaSrFeO_4}$ is of interest because it lies on the border between Mott-Hubbard and charge-transfer systems. The layered structure of $\mathrm{LaSrFeO_4}$ is expected to give rise to a pronounced anisotropy of the optical spectra, which can be used to disentangle Mott-Hubbard and charge-transfer absorption bands and thereby shed light on the character of $\mathrm{LaSrFeO_4}$.
$\mathrm{LaSrFeO_4}$ exhibits a high-spin $3d^5$ electron configuration on the $\mathrm{Fe^{3+}}$ sites with a Néel temperature of $T_N = 366\,\mathrm{K}$. As a consequence, spin-spin and orbital-orbital correlations between nearest neighbors do not vary strongly below room temperature. Thus, the temperature dependence of the Mott-Hubbard excitations is expected to be rather small, which makes $\mathrm{LaSrFeO_4}$ an interesting candidate for the investigation of other effects on the temperature dependence of the spectral weight, such as the thermal expansion of the lattice, bandstructure effects, or excitonic contributions.

Yet another concern of this thesis lies on the physics of cobaltates. The focus is on the pseudocubic perovskites $\mathrm{LaCoO_3}$ and $\mathrm{EuCoO_3}$ with electron configuration $3d^6$ on the $\mathrm{Co^{3+}}$ sites, and the single-layered perovskites $\mathrm{La_{2-x}Sr_xCoO_4}$ ($x = 0,\ 0.33,\ 0.45,\ 0.5,\ 0.9$) and $\mathrm{La_{1.5}Ca_{0.5}CoO_4}$, which contain both, $\mathrm{Co^{3+}}$ ions with $3d^6$ electron configuration and $\mathrm{Co^{2+}}$ ions with $3d^7$ electron configuration. The physics of cobaltates is dominated by the spin-state issue. Particularly the spin state of the $3d^6$ electron configuration of the $\mathrm{Co^{3+}}$ ions can act as an additional degree of freedom, which is expected to control electronic and magnetic properties. A $3d^6$ electron configuration in an octahedral surrounding is particular interesting as a competition arises between the crystal-field splitting and the Hund exchange. While the domination of the former gives rise to a nonmagnetic low-spin state (spin $S = 0$), the latter favors parallel spins, i.e. a magnetic high-spin state with spin $S = 2$. Also the compromise in form of an intermediate-spin state with spin $S = 1$ has been discussed to become energetically favorable due to band-structure effects or large distortions of the oxygen octahedra [24, 25].
The magnetic susceptibility of the pseudocubic perovskite $\mathrm{LaCoO_3}$ exhibits quite unusual behavior which has been attributed to a thermal population of higher spin states from a low-spin ground state starting at $T \gtrsim 25\,\mathrm{K}$ [25, 26]. The cobaltates

can be characterized as charge-transfer insulators. A change of the spin state of the Co^{3+} ions is supposed to greatly affect the reachable final states of the charge-transfer excitations. However, temperature-dependent reflectivity data on $LaCoO_3$ hardly vary across the so-called spin-state transition [27]. In $EuCoO_3$ the spin-state transition is shifted to much higher temperatures. The literature on single-layered cobaltates gives evidence for both, temperature and a doping induced spin-state transitions taking place on the Co^{3+} sites [28–32]. The elaborate ellipsometric analysis presented in this work focuses on three different aspects, the temperature, polarization, and doping dependence of the optical spectra. It is the aim of this investigation to study the impact of the Co^{3+} spin-state on the optical spectra and to gain further insight into the physics of this interesting class of materials.

The structure of this thesis is as follows: In chapter 2 the physics of correlated electron systems is briefly discussed. A short introduction into the field of optical spectroscopy is given in chapter 3. The second part of chapter 3 is exclusively devoted to ellipsometry. A description of the experimental setup and a discussion of the analysis of the ellipsometric data follows in chapter 4. The results of the detailed optical investigations on $R\mathrm{VO}_3$ are presented in chapter 5. Chapter 6 discusses the optical data of $LaSrFeO_4$. Finally, chapter 7 deals with the results of the elaborate optical study on pseudocubic and single-layered cobaltates. The thesis ends with a conclusion in chapter 8.

2 Electronic structure of correlated electron systems

2.1 The Hubbard model

In a correlated electron system the Coulomb repulsion between individual electrons of the valence band plays a significant role. As a consequence, the electronic properties of these systems cannot be described by band theory. Band theory makes use of an independent electron approximation, i.e. an electron moves in a mean potential of all other electrons. It is very successful in classifying a great number of crystalline solids as metals or insulators. However it fails e.g. in the description of transition-metal compounds with partially filled d shells, which are classified as metals by band theory, but some of them show insulating behavior in experiments [33]. A model which includes correlation effects between electrons that go beyond band theory is the so-called Hubbard model. The single-band Hubbard model represents its most simple form [5, 6]:

$$H = H_t + H_{int} = -t \sum_{\langle i,j \rangle \ \sigma} (c^\dagger_{i\sigma} c_{j\sigma} + h.c.) + U \sum_i n_{i\uparrow} n_{i\downarrow} \tag{2.1}$$

Here, $n_{i\uparrow(\downarrow)}$ is the occupation number operator, it counts the electrons with spin $\uparrow$ ($\downarrow$) at lattice site i, $c^\dagger_{i\sigma}$ ($c_{i\sigma}$) creates (annihilates) an electron with spin $\sigma = \uparrow, \downarrow$ at lattice site i and the sum over $\langle i, j \rangle$ is carried out over nearest neighbors. The first term of Eq. 2.1 is the ordinary band term which describes the behavior of electrons in a periodic potential. The electrons gain kinetic energy by hopping from lattice site i to the neighboring lattice site j. The strength of the hopping amplitude t is given by the overlap between neighboring orbitals. The second term of Eq. 2.1 stems from the on-site Coulomb repulsion between two electrons, double occupancy has to be paid for by the Coulomb energy U. At half filling, i.e. one electron per lattice site, the electronic properties of the system are governed by the ratio U/t. On the one hand, the movement of an electron results in an energy gain t, but on the other hand, it generates double occupancy costing the energy U. While the system is a Mott-Hubbard insulator with one electron per lattice site in the limit $U/t \gg 1$ (strong coupling limit) where double occupancy is prevented by the large energy cost U, the system has metallic properties for $U/t \ll 1$. The variation of U/t thus leads to a metal-insulator transition [33, 34].

The insulating behavior can be visualized by a splitting of the valence band [33], as sketched in Fig. 2.1. It has to be noted, however, that the resulting "bands" cannot be understood in a single-electron picture, but are a result of the interactions among electrons. Instead of the density of states in a single-electron picture, one sketches the $(N-1)$-particle states (i.e. the spectrum of photoemission spectroscopy) as well as the $(N+1)$-particle states (i.e. the spectrum of inverse photoemission spectroscopy). The valence band is split into the band with $(N-1)$ particles, the so-called lower Hubbard band (LHB) and the band with $(N+1)$ particles, the so-called upper Hubbard band (UHB). The bands are separated from each other by the Coulomb energy U. As hole and double occupancy can move freely, the bands have a finite band width W, which is determined by the hopping amplitude t and the number of nearest neighbors z. In a crystal with cubic symmetry it is given by $W = 2zt$ [33]. LHB and UHB are far away from each other in the limit $U/t \gg 1$ representing insulating behavior, whereas the overlap of LHB and UHB in the other limit $U/t \ll 1$ characterizes a metallic system.
In Eq. 2.1 hopping only takes place between nearest neighbors, also the model only accounts for a Coulomb interaction between electrons on the same lattice site. Furthermore, the single-band Hubbard model is restricted to one orbital per lattice site and does not allow for different (degenerate) orbitals on each site. However, depending on the physical system under investigation, the model can be expanded by the relevant terms (see Sec. 2.3 below).

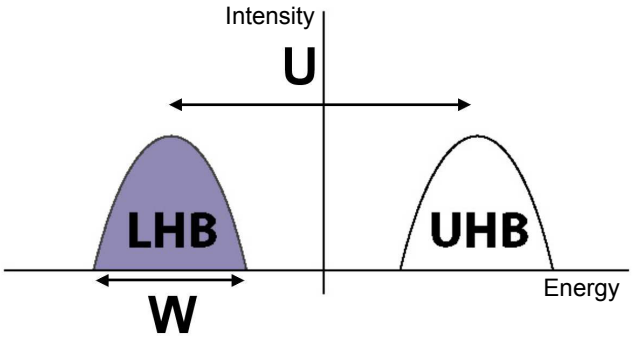

Figure 2.1: The valence band is split into the lower Hubbard band (LHB) and the upper Hubbard band (UHB). See the main text for details.

2.2 On-site properties

2.2.1 Crystal structure and crystal-field splitting

The discussion of the on-site electronic properties is of great importance for the understanding of our optical spectra. The transition-metal compounds investigated within the framework of this study crystallize either in a (distorted) perovskite-type crystal structure or in a (distorted) single-layered perovskite-type structure. The (pseudo-) cubic perovskites have the chemical formula ABX_3, for the compounds investigated within this these, A refers to a rare-earth ion or Y, B represents a transition-metal ion, and X is an oxygen ion. The chemical formula of the single-layered perovskites is A_2BX_4. The unit cell of both structures is depicted in Fig. 2.2. Most of the crystals examined within the framework of this study show a distortion away from the ideal cubic or tetragonal crystal structure. Compared to the ideal perovskite the BX_6 octahedra are rotated, tilted, and distorted. The distortions away from the cubic/tetragonal arrangement are mainly due to a mismatch of ionic sizes, so-called steric effects. The crystal symmetry is often reduced to orthorhombic. The lattice constants of the orthorhombic unit cell characterizing the pseudocubic perovskite are related to the ones of the ideal cubic structure (with lattice constant a_c) by $a \approx b \approx \sqrt{2}a_c$ and $c \approx 2a_c$. Figure 2.3 shows the orthorhombic unit cell of the distorted structure. In the case of the tetragonal symmetry of the single-layered structure, the BX_6 octahedra (being neither tilted nor rotated) are elongated along the c axis. The lattice constants of the distorted layered structure are related to the ones of an ideal layered perovskite (with lattice constants a_{tet} and c_{tet}) by $a \approx b \approx \sqrt{2}a_{tet}$ and $c \approx c_{tet}$.
The relevant physics takes place in the $3d$ shell of the transition-metal (TM) ions which are surrounded by the oxygen octahedra. Both, the rare-earth ions (or Y) and the oxygen ions have closed shells in a purely ionic scenario. Since the compounds of interest can be characterized as correlated insulators, the electrons are mostly localized on their lattice sites. The compound YVO_3, for instance, is composed of the ions $Y^{3+} = [Kr]4d^0$, $V^{3+} = [Ar]3d^2$, and $O^{2-} = [He]2s^22p^6$ and e.g. $LaSrFeO_4$ consists of $La^{3+} = [Xe]5d^0$, $Sr^{2+} = [Kr]5s^0$, $Fe^{3+} = [Ar]3d^5$, and $O^{2-} = [He]2s^22p^6$.
The local properties of the TM ion are derived by the use of the so-called *crystal-field theory* [33, 35, 36]. It considers a scenario in which the TM ion is placed in the potential of point-like charges of the surrounding ligands. The electric field lifts the degeneracy of the $3d$ level. A cubic crystal field splits the five $3d$ orbitals into a lower-lying, triply degenerate t_{2g} level (the d_{xy}, d_{yz}, and d_{zx} orbitals) and a higher-lying, doubly degenerate e_g level (the $d_{x^2-y^2}$ and d_{3z-r^2} orbitals), the resulting orbitals are sketched in Fig. 2.4. The energetic separation is commonly denoted by $10\,Dq$. Typical values of $10\,Dq$ in TM compounds amount to $1-5$ eV [9, 12, 37–39]. The e_g orbitals lie higher in energy because their lobes point

directly onto the negatively charged oxygen ions, whereas the lobes of the t_{2g} orbitals avoid them (see Fig. 2.4) [35]. The degeneracy of the t_{2g} and e_g levels is further lifted by a distortion of the BX_6 octahedra. In addition to steric effects, also the Jahn-Teller effect is an important driving force for lifting the degeneracy. It is active if the number of electrons cannot be uniformly distributed over the degenerate orbitals [40]. Up to a certain limit, the energy that can be gained by lowering the energy of the occupied orbitals with respect to the unoccupied ones outweighs the energy cost for distorting the octahedra. Also the spin-orbit coupling leads to a level splitting. However, its effect is comparably small in the compounds of interest for this work and can mostly be neglected.
Crystal-field theory is not always sufficient for the description of the compounds of interest relevant for this work as it does not account for hybridization. The hybridization of the TM ions with the surrounding oxygen ions might, however, play an important role for the understanding of our optical spectra. A theory that goes beyond crystal-field theory is the so-called *molecular-orbital theory*. Molecular-orbital theory is able to describe the phenomena of chemical bonding. Molecular orbital wave functions are constructed out of linear combinations of the atomic orbital wave functions [41].

2.2.2 Multiplets

In the case that more than one electron resides in the $3d$ shell, the on-site properties are determined by many-electron wave functions. In the following discussion we assume cubic symmetry, effects resulting from deviations thereof will be discussed in the relevant chapters. Here, we will follow the argumentation of Ref. [35]. The many-electron wave functions in the cubic case are constructed out of the single-electron functions t_{2g} and e_g. Let us consider the simple case of placing two electrons into the t_{2g} shell. There are 6 possibilities for placing the first electron in the shell (as one can choose between three t_{2g} orbitals and spin up or down) and 5 possibilities for the second electron (respecting the Pauli principle). One obtains 15 states (as the product of 6×5 has to be divided by 2 to avoid double counting), which have the same energy if the Coulomb interaction between the electrons is neglected. The many-electron wave function is, however, not simply a product of the single-electron functions as the antisymmetry of the fermionic wave function has to be taken into account. This is ensured by making use of Slater determinants. The Coulomb interaction between the electrons leads to a splitting of the energy levels of the many-electron states. The eigenstates corresponding to a certain energy level are the basis of an irreducible representation Γ of the octahedral symmetry group. Since there is no spin operator in the crystal-field Hamiltonian, the eigenstates have a definite spin quantum number S. The different energy levels are called d^n multiplets and are denoted by $^{2S+1}\Gamma$. They have $(2S+1) \times (\Gamma)$ fold degeneracy, where (Γ) denotes the dimension of the irreducible representation Γ.

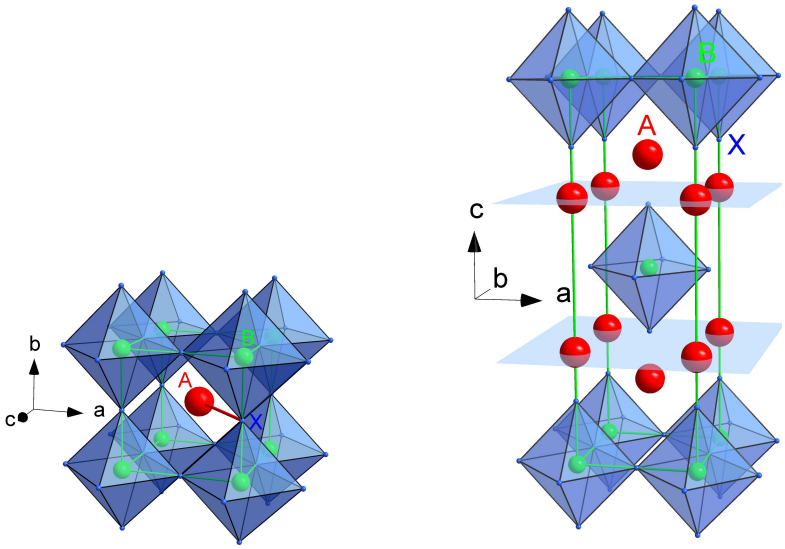

Figure 2.2: Left: Crystal structure of the ideal cubic perovskite with chemical formula ABX_3 (cubic, space group $Pm\bar{3}m$), Right: Crystal structure of the ideal single-layered perovskite with chemical formula A_2BX_4 (tetragonal, space group $I4/mmm$), the BX_6 octahedra are elongated along the c axis. Taken from Ref. [42].

The eigenenergy value of each multiplet depends on the spin configuration and the orbital occupation. It is described by the three Racah parameters A, B, and C, which describe the Coulomb interaction between two electrons on the same ion[1], and the crystal-field parameter $10\,Dq$, describing the $t_{2g} - e_g$ splitting [35]. In the Sugano-Tanabe-Kamimura diagrams the multiplet energies are plotted as a function of Dq/B. It is possible to reduce the number of parameters since the energy splitting between the multiplet states is independent of the Racah parameter A (A determines the absolute energy value only). Furthermore the ratio C/B is nearly independent of the number of electrons in the d shell as well as of the atomic number and deviates only slightly from the free-ion value (which is mostly known from spectroscopic data) [35, 44]. We will make use of the Sugano-Tanabe-Kamimura diagrams for the peak assignment of our spectroscopic data (see the relevant chapters). The approximate values of Dq/B are mostly known

[1]The Racah parameters A, B, and C follow from the Slater integrals F^0, F^2, and F^4 by $A = F^0 - 49/441\ F^4$, $B = 1/49F^2 - 5/441\ F^4$, $C = 35/441\ F^4$ with $F^k = \int_0^\infty r_1^2 dr_1 \int_0^\infty r_2^2 dr_2 R_d^2(r_1) R_d^2(r_2) r_<^k / r_>^{k+1}$, where R_d denotes the radial wave function and $r_<$ and $r_>$ are the minimum and maximum values of r_1 and r_2, respectively [35].

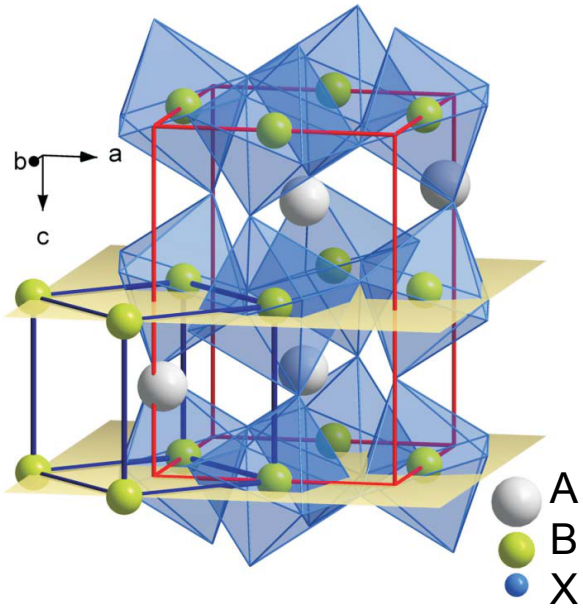

Figure 2.3: Crystal structure of the distorted perovskite (orthorhombic, space group *Pbnm*). The orthorhombic (red) and the cubic (blue) unit cell are displayed. Taken from Ref. [37].

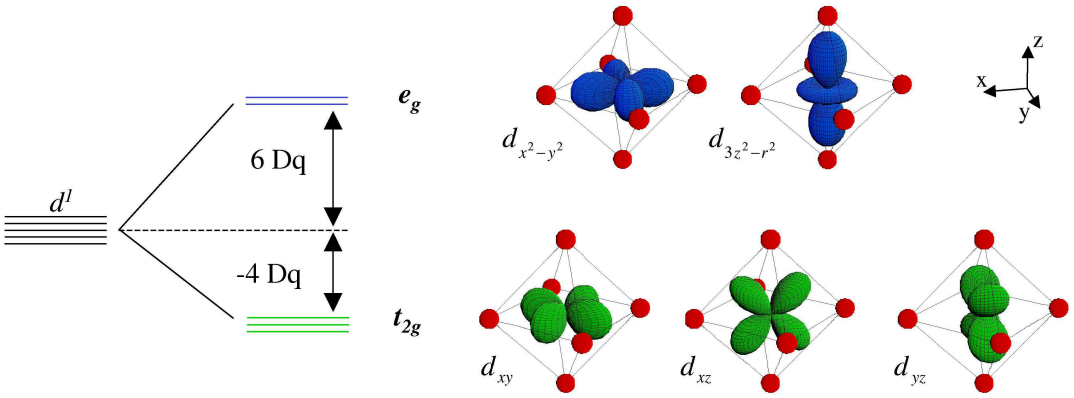

Figure 2.4: The cubic crystal field of the surrounding oxygen (O^{2-}) octahedron splits the d level of the transition-metal ion into a lower-lying triply degenerate t_{2g} level (d_{xy}, d_{yz}, and d_{zx}) and a higher-lying doubly degenerate e_g level ($d_{x^2-y^2}$ and $d_{3z^2-r^2}$). The value of the splitting amounts to $10\,Dq$. Taken from Ref. [43].

from the literature. The crystal-field parameter $10\,Dq$ depends mainly on the size of the TM $-$ O octahedra. For a detailed discussion of crystal-field theory we refer e.g. to Refs. [35, 36].

2.3 The multi-orbital Hubbard model

The orbital degree of freedom is of great importance for the systems under investigation in this work with partially filled $3d$ shells. A multi-orbital Hubbard model has to be considered which allows for different (possibly degenerate) orbitals per lattice site. The system Hamiltonian in this case is given by [45]:

$$H = H_t + H_{int} \tag{2.2}$$

with

$$H_t = \sum_{\langle i,\ j\rangle,\ \alpha,\ \beta,\ \sigma} t^{\alpha\beta}(c^{\dagger}_{i\alpha\sigma}c_{j\beta\sigma} + h.c.) \tag{2.3}$$

and

$$H_{int} = \sum_{i,\ \alpha,\ \beta,\ \sigma,\ \sigma'} (1-\delta_{\alpha\beta}\delta_{\sigma\sigma'})U^{\alpha\beta}n_{i\alpha\sigma}n_{i\beta\sigma'} - \sum_{i,\ \alpha,\ \beta} J_H^{\alpha\beta}\vec{S}_{i\alpha}\cdot\vec{S}_{i\beta}(1-\delta_{\alpha\beta}) \tag{2.4}$$

Here, the hopping amplitude $t^{\alpha\beta}$ depends on the type of the involved orbitals, it is zero if there is no overlap between the orbitals α and β [45]. In the TM compounds considered in this work the intersite hopping takes place via σ or π bonds of the ligand oxygen orbitals. Also the on-site Coulomb repulsion $U^{\alpha\beta}$ varies depending on the pair of orbitals considered. The last term in H_{int} stems from the on-site Hund exchange interaction, stating that parallel spin alignment is preferred to antiparallel alignment for electrons in different orbitals. The values of $U^{\alpha\beta}$ and $J_H^{\alpha\beta}$ are determined by the Racah parameters A, B, and C, which have been introduced in the previous section.

2.4 Superexchange

The ground state of the single-band Hubbard model in the atomic limit (hopping amplitude $t = 0$) has 2^N fold degeneracy in the case of half filling (N = number of lattice sites). Electrons on different lattice sites do not interact and each spin can be either up or down. For a small value of t the hopping term H_t of the Hamiltonian in Eq. 2.1 can be treated as a weak perturbation of the Hubbard interaction H_{int} [34]. In the strong coupling limit $U/t \gg 1$ double occupancy is suppressed for low energies and further considerations can be restricted to the subspace of singly occupied lattice sites. Making use of a canonical transformation

and considering perturbation terms up to second order, one obtains the low-energy superexchange Hamiltonian [34]:

$$H_{eff} = J \sum_{\langle i,j \rangle} \vec{S}_i \cdot \vec{S}_j \tag{2.5}$$

This is the Hamiltonian of the well-known Heisenberg model with superexchange constant $J \propto t^2/U$. For positive values of J the coupling is antiferromagnetic (AFM). In the case of 180° bonds, the ground state of the single-band Hubbard model at half filling has thus AFM spin order. Antiparallel spins gain kinetic energy by virtual hopping processes to neighboring sites, whereas hopping is blocked in the ferromagnetic (FM) case by the Pauli principle. These virtual charge excitations that cause an interaction between electrons on neighboring lattice sites are called superexchange interactions [46].
In the more complex case of the TM compounds with partially filled $3d$ shells different terms contribute to the superexchange interactions between neighboring lattice sites. These different contributions result from the multiplet structure of the virtually excited states and not only the spin degree of freedom but also the orbital degree of freedom plays an important role. Figure 2.5 exemplifies on a simple model of a system with one electron and two orbitals per lattice site how FM and AFM correlations can emerge.
Kugel and Khomskii were the first to derive low-energy effective superexchange Hamiltonians for compounds with partially filled degenerate orbitals [47]. These so-called spin-orbital models tread coupled spin and orbital degrees of freedom. They allow for both, FM and AFM spin correlations. They are successful in explaining the splitting of degenerate orbitals due to superexchange and describe orbital ordering phenomena. In addition to the actual orbital state, these complex spin-orbital models are controlled by only a small number of physical parameters, the superexchange constant $J \propto t^2/U$ and the normalized Hund exchange J_H/U [8][2]. It has to be noted, however, that as opposed to the spin part, where interaction between neighboring lattice sites are exclusively mediated by superexchange, the orbital occupation of neighboring lattice sites can additionally be a affected by orbital-lattice coupling (i.e. steric effects or the cooperative Jahn-Teller effect, see Sec. 2.5 below). In the case of orbital degeneracy, the superexchange interactions are composed of virtual charge excitations to the various multiplet states forming the UHB. The effective low-energy Hamiltonian, which connects the lattice sites i and j, can thus be written as a superposition of each individual

[2]Here, U is the on-site intra-orbital Coulomb interaction energy, J_H is Hund exchange element which depends on the involved orbitals and t is the effective hopping element between the relevant orbitals of the system under consideration.

contribution to the superexchange [8]:

$$H_{eff} = \sum_{n} \sum_{\langle i,j \rangle || \gamma} H_n^{\gamma}(ij) \tag{2.6}$$

The individual charge excitations which contribute to superexchange are labeled by n. Since the orbital operators depend on the bond direction, the index $\gamma = a, b, c$ has been introduced to specify the different crystallographic directions [8]. We will see in Sec. 2.6 that the effective low-energy Hamiltonian of Eq. 2.6 also determines the intensity of the high-energy optical transitions across the band gap. The intersite transitions that are seen in optics are thus intimately related to the low-energy superexchange interactions [8,10]. In chapter 5 we will make use of this interrelation to understand the temperature dependence of the complex multi-peak structure observed in the optical spectra of the compounds $R\mathrm{VO}_3$ (with R = rare-earth ion or Y).

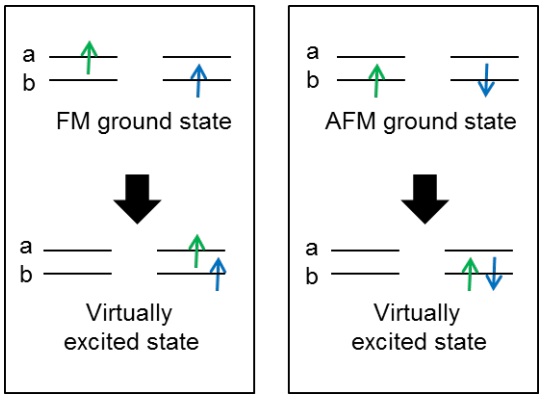

Figure 2.5:
Simple model of a system with one electron and two orbitals (a and b) per lattice site. The correlations can be FM due to the Hund coupling or AFM due to the Pauli principle.

2.5 Orbital correlations due to orbital-lattice coupling

In addition to the superexchange which mediates an interaction between spins and orbitals on neighboring lattice sites, also the coupling of the orbitals to the lattice has to be taken into account as a potential source for orbital ordering [48,49]. In Sec. 2.2.1 we have already discussed steric effects and the Jahn-Teller effect as possible causes for the level splitting on one particular TM site. The interrelation between the individual oxygen octahedra in a crystal lattice can induce a collective lattice distortion (see Fig. 2.6), the so-called collective Jahn-Teller effect.
The collective Jahn-Teller effect and the superexchange interactions do not necessarily support the same kind of orbital ordering pattern. The competition between different mechanisms for orbital ordering can be the source of a rich spin

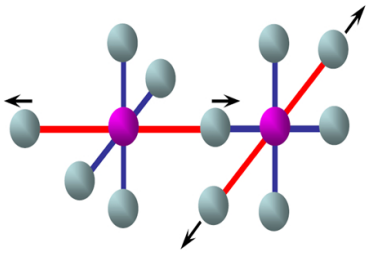

Figure 2.6:
Simple sketch of a collectively distorted crystal structure, the so-called collective Jahn-Teller effect.

and orbital ordering phase diagram. In systems with active e_g orbitals the coupling to the lattice typically plays an important role. In the e_g system $LaMnO_3$ with $3d^4$ electron configuration for instance, the collective Jahn-Teller effect induces an orbital ordering phase transition taking place at a temperature as high as $T_{OO} = 780\,\mathrm{K}$ [11], therefore the superexchange between orbitals can be neglected [8, 49]. In the t_{2g} system YVO_3 with $3d^2$ electron configuration, however, the competition between steric effects, the Jahn-Teller effect, and superexchange interactions is recognized to be the origin of a complex spin and orbital ordering phase diagram [14, 48, 49] (which will be presented in Sec. 5).

2.6 Mott-Hubbard excitations and their temperature dependence

The absorption spectra of TM compounds in the energy region relevant for this work, ranging from the near infrared to the middle ultraviolet region ($0.75\,\mathrm{eV} - 5.5\,\mathrm{eV}$), are dominated by two types of electronic excitations: the Mott-Hubbard (MH) excitations and the charge-transfer (CT) excitations. In this section we address the former whereas the latter are discussed in the next section. A MH excitation corresponds to an electron transfer between neighboring TM ions, $|d_i^1\ d_j^1\rangle \rightarrow |d_i^2\ d_j^0\rangle$ (considering the simplified case of one electron per lattice site first), where d^n refers to the d shell of a TM ion that is occupied by n electrons. The double occupancy of lattice site i costs the Coulomb-interaction energy U. The MH excitations are the real counterparts of the virtual charge excitations discussed in Sec. 2.4 in the context of superexchange. Their optical spectral weight is intimately connected to the low-energy superexchange interactions. Let us consider the simplified case of a 1D single-band Hubbard chain at half filling in the strong coupling limit ($U/t \gg 1$), see Fig. 2.7. We only consider electric dipole transitions since the intensities of magnetic dipole and electric quadrupole transitions are smaller by a factor of $10^{-5} - 10^{-6}$ [50, 51]. According to the spin selection rule, the total spins of the initial and the final state have to be equal, i.e. $S_i^z = S_f^z$ (assuming that the orbital moment is quenched or the spin-orbit coupling is small, as appropriate for the systems of interest for this work). In the case of AFM spin

order, the excited state resulting from a MH excitation corresponds to a double occupancy of lattice site i with electrons of opposite spin (see Fig. 2.7 (a)). In contrast, the electron transfer is blocked for FM spin order by the Pauli principle (see Fig. 2.7 (b)). This simple model greatly demonstrates that the optical spectral weight of a MH excitation depends sensitively on nearest-neighbor spin-spin correlations.

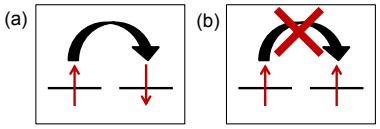

Figure 2.7:
Depending on the orientation of neighboring spins, the MH excitation is either allowed ((a) AFM spin order) or forbidden ((b) FM spin order).

A more difficult situation comes up in the case of partially filled degenerate orbitals. The MH excitations have the general form: $|d_i^n \; d_j^n\rangle \rightarrow |d_i^{n+1} \; d_j^{n-1}\rangle$. The complex multiplet structure of the excited state is reflected in a complex multi-peak structure of the optical spectra [8,9]. In addition to the spin selection rule also the orbital selection rule has to be taken into account, which is determined by the overlap between orbitals on neighboring lattice sites. In a cubic perovskite with 180° bonds, t_{2g} and e_g orbitals do not overlap, there is only overlap between t_{2g} orbitals of the same type, whereas all e_g orbitals have overlap with each other. Consequently, the optical spectral weight of a MH excitation into a certain $|d_i^{n+1} \; d_j^{n-1}\rangle$ multiplet is determined by the orbital occupation of neighboring lattice sites. A change of the nearest-neighbor spin-spin or orbital-orbital correlation function with temperature leads to a spectral weight transfer between the individual components of the optical multiplets [10]. The optical intensity of a MH excitation into a certain multiplet state labeled by n along the cubic axis γ is related to the respective contribution to the superexchange Hamiltonian of Eq. 2.6 via the optical sum rule [8,10]:

$$\int_0^\infty \sigma_n^{(\gamma)}(\omega) d\omega \propto \left\langle H_n^{(\gamma)}(ij) \right\rangle \tag{2.7}$$

Here, $\sigma_n^{(\gamma)}(\omega)$ denotes the contribution to the real part of the optical conductivity $\sigma_1(\omega)$ stemming from the excitation into the multiplet state n along γ. One great example for this correlation is given by ellipsometric data on the $3d^4$ system $LaMnO_3$ (with $t_{2g}^3 e_g^1$, $S = 2$ electron configuration) [11]. As discussed above, the coupling of the e_g orbitals to the lattice is strong and orbital ordering sets in at $T_{OO} = 780\,\mathrm{K}$ in $LaMnO_3$, far above the spin ordering temperature of $T_N = 150\,\mathrm{K}$. Consequently, only the spin degree of freedom has to be considered at lower temperatures. The spin ordering below T_N is of A type, i.e. parallel spins in the ab plane and antiparallel spins along the c axis, see the inset of Fig. 2.8, left

panel. The low-energy band at approx. $2\,\mathrm{eV} - 2.5\,\mathrm{eV}$ in the optical spectra (see Fig. 2.8, left panel) has been assigned to the MH excitation $|3d_i^4\ 3d_j^4\rangle \rightarrow |3d_i^5\ 3d_j^3\rangle$ into the $3d^5$ high-spin ($S = 5/2$) state. Due to the high-spin character, parallel spins on adjacent sites in the initial state are expected to give rise to a larger spectral weight than antiparallel spins. As a consequence, an increase of spectral weight is expected in the ab direction when lowering the temperature across T_N, whereas a reduction of spectral weight is expected along c. This is in striking agreement with the observations (see Fig. 2.8) and greatly demonstrates that the peak assignment is correct. In the opposite sense, optical spectroscopy can be applied as an effective tool for the investigation of nearest-neighbor spin-spin and/or orbital-orbital correlations in TM compounds. We will use this concept for the analysis of our spectra of the $3d^2$ compounds $R\mathrm{VO_3}$ (R=Y, Gd, Ce) (see Sec. 5). In contrary to the e_g system $\mathrm{LaMnO_3}$ the coupling to the lattice is rather weak for these compounds with active t_{2g} orbitals and coupled spin-orbital degrees of freedom have to be considered.

2.7 Mott-Hubbard and charge-transfer insulators

A second type of intersite transition that is of importance for the understanding of our ellipsometric data is the CT excitation. It corresponds to an electron transfer from the ligand oxygen $2p$ band to the TM $3d$ band (UHB): $|p^6\ d^n\rangle \rightarrow |p^5\ d^{n+1}\rangle$. The energy separation between the two bands is given by the CT energy Δ. Depending on the relative size of U_{eff} and Δ_{eff}, the lowest intersite transition corresponds to a MH or a CT excitation[3]. Accordingly, the TM compounds are classified into so-called MH ($U_{eff} < \Delta_{eff}$) and CT ($\Delta_{eff} < U_{eff}$) insulators within the Zaanen-Sawatzky-Allen scheme [52], see Fig. 2.9. Early transition-metal compounds (e.g. TM = Ti, V) are typically classified into the group of MH insulators, whereas late ones (e.g. TM = Ni, Cu) are identified as being of CT type [53–57]. With increasing atomic number U increases whereas Δ decreases [53, 57], which reflects the decreasing spatial extension of the $3d$ orbitals and the increasing electronegativity of the TM ions, respectively. Both intersite transitions are sketched in Fig. 2.10. In TM oxides, typical values for the real part of the optical conductivity $\sigma_1(\omega)$ are of a few $1000\,(\Omega\mathrm{cm})^{-1}$ for CT excitations, whereas for MH excitations the value of $\sigma_1(\omega)$ typically amounts to only a few $100\,(\Omega\mathrm{cm})^{-1}$ [1, 12, 23, 57, 58]. The difference is due to the fact that CT excitations are a first and MH excitations a second order process since the $d_i - d_j$ electron transfer that corresponds to a MH excitation takes place via the ligand O $2p$ orbital. This results in $\sigma_1(\omega) \propto t_{pd}^2/\Delta$ for CT and $\sigma_1(\omega) \propto t_{pd}^4/\Delta^2$ for MH excitations, where

[3] Here, the effective charge-transfer energy Δ_{eff} and the effective Coulomb-interaction energy U_{eff} refer to the lowest excitation energies of the CT excitations and the MH excitations in a multi-orbital system, respectively.

t_{pd} is the TM − O hopping amplitude. A further important difference between MH and CT excitations is the fact that CT excitations are expected to be independent of magnetic properties [59]. As the O $2p$ band is completely filled the oxygen can provide both, up and down spin, and a CT excitation is not blocked by a certain spin alignment on the TM ion (see Fig. 2.10). Consequently, as opposed to the MH excitations, one expects no changes of the spectral weight of a CT excitation across magnetic ordering temperatures. However, due to hybridization an excitation is never of pure MH or CT type in a realistic picture. Therefore the above mentioned is only true in a first approximation.

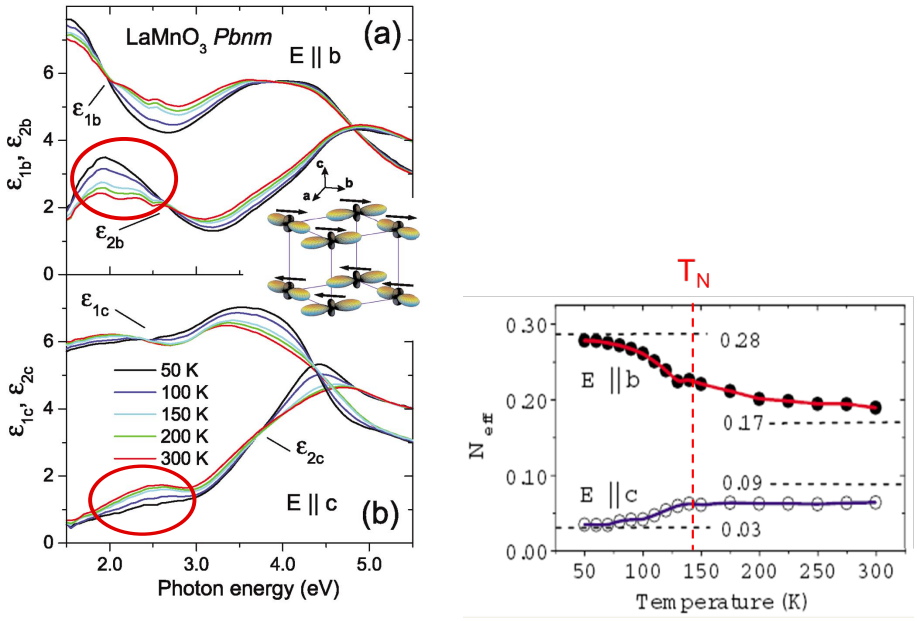

Figure 2.8: Left panel: The dielectric function ε of $LaMnO_3$ corresponding to $E \parallel b$ (a) and $E \parallel c$ (b) for different temperatures as obtained by Kovaleva *et al.* [11] by the use of ellipsometry. Here the focus lies on the temperature dependence of the low-energy absorption band at $\approx 2\,\mathrm{eV} - 2.5\,\mathrm{eV}$ (marked in red). The inset sketches the spin and orbital ordering pattern. Right panel: Spectral weight of the low-energy absorption band for $E \parallel b$ and $E \parallel c$ in terms of the effective carrier concentration N_{eff} which results from a Lorentz fit to the measured data. The dashed lines refer to the result of theoretical calculations based on a superexchange model for the low-temperature ordered and the asymptotic high-temperature disordered phase. Both figures are taken from Ref. [11].

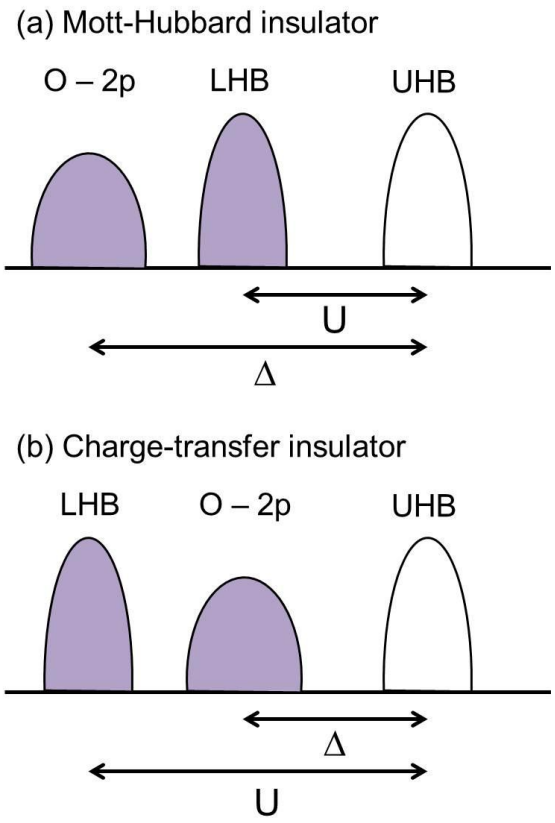

Figure 2.9: Sketch of the photoemission (PES) and inverse photoemission spectra (IPES) of (a) a Mott-Hubbard insulator and (b) a charge-transfer insulator. Full symbols represent fully occupied bands, whereas open symbols represent unoccupied bands.

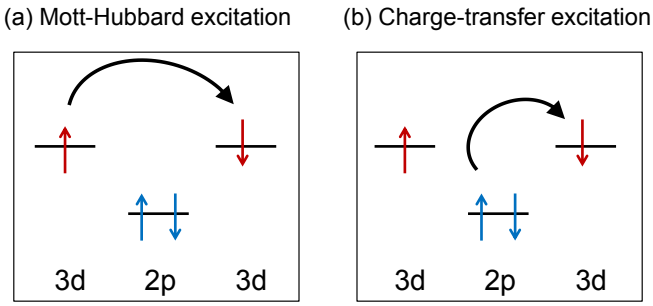

Figure 2.10: Sketch of (a) a Mott-Hubbard excitation and (b) a charge-transfer excitation. While the Mott-Hubbard excitations depend on the spin-spin correlations the charge-transfer excitations are independent of the spin alignment.

3 Optical Spectroscopy

Optical spectroscopy is a very popular technique in solid state physics that is used to investigate the band structure of solids. Furthermore, a variety of excitations, e.g. phonons, magnons, or interband excitations can be detected. Within the framework of this thesis the optical technique ellipsometry is applied, which makes use of the polarization properties of electromagnetic waves.
The chapter on hand is organized as follows. The first section introduces the optical constants, i.e. the quantities of interest in optical spectroscopy. To embed their meaning in a general context, a short introduction into linear response theory is given. The different formulations of the optical constants are presented and the Kramers-Kronig relation is introduced. The reflection properties of electromagnetic waves are briefly discussed and model functions for the optical constants are presented, which are needed for the analysis of the measured data. The second section of this chapter deals exclusively with ellipsometry.

3.1 Linear response functions and optical constants

3.1.1 Linear response theory

Every spectroscopic experiment is based on the principle of response theory. One probes the response of a physical system to the application of an external perturbation. Optical spectroscopy makes use of the interaction properties of electromagnetic waves with matter. The perturbation of a system by an electromagnetic wave leads to a response that is characteristic for its physical properties. Thus, for an external perturbation, the record of the response yields information about the properties of the physical system under consideration. The response $X(\vec{r},t)$ of the system is linked to the external perturbation $S(\vec{r},t)$ by the response function $R(\vec{r},t)$. While $S(\vec{r},t)$ is an externally controllable quantity, the response function $R(\vec{r},t)$ is an intrinsic characteristic of the physical system [34]. The relation between perturbation and response is in general very complicated. However, a linear approximation can be applied if the perturbation operator yields only a small contribution to the Hamiltonian and can be treated in first order. In this case the functional relation between response and external perturbation has the

form [34]:

$$X(\vec{r},t) = \int R(\vec{r},\vec{r}\,',t,t')S(\vec{r}\,',t')d(\vec{r}\,',t') \tag{3.1}$$

Due to the law of causality the perturbation cannot cause an effect before actually acting, the response function is thus a retarded function, i.e. $R(\vec{r},\vec{r}\,',t,t') = 0$ for $t < t'$.
For optical frequencies, an external perturbation in form of an electric field gives rise to phenomena like dispersion, refraction, absorption, and reflection, whereas the interaction of a magnetic field with matter can mostly be neglected.
Many systems fulfill the following conditions:

- The Hamiltonian of the system does not explicitly depend on time. In this case the response function depends only on the difference between the time coordinates, $R(\vec{r},\vec{r}\,',t,t') = R(\vec{r},\vec{r}\,',t-t')$ [34].

- The crystal is translationally invariant with lattice constants much smaller than the optical wavelengths. In this case the response function depends only on the difference of the coordinates of space, $R(\vec{r},\vec{r}\,',t,t') = R(\vec{r}-\vec{r}\,',t,t')$ [34].

If the above mentioned conditions are fulfilled, it is convenient to express Eq. 3.1 in frequency and momentum space. Temporal and spatial Fourier transformation leads to the relation:

$$X(\vec{k},\omega) = R(\vec{k},\omega) \cdot S(\vec{k},\omega) \tag{3.2}$$

It follows from Eq. 3.2 that a monochromatic perturbation which acts at a frequency ω will produce a response of the same frequency. The same holds true for the momentum $\vec{k}$. A peak of the function $X(\vec{k},\omega)$ at a certain frequency ω and momentum $\vec{k}$ corresponds to a peak of the response function $R(\vec{r},t)$ at the same frequency and momentum. It is thus in principle possible to extract the full dispersion relation of the excitations of the system by the use of a linear response measurement [34].
Due to the dispersion relation of light ($\omega = \frac{c}{n} \cdot |\vec{k}|$; c: velocity of light in vacuum; n: refractive index, see below) the order of magnitude of the momentum $|\vec{k}|$ is much smaller than the order of magnitude of the reciprocal lattice vectors for optical frequencies. Thus, one can assume $|\vec{k}| \approx 0$. As a consequence, optics does only allow for excitations with momentum $|\vec{k}| \approx 0$. However, finite momenta are possible if the photon of the electromagnetic wave interacts with more than just one particle of the system, in this case only the sum of the individual momenta has to be equal to zero.

3.1.2 The optical constants

The interaction of an electric field $\vec{E}(\omega)$ with matter induces a complex polarization $\vec{P}(\omega)$. The response function which relates electric field $\vec{E}(\omega)$ and polarization $\vec{P}(\omega)$ to each other is called electric susceptibility $\chi(\omega)$ [60,61]:

$$\vec{P}(\omega) = \varepsilon_0 \chi(\omega) \cdot \vec{E}(\omega) \tag{3.3}$$

In general, $\chi(\omega) = \chi_1(\omega) + i\chi_2(\omega)$ is a complex second-order tensor, which becomes a complex scalar in the case of an isotropic medium. The permittivity of vacuum ε_0 amounts to $8.8542 \cdot 10^{-12}\mathrm{C^2N^{-1}m^{-2}}$ [62].
The electric susceptibility $\chi(\omega)$ is related to the real part of the optical conductivity $\sigma_1(\omega)$ and the real part of the dielectric function $\varepsilon_1(\omega)$ by [60]

$$\chi(\omega) = \chi_1(\omega) + i\chi_2(\omega) = \varepsilon_1(\omega) - 1 + i\frac{1}{\varepsilon_0 \omega}\, \sigma_1(\omega). \tag{3.4}$$

In the limit $\omega = 0$, $\sigma_1(\omega = 0)$ corresponds to the DC electrical conductivity σ_{DC} which is known from Ohm's law ($\vec{j} = \sigma_{DC} \cdot \vec{E}$, where $\vec{j}$ denotes the current density). Both quantities, $\sigma_1(\omega)$ and $\varepsilon_1(\omega)$, are functions of the microscopic elements of the system. They describe the optical properties of the solid and depend on its possible excitations, e.g. lattice vibrations, free carrier absorption in a metal, excitations across the band gap in an insulator, excitonic excitations, orbital excitations, spin excitations, etc. [60].
Combining Eq. 3.3 and Eq. 3.4 leads to:

$$\vec{P}(\omega) = \varepsilon_0 \chi_1(\omega)\vec{E}(\omega) + i\frac{1}{\omega}\sigma_1(\omega)\vec{E}(\omega) \tag{3.5}$$

$$= Re\left[\vec{P}(\omega)\right] + i\frac{1}{\omega}\vec{j}(\omega) \tag{3.6}$$

While the real part of the polarization $Re\left[\vec{P}(\omega)\right]$ describes the electric dipole moment that is induced per unit volume, the imaginary part corresponds to an induced current density $\vec{j}(\omega)$ which leads to a loss of energy, i.e. absorption.
The complex dielectric function (also called dielectric tensor in the anisotropic case)

$$\varepsilon(\omega) = \varepsilon_1(\omega) + i\varepsilon_2(\omega) = \varepsilon_1(\omega) + i\frac{1}{\varepsilon_0 \omega}\sigma_1(\omega) = \chi(\omega) + 1, \tag{3.7}$$

the complex optical conductivity

$$\sigma(\omega) = \sigma_1(\omega) + i\sigma_2(\omega) = \sigma_1(\omega) + i\varepsilon_0\omega(1 - \varepsilon_1(\omega)), \tag{3.8}$$

and the complex electric susceptibility $\chi(\omega)$ are different formulations of the so-called optical constants. While $\varepsilon(\omega)$ and $\chi(\omega)$ are dimensionless, the optical conductivity $\sigma(\omega)$ has the unit $[\sigma] = \Omega^{-1}\mathrm{cm}^{-1}$. Only ε_1 and σ_1 are defined for $\omega = 0$.

The wave equation for the propagation of electromagnetic waves in a medium with dielectric function ε can be derived from Maxwell's equations [60]. It follows:

$$\nabla^2 \cdot \vec{E} = \frac{\varepsilon}{c^2} \frac{\partial^2 \vec{E}}{\partial t^2} \tag{3.9}$$

Harmonic plane waves represent solutions of the wave equation:

$$\vec{E}(\vec{r}, t) = \vec{E}_0 e^{i(\vec{k}\vec{r} - \omega t)} \tag{3.10}$$

with

$$\vec{k}^2 = \frac{\omega^2}{c^2} \cdot \varepsilon \tag{3.11}$$

The complex index of refraction N, which is yet another representation of the optical constants, is defined as

$$N = n + ik = (\varepsilon_1 + i\varepsilon_2)^{\frac{1}{2}}. \tag{3.12}$$

Inserting Eq. 3.12 into Eq. 3.10 leads to

$$\vec{E}(\vec{r}, t) = \vec{E}_0 e^{i(\frac{\omega}{c} n \vec{n}_k \vec{r} - \omega t)} \cdot e^{-\frac{\omega}{c} k \vec{n}_k \vec{r}}. \tag{3.13}$$

The refractive index n is linked to the phase speed in the material, while the imaginary part of the complex index of refraction k is a measure of the loss of intensity caused by absorption when the electromagnetic wave is propagating through the material. Here, $\vec{n}_k$ is the unit vector pointing into the direction of propagation.
Although the optical constants are represented by arbitrary second-order tensors in the general case, for a system with orthorhombic or higher symmetry they are represented by tensors with vanishing off-diagonal elements [63] (if the magnetization can be neglected):

$$\varepsilon_{\mathrm{orthorhombic}}(\omega) = \begin{pmatrix} \varepsilon^a(\omega) & 0 & 0 \\ 0 & \varepsilon^b(\omega) & 0 \\ 0 & 0 & \varepsilon^c(\omega) \end{pmatrix} \tag{3.14}$$

In the case of orthorhombic crystal symmetry the tensor axes coincide with the crystallographic axes.

3.1.3 The Kramers-Kronig relation

The law of causality implies that real and imaginary part of the response function are related to each other. They obey a functional relationship that is called Kramers-Kronig relation. For the dielectric functions $\varepsilon(\omega)$ the relation has the form [61]:

$$\varepsilon_1(\omega) - 1 = \frac{2}{\pi} P \int_0^\infty \frac{\omega' \varepsilon_2(\omega')}{\omega'^2 - \omega^2} d\omega' \tag{3.15}$$

$$\varepsilon_2(\omega) = -\frac{2\omega}{\pi} P \int_0^\infty \frac{\varepsilon_1(\omega') - 1}{\omega'^2 - \omega^2} d\omega' \tag{3.16}$$

Here, P denotes the Cauchy principal value of the integral. This relationship gives additional information for the acquisition of the optical constants from experiments. The application of the relation requires the knowledge of the real or imaginary part of the response function for ω ranging from 0 to ∞. However, a finite energy range in combination with a reasonable extrapolation is often sufficient in order to get a good result. The Kramers-Kronig relation allows for the determination of the optical constants from, e.g., reflectivity measurements alone. Otherwise, if the real and imaginary part of the optical constants are both deduced from the experiment independently, the consistency can be checked with the help of the Kramers-Kronig relation. The latter applies to an ellipsometric measurement, as will be discussed in the second part of this chapter (Sec. 3.2).

3.1.4 Reflection properties of electromagnetic waves

Ellipsometry is based on the reflection of an electromagnetic wave from the surface of the sample under consideration. In the following, the relevant physics is briefly introduced. The angle between the normal to the sample surface and the beam incident on, and reflected from the sample are called the angle of incidence Φ_i, and the angle of reflection Φ_r, respectively. The incoming beam of light and the normal to the sample surface constitute the plane of incidence. The electric field vector of the transversal electromagnetic wave is decomposed into its components parallel (E_p) and perpendicular (E_s) to the plane of incidence. The following expressions are used for the incoming, reflected, and transmitted wave:

$$\vec{E}_i = \begin{pmatrix} E_p^i \\ E_s^i \end{pmatrix} e^{i(\vec{k}_i\vec{r}-\omega_i t)}; \quad \vec{E}_r = \begin{pmatrix} E_p^r \\ E_s^r \end{pmatrix} e^{i(\vec{k}_r\vec{r}-\omega_r t)}; \quad \vec{E}_t = \begin{pmatrix} E_p^t \\ E_s^t \end{pmatrix} e^{i(\vec{k}_t\vec{r}-\omega_t t)} \tag{3.17}$$

The following important relations can be deduced from Maxwell's equations [64]:

- $\omega_i = \omega_r = \omega_t$
- $\vec{k}_i$, $\vec{k}_r$, and $\vec{k}_t$ lie in the plane of incidence.
- angle of incidence Φ_i = angle of reflection $\Phi_r = \Phi$.
- The law of refraction (also called Snell's law) which is given by

  $$\sin\Phi_i = n \sin\Phi_t$$

  can be derived in the simple case of an isotropic sample. Here, Φ_t denotes the angle between the normal to the sample surface and the transmitted

beam of light and n is the refractive index of the sample (which has been introduced in Eq. 3.12).

- If we assume only linear changes of the initial field amplitudes upon reflection from the sample surface, incoming and reflected electric field vectors $\vec{E}_i$ and $\vec{E}_r$ are related by [63]

$$\begin{pmatrix} E_p^r \\ E_s^r \end{pmatrix} = \begin{pmatrix} r_{pp} & r_{sp} \\ r_{ps} & r_{ss} \end{pmatrix} \begin{pmatrix} E_p^i \\ E_s^i \end{pmatrix}. \tag{3.18}$$

  The complex quantities r_{pp}, r_{ss}, r_{ps}, r_{sp} are functions of the dielectric tensor of the sample, the angle of incidence, and in the case of an anisotropic sample of its orientation. They are given by the Fresnel formulas, which follow directly from Maxwell's equations.

Let us define the ellipsometer coordinate system (x, y, z) according to Ref. [65] (see Fig. 3.1). The x axis lies in the sample surface, aligned parallel to the plane of incidence. The y axis lies in the sample surface, aligned perpendicular to the plane of incidence. The z axis is normal to the sample surface and points into the sample, in agreement with a right-handed coordinate system.
The off-diagonal elements r_{ps} and r_{sp} of Eq. 3.18 vanish for isotropic media and for orthorhombic crystals that are oriented such that the crystallographic axes (a, b, c) are parallel to the ellipsometer coordinate system (x, y, z). If the crystallographic axes (a, b, c) are parallel to (x, y, z), respectively, r_{pp} and r_{ss} are given by [66]:

$$r_{pp} = \frac{E_p^r}{E_p^i} = \frac{\sqrt{\varepsilon_a \varepsilon_c}\cos\Phi_i - \sqrt{\varepsilon_c - \sin^2\Phi_i}}{\sqrt{\sqrt{\varepsilon_a \varepsilon_c}\cos\Phi_i + \varepsilon_c - \sin^2\Phi_i}} \tag{3.19}$$

$$r_{ss} = \frac{E_s^r}{E_s^i} = \frac{\cos\Phi_i - \sqrt{\varepsilon_b - \sin^2\Phi_i}}{\cos\Phi_i + \sqrt{\varepsilon_b - \sin^2\Phi_i}} \tag{3.20}$$

$$r_{ps} = r_{sp} = 0 \tag{3.21}$$

If the symmetry is lower than orthorhombic, the off-diagonal elements can be finite for any orientation. Finite off-diagonal elements can also occur as a consequence of depolarizing effects. The ratios of r_{pp}, r_{ss}, r_{ps}, and r_{sp} represent the measured variables of ellipsometry[1], Fig. 3.2 shows an exemplary plot of $\frac{r_{pp}}{r_{ss}}$ as a function of the angle of incidence Φ_i for different isotropic media at a fixed energy.

[1] They will be discussed in detail in Sec. 3.2.

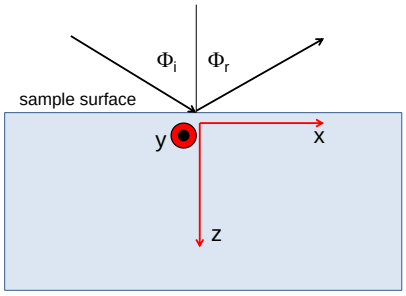

Figure 3.1: The ellipsometer coordinate system is defined by (x, y, z).

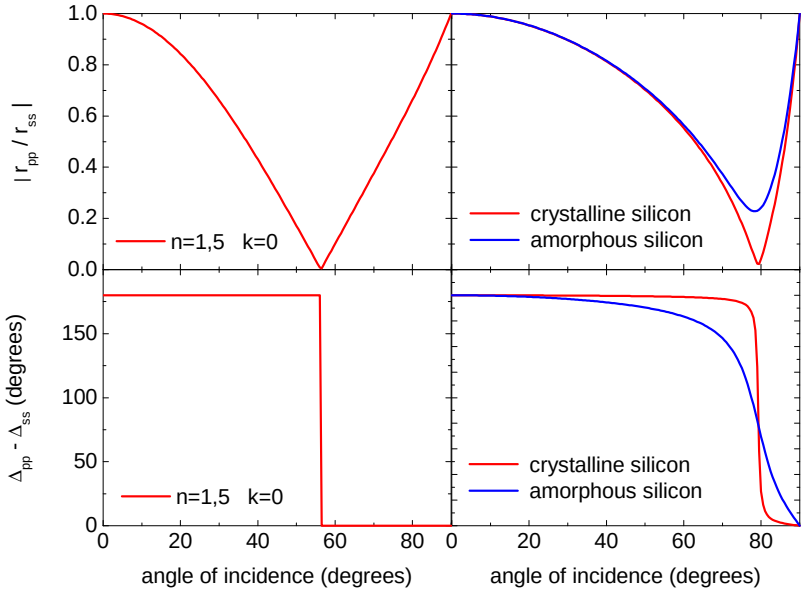

Figure 3.2: The ratio of $r_{pp} = |r_{pp}|\, e^{i\Delta_{pp}}$ and $r_{ss} = |r_{ss}|\, e^{i\Delta_{ss}}$ as a function of the angle of incidence for a material with $n = 1.5$ and $k = 0$ (left) and for crystalline and amorphous silicon at $E = 3\,\mathrm{eV}$ (right). The ratio of the amplitudes $\left|\frac{r_{pp}}{r_{ss}}\right|$ is shown in the upper panels, whereas the lower panels show the phase difference $\Delta_{pp} - \Delta_{ss}$. The simulation has been performed by the use of the software *WVASE32* (J.A. Woollam).

3.1.5 Modeling the dielectric function

To extract the optical constants of the system under investigation from the measured data, it is useful to describe the dielectric function by a parametric model. In the following different models are introduced that are used for the analysis of our ellipsometric data.

The Drude-Lorentz model for the dielectric function is based on the assumption, that the solid consists of a set of non-interacting, damped, harmonic oscillators j with effective mass m^j_{eff}, effective charge e^j_{eff}, damping γ^j, and center energy ω^j_0. The resulting $\varepsilon(\omega)$ is given by a sum of Lorentz oscillators [60]:

$$\varepsilon(\omega) = \varepsilon_\infty + \sum_j \frac{n^j (e^j_{\text{eff}})^2}{\varepsilon_0 m^j_{\text{eff}}} \cdot \frac{1}{(\omega^j_0)^2 - \omega^2 - i\omega\gamma^j}, \tag{3.22}$$

where n^j denotes the number of oscillators j per unit volume. The contributions to ε_1 that result from oscillators with center energies ω_0 far above the measured energy range are given by the real number ε_∞. In the absence of such contributions ε_∞ equals unity. The strength of the oscillator j is given by its plasma frequency $\omega_p = \sqrt{\frac{n^j (e^j_{\text{eff}})^2}{\varepsilon_0 m^j_{\text{eff}}}}$, whereas the damping γ^j is a measure of the width of the corresponding peak in ε_2. The Drude-Lorentz model is consistent with the Kramers-Kronig relation. It is also suited to describe the free-carrier absorption of a metal by adding oscillators with center energies $\omega_0 = 0$, the so-called Drude terms.

The focus of this work is on the interband excitations across the band gap. These excitations often consist of a great number of continuously overlapping excitations. The dielectric function can therefore be composed of a sum of several Lorentz oscillators resulting in a total line shape that can strongly deviate from a Lorentzian form. In particular, using the Drude-Lorentz model for the description of the dielectric function close to a band edge does not often yield a good fit. In this spectral range the line shape of $\varepsilon_2(\omega)$ is much better reproduced by the real, asymmetric Tauc-Lorentz oscillator

$$\varepsilon_2(\omega) = \frac{A\ \omega_0\ \gamma\ (\omega - \omega_g)^2}{(\omega^2 - \omega_0^2)^2 + \gamma^2\omega^2} \cdot \frac{\Theta(\omega - \omega_g)}{\omega}, \tag{3.23}$$

which is determined by its center energy ω_0, strength A, damping γ, and band edge ω_g. Here, $\Theta(\omega)$ denotes the step function ($\Theta(\omega) = 1$ for $\omega \geq 0$ and $\Theta(\omega) = 0$ for $\omega < 0$), consequently $\varepsilon_2(\omega)$ is zero per definition below the band edge ω_g. The Kramers-Kronig transformation yields $\varepsilon_1(\omega)$.

We have experienced that, frequently, the form of $\varepsilon_2(\omega)$ is best described by a sum of real Gaussian oscillators. A Gaussian oscillator does not have the long tail characteristic for the Lorentzian line shape and therefore often yields a better fit to the experimental data especially in the spectral range of a strong absorption edge. More precisely, the Gaussian oscillator is defined by

$$\varepsilon_2(\omega) = \sum_j \left(A^j e^{-\left(\frac{\omega-\omega_0^j}{\Gamma^j}\right)^2} - A^j e^{-\left(\frac{\omega+\omega_0^j}{\Gamma^j}\right)^2} \right), \tag{3.24}$$

with $\mathrm{Br}^j = \Gamma^j \cdot 2\sqrt{\ln(2)}$ being the full width at half maximum (FWHM). Here, ω_0^j and A^j denote the center energy and the amplitude of the oscillator j, respectively. Again, one obtains ε_1 by applying a Kramers-Kronig transformation.
An example for ε_2 consisting of a single Lorentz, Gaussian and Tauc-Lorentz oscillator, respectively, is shown in Fig. 3.3.

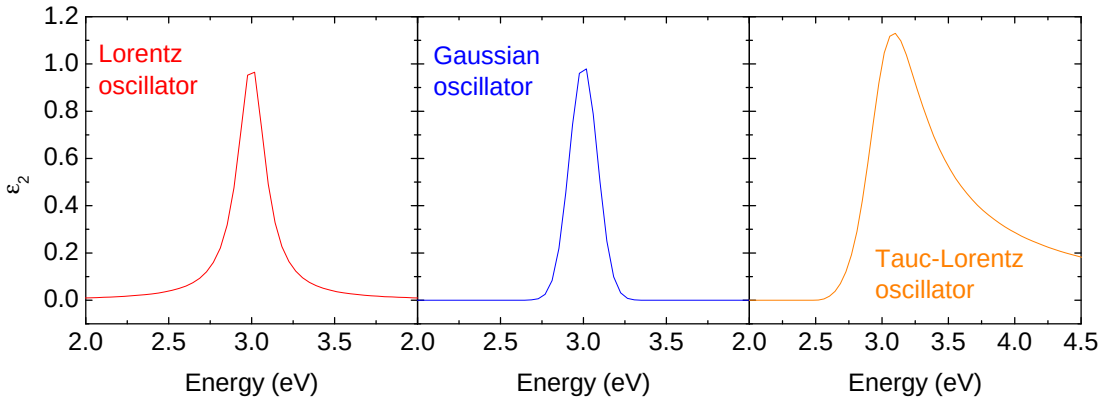

Figure 3.3: Example for ε_2 consisting of a single Lorentz, Gaussian, and Tauc-Lorentz oscillator, respectively. (Parameters: Lorentz: $\omega_p^2/(\omega_0\gamma) = 1$, $\omega_0 = 3\,\mathrm{eV}$, $\gamma = 0.2\,\mathrm{eV}$; Gaussian: $A = 1$, $\omega_0 = 3\,\mathrm{eV}$, Br= 0.2,eV; Tauc-Lorentz: $A = 18\,\mathrm{eV}$, $\omega_0 = 3\,\mathrm{eV}$, $\gamma = 0.5\,\mathrm{eV}$, $\omega_g = 2.5\,\mathrm{eV}$.)

The dielectric function in the non-absorbing spectral range of semiconductors or insulators can be modeled by the use of the Cauchy model [65],

$$n(\lambda) = A + \frac{B}{\lambda^2} + \frac{C}{\lambda^4}, \tag{3.25}$$

where A, B, and C are real numbers. The parameter A represents the index of refraction for infinite wavelength $\lambda = \infty$ (corresponding to energy $\omega = 0$), whereas the dispersion terms B and C have to be chosen so that they generate a positive slope for decreasing wavelengths.

3.2 Ellipsometry

Ellipsometry makes use of the polarization of light to determine the optical properties of materials. For a known polarization of the incoming wave, the polarization of the reflected wave can be measured by acquiring the ratio of the intensities of two independent components and their relative phase shift. The determination of two independent parameters is an advantage of ellipsometry compared to a common reflectivity measurement as there is no need of a Kramers-Kronig transformation to obtain the complex optical conductivity. Furthermore, no reference measurement is necessary as only the ratio of two intensities is relevant. Due to the determination of a relative phase shift, ellipsometry is a very precise measuring method. As the phase shift is particularly sensitive to the surface properties of the reflecting material, ellipsometry is very well suited to study surface structures or thin surface layers. On the other hand, if the bulk properties of a single crystal are of importance, possible surface layers have to be taken into account in the modeling of the data.
A basic sketch of an ellipsometric experiment is shown in Fig. 3.4. The incoming wave has a known polarization, which in general is changed upon reflection from the sample surface. The polarization state of the reflected wave is measured. The change of the polarization state is a function of the optical constants of the sample, the angle of incidence, the wavelength of the incoming wave, and the optical constants and the thickness of a possible surface layer. In the case of an anisotropic sample, the change of the polarization state depends also on the orientation of the sample.
The measurement of a polarization state should lead to the acquisition of the optical constants of the reflecting sample. Therefore a formalism is needed to describe the propagation of electromagnetic waves through an optical system. In Sec. 3.2.1, two different formalisms are introduced, the Jones and the Mueller-matrix formalism. While the Jones formalism is only suited to describe the propagation of totally polarized light, it has the advantage of being more straight forward. The propagation of only partially polarized light can be described by the more complex Mueller-matrix formalism. A formal description of all optical elements, which are relevant for the experimental setup, is derived in both formalisms and the measured variables of both formalisms are introduced. Major parts of these sections follow the argumentations of Ref. [63]. In Sec. 3.2.2 it is shown which information can be directly deduced from the measured variables without any data analysis. In Sec. 3.2.3 the working principle of the ellipsometer is presented. Finally, in Sec. 3.2.4, some parameters that are of importance for the fitting procedure are introduced.

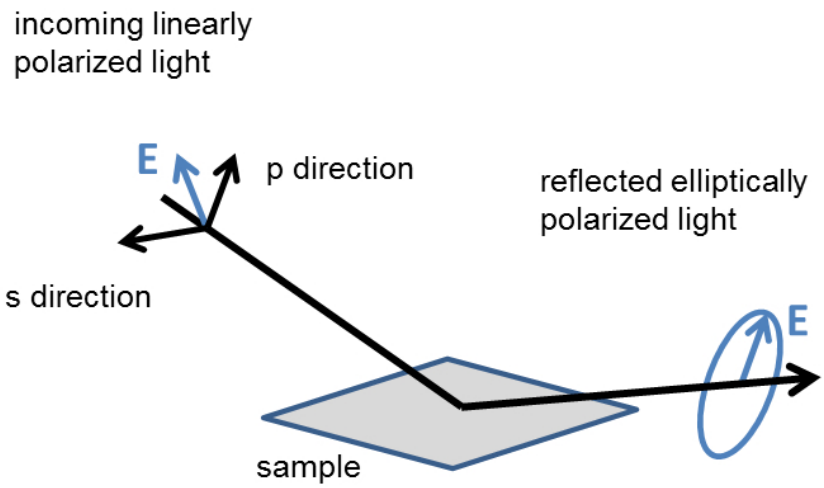

Figure 3.4: Sketch of an ellipsometric experiment.

3.2.1 Jones and Mueller-matrix formalism

In this section the Jones formalism and the Mueller-matrix formalism are introduced. The approach outlined in the following mainly reproduces the argumentation of Ref. [63].

Jones formalism

In the Jones formalism the polarization state of an electromagnetic wave is expressed by a vector of two components, the so-called Jones vector, while an optical element is expressed by a 2×2 matrix, the so-called Jones matrix. The change of polarization state upon passing an optical element is described by multiplying the Jones vector with the Jones matrix. Let us begin with the introduction of the Jones vector.
In general, a monochromatic electromagnetic wave is elliptically polarized.

$$\vec{E} = \begin{pmatrix} E_p \\ E_s \end{pmatrix} = \begin{pmatrix} |E_p|\, e^{i\Delta_p} \\ |E_s|\, e^{i\Delta_s} \end{pmatrix} e^{i(\vec{k}\vec{r}-\omega t)}$$

$$= (|E_p|^2 + |E_s|^2)^{\frac{1}{2}} \begin{pmatrix} \sin\Psi e^{i(\Delta_p-\Delta_s)} \\ \cos\Psi \end{pmatrix} e^{i(\vec{k}\vec{r}-\omega t+\Delta_s)}$$

$$= (|E_p|^2 + |E_s|^2)^{\frac{1}{2}} \vec{J}_{\Psi\Delta} \cdot e^{i(\vec{k}\vec{r}-\omega t+\Delta_s)}$$

with

$$\vec{J}_{\Psi\Delta} = \begin{pmatrix} \sin\Psi e^{i\Delta} \\ \cos\Psi \end{pmatrix}; \quad \Psi \in \left[0; \frac{\pi}{2}\right]; \quad \Delta = \Delta_p - \Delta_s; \quad \Delta \in]-\pi; \pi]$$

The normalized vector $\vec{J}_{\Psi\Delta}$ is the Jones vector. The variables Ψ and Δ determine the polarization state. Both, the absolute value of the vector $\begin{pmatrix} |E_p|\, e^{i\Delta_p} \\ |E_s|\, e^{i\Delta_s} \end{pmatrix}$, which is proportional to the intensity of the wave, and the absolute phase of the wave are not relevant for the description of the polarization state. A measurement of the polarization state does thus imply the determination of the Jones vector, i.e. the acquisition of the variables Ψ and Δ for each frequency.
The sign of Δ determines the sense of precession of the polarization ellipse. For positive values of Δ it is clockwise and the polarization is called right-handed. For negative values of Δ it is counter-clockwise and the polarization is called left-handed.
The Jones vectors of linearly polarized light in the plane of incidence, perpendicular to the plane of incidence, right-handed circularly polarized light, and left-handed circularly polarized light are [63]

$$\vec{J}_p = \begin{pmatrix} 1 \\ 0 \end{pmatrix}, \quad \vec{J}_s = \begin{pmatrix} 0 \\ 1 \end{pmatrix}, \quad \vec{J}_{\sigma^+} = \frac{1}{\sqrt{2}} \begin{pmatrix} i \\ 1 \end{pmatrix}, \text{ and } \vec{J}_{\sigma^-} = \frac{1}{\sqrt{2}} \begin{pmatrix} -i \\ 1 \end{pmatrix}, \quad (3.26)$$

respectively.

As already mentioned, the change of the polarization state of a beam of light upon passing an optical element is described by the multiplication of the Jones vector with the Jones matrix $\widehat{J}$ characterizing the optical element:

$$\begin{pmatrix} E'_a \\ E'_b \end{pmatrix} = \widehat{J} \begin{pmatrix} E_x \\ E_y \end{pmatrix} = \begin{pmatrix} J_{11} & J_{12} \\ J_{21} & J_{22} \end{pmatrix} \begin{pmatrix} E_x \\ E_y \end{pmatrix} \quad (3.27)$$

It is important to note that the Jones matrix depends on the coordinate system, which can be different for the incoming and the reflected wave. In Eq. 3.27 the coordinate systems (x, y) and (a, b) in the plane of polarization are used for the incoming and reflected wave, respectively. The z axis points towards the respective direction of propagation. In Eq. 3.27 only linear changes of the polarization state of a fully polarized monochromatic wave are considered.

In the following the Jones matrices of the optical elements relevant for our experimental setup are derived. Therefore a matrix is needed which links two coordinate systems (x, y) and (x', y'). Let the coordinate system (x', y') originate from a counter-clockwise rotation of the coordinate system (x, y) by an angle α about

the common z axis. If $\begin{pmatrix} E_x \\ E_y \end{pmatrix}$ und $\begin{pmatrix} E_{x'} \\ E_{y'} \end{pmatrix}$ specify the same polarization state in the different coordinate systems (x, y) and (x', y'), respectively, it follows [63]:

$$\begin{pmatrix} E_{x'} \\ E_{y'} \end{pmatrix} = \widehat{R}_J(\alpha) \begin{pmatrix} E_x \\ E_y \end{pmatrix} = \begin{pmatrix} \cos\alpha & \sin\alpha \\ -\sin\alpha & \cos\alpha \end{pmatrix} \begin{pmatrix} E_x \\ E_y \end{pmatrix} \tag{3.28}$$

where $\widehat{R}_J(\alpha)$ is the rotation matrix. With the help of Eq. 3.28 the transformation properties of the Jones matrix can be derived [63]. Let the coordinate systems (x', y') and (a', b') originate from a rotation of the (x, y) and (a, b) coordinate systems, respectively, by the angle α about the common z axis.

$$\begin{pmatrix} E_{x'} \\ E_{y'} \end{pmatrix} = \widehat{R}_J(\alpha) \begin{pmatrix} E_x \\ E_y \end{pmatrix}; \quad \begin{pmatrix} E'_{a'} \\ E'_{b'} \end{pmatrix} = \widehat{R}_J(\alpha) \begin{pmatrix} E'_a \\ E'_b \end{pmatrix} \tag{3.29}$$

Therewith it follows for the Jones matrices $\widehat{J}$ and $\widehat{J}'$ which describe the same transformation in different coordinate systems $(x, y)(a, b)$ and $(x', y')(a', b')$, respectively [63]

$$\begin{pmatrix} E'_a \\ E'_b \end{pmatrix} = \widehat{J} \begin{pmatrix} E_x \\ E_y \end{pmatrix}; \quad \begin{pmatrix} E'_{a'} \\ E'_{b'} \end{pmatrix} = \widehat{J}' \begin{pmatrix} E_{x'} \\ E_{y'} \end{pmatrix} \tag{3.30}$$

the relation

$$\widehat{J}' = \widehat{R}_J(\alpha)\ \widehat{J}\ \widehat{R}_J(-\alpha). \tag{3.31}$$

To create a polarized beam of light, a polarizer is needed in the experimental setup. A linear polarizer changes any polarization state of the beam of light to linear polarized light. In the following the Jones matrix of a linear polarizer with an arbitrary polarization axis is introduced. For a polarizer with polarization axis parallel to the x axis, the Jones matrix is given by [63]:

$$\widehat{J}_{\mathrm{Pol}} = \begin{pmatrix} 1 & 0 \\ 0 & 0 \end{pmatrix}. \tag{3.32}$$

Here, an ideal linear polarizer with no attenuation and zero phase shift is assumed. If the polarization axis is rotated by an angle P away from the x axis the corresponding Jones matrix has the form [63]:

$$\widehat{J}_{\mathrm{Pol}_P} = \widehat{R}_J(-P) \begin{pmatrix} 1 & 0 \\ 0 & 0 \end{pmatrix} \widehat{R}_J(P) \tag{3.33}$$

Another component of the experimental setup is a linear retarder. In an ideal linear retarder, the light polarized linearly along its so-called slow axis experiences a phase retardation by an angle Δ_r. A linear polarizer with variable angle P in

combination with a variable retarder can produce any arbitrary elliptic polarization. If the slow axis is oriented along the x axis the Jones matrix of the linear retarder $\widehat{J}_{\mathrm{Ret}_{\Delta_r}}$ becomes [63]:

$$\widehat{J}_{\mathrm{Ret}_{\Delta_r}} = \begin{pmatrix} e^{-i\Delta_r} & 0 \\ 0 & 1 \end{pmatrix} \tag{3.34}$$

If the slow axis is rotated by an angle R away from the x axis, the Jones matrix transforms as

$$\widehat{J}_{\mathrm{Ret}_{\Delta_r,R}} = \widehat{R}_J(-R) \begin{pmatrix} e^{-i\Delta_r} & 0 \\ 0 & 1 \end{pmatrix} \widehat{R}_J(R). \tag{3.35}$$

The measured variables of the Jones formalism are the entries of the Jones matrix $\widehat{J}_{\mathrm{sample}}$ which describes the reflection of the electromagnetic wave on the sample surface:

$$\begin{pmatrix} E_p^r \\ E_s^r \end{pmatrix} = \widehat{J}_{\mathrm{sample}} \cdot \begin{pmatrix} E_p^i \\ E_s^i \end{pmatrix} = \begin{pmatrix} r_{pp} & r_{sp} \\ r_{ps} & r_{ss} \end{pmatrix} \begin{pmatrix} E_p^i \\ E_s^i \end{pmatrix} \tag{3.36}$$

The Jones matrix consists of four complex reflection coefficients. As ellipsometry does not determine the absolute phase and absolute intensity of the reflected wave, six independent measured variables remain. Mostly, they are defined as follows [63]:

$$\rho_{pp} = \frac{r_{pp}}{r_{ss}} = \tan\Psi_{pp} \cdot e^{i\Delta_{pp}} \tag{3.37}$$

$$\rho_{ps} = \frac{r_{ps}}{r_{pp}} = \tan\Psi_{ps} \cdot e^{i\Delta_{ps}} \tag{3.38}$$

$$\rho_{sp} = \frac{r_{sp}}{r_{ss}} = \tan\Psi_{sp} \cdot e^{i\Delta_{sp}} \tag{3.39}$$

In the case of an isotropic sample, the off-diagonal elements r_{ps} and r_{sp} vanish and the measured variables are reduced to the complex quantity ρ_{pp} [63,65]. The quantities Ψ_{pp} and Δ_{pp} that define ρ_{pp} are called the ellipsometric variables. As ellipsometry acquires two independent parameters per measuring point, one measurement suffices to obtain Ψ_{pp} and Δ_{pp}. To determine the six independent parameters of an anisotropic crystal, data has to be acquired for three different polarization states of the incoming wave. As the measured variables of an anisotropic sample are not sensitive to all entries of its dielectric tensor, data has to be taken at different orientations of the crystal to obtain the full optical properties. To already mention a key aspect of the detailed discussion of Sec. 3.2.2, the Jones matrix of an anisotropic crystal that is oriented with its crystallographic axes parallel to the ellipsometer coordinate system has vanishing off-diagonal elements. This simplifies the measuring process considerably: A proper oriented anisotropic crystal can be measured in the time-saving isotropic measuring mode (data for one polarization state of the incoming wave suffices) acquiring only the ellipsometric variables Ψ_{pp} and Δ_{pp}.

Mueller-Stokes formalism

In contrast to the Jones formalism the Mueller-Stokes formalism deals with the problem of only partially polarized light. Here, the polarization state is represented by a vector of four components, the so-called Stokes vector. An optical element is represented by a 4×4 matrix, the so-called Mueller matrix [63]. In opposition to Jones vector and Jones matrix, the entries of Stokes vector and Mueller matrix are real numbers. The Stokes vector is defined using the (p, s) coordinate system in the plane of polarization, where p and s denote the component which is polarized parallel and perpendicular to the plane of incidence, respectively. The four Stokes parameters, which are written in a column vector $\vec{S}$, are given by [63]:

$$\vec{S} = \begin{pmatrix} S_0 \\ S_1 \\ S_2 \\ S_3 \end{pmatrix} = \begin{pmatrix} I_0 \\ I_p - I_s \\ I_{45^\circ} - I_{-45^\circ} \\ I_{\sigma^+} - I_{\sigma^-} \end{pmatrix} \tag{3.40}$$

Here, I_0 denotes the total intensity of the analyzed beam, I_p and I_s denote the intensity of the component which is polarized along p and s, respectively, I_{45° and I_{-45° denote the intensity of the component which is polarized at an angle of 45° and -45° away from the p direction, respectively. Finally, I_{σ^+} and I_{σ^-} denote the intensity of the component which is right-handed and left-handed circularly polarized, respectively.
The Stokes vectors of linear polarizations along p and s, right-handed and left-handed circular polarizations are [63]:

$$\vec{S}_p = I_0 \begin{pmatrix} 1 \\ 1 \\ 0 \\ 0 \end{pmatrix}, \quad \vec{S}_s = I_0 \begin{pmatrix} 1 \\ -1 \\ 0 \\ 0 \end{pmatrix}, \quad \vec{S}_{\sigma^+} = I_0 \begin{pmatrix} 1 \\ 0 \\ 0 \\ 1 \end{pmatrix}, \quad \vec{S}_{\sigma^-} = I_0 \begin{pmatrix} 1 \\ 0 \\ 0 \\ -1 \end{pmatrix}, \tag{3.41}$$

respectively.
The Stokes vector of a totally elliptically polarized beam $\vec{S}_{\Psi\Delta}$ that is characterized by the variables Ψ and Δ (which have been introduced on page 29) reads:

$$\vec{S}_{\Psi\Delta} = I_0 \begin{pmatrix} 1 \\ -\cos(2\Psi) \\ \sin(2\Psi)\cos\Delta \\ -\sin(2\Psi)\sin\Delta \end{pmatrix} \tag{3.42}$$

It can be derived from the corresponding Jones vector as follows:

$$S_0 = I_0$$

$$S_1 = I_p - I_s = I_0(\sin^2\Psi - \cos^2\Psi) = -I_0\cos(2\Psi)$$

$$S_2 = I_{45} - I_{-45} = I_0\left|\frac{1}{\sqrt{2}}\begin{pmatrix}1\\1\end{pmatrix}\begin{pmatrix}\sin\Psi e^{i\Delta}\\\cos\Psi\end{pmatrix}\right|^2 - I_0\left|\frac{1}{\sqrt{2}}\begin{pmatrix}1\\-1\end{pmatrix}\begin{pmatrix}\sin\Psi e^{i\Delta}\\\cos\Psi\end{pmatrix}\right|^2$$

$$= I_0\left\{\frac{1}{2}\left|\sin\Psi e^{i\Delta} + \cos\Psi\right|^2 - \frac{1}{2}\left|\sin\Psi e^{i\Delta} - \cos\Psi\right|^2\right\} =$$

$$I_0\left\{\left(\frac{1}{2} + \sin\Psi\cos\Psi\cos\Delta\right) - \left(\frac{1}{2} - \sin\Psi\cos\Psi\cos\Delta\right)\right\} = I_0\sin(2\Psi)\cos\Delta$$

$$S_3 = I_{\sigma^+} - I_{\sigma^-} = I_0\left|\frac{1}{\sqrt{2}}\begin{pmatrix}i\\1\end{pmatrix}\begin{pmatrix}\sin\Psi e^{i\Delta}\\\cos\Psi\end{pmatrix}\right|^2 - I_0\left|\frac{1}{\sqrt{2}}\begin{pmatrix}-i\\1\end{pmatrix}\begin{pmatrix}\sin\Psi e^{i\Delta}\\\cos\Psi\end{pmatrix}\right|^2$$

$$= I_0\left\{\frac{1}{2}\left|i\sin\Psi e^{i\Delta} + \cos\Psi\right|^2 - \frac{1}{2}\left|-i\sin\Psi e^{i\Delta} + \cos\Psi\right|^2\right\} =$$

$$I_0\left\{\left(\frac{1}{2} - \sin\Psi\cos\Psi\sin\Delta\right) - \left(\frac{1}{2} + \sin\Psi\cos\Psi\sin\Delta\right)\right\} = -I_0\sin(2\Psi)\sin\Delta$$

The degree of polarization $P_{\Psi\Delta}$ refers to the fraction of polarized intensity in the total intensity. It can be directly derived from the Stokes vector [63]:

$$P_{\Psi\Delta} = \frac{\sqrt{S_1^2 + S_2^2 + S_3^2}}{S_0} \tag{3.43}$$

The degree of polarization adopts values from zero for fully unpolarized light to unity for totally polarized light. The Stokes vector of a fully unpolarized beam reads [63]:

$$\vec{S}_{\text{unpol}} = I_0\begin{pmatrix}1\\0\\0\\0\end{pmatrix} \tag{3.44}$$

The Stokes vector of a partially polarized beam has the form [63]:

$$\vec{S}_{P_{\Psi\Delta}} = I_0\left[P_{\Psi\Delta}\begin{pmatrix}1\\-\cos(2\Psi)\\\sin(2\Psi)\cos\Delta\\-\sin(2\Psi)\sin\Delta\end{pmatrix} + (1 - P_{\Psi\Delta})\begin{pmatrix}1\\0\\0\\0\end{pmatrix}\right] \tag{3.45}$$

Analogous to the Jones formalism, the Mueller-Stokes formalism describes the propagation of a polarized beam through an optical system by successively multiplying the corresponding Stokes vector with the Mueller matrices $\widehat{M}$ which describe the actions of the individual optical elements. Without depolarization, the 4×4 Mueller and the 2×2 Jones matrix are directly related to each other [63]:

$$\widehat{M} = \widehat{A} \cdot (\widehat{J} \otimes \widehat{J}^*) \cdot \widehat{A}^{-1} \tag{3.46}$$

The symbol $\otimes$ denotes the direct product of two matrices. The matrix $\widehat{A}$ has the form:

$$\widehat{A} = \begin{pmatrix} 1 & 0 & 0 & 1 \\ 1 & 0 & 0 & -1 \\ 0 & 1 & 1 & 0 \\ 0 & i & -i & 0 \end{pmatrix} \tag{3.47}$$

Equation 3.46 does not hold true if depolarizing effects are present, as depolarization cannot be expressed by the Jones formalism. Since the Stokes vectors are defined with respect to a specific coordinate system within the plane of polarization, the Mueller matrix also depends on the chosen coordinate system. The definition of the Stokes vector implies that the polarization state of the incoming and reflected beam is expressed in the (p, s) coordinate system. However, Stokes vector and Mueller matrix could alternatively be expressed in any other coordinate system that lies in the plane of polarization.
To obtain the Mueller matrix of the optical elements, as in the Jones formalism, a matrix is needed that links two coordinate systems, which result from each other by a rotation by an angle α. It has the form [63]:

$$\widehat{R}_M(\alpha) = \begin{pmatrix} 1 & 0 & 0 & 0 \\ 0 & \cos(2\alpha) & \sin(2\alpha) & 0 \\ 0 & -\sin(2\alpha) & \cos(2\alpha) & 0 \\ 0 & 0 & 0 & 1 \end{pmatrix}. \tag{3.48}$$

Equation 3.31 holds true for the Mueller-Stokes formalism when replacing the Jones matrix by the Mueller matrix and the matrix $\widehat{R}_J(\alpha)$ by $\widehat{R}_M(\alpha)$.
The Mueller matrix of an ideal linear polarizer with the polarization axis rotated by an angle P away from the plane of incidence is given by [63]:

$$\widehat{M}_{Pol_P} = \widehat{R}_M(-P)\, \frac{1}{2} \begin{pmatrix} 1 & 1 & 0 & 0 \\ 1 & 1 & 0 & 0 \\ 0 & 0 & 0 & 0 \\ 0 & 0 & 0 & 0 \end{pmatrix} \widehat{R}_M(P) \tag{3.49}$$

The Mueller matrix of a linear retarder, which induces a phase shift Δ_r between the component which is rotated by an angle R away from the p axis and the

thereto perpendicular component has the form [63]:

$$\widehat{M}_{\mathrm{Ret}_{\Delta_r,R}} = \widehat{R}_M(-R) \begin{pmatrix} 1 & 0 & 0 & 0 \\ 0 & 1 & 0 & 0 \\ 0 & 0 & \cos\Delta_r & \sin\Delta_r \\ 0 & 0 & -\sin\Delta_r & \cos\Delta_r \end{pmatrix} \widehat{R}_M(R) \tag{3.50}$$

The measured quantities of the Mueller-Stokes formalism are the 16 entries of the Mueller matrix which describe the reflection of the beam of light on the sample surface. In the special non-depolarizing case of an isotropic or orthorhombic crystal with crystallographic axes parallel to the ellipsometer coordinate system the Mueller matrix can be written as [63]:

$$\widehat{M}_{\text{sample, isotropic}} = \frac{|r_{pp}|^2 + |r_{ss}|^2}{2} \cdot$$

$$\begin{pmatrix} 1 & -\cos(2\Psi_{pp}) & 0 & 0 \\ -\cos(2\Psi_{pp}) & 1 & 0 & 0 \\ 0 & 0 & \sin(2\Psi_{pp})\cos\Delta_{pp} & \sin(2\Psi_{pp})\sin\Delta_{pp} \\ 0 & 0 & -\sin(2\Psi_{pp})\sin\Delta_{pp} & \sin(2\Psi_{pp})\cos\Delta_{pp} \end{pmatrix}$$

$$= \frac{|r_{pp}|^2 + |r_{ss}|^2}{2} \begin{pmatrix} 1 & -N & 0 & 0 \\ -N & 1 & 0 & 0 \\ 0 & 0 & C & S \\ 0 & 0 & -S & C \end{pmatrix} \tag{3.51}$$

It is directly related to the corresponding Jones matrix by Eq. 3.46. Here, between N, C, and S holds the relation $N^2 + C^2 + S^2 = 1$, i.e. N, C, and S are not independent of each other. Just as in the Jones formalism, the independent parameters are Ψ_{pp} and Δ_{pp}. In the Mueller matrix of Eq. 3.51, 10 entries are zero or unity. A deviation thereof indicates either that the crystallographic axes of an anisotropic crystal are not aligned parallel to the ellipsometer coordinate system or that depolarization is important.
The Mueller matrix of a sample with simple depolarizing properties is given by [63]:

$$\widehat{M}_{\text{sample, }\gamma} = \gamma \widehat{M}_{\text{sample, }P} + (1-\gamma) \begin{pmatrix} 1 & 0 & 0 & 0 \\ 0 & 0 & 0 & 0 \\ 0 & 0 & 0 & 0 \\ 0 & 0 & 0 & 0 \end{pmatrix}. \tag{3.52}$$

Here, $\gamma \in [0,1]$ is the fraction of polarized light in the reflected beam and $\widehat{M}_{\text{sample, }P}$ is the Mueller matrix of the non-depolarizing sample. Hence, the Mueller matrix now contains an additional independent parameter. In the case of an isotropic

material the Mueller matrix of Eq. 3.52 has the form

$$\widehat{M}_{\text{sample, isotropic, }\gamma} = \frac{|r_{pp}|^2 + |r_{ss}|^2}{2} \begin{pmatrix} 1 & -\widetilde{N} & 0 & 0 \\ -\widetilde{N} & \gamma & 0 & 0 \\ 0 & 0 & \widetilde{C} & \widetilde{S} \\ 0 & 0 & -\widetilde{S} & \widetilde{C} \end{pmatrix} \tag{3.53}$$

with

$$\widetilde{N} = \gamma \cdot \cos(2\Psi_{pp})$$
$$\widetilde{C} = \gamma \cdot \sin(2\Psi_{pp}) \sin \Delta_{pp}$$
$$\widetilde{S} = \gamma \cdot \sin(2\Psi_{pp}) \cos \Delta_{pp}$$

and

$$\gamma = \sqrt{\widetilde{N}^2 + \widetilde{C}^2 + \widetilde{S}^2}. \tag{3.54}$$

In contrast to the non-depolarizing case, $\widetilde{N}$, $\widetilde{C}$, and $\widetilde{S}$ are independent parameters. A partially depolarized reflected wave can be caused by various phenomena. Backside reflections which interfere incoherently with the main beam can occur in sufficiently transparent samples. Rough sample surfaces can be another reason for depolarization. Real monochromators produce a beam of light with a finite band width, which also leads to depolarization.

3.2.2 The pseudo-dielectric function

For an isotropic sample the optical constants can be directly obtained by inverting the ellipsometric variables Ψ_{pp} and Δ_{pp} with the help of the Fresnel equations. In this case, a bulk crystal without surface layers is assumed. However, thin cover layers due to oxides or contaminations are always present to some extent. The dielectric function obtained by simple inversion is thus called pseudo-dielectric function $< \varepsilon > = < \varepsilon_1 > \ + i < \varepsilon_2 >$.

$$< \varepsilon > = < \varepsilon_1 > \ + i < \varepsilon_2 > = \sin^2(\Phi) \left(1 + \left[\frac{1 - \rho_{pp}}{1 + \rho_{pp}} \right]^2 \tan^2(\Phi) \right) \tag{3.55}$$

Again, Φ is the angle of incidence. The pseudo-dielectric function is just another representation of the ellipsometric variables Ψ_{pp} and Δ_{pp}. In contrast to Ψ_{pp} and Δ_{pp}, it does not depend on the angle of incidence. However, surface layers or backside reflections can lead to a Φ dependence of $< \varepsilon >$. Hence, a comparison of $< \varepsilon >$ measured at different Φ values can give information about the possible existence of surface layers.
For an orthorhombic system the whole dielectric tensor consisting of three complex numbers is needed to describe the optical properties. At first sight, Eq. 3.55

is not of any use in this case. However, D. Aspnes [67] has theoretically shown the following:

- Inserting the Ψ_{pp} and Δ_{pp} values that are obtained by measuring a biaxial sample into Eq. 3.55 yields mainly the component of the dielectric tensor that lies in the cross-section of the sample surface and the plane of incidence. As a consequence, if the crystallographic axes of an anisotropic crystal are oriented parallel to the ellipsometer coordinate system the approximate components of the dielectric tensor can be directly read off from the measured pseudo-dielectric function without any data modeling.

The statement of D. Aspnes [67] only holds true if the following conditions are fulfilled [67]:

- ε^a, ε^b, and ε^c are given by

$$\varepsilon^a = \varepsilon^{\text{mean}} + \Delta\varepsilon^a \tag{3.56}$$

$$\varepsilon^b = \varepsilon^{\text{mean}} + \Delta\varepsilon^b \tag{3.57}$$

$$\varepsilon^c = \varepsilon^{\text{mean}} + \Delta\varepsilon^c \tag{3.58}$$

  where $\varepsilon^{\text{mean}}$ is a suitable isotropic mean value. The additional terms represent anisotropic corrections which are small and can be treated in first order.

- $|\varepsilon^{\text{mean}}|$ is moderately large, i.e. on the order of 10.

- Typical angles of incidence of about 70° are assumed.

To obtain the exact components of the dielectric tensor, including possible surface layers, a modeling of the ellipsometric data is necessary.
Since the data that is obtained from the measurement of an anisotropic crystal is not sensitive to all three components ε^a, ε^b, and ε^c of the dielectric tensor, data has to be taken at different orientations of the crystal. To obtain the optical constants of a uniaxial material, data has to be taken at least at two different orientations of the sample. For incidence, a (100) plane could be measured with the optical axis (c axis) lying parallel and perpendicular to the plane of incidence. The full optical information of a biaxial material can only be obtained by measuring at least three different orientations of the sample. Here, at least two different sample surfaces are necessary. In this case, data could be taken from a (001) surface with the a and the b axis lying in the plane of incidence, respectively, and a (100) surface with the c axis lying in the plane of incidence.

3.2.3 The working principle of a rotating analyzer ellipsometer

The measurements reported in this work are carried out with a "rotating analyzer ellipsometer" (RAE). Its working principle will be introduced in this section. The combination of a variable polarizer and a variable retarder in front of the sample produces any arbitrary elliptic polarization state of the beam of light leaving the monochromator. The modified polarization state of the reflected wave is determined by using a second linear polarizer with a harmonically rotating transmission axis, which is called rotating analyzer. The detector signal is proportional to the intensity of the beam of light hitting the detector. In the following an expression is derived for the light intensity that enters the detector. It depends on the polarizer angle P, the retardation Δ_r introduced by the retarder, the analyzer angle $A(t)$, and the Mueller-matrix elements m_{ij} of the sample. Using the Mueller-Stokes formalism, the Stokes vector of the transformed wave $\vec{S}^r$ results from the Stokes vector of the incoming wave $\vec{S}^i$ by successively multiplying the Mueller matrices describing the optical elements:

$$\vec{S}^r = \widehat{M}_{\mathrm{Pol}_{A(t)}} \cdot \widehat{M}_{\mathrm{sample}} \cdot \widehat{M}_{\mathrm{Ret}_{\Delta_r, R=0}} \cdot \widehat{M}_{\mathrm{Pol}_P} \cdot \vec{S}^i \tag{3.59}$$

The detector measures the time-dependent total intensity which is the first component of the Stokes vector. Inserting the expressions of Eqs. 3.49 and 3.50 into Eq. 3.59 one obtains [43]:

$$S_0^r = \frac{1}{2}(T_0 + T_1\cos(2A(t)) - T_2\sin(2A(t)) = \frac{1}{2}T_0(1 + \alpha\cos(2A(t)) + \beta\sin(2A(t)) \tag{3.60}$$

where

$$T_0 = \frac{1}{2}(m_{11} + m_{12}\cos(2P)) + (m_{13}\cos\Delta_r - m_{14}\sin\Delta_r)\sin(2P)$$

$$T_1 = \frac{1}{2}(m_{21} + m_{22}\cos(2P)) + (m_{23}\cos\Delta_r - m_{24}\sin\Delta_R)\sin(2P)$$

$$T_2 = \frac{1}{2}(m_{31} + m_{32}\cos(2P)) + (m_{33}\cos\Delta_r - m_{34}\sin\Delta_r)\sin(2P)$$

The intensity at the detector does not depend on the fourth row of the Mueller matrix. As a consequence, it cannot be determined by a measurement using the above mentioned setup. A second retarder between sample and analyzer is necessary for its determination. Closer inspection of the above equations reveals, that without a retarder between polarizer and sample also the last column of the Mueller matrix could not have been determined.
The measured variables are the Fourier coefficients α and β of Eq. 3.60. To deduce

the Mueller-matrix elements from α and β data has to be acquired at different values of P and Δ_r. The ellipsometer software acquires more data than necessary and obtains the Mueller-matrix elements through regression. In the special case of an isotropic sample without a retarder ($\Delta_r = 0$) α and β obey the following equations [65]:

$$\alpha = \frac{\tan^2 \Psi_{pp} - \tan^2 P}{\tan^2 \Psi_{pp} + \tan^2 P} \tag{3.61}$$

and

$$\beta = \frac{2 \tan \Psi_{pp} \cos \Delta_{pp} \tan P}{\tan^2 \Psi_{pp} + \tan^2 P} \tag{3.62}$$

Hence, Ψ_{pp} and Δ_{pp} are determined by:

$$\tan \Psi_{pp} = \sqrt{\frac{1+\alpha}{1-\alpha}}\, |\tan P| \tag{3.63}$$

and

$$\cos \Delta_{pp} = \frac{\beta}{\sqrt{1-\alpha^2}}\, \frac{\tan P}{|\tan P|} \tag{3.64}$$

The highest measuring precision is reached when $\alpha = \beta = 0$ [63]. This corresponds to circularly polarized light entering the detector. In order to achieve this condition one must have $\Delta_{pp} = \frac{\pi}{2}$ and $\Psi_{pp} = P$. Consequently, the best measurement conditions are achieved by adjusting the polarizer angle P in order to approach the value of Ψ_{pp}. The condition $\Delta_{pp} \approx \frac{\pi}{2}$ is fulfilled if the angle of incidence is close to the Brewster angle. Since only the cosine of Δ_{pp} is determined, a high noise level is expected for Δ_{pp} being close to 0 or π. Additionally, the cosine of Δ_{pp} does not yield the sign of Δ_{pp}. Both issues are solved by the variable retarder placed between polarizer and sample. The determination of the sign of Δ_{pp} requires data at two different retarder positions. It should also be mentioned that a circularly polarized reflected beam of light reduces several instrument errors that affect the measuring precision [63].

3.2.4 A brief presentation of the quantities relevant for the fitting procedure

The data analysis is performed with the help of the software of the ellipsometer *WVASE32* (J.A. Woollam). Further details concerning the data analysis are given in Sec. 4.2. A physical model of the sample has to be developed. The software *WVASE32* uses this model together with the Mueller-Stokes or Jones formalism to anticipate the result of a measurement on a sample of known optical properties. The physical parameters of the model are adjusted in order to obtain calculated data which best agree with the experimental data [65]. The software *WVASE32* makes use of the Levenberg-Marquardt multivariate regression algorithm for the

fitting procedure. The quality of the agreement between the experimental data and the calculated data is given by the mean-squared error (MSE) [65]:

$$MSE = \frac{1}{2N - M} \sum_{i=1}^{N} \left(\frac{\rho_i^{mod}(\vec{x}, \vec{a}) - \rho_i^{exp}}{\sigma_i^{exp}} \right)^2 \tag{3.65}$$

Here, ρ_i^{exp} are the experimentally obtained and ρ_i^{mod} the calculated parameters, N is the number of measured parameters, M refers to the number of variable parameters of the physical model, and σ_i^{exp} are the standard deviations of the experimentally obtained parameters. The calculated parameters ρ_i^{mod} depend on the known parameters of the model $\vec{x}$ (e.g. angle of incidence, photon energy, etc.) and the desired parameters $\vec{a}$.
The curvature matrix

$$\alpha_{kl} = \sum_{i=1}^{N} \frac{1}{(\sigma_i^{exp})^2} \frac{\partial \rho_i^{mod}}{\partial a_k} \frac{\partial \rho_i^{mod}}{\partial a_l} \tag{3.66}$$

can be used to check if the fit is sensitive to all fit parameters or if strong correlations between the parameters prevail. Here, a_j are the components of the vector $\vec{a}$. *WVASE32* determines the figure of merit (FOM) to specify error bars of the parameters a_j. It is defined in the *WVASE32* manual (Ref. [65]) as:

$$FOM_k = 1.65 \cdot \sqrt{C_{kk}} \cdot \sqrt{MSE} \tag{3.67}$$

The covariance matrix C follows from the curvature matrix α by [65]

$$C = (\alpha)^{-1}. \tag{3.68}$$

The correlation between two parameters k and l is specified by the two parameter correlation function which is given by [65]:

$$S_{kl} = \frac{C_{kl}}{\sqrt{C_{kk}}\sqrt{C_{ll}}} \tag{3.69}$$

An absolute value of S_{kl} close to unity is an indication for possible correlations between the parameters a_k and a_l.[2]

[2]The staff of the J.A. Woollam Co. considers 0.92 as a critical value. If S_{kl} exceeds this value, the parameters a_k and a_l are strongly correlated and the model should be revised.

4 Data acquisition and analysis

The first part of this chapter discusses the experimental work that has been performed within the framework of this thesis. The different components of the ellipsometer are introduced and the sample preparation is discussed. Working procedures such as the mounting of the sample into the ellipsometer, the calibration routine, and the measuring process at variable temperatures are presented. The second part of this chapter deals with the analysis of the experimental data. It has already been discussed in Sec. 3.2 that the desired optical constants of the sample cannot be extracted directly from the ellipsometric measurement. The analysis of the ellipsometric data is as challenging as the data acquisition itself. The company J.A. Woollam provides the software *WVASE32* that is used for both, the control of the measurement and the data analysis.

4.1 Data acquisition

4.1.1 The experimental setup

The main components for the ellipsometric studies at variable temperatures are a commercial ellipsometer (VASE, J.A. Woollam) and a liquid-He flow cryostat (KONTI cryostat, CryoVac). The ellipsometer with cryostat at hand for this work is shown in Fig. 4.1. The setup of the ellipsometric measurement is sketched in Fig. 4.2. As light source a broad-band Xe-lamp ($190\,\mathrm{nm} - 2000\,\mathrm{nm}$) is used. A Czerny-Turner monochromater based on double grating selects the desired wavelength. A chopper modulates the light in order to make use of synchronous detection which allows for measurements in an illuminated room. An optical fibre of a thickness of $200\,\mu$m couples the beam to the input unit. The fibre shows strong absorption in the energy range $1350\,\mathrm{nm} - 1450\,\mathrm{nm}$, this energy range is thus not accessible for data acquisition. The input unit comprises a collimator consisting of a MgF_2 lens and a linear polarizer (Rochon prism, MgF_2), with arbitrary polarization axis. The polarizer is mounted on a rotation unit, which works at high accuracy due to a stepper motor. The input unit further comprises a variable retarder, which consists of a computer controlled MgF_2 Berek waveplate. The prepared beam of light leaves the input unit and hits the sample, which is placed inside the cryostat. The cryostat has six windows in order to make light propagation through the cryostat possible, see Fig. 4.1. Depending on the positioning

of the cryostat, measurements at angles of incidence of 50°, 55°, and 70° are possible. The measurements at variable temperatures that are performed within the framework of this thesis are carried out at an angle of incidence of 70°. Room-temperature measurements on air can be conducted without the cryostat making use of a simple sample holder. In this case variable angles of incidence between 20° and 90° can be used. The reflected beam of light passes a continuously rotating analyzer (rotating polarizer, rochon prism, MgF_2) and the time-dependent intensity is detected by the use of a stacked detector consisting of Si ($185 - 1100\,\mathrm{nm}$) and InGaAs ($800 - 1700\,\mathrm{nm}$), which switches automatically. All components are controlled by the computer utilizing the same software *WVASE32* which is used for the data analysis. Figure 4.3 shows the whole ellipsometer setup, including the box holding the monochromator and the Xe-lamp, the control unit VB-400, and the temperature controller.
Within the framework of this thesis, it is further made use of an ellipsometer working in the infrared (IR) frequency range. The IR ellipsometric measurements have been performed on the IR ellipsometer of the workgroup of D. Basov at the University of California San Diego. The IR ellipsometer is a variable-angle spectroscopic ellipsometer for the infrared from the J.A. Woollam Co., that uses a Fourier-transform infrared spectrometer as the light source. It covers the frequency range from 0.07 eV to 0.65 eV. Inside the cryostat, measurements can only be performed at an angle of incidence of 60°. The cryostat does not allow for measurements above room temperature.

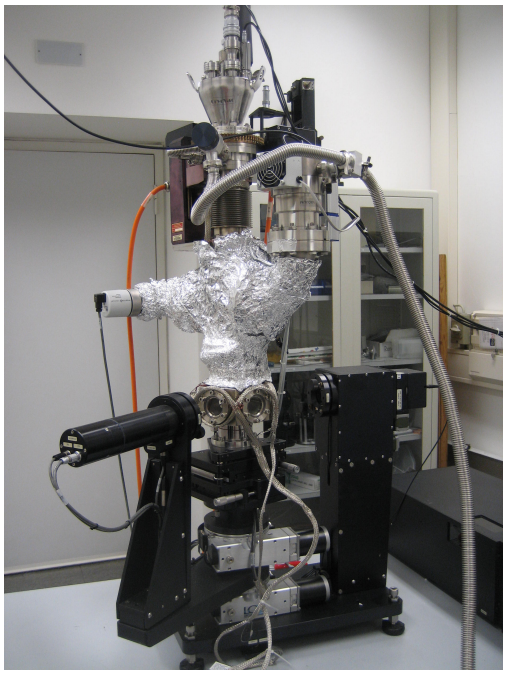

Figure 4.1:
The ellipsometer (J.A. Woollam, VASE) equipped with the liquid helium flow cryostat. The input unit comprising the polarizer (right), two windows of the cryostat (middle), and the output unit comprising the detector (left) can be seen.

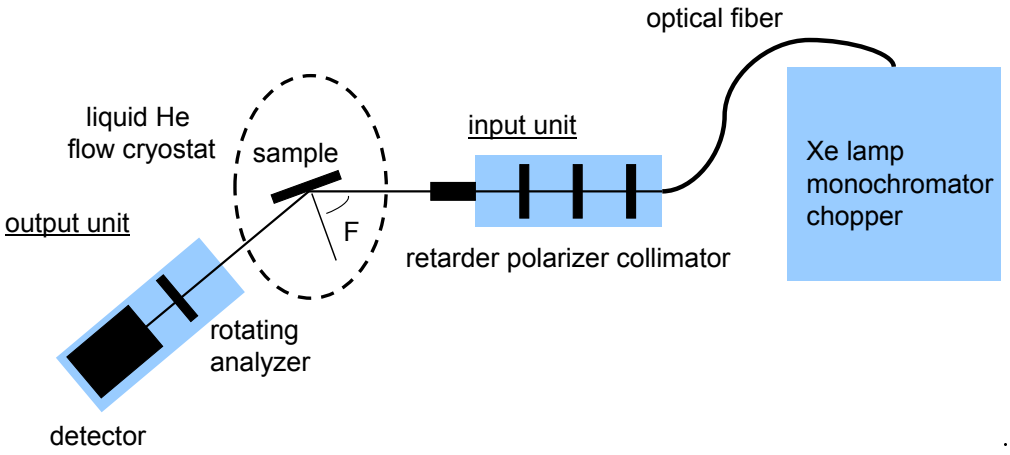

Figure 4.2: Sketch of the setup of the ellipsometric measurements.

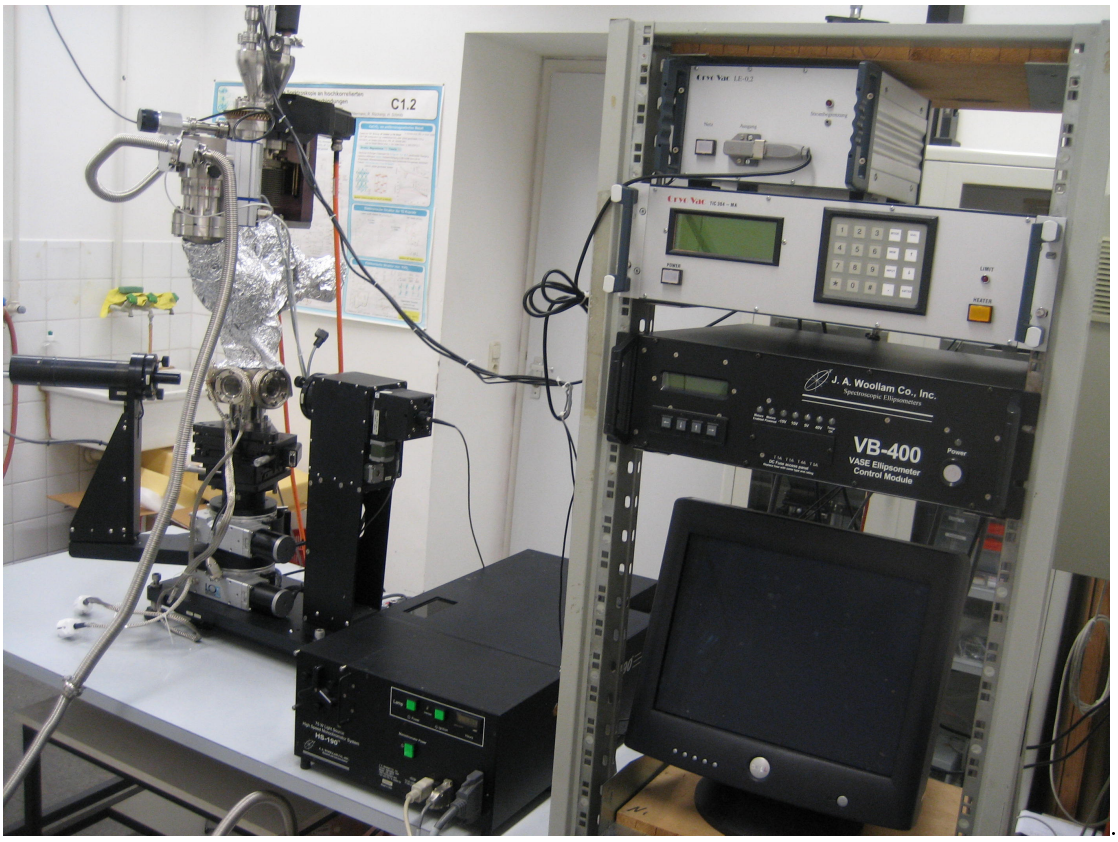

Figure 4.3: The ellipsometer with the box (HS-190) holding monochromator and Xe-lamp. On the right one sees the control unit VB-400 and the temperature controller which is placed above the VB-400.

4.1.2 Sample preparation

The single crystals analyzed in this work are prepared using the floating-zone method. Details can be found in Refs. [68–70][1]. The purities, stoichiometries, and single-phase structures of the crystals are checked by x-ray diffraction and thermo-gravimetry.
The single crystals are oriented with the help of the Laue method. The software *Cologne Laue Indexation Program* (*CLIP*) is used for the analysis of the Laue patterns. An exemplary Laue pattern of a single crystal of $GdVO_3$ is depicted with the respective fit in Fig. 4.4.
The oriented samples are sawed making use of an inside-hole saw to obtain the desired surface.
For an ellipsometric measurement the samples have to be polished in order to obtain a very clean reflecting surface. This is done with the help of a commercial polishing machine (Logitech PM2), which is depicted in Fig. 4.5.
Before the actual polishing process, the samples are lapped, i.e. fine grinded, to obtain coplanar sample surfaces. Therefore the polishing machine is equipped with a plate made of cast iron and a suspension which consists of abrasive aluminum-oxide powder (fused aluminum oxide, 3 micron, Logitech LDT) in water is used. For the samples of La_2CoO_4, which are sensitive to water, the suspension is replaced by aluminum-oxide powder in ethylene glycol (ethan diole, $HOCH_2CH_2OH$).
The actual polishing process takes place on a plate coated with a polyurethane foam, which has small holes to hold the suspension. Here, the suspension is a colloid containing SiO_2 with a grading of 0.032 μm (SF1, colloidal silica, Logitech LTD). It is replaced by a suspension of cerium-oxide polishing powder (0.5 micron, Logitech LDT) in ethylene glycol for watersoluble La_2CoO_4.
The polished samples are removed from the sample holder by the use of a bath of acetone. Afterwards, they are cleaned consecutively in an ultrasonic bath of fresh acetone, of distilled water, of ethanol, and of distilled water. Straight after the polishing procedure the samples are mounted into the ellipsometer (see the next section).

[1] The vanadates YVO_3, $GdVO_3$, and $CeVO_3$ have been provided by A. A. Nugroho and T. T. M. Palstra (Zernike Institute for Advanced Materials, University of Groningen, The Netherlands; Faculty of Mathematics and Natural Sciences, Institut Teknologi Bandung, Indonesia). The single crystal of $LaSrFeO_4$ has been prepared by N. Qureshi (II. Physikalisches Institut, Universität zu Köln). All layered cobaltates $La_{2-x}Sr_xCoO_4$ and $La_{1.5}Ca_{0.5}CoO_4$ have been grown by A. C. Komarek (II. Physikalisches Institut, Universität zu Köln; Max-Planck-Institut CPfS, Dresden). Single crystals of $LaCoO_3$ and $EuCoO_3$ have been prepared by M. Reuter (II. Physikalisches Institut, Universität zu Köln).

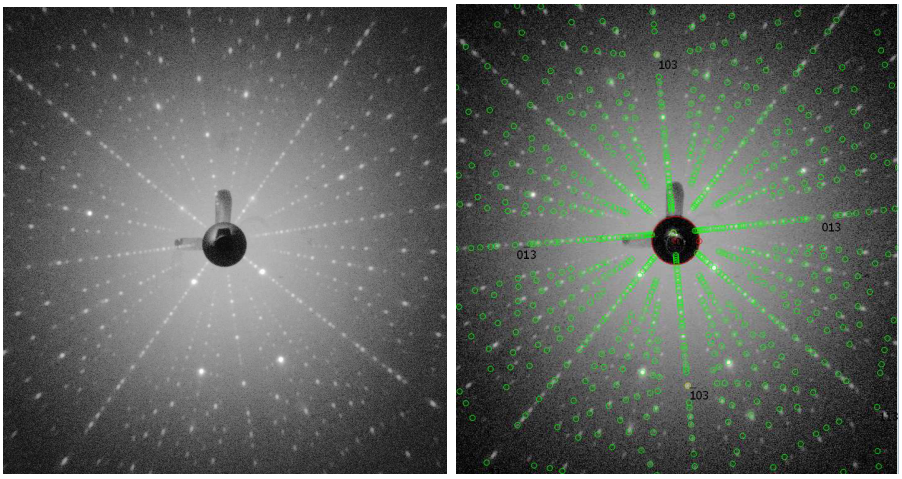

Figure 4.4: Exemplary Laue pattern of $GdVO_3$ (left) with fit (right).

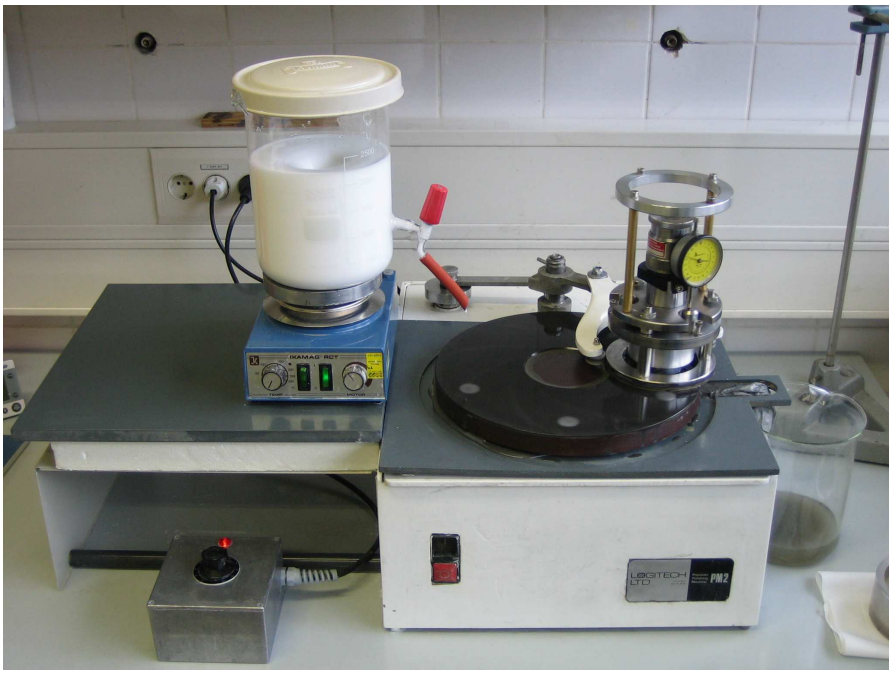

Figure 4.5: The polishing machine working at the lapping procedure. One sees the sample holder which is placed on top of the plate of cast iron (right) and the bowl containing the suspension (left), which drips slowly on the rotating plate.

4.1.3 Mounting, aligning, and calibrating the sample

For measurements at variable temperatures the sample is glued with silver paint onto a copper plate and mounted on the cold finger of the cryostat. For small samples (area of the sample surface $\lesssim$ diameter of the beam of light) a cone made out of brass is used instead of the copper plate. This has the advantage that the light which does not hit the sample is not scattered into the detector but reflected away. The surface of the cone is polished to obtain good reflection properties. A picture of the cone is shown in Fig. 4.6.

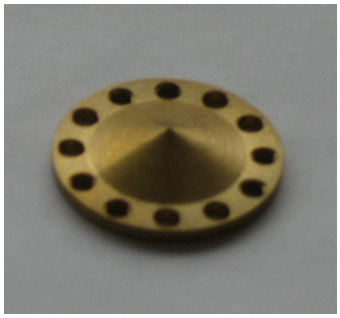

Figure 4.6:
For samples with a small diameter the sample holder has the form of a cone which is made out of brass. This has the advantage that the light which does not hit the sample is reflected back far away from the detector.

Next to the sample a piece of a silicon wafer, which is needed for the calibration routine, is placed on the cold finger as well. The cryostat is evacuated by the use of a series of two turbo pumps until the pressure is below $\approx 10^{-7}$ mbar. Due to the surface sensitivity of ellipsometry an even better vacuum is necessary. Otherwise an ice layer is formed on top of the sample surface at lower temperatures [43]. To prevent this problem a bake out routine is applied by heating the system for 50 h at 400 K and cooling down for another 24 h. The so obtained end pressure amounts to about $5 \cdot 10^{-10}$ mbar at room temperature. By cooling the system with liquid helium, a minimum temperatures of 15 K can be reached. The high-temperature limit is 490 K. The temperature $T_{\text{ellipsometer}}$ at the cooling unit deviates from the temperature $T_{\text{sample holder}}$ at the position of the sample on the cold finger [43]. It is made use of a calibration curve obtained by A. Gössling [43] for the determination of the sample temperatures. A. Gössling is a former member of the optics group in Cologne who put the ellipsometer at hand into operation. The calibration curve is depicted in Fig. 4.7.

Before being able to start the measuring process or the calibration routine, the sample has to be aligned properly. Therefore an alignment detector is used which is placed in front of the input unit. A picture of the setup used for the sample alignment is shown in Fig. 4.8. The beam of light passes through the alignment detector before hitting the sample. The alignment detector consists of a silicon photo diode which is divided into four quadrants. It contains a hole in the middle, i.e. in the intersection of the four quadrants. Alignment takes place at an angle of

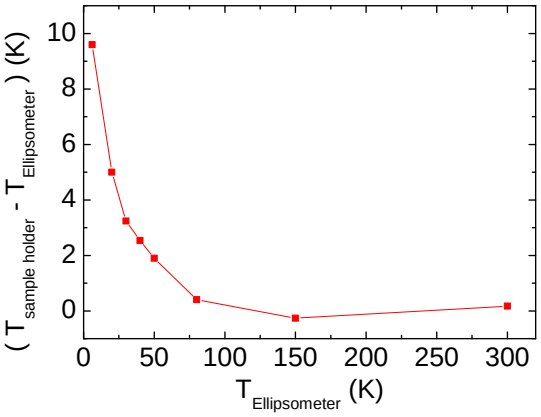

Figure 4.7:
Calibration curve as obtained by A. Gössling [43]. The temperature difference between the temperature $T_{\text{sample holder}}$ at the position of the sample on the cold finger and the temperature $T_{\text{ellipsometer}}$ at the cooling unit has been determined as a function of temperature by mounting a second thermometer directly at the sample holder.

incidence of 0° so that the beam of light is reflected back from the sample into the alignment detector. The software *WVASE32* is used to adjust the sample holder in order to have equal intensity in each of the four quadrants of the alignment detector.

Before starting the measuring process a calibration routine is required. It determines both the absolute positions of polarizer and analyzer and the attenuation of the AC signal at the computer compared to the DC signal at the detector, caused by the signal processing electronics [65]. A sample with good reflection properties is required, i.e. no depolarization, surface roughness, or anisotropy. The standard silicon wafer with a thin cover layer of approx. 20 nm SiO_2 is a good choice. During the calibration routine, the time-dependent detector signal is acquired for different polarizer and analyzer positions. Subsequently, the desired variables are obtained by applying a fitting procedure.

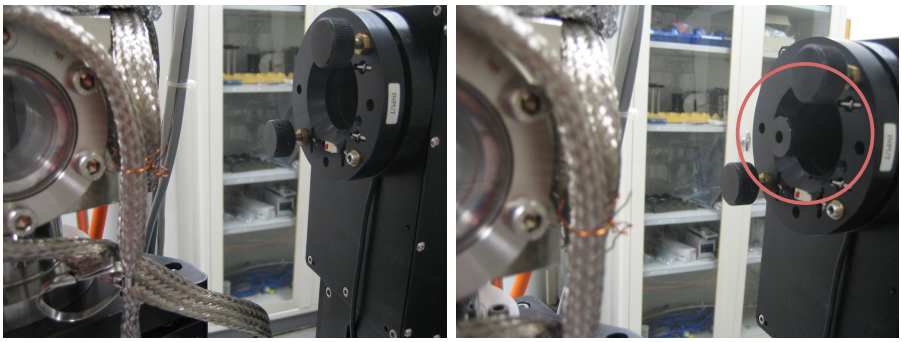

Figure 4.8: Input unit without (left) and equipped with (right) the alignment detector. The alignment detector is placed in front of the input unit for the sample alignment.

If the cryostat is used for the data acquisition process, also the knowledge of the window effects is needed. The windows of the cryostat lead to an anisotropic change of the polarization state of the incoming and reflected wave. To determine the window effects, data has to be acquired on a sample with known optical properties, i.e. one has to make use of the silicon wafer again. A comparison of the measured and calculated data yields the effects of the windows. The thickness of the SiO_2 cover layer which is present on top of the crystalline silicon is varied in a fit.
When the calibration routine is completed, the actual measuring process can be initialized. The measuring process is fully computer controlled by the software *WVASE32* (J.A. Woollam). It can be chosen between different measuring settings. That means, for instance, all accessible Mueller-matrix elements can be acquired or the data acquisition can be limited to the ellipsometric variables Ψ_{pp} and Δ_{pp} (see Sec. 3.2.1 where the Mueller matrix and the ellipsometric variables Ψ_{pp} and Δ_{pp} are introduced).

4.2 Data analysis

This section deals with the analysis of the raw ellipsometric data. It is performed by the use of the software *WVASE32* (J.A. Woollam), which contains all necessary tools to build physical models that describe the optical properties of any layered or anisotropic physical system. A variety of parametric models or tabulated optical constants are available for the description of the dielectric functions. In the following, a brief introduction is given how to use the software *WVASE32* for the analysis of data taken on anisotropic bulk single crystals. Finally, the spectral weight of an optical excitation is introduced and it is shown how the optical data is further analyzed in order to obtain meaningful information about the temperature dependence of different absorption bands.
All data of this work are acquired on properly aligned single crystals, i.e. with the crystallographic axes parallel to the ellipsometer coordinate system[2]. Consequently it is sufficient to acquire the ellipsometric variables Ψ_{pp} and Δ_{pp} (cf. Sec. 3.2.1), which reduces the data acquisition time considerably. This is desirable since temperature dependent ellipsometric data should be taken consecutively in one temperature sequence in order to detect even small temperature-dependent variations of the spectral weights. However, in all cases all accessible Mueller-matrix elements are acquired at room temperature to check for possible misalignment or depolarization. In most cases only the ellipsometric variables Ψ_{pp} and Δ_{pp} are used for the final fitting process (for details see the chapters of the individual compounds).

[2]The ellipsometer coordinate system has been introduced in Sec. 3.1.4 , Fig. 3.1.

4.2.1 Surface effects

Despite the elaborate polishing procedure it is assumed that a thin cover layer due to oxidation or contamination develops on the surface of the single crystals. As ellipsometry is very sensitive to surface effects this has to be accounted for in the data modeling. Room-temperature data are acquired on the single crystals of interest for this work at different angles of incidence Φ. The data show that the pseudo-dielectric function $< \varepsilon >$ is nearly independent of Φ, indicating an only thin cover layer $< 100\,\text{Å}$ (see Sec. 3.2.2 where the pseudo-dielectric function $< \varepsilon >$ is introduced). The spectra are thus mainly determined by the bulk properties of the single crystals, while the cover layer only leads to minor effects. We have experienced that the cover layer produces an energy-dependent vertical shift of the measured $< \varepsilon(\omega) >$ spectrum but does hardly affect the temperature dependence of the spectral weights of individual absorption bands, which is the main interest of this work. Nevertheless, it is desirable to describe the cover layer accurately in the data modeling to come as close as possible to the actual absolute value of the optical constants of the bulk material.
As the cover layer is too thin to be fully characterized, it is modeled by the use of the layer *Srough* of the Software *WVASE32* which simulates a surface roughness. It consists of 50% *Void* (vacuum) and 50% of space are filled with the sample optical constants. Most information about the cover layer, e.g. the thickness, can be extracted from a non-absorbing energy range ($\varepsilon_2 \approx 0$) of the sample. Here, the data can be modeled using the *Cauchy* layer [3] of the software *WVASE32* for the substrate and the layer *Srough* with thickness D for the cover layer. A fit yields the parameters of the *Cauchy* layer and the thickness D of the layer *Srough* which is fixed in the remaining fitting process. The crystals examined within the framework of this work yield values for D between 10 Å and 80 Å. If a crystal is absorbing in the whole accessible energy range a reasonable surface roughness has to be estimated. Figure 4.9 exemplary shows the results for ε_2^a following from the fit to the measured data on $LaSrFeO_4$ assuming a surface roughness of 10 Å and 60 Å, respectively.

4.2.2 Parametric models

In this work the optical constants of the anisotropic crystals under examination are described by parametric models. A parametric model ensures Kramers-Kronig consistency and it reduces the number of parameters that have to be varied in a fit. Furthermore, the use of a parametric model has the advantage that a slight variation of the parameters suffices to describe the dielectric function of samples with similar physical properties (e.g. substitution of the rare earth ion, variation of

[3] The *Cauchy* layer uses the Cauchy model (see Sec. 3.1.5) to describe the optical constants of semiconductors or insulators.

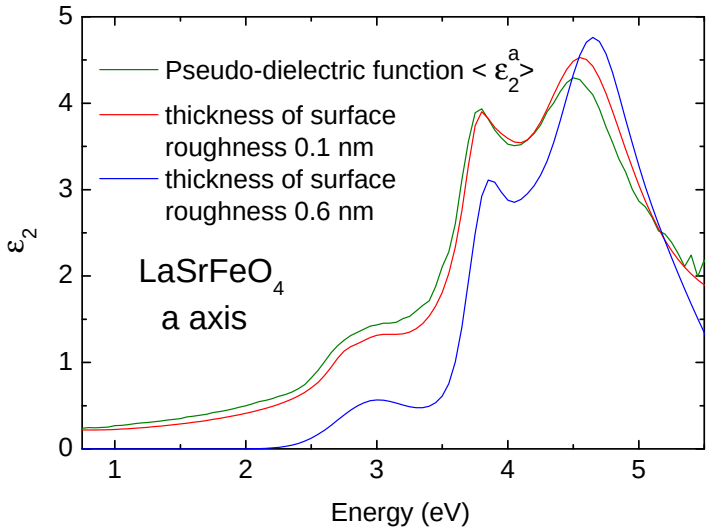

Figure 4.9: The pseudo-dielectric function $< \varepsilon_2^a >$ (green curve) corresponds to the measured data on $LaSrFeO_4$. The results for ε_2^a following from the fit to the measured data on $LaSrFeO_4$ assuming a surface roughness with a thickness of 10 Å (red curve) and 60 Å (blue curve) are shown. The deviations from zero below approx. 2.2 eV of $< \varepsilon_2^a >$ are an artifact of the pseudo-dielectric function. One obtains $\varepsilon_2^a \approx 0$ for $\omega \lesssim 2.2\,\text{eV}$ as expected below the band gap of $LaSrFeO_4$ when assuming a surface roughness with a thickness of 60 Å in the physical model used for the fit.

the doping levels) or of the same sample at different temperatures. Here, it is made use of the *General oscillator layer* of the software *WVASE32* which provides a great amount of parametric (oscillator) models (including the Lorentz-, Gaussian-, and Tauc-Lorentz oscillator models as introduced in Sec. 3.1.5) to choose from. Furthermore, ε_∞ can be varied and poles[4] can be added outside the measured range. To describe the dielectric tensor of an anisotropic material, a *General oscillator layer* is needed for each independent entry of the dielectric tensor. In the case of an orthorhombic crystal three *General oscillator layer*s are needed to describe ε^a, ε^b, and ε^c, respectively. The full physical model thus consists of a *General oscillator layer* with a certain amount of fit parameters for each independent entry of the dielectric tensor and a cover layer *Srough* with fixed thickness D (that has been determined in advance) for each sample surface. The

[4] A pole is a Lorentz oscillator without damping ($\gamma = 0$), it has a pole at ω_0 and shows $\varepsilon_2 = 0$ for $\omega \neq \omega_0$. A pole outside the measured range thus effects only ε_1. As opposed to ε_∞ a pole leads to a dispersion in ε_1.

model is fit to all experimental data sets that are available for the sample (obtained from measurements on different sample surfaces and for different orientations) simultaneously.[5] At the very end of the fitting process, the final results for the dielectric function of the sample can be read off the *General oscillator layer*s.[6]

4.2.3 The spectral weight

Besides the determination of the pure form of the dielectric function, the aim of this work is the study of the temperature dependence of the individual absorption bands constituting the dielectric function. An important quantity is the optical spectral weight (SW), which is defined as the integral over the real part of the optical conductivity $\sigma_1(\omega)$:

$$SW = \int_0^\infty \sigma_1(\omega)\ d\omega. \tag{4.1}$$

To apply this formula, σ_1 must be given in units of $1/(\Omega\mathrm{m})$ and the energy ω equals $2\pi\nu$ with frequency ν in Hertz.
Often the spectral weight is specified in the form of an effective carrier concentration N_{eff}, which is defined as:

$$N_{eff} = \frac{2mV}{\pi e^2} \cdot \int_0^\infty \sigma_1(\omega)\ d\omega \tag{4.2}$$

Here, m is the free electron mass, e the elementary electric charge, and V is the volume per magnetic ion. The effective carrier concentration N_{eff} is dimensionless. If the physical model used for the data analysis consists of a number of Lorentz or Gaussian oscillators which describe the different absorption bands, the spectral weight of an individual absorption band can directly be obtained by the use of the parameters of the corresponding oscillator. The spectral weight of a single Lorentz oscillator (as defined in Sec. 3.1.5) is related to its plasma frequency ω_p by:

$$\int_0^\infty \sigma_1(\omega)\ d\omega = \frac{\pi}{2}\ \varepsilon_0\ \omega_p^2 \tag{4.3}$$

or

$$N_{eff} = \frac{mV\varepsilon_0\omega_p^2}{e^2} \tag{4.4}$$

[5] The *General oscillator layer*s for the different entries of the dielectric tensor are incorporated into the layer *Biaxial* of the software *WVASE32*. The layer *Biaxial* also contains the information on the sample orientation that corresponds to the experimental data sets.

[6] A detailed description of the data modeling with the software *WVASE32* of ellipsometric data on anisotropic bulk single crystals can be found in my diploma thesis (Ref. [71]).

where the frequencies ω and ω_p correspond to $2\pi\nu$ with frequency ν in Hertz. If the plasma frequency ω_p is given in units of eV, the effective carrier concentration N_{eff} can be calculated by the use of the following formula[7]:

$$N_{eff} = \frac{mV\varepsilon_0\omega_p^2}{\hbar^2} \tag{4.5}$$

The spectral weight of a single Gaussian oscillator (parameters as defined in Sec. 3.1.5) is given by:

$$\int_0^\infty \sigma_1(\omega)\ d\omega = \varepsilon_0\sqrt{\pi}\cdot A\Gamma\omega_0, \tag{4.6}$$

or

$$N_{eff} = \frac{2mV}{\pi e^2}\varepsilon_0\sqrt{\pi}\cdot A\Gamma\omega_0, \tag{4.7}$$

The amplitude A is dimensionless, Γ and ω_0 correspond to $2\pi\nu$ with frequency ν in Hertz. If ω_0 and Γ are given in units of eV, the effective carrier concentration N_{eff} can be calculated by the use of the following formula[8]:

$$N_{eff} = \frac{2mV}{\pi\hbar^2}\varepsilon_0\sqrt{\pi}\cdot A\Gamma\omega_0 \tag{4.8}$$

It has to be pointed out that in a first step a model has to be found that achieves a very good description of the experimentally measured data. It is desirable to use as few oscillators as possible, but enough oscillators to not miss any relevant features of the line shape. The analysis of the spectral weight of individual absorption bands can be done in a second step. In some cases it is well possible to describe individual absorption bands by single Lorentz or Gaussian oscillators and analyze their spectral weights by the above mentioned formulas. In other cases, however, the absorption bands overlap strongly which leads to a model with overlapping oscillators. Also the line shape of some absorption bands has to be described by several oscillators rather than a single one. In these cases it does not appear physically meaningful to analyze the spectral weights of the individual oscillators. Therefore other ways have to be considered to obtain none the less a result for the temperature dependence of the spectral weights of the individual absorption bands. This can be done by analyzing, e.g., the sum of the spectral weights of several oscillators, the mathematical integral over a part of the $\sigma_1(\omega)$ spectrum, or the value of $\sigma_1(\omega)$ at a specific energy ω', etc.

[7] Within the *General oscillator layer* of the software *WVASE32* the parameters of the Lorentz oscillator in style Lor.0 [eV] are *Amp*, *En*, and *Br*, the parameter *Amp* is dimensionless, *En* and *Br* are given in units of eV. The square of the plasma frequency ω_p^2 in eV^2 can be obtained from *Amp*, *En*, and *Br* by multiplication: $\omega_p^2 = Amp \cdot En \cdot Br$.

[8] Within the *General oscillator layer* of the software *WVASE32* the parameters of the Gaussian oscillator in style Gau.0 [eV] are *Amp*, *En*, and *Br*, the parameter *Amp* is dimensionless, *En* and *Br* are given in units of eV. Our parameter A corresponds to *Amp*, ω_0 corresponds to *En*, and Γ corresponds to $Br/2\sqrt{ln2}$ (*Br* is the FWHM in eV).

5 Probing orbital fluctuations in $R\mathrm{VO_3}$ ($R = \mathrm{Y}$, rare earth ion)

The competition between orbital, spin, and lattice degrees of freedom is the origin of a great number of fascinating physical properties observed in the oxovanadates $R\mathrm{VO_3}$ ($R = \mathrm{Y}$, rare earth ion). The compounds undergo a series of temperature-induced phase transitions between phases with different spin and orbital ordering patterns. The temperature-dependent changes of spin and orbital correlations are expected to be reflected in a pronounced dependence on temperature and polarization of the optical spectra [8, 10–12, 21, 23]. Here, a detailed ellipsometric analysis of the optical conductivity $\sigma_1(\omega)$ of $\mathrm{YVO_3}$, $\mathrm{GdVO_3}$, and $\mathrm{CeVO_3}$ in the energy range from 0.75 eV to 5.0 eV for temperatures ranging from 15 K to 490 K is presented. The optical spectra are analyzed considering predictions based on nearest-neighbor spin-spin and orbital-orbital correlations.

There is a striking disagreement concerning the optical data reported for the compound $\mathrm{YVO_3}$ in the literature [21–23], none of the different experimental data sets is in agreement with theoretical predictions. It is the aim of this chapter to clarify these discrepancies.

Furthermore, the importance of orbital fluctuations in $R\mathrm{VO_3}$ is studied. Different groups have claimed that orbital fluctuations may be strong in the Mott-Hubbard insulators $R\mathrm{VO_3}$ [8, 10, 14–17, 37]. Their claim is based on the fact that the orbital-lattice coupling is relatively weak in these systems with partially filled t_{2g} orbitals. As a consequence, coupled spin/orbital degrees of freedom have to be considered, which leads to strongly frustrated spin-orbital superexchange interactions on a nearly cubic lattice and quantum energy can be gained from fluctuating orbitals [14]. Experimentalists claim for $\mathrm{YVO_3}$ the observation of e.g. a one-dimensional orbital liquid, of an orbital Peierls phase, and of bi-orbitons [15, 18]. On the other hand, LDA+U (local density approximation + U) and LDA+DMFT (local density approximation + dynamical mean-field theory) studies rule out strong orbital fluctuation in $\mathrm{YVO_3}$ due to the sizable crystal field splitting, but consider fluctuating orbitals to be important for compounds with larger R ions such as $\mathrm{LaVO_3}$ [19, 20].

The experimental determination of low-energy orbital fluctuations is a difficult task. Optical spectroscopy offers an efficient means by taking advantage of the sensitive dependence of the optical spectral weight on nearest-neighbor spin-spin

and orbital-orbital correlations. A comparison of our experimental results for $R = \mathrm{Y}$, Gd, and Ce with a theory based on a low-energy spin-orbital superexchange Hamiltonian leads to a conclusion about the importance of orbital fluctuations in $R\mathrm{VO}_3$.
The line shape of the optical conductivity gives evidence for the importance of excitonic effects in $R\mathrm{VO}_3$. It is argued that not only the Coulomb interaction, but also the kinetic energy plays an important role for exciton formation in Mott-Hubbard insulators.

The chapter on hand is organized as follows. In the first section the structural and physical properties of the compounds $R\mathrm{VO}_3$ are discussed. Due to their fascinating magnetic properties as well as the importance of coupled spin and orbital degrees of freedom, the series $R\mathrm{VO}_3$ has attracted a huge research activity over the past years. A brief summary of the results that are most important for our optical investigations is presented. It follows the presentation of the experimental data in the second section of this chapter. The discussion of the data in the third section includes the peak assignment, the comparison of our measured data with the data reported in the literature, and the analysis of the importance of orbital fluctuations in $R\mathrm{VO}_3$. The fourth section deals with our observation of an excitonic resonance in the data of $R\mathrm{VO}_3$. Finally, a conclusion is given in the last section of this chapter.

5.1 The compounds $R\mathrm{VO}_3$ ($R = \mathrm{Y}$, rare-earth ion)

5.1.1 The crystal structure

At room temperature, perovskite-type $R\mathrm{VO}_3$ exhibits an orthorhombic crystal structure with space group $Pbnm$ [68, 72–75]. It emerges from the cubic perovskite structure (space group $Pm\bar{3}m$) with lattice constant a_c by the so-called GdFeO_3 distortion, i.e. a tilting and rotation of the corner sharing VO_6 octahedra, resulting in lattice constants $a \approx b \approx \sqrt{2}a_c$ and $c \approx 2a_c$ (see Fig. 5.1). Structural investigations of the compounds $R\mathrm{VO}_3$ show that smaller rare-earth ions R favor stronger tiltings of the VO_6 octahedra [72, 74], indicating the influence of steric effect. The compound LaVO_3 is thus among the less distorted members of the series, the compound on hand YVO_3 is hugely distorted. A measure for the degree of orthorhombic distortion is the orthorhombic splitting $\varepsilon = 2|b-a|/(b+a)$ between the lattice parameters a and b. It amounts to 0.06 for $R = \mathrm{Y}$ and Gd, and only 0.006 for Ce [72, 74, 76]. The values of the orthorhombic splitting ε are summarized in Fig. 5.2 for $R\mathrm{VO}_3$. The degree of orthorhombic distortion is further reflected in the $\mathrm{V}-\mathrm{O}-\mathrm{V}$ bond angle, which increases from $\approx 144°$ in YVO_3

to $\approx 156°$ in LaVO_3 [68, 74, 77].
By lowering the temperature, the compounds $R\mathrm{VO}_3$ undergo a second-order structural phase transition at T_{OO} where the crystal structure changes to monoclinic (space group $P2_1/b$) [68, 72–74, 78]. The compounds with smaller R ions (Lu, Yb, Ho, Er, Y) recover the orthorhombic crystal structure with space group $Pbnm$ below a phase transition of first order at $T_S < T_{OO}$ [68, 72, 73, 78] (see Fig. 5.3).

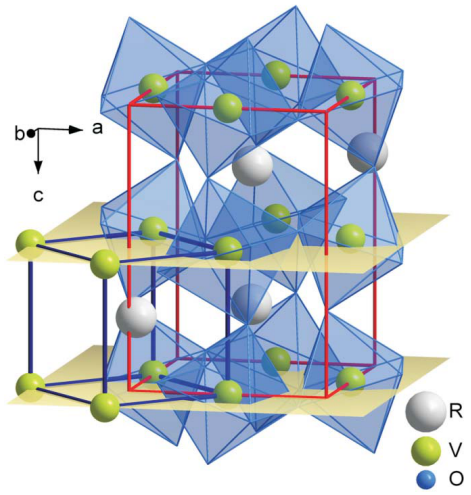

Figure 5.1: At room temperature $R\mathrm{VO}_3$ exhibits an orthorhombic crystal structure with space group $Pbnm$. The oxygen octahedra are rotated and tilted compared to the ideal cubic perovskite structure. The orthorhombic unit cell ($Pbnm$, red) and the cubic unit cell ($Pm\bar{3}m$; dark blue) are shown. Taken from Ref. [37].

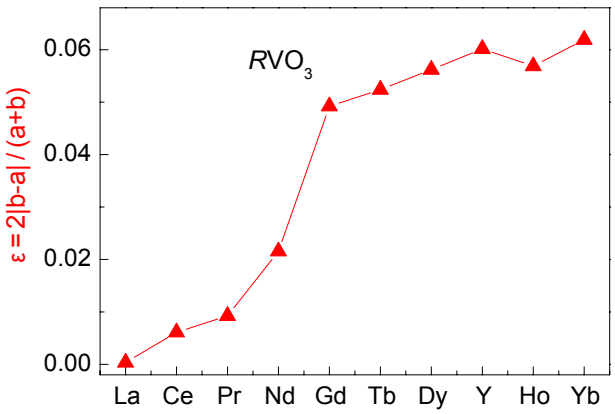

Figure 5.2: Orthorhombic splitting $\varepsilon = 2|b-a|/(b+a)$ of the compounds $R\mathrm{VO}_3$. The figure is taken from Ref. [37], where the values of the lattice parameters a and b are taken from Refs. [72, 76, 77, 79, 80].

5.1.2 Spin and orbital ordering phase diagram

The compounds $R\mathrm{VO}_3$ are Mott-Hubbard (MH) insulators with two localized electrons in the $3d$ shell of the vanadium V^{3+} ion. In the ground state, both electrons occupy t_{2g} orbitals with total spin 1. The value of Dq, which determines the size of the $t_{2g} - \mathrm{e}_g$, splitting has been determined to be approx. 2 eV for YVO_3 [23,37]. The t_{2g} manifold is split into d_{xy}, d_{zx}, and d_{yz} orbitals, the total splitting is on the order of $0.1\,\mathrm{eV} - 0.2$ eV [18,20,81,82]. As the Jahn-Teller coupling is weak for partially occupied t_{2g} orbitals, the intrinsic frustration between spin and orbital degrees of freedom is the origin of a complex spin and orbital ordering phase diagram [14] (see Fig. 5.3). This is in contrast to systems with e_g orbital degeneracy. Here, the orbital degeneracy is usually lifted due to the strong coupling of the orbitals to the lattice leading to a structural phase transition which takes place well above the magnetic ordering temperature [16]. In the orbitally ordered phases of $R\mathrm{VO}_3$, the d_{xy} orbital is occupied by one electron at each V site. The occupation of d_{xz} and d_{yz} by the second electron can be viewed as a pseudospin, and both spins and pseudospins have been reported to show ordering patterns of either the G type (antiferro along all bonds, i.e., d_{zx} and d_{yz} alternate) or the C type (ferro along c, antiferro within the ab plane), see Fig. 5.4.

In $R\mathrm{VO}_3$ C-type spin order is observed below the Néel temperature T_N, which is continuously shifted to higher temperatures with increasing R-ion radius [68, 73, 78, 83, 84], from 104 K for YbVO_3 [85] to 143 K for LaVO_3 [73]. This can be reasoned by the decrease of the octahedra tilt angle with the increase of the R-ion radius, which in turn can be recognized as the origin of an increased $\mathrm{V} - \mathrm{O} - \mathrm{V}$ superexchange. The structural phase transition which occurs at T_S only in compounds with smaller rare-earth ions (Lu, Yb, Ho, Er, Y) is accompanied by a change of the spin ordering pattern. Below T_S the spin order is observed to be of G type. It is well established that the G-type SO is accompanied by C-type orbital order (see Fig. 5.4 (b)) [14, 20, 23, 68, 72, 74, 86]. The correct description of the orbitals in the monoclinic phase is controversial. Orbital order of G type (see Fig. 5.4 (a)) setting in at T_{OO} has been predicted on the basis of neutron and x-ray diffraction studies [68,86].

Miyaska *et al.* [78] use the known magnetic and structural properties of Refs. [83, 84, 86–88] in combination with their measurements of specific heat, magnetization, and Raman-scattering spectra to extract the spin and orbital ordering phase diagram of $R\mathrm{VO}_3$, as shown in Fig. 5.3, left panel. It is interesting to note that the orbital ordering temperature T_{OO} shows a non-monotonic dependence on the radius of the rare-earth ion R. According to Ref. [78] the behavior of the compounds with large R ions LaVO_3 and CeVO_3 is strikingly different. Here, magnetic ordering is reported to set in even above the structural phase transition at T_{OO}, which is accompanied by the onset of G-type orbital order. Results from synchrotron x-ray diffraction [73] confirm these findings for LaVO_3, whereas they

are in disagreement with Ref. [78] in the case of CeVO_3. The dispute concerning the phase-transition temperatures in CeVO_3 is discussed in detail in Sec. 5.1.5.
A modified phase diagram has been proposed by Sage *et al.* [74], see Fig. 5.3, right panel. They report on a detailed study of the spin and orbital ordering phase diagram of $R\mathrm{VO}_3$ by high-resolution x-ray powder diffraction and thermal expansion. According to Sage *et al.* [74] a phase with coexisting orbital orderings of C type and G type and coexisting monoclinic and orthorhombic crystal structure sets in at a temperature T_S^* closely below T_N for intermediate size rare-earth ions (R = Tb, Gd, Eu, and Sm). The C-type phase fraction is reported to increase with the degree of octahedral tilting.
Horsch *et al.* [48] apply a theoretical approach based on a microscopic theory to analyze the phase diagram of $R\mathrm{VO}_3$. They treat coupled spin-orbital degrees of freedom in an extended spin-orbital model, which includes the superexchange interaction, the crystal-field splitting that is induced by the GdFeO_3-type distortion, orbital-orbital interaction resulting from the orbital-lattice coupling, and orbital-strain coupling [48]. They point out that the non-monotonic behavior of T_{OO} is a result of the competition between the Jahn-Teller term and the orbital occupation favored by the orthorhombic distortion of the VO_6 octahedra. They show that the inclusion of the coupling of the orbitals to the lattice distortion is an important ingredient in order to reproduce the general trends observed for the spin and orbital ordering transition temperatures T_N and T_{OO}, respectively. The main results of Ref. [48] are shown in Fig. 5.5.

5.1.3 Importance of orbital fluctuations

Different groups have pointed out that orbital fluctuations may be strong in $R\mathrm{VO}_3$ in the intermediate-temperatue phase, the monoclinic phase with C-type magnetic order. In the following the most relevant studies concerning the orbital degree of freedom of $R\mathrm{VO}_3$ are briefly discussed.
Khaliullin, Horsch, and Oles [14] report theoretical investigations based on a spin-orbital model to investigate the role played by quantum fluctuations among orbitals. Starting point is the assumption that the Jahn-Teller coupling is only weak for the t_{2g} orbitals in $R\mathrm{VO}_3$. In this case, superexchange interactions among spins and orbitals are highly frustrated on a nearly cubic lattice. This scenario is supported by the occurrence of two strikingly different magnetic and orbital ordering patterns in $R\mathrm{VO}_3$, depending on the temperature and the size of the rare-earth ion. Also Hartree-Fock calculations indicate that indeed C- and G-type spin ordered phases are energetically close [89]. The authors of Ref. [14] recognize the Jahn-Teller effect as the dominant driving force for the orbital and spin ordering pattern observed in the low-temperature orthorhombic phase of the hugely distorted compounds with smaller R ions (Lu, Yb, Ho, Er, Y). They point out that the Jahn-Teller coupling favors a C-type orbitally ordered ground state

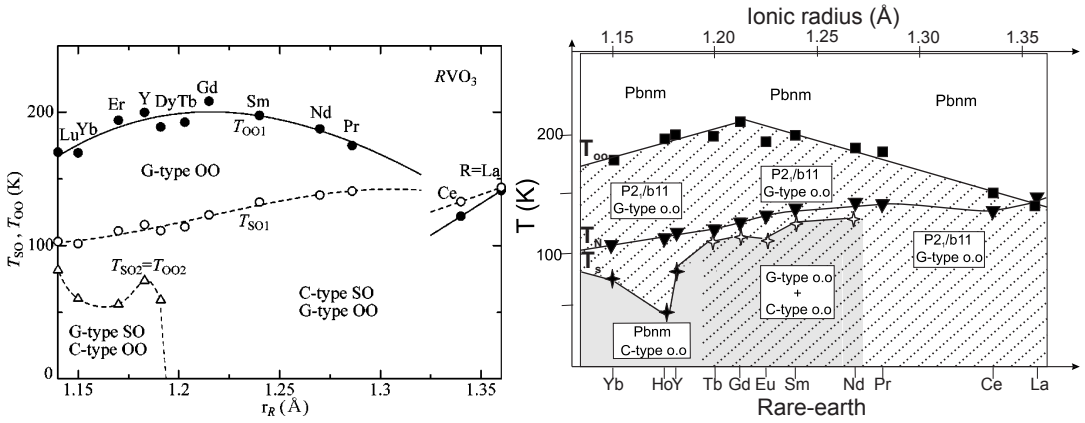

Figure 5.3: Left: Spin and orbital ordering phase diagram of $R\mathrm{VO}_3$ as proposed by Miyasaka *et al.* [21] as a function of the radius of the R ion (orbital ordering temperature T_{OO}: filled circles, Néel temperature T_N: open circles, phase-transition temperature into phase with changed spin and orbital order T_S: open triangles). Right: Spin and orbital ordering phase diagram of $R\mathrm{VO}_3$ as proposed by Sage *et al.* [74] (T_{OO}: filled squares, T_N: filled triangles, T_S: filled stars. Additionally, a transition into a phase with coexisting C-type and G-type orbital ordering is proposed for compounds with intermediate R radius at a transition temperature T_S^*, represented by open stars.). Taken from Refs. [21] and [74].

which is accompanied by antiferromagnetic (AFM) spin order along all three directions (spin order of G type). According to Ref. [14] the Jahn-Teller energy is overbalanced by the energy that can be gained from orbital fluctuations at higher temperatures. Due to the large spin $S = 1$ at the V^{3+} sites it is assumed that the spins pick up a classical configuration in such a way that the energy gain from orbital fluctuations is maximized [14]. The degeneracy of the d_{yz} and d_{zx} orbitals is supposed to not be lifted by lattice distortions and to control the orbital superexchange interactions along c [14]. Orbital quantum energy can be gained for parallel spins when d_{yz} and d_{zx} orbitals along the c axis form an orbital singlet. The ferromagnetic (FM) spin configuration is additionally favored by the Hund exchange. Thus, the classical orbital order in the intermediate-temperature phase is assumed to involve only the d_{xy} orbital, which is occupied by one electron at each V site, leading to AFM superexchange interactions in the ab plane. The superexchange interactions involve virtual d^3 states with doubly occupied d_{xy} orbitals, which are considered to block orbital fluctuations in the ab plane. The authors of Ref. [14] point out that the fluctuations of the t_{2g} orbitals along the c axis, which release high entropy, can be recognized as the origin of a C-type spin

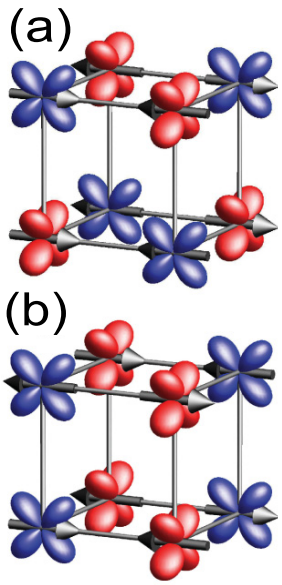

Figure 5.4: (a) G-type orbital order with C-type spin order, (b) C-type orbital order with G-type spin order. The vertical axis corresponds to the c axis.

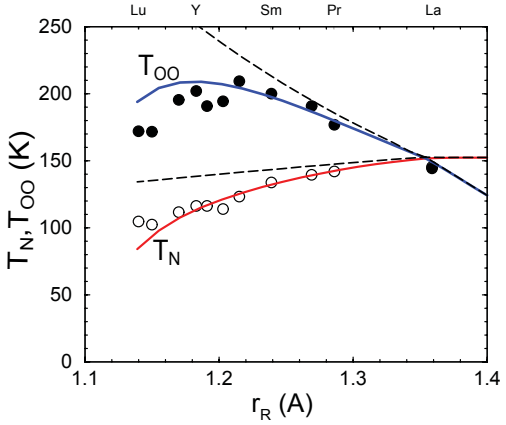

Figure 5.5:
The result obtained by Horsch *et al.* [48] for the spin ordering temperature T_N (red line) and orbital ordering temperature T_{OO} (blue line) in RVO_3 for varying rare-earth radius (denoted as r_R). The full (T_{OO}) and empty (T_N) circles correspond to the experimental results of Ref. [78]. Taken from Ref. [48].

ordered phase with 1D orbital disorder. The less distorted crystal structure of the compounds with larger R ions is supposed to stabilize this exotic phase down to lowest temperatures.
Magnetic neutron scattering data on YVO_3 collected by Ulrich *et al.* [15] reveal an anomalously small magnitude and large canting angle of the ordered moment in the intermediate-temperature phase, giving experimental evidence for the importance of strong orbital fluctuations. Reehuis *et al.* [72, 75] report an ordered

magnetic moment that is considerably smaller than the free-ion value also for CeVO_3, NdVO_3, and TbVO_3. Ulrich *et al.* [15] further observe (i) a splitting of the FM spin waves into optical and acoustic branches and (ii) a FM exchange coupling along c that is much stronger than the in-plane AFM exchange. This is in contradiction with the Goodenough-Kanamori-Anderson rules according to which AFM superexchange interactions are generally stronger than FM interactions. The authors argue that the optical/acoustic splitting can be described by alternating FM exchange bonds along c, which may be a strong indication for the highly unusual orbital correlations. By the use of the model introduced in Ref. [14], that requires degenerate d_{yz} and d_{zx} orbitals, they show that the quasi-one-dimensional band of spin-orbital fluctuations along c is unstable against dimerization and that this so called orbital Peierls instability may be the origin of the unusual magnetic properties [15,16]. The instability towards dimerization along the FM direction in the intermediate-temperature phase has been further claimed theoretically based on a spin-orbital model with spin $S = 1$ [17,90]. The formation of dimer states is supposed to release high entropy holding the key for the stabilization of the exotic C-type AFM order observed in the intermediate-temperature phase [17,90].
On the contrary, Fang and Nagaosa [19] argue based on their LDA+U calculations that the quantum orbital fluctuations are suppressed in YVO_3 and LaVO_3 due to the large Jahn-Teller distortion. They point out that the splitting of the spin-wave dispersion in the intermediate-temperature phase observed by Ulrich *et al.* [15] can be well reproduced within a Jahn-Teller picture assuming two inequivalent VO_2 layers with different *ab* plane exchange parameters instead of the orbital Peierls state [19]. Studies based on LDA+DMFT [20] find that orbital fluctuations are negligible in LaVO_3 in the C-type AFM monoclinic phase but support strong orbital fluctuations at room temperature, whereas for compounds with smaller R ions such as YVO_3 quantum effects are also suppressed at 300 K due to the larger crystal-field splitting.
Evidence for the importance of inter-atomic orbital-exchange interactions is provided by optical data collected by Benckiser *et al.* [18]. The temperature and polarization dependence of an absorption band observed in the optical spectra of YVO_3 and HoVO_3 for polarization $E \parallel c$ at 0.4 eV strongly suggests the interpretation in terms of an excitation based on the exchange of two orbital occupations on adjacent sites [18]. In other words, it has been attributed to a direct excitation of two orbitons, termed two-orbiton excitation. Furthermore, two broad bands at around 43 meV and 62 meV observed in the resonant Raman scattering spectra of LaVO_3, NdVO_3, and YVO_3 have also been interpreted in terms of two-orbiton excitations, as they show a remarkable resonance with the MH gap transition [91,92]. However, the emergence of these bands only below $\mathrm{T}_N = 116$ K in YVO_3 questions this interpretation since orbital order is already observed below $T_{OO} = 200$ K. A different interpretation of the observed Raman modes in YVO_3 is proposed in Ref. [93], where the bands at around 43 meV and 62 meV are interpreted in terms

of a one-orbiton excitation and a Jahn-Teller phonon mode, respectively. Instead, another Raman peak has been assigned to a two-orbiton excitation in Ref. [93]. The results of Ref. [94] for the $\mathrm{V-O}$ bond length pattern obtained in the framework of a detailed structural investigation of $\mathrm{HoVO_3}$ by the use of a combination of single-crystal neutron diffraction and synchrotron x-ray and neutron powder diffraction give further evidence for the importance of orbital fluctuations, but on the other hand the structural data strongly indicate that the orbital fluctuations may not be strong enough to cause a long-range orbitally dimerized state as theoretically predicted [94].
To sum up, the question concerning the role played by orbital fluctuations in $R\mathrm{VO}_3$ is still a highly debated issue. Clear experimental evidence for or against the importance of fluctuating orbitals is still missing. Our approach involves a very detailed analysis of the temperature dependence of the optical conductivity. Ellipsometry is our method of choice as it has proven to be very successful in capturing the temperature dependent changes of the optical spectral weights [11, 12]. In the case of $\mathrm{LaMnO_3}$ and $\mathrm{LaSrMnO_4}$, for example, the result for the spectral-weight transfer which originates from changes in the nearest-neighbor spin-spin correlation function agrees astonishingly well with the theoretical predictions (cf. Sec. 2.6 and Refs. [11, 12]).

5.1.4 Details on $\mathrm{YVO_3}$

The compound $\mathrm{YVO_3}$ has been extensively studied experimentally as well as theoretically. Many of the results have already been discussed in the previous section. The structural properties of $\mathrm{YVO_3}$ have been elaborately investigated by Blake *et al.* [68] and Reehuis *et al.* [72] by the use of neutron and synchrotron x-ray diffraction. The lattice parameters for various temperatures are summarized in table 5.1. The system undergoes a second-order structural phase transition at $T_{OO} = 200\,\mathrm{K}$ from the room-temperature orthorhombic phase (space group $Pbnm$) to the intermediate-temperature monoclinic phase (space group $P2_1/b$). Structural investigations yield three different $\mathrm{V-O}$ bond distances within one $\mathrm{VO_6}$ octahedron above 200 K. For the monoclinic phase below 200 K two symmetrically unequivalent V sites have been reported, V(1) and V(2), that alternate along c. This leads to overall six different $\mathrm{V-O}$ bond distances. Each $\mathrm{V(1)O_6}$ and $\mathrm{V(2)O_6}$ octahedron consists of two only slightly different bond distances and one long distance. The long distance lies in the ab plane and alternates along c, in accordance with the claim for G-type orbital order in this phase. AFM order of C type is observed below $T_N = 116\,\mathrm{K}$ [83]. The coupled spin and orbital degrees of freedom are recognized as the origin of a number of exotic properties observed in this phase, as discussed in the preceding section. The spin order changes to G type and the orthorhombic crystal structure is recovered below the first-order structural phase transition at $T_S = 77\,\mathrm{K}$. Below 77 K all V sites are equivalent,

again a long $\mathrm{V}-\mathrm{O}$ bond distance is present in the ab plane, which now has a constant direction along c, in accordance with orbital order of C type. Optical and neutron spectroscopy studies on YVO_3 single crystals give evidence that the symmetry in the monoclinic phase is lower than $P2_1/b$, proposing the monoclinic space group $Pb11$. The symmetry $Pb11$ allows for dimerization along the c axis, in accordance with results from neutron scattering, suggesting an orbital Peierls state for the monoclinic phase [15], see the discussion in the preceding section. However, Reehuis *et al.* [72] did not succeed in resolving the small deviation of the atomic positions in $Pb11$ compared to $P2_1/b$ in their synchrotron x-ray diffraction data.

Temp.	space group	a(Å)	b(Å)	c(Å)	α (°)	Ref.
5K	$Pbnm$	5.28551(6)	5.59264(5)	7.55615(7)	90	[72]
65K	$Pbnm$	5.28164(3)	5.58868(3)	7.55030(4)	90	[68]
80K	$P2_1/b$	5.27243(3)	5.62058(3)	7.53254(4)	89.977(3)	[68]
85K	$Pbnm$	5.28547(7)	5.62399(7)	7.53979(1)	90	[72]
85K	$P2_1/b$	5.27650(5)	5.62401(5)	7.53980(7)	89.980	[72]
100K	$P2_1/b$	5.27272(3)	5.61940(3)	7.53499(4)	89.979(3)	[68]
140K	$P2_1/b$	5.27393(3)	5.61602(3)	7.54235(4)	89.973(3)	[68]
180K	$P2_1/b$	5.27474(4)	5.61126(3)	7.55316(4)	89.978(3)	[68]
230K	$Pbnm$	5.27953(8)	5.61072(8)	7.57214(1)	90	[72]
240K	$Pbnm$	5.27574(3)	5.60679(3)	7.56714(4)	90	[68]
295K	$Pbnm$	5.27722(3)	5.60453(3)	7.57294(4)	90	[72]
295K	$Pbnm$	5.27839(3)	5.60608(3)	7.57421()	90	[68]

Table 5.1: Temperature dependence of the lattice parameters of YVO_3.

5.1.5 Details on CeVO_3

The crystal and magnetic structure of CeVO_3 has been studied in detail by Reehuis *et al.* [75] making use of high-resolution x-ray powder diffraction and single-crystal neutron diffraction. A structural phase transition from the orthorhombic phase (space group $Pbnm$) to the monoclinic phase (spacegroup $P2_1/b$) has been observed at $T_{OO} = 136\,\mathrm{K}$. In the monoclinic phase two out of four $\mathrm{V}-\mathrm{O}$ bonds that lie almost in the ab plane are strongly elongated in consistence with an orbital ordering pattern of G type. Spin ordering of C type is reported to set in at the Néel temperature $T_N = 124\,\mathrm{K}$ [75]. Both transition temperatures are considerably lower than those observed in other compounds of the series $R\mathrm{VO}_3$.
A second study based on high-energy synchrotron x-ray diffraction in combination with specific heat measurements performed by Ren *et al.* [73] reveal transition

temperatures that are about 20 K higher. According to Ren *et al.* [73] the crystal symmetry is lowered to monoclinic $P2_1/b$ together with the onset of orbital ordering at $T_{OO} = 154\,\mathrm{K}$ at a second-order phase transition. They confirm the orbital ordering pattern of G type in the monoclinic phase. Ref. [73] reports that Néel ordering takes place at $T_N = 134\,\mathrm{K}$ and is accompanied by a sudden lattice change at a phase transition of first order.
Also the sequence of the spin and orbital ordering transitions in CeVO_3 has been disputed. The opposite sequence has been reported by Miyasaka *et al.* [78] ($T_N = 133\,\mathrm{K}$ and $T_{OO} = 122\,\mathrm{K}$) and Mũnoz *et al.* [76] ($T_N = 136\,\mathrm{K}$ and $T_{OO} = 124\,\mathrm{K}$). We trust the sequence reported in Ref. [75] and Ref. [73] as single-crystal neutron diffraction is expected to be more sensitive than the neutron powder diffraction used in Ref. [76]. This sequence is further confirmed by Fujioka *et al.* [95]. They investigate the spin/orbital ordering phase diagram for mixed crystals of $\mathrm{Pr}_{1-x}\mathrm{La}_x\mathrm{VO}_3$ by the use of magnetization and specific heat measurements. With an increasing La-doping concentration x in $\mathrm{Pr}_{1-x}\mathrm{La}_x\mathrm{VO}_3$ the GdFeO_3-type orthorhombic distortion is found to be systematically reduced. It is reported that T_{OO} is still higher than T_N for a doping concentration of $x = 0.73$. For this value of x the effective rare-earth radius is almost identical to that of CeVO_3. T_{OO} becomes lower that T_N only just before $x = 1$ (LaVO_3) is reached. For our analysis we use the values of T_{OO} and T_N reported in Ref. [73], since they use the same high-quality single crystals for their analysis as us, produced by A. A. Nugroho and T. T. M. Palstra.
According to Reehuis *et al.* [75] the magnitude of the unit cell volume of CeVO_3 deviates from the monotonic dependence on the size of the rare-earth ion that is observed for the other compounds $R\mathrm{VO}_3$. A possible explanation is given in terms of a deviation of the Ce valence from 3+, resulting in a contraction of the Ce ion due to its higher charge. The lattice constants of CeVO_3 that have been deduced by Reehuis *et al.* [75] from their synchrotron powder x-ray diffraction data are reproduced in table 5.2.

Temp.	space group	a(Å)	b(Å)	c(Å)	α (°)
10 K	$P2_1/b$	5.52347(2)	5.57933(2)	7.71817(3)	90.0798(3)
160 K	Pbnm	5.51680(2)	5.55429(2)	7.79260(3)	90

Table 5.2: Temperature dependence of the lattice parameters of CeVO_3 as obtained by Reehuis *et al.* [75].

5.1.6 Details on $GdVO_3$

The compound $GdVO_3$ has been investigated to a much lesser extent compared to YVO_3 and $CeVO_3$. The structural properties have been extracted by Sage *et al.* [74] through a combined study of high-resolution x-ray diffraction and thermal expansion on powdered samples within the framework of a very detailed investigation of the orbital ordering phase diagram of a huge number of $R\mathrm{VO}_3$ compounds (R = Tb, Gd, Eu, Sm, Nd, Pr, see the discussion in Sec. 5.1.2). They confirm the orthorhombic crystal structure (space group *Pbnm*) at room temperature and the transition to a G-type orbitally ordered monoclinic phase (space group $P2_1/b$) taking place at $T_{OO} \approx 210\,\mathrm{K}$. Néel ordering of C type is reported to set in at $T_N \approx 130\,\mathrm{K}$. The authors of Ref. [74] find evidence for a coexistence of phases with monoclinic and orthorhombic symmetry which develops shortly below T_N at T_S^*. The data provides strong evidence that orbital order of G (C) type is present in the monoclinic (orthorhombic) phase fraction. However, Voigt [96] acquired infrared reflectance and transmittance data on our $GdVO_3$ single crystals by the use of a Fourier-transform spectrometer, which clearly indicate that our samples do not show phase coexistence. A transition to a phase-separated state should be visible in the phonon spectrum by the emergence of additional modes, but such modes have not been observed [96]. In Ref. [74] it has been claimed that the fraction of the orthorhombic phase increases from 0% at T_S^* up to approx. 67% at $T = 60\,\mathrm{K}$ and remains constant at lower temperatures. Consequently, we expect that the modes which are only visible in the monoclinic phase should loose weight with decreasing temperature starting at T_S^*. However, this has not been observed either [96], see Figs. 5.6 and 5.7. Further evidence for the absence of phase coexistence in our single crystals comes from the analysis of the spin-forbidden local crystal-field excitations ($3d^2 \rightarrow 3d^{2,*}$) by means of transmittance measurements performed by Voigt [96]. He compares his data on $GdVO_3$ with data on YVO_3 and $HoVO_3$ of Ref. [37]. The 5 K data of $GdVO_3$ show similar features as the data of YVO_3 and $HoVO_3$ in the monoclinic phase. The peak structure characteristic for the low-temperature orthorhombic phase of YVO_3 and $HoVO_3$ is not visible at any temperature in the data of $GdVO_3$, see Fig. 5.8. It can therefore be safely concluded that our single crystals of $GdVO_3$ show a homogeneous C-type spin and G-type orbitally ordered phase below T_N.

The lattice constants at room temperature amount to $a = 5.342$ Å, $b = 5.604$ Å, and $c = 7.637$ Å [97]. The phase-transition temperatures as extracted from the spin and orbital ordering phase diagram presented by Miyasaka *et al.* [78] are $T_{OO} = 208\,\mathrm{K}$ and $T_N = 122\,\mathrm{K}$.

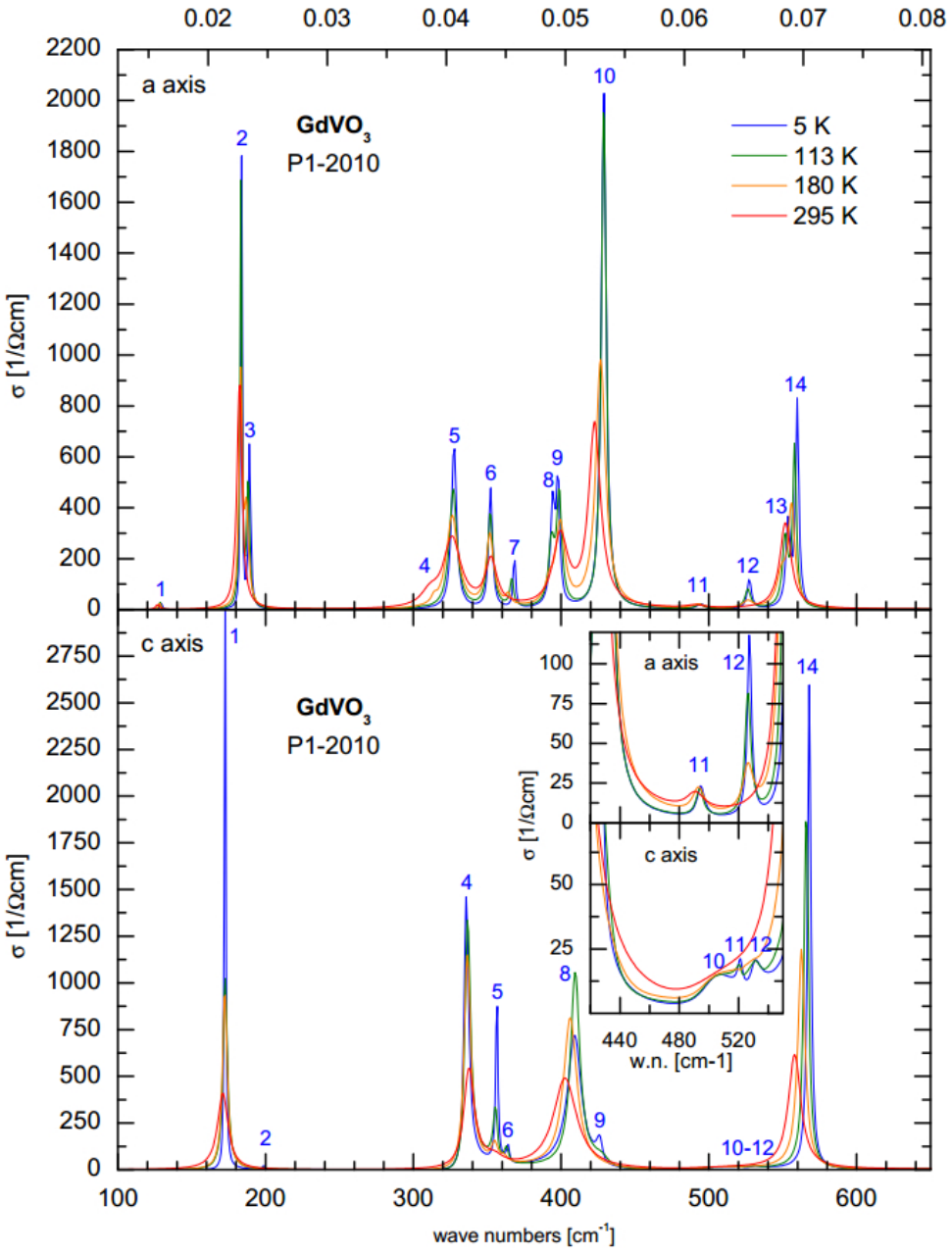

Figure 5.6: Phonon spectrum of $GdVO_3$ in the energy range from $100\,\mathrm{cm}^{-1}$ to $650\,\mathrm{cm}^{-1}$ ($\approx 0.01\,\mathrm{eV} - 0.08\,\mathrm{eV}$) as obtained by Voigt [96]. Taken from Ref. [96].

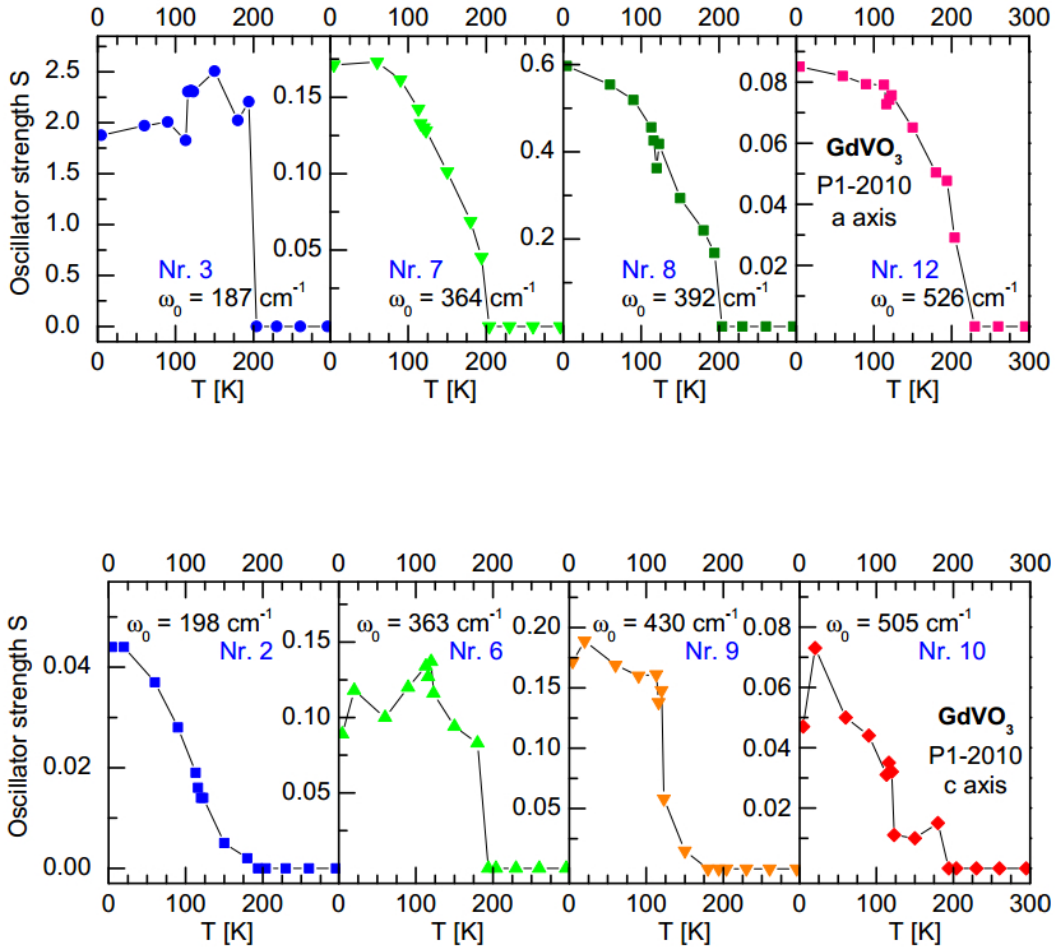

Figure 5.7: Oscillator strength of the phonon modes of GdVO_3 (the numbers correspond to the numbering of the modes in Fig. 5.6) which become visible across the structural phase transition at 208 K from the orthorhombic to the monoclinic phase. A transition to a phase separated state developing below T_N should be reflected in a loss of their oscillator strengths with decreasing temperature, which is not observed. The modes corresponding to the a (c) axis are shown in the upper (lower) panel. Taken from Ref. [96].

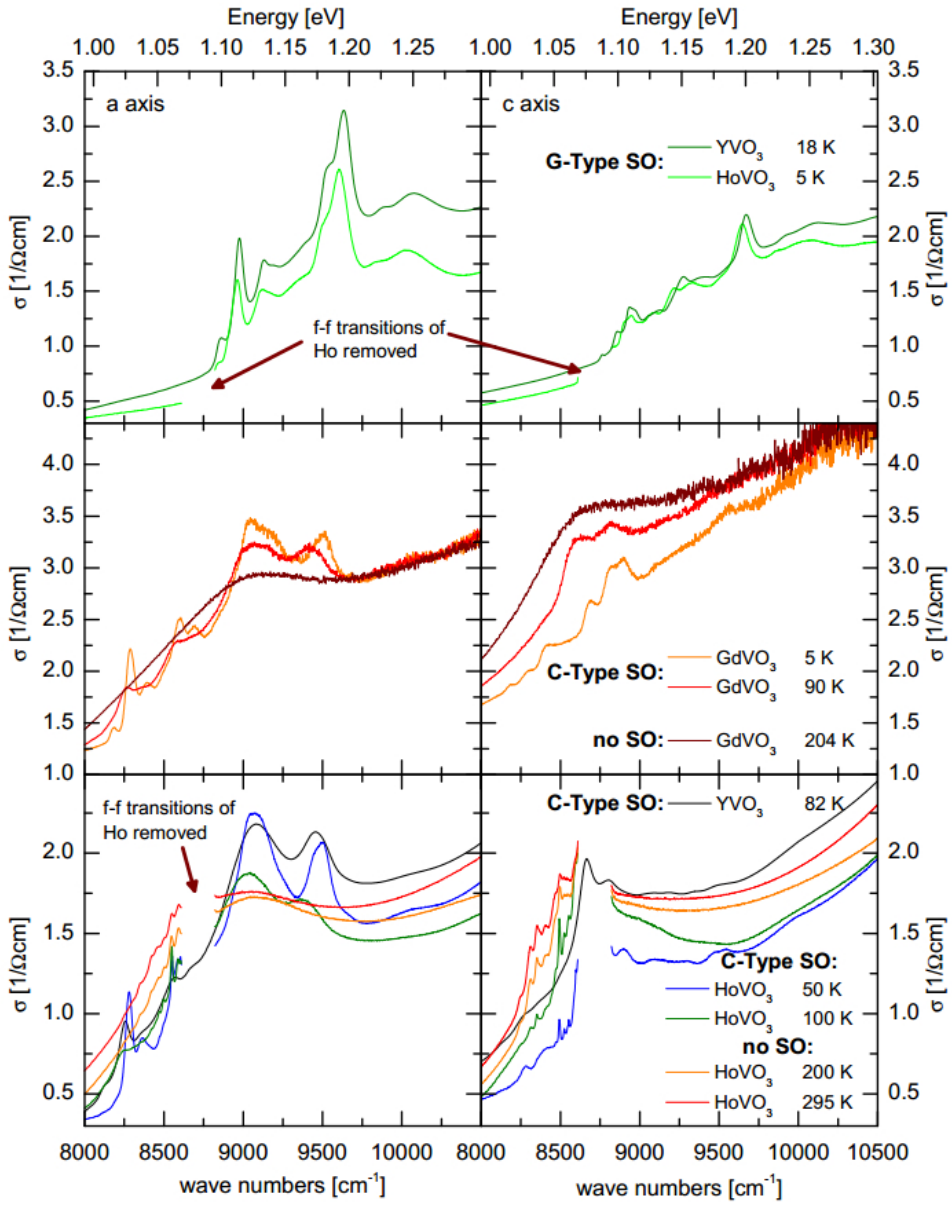

Figure 5.8: Comparison of the spin-forbidden local crystal-field excitations ($3d^2 \rightarrow 3d^{2,*}$) in $GdVO_3$, YVO_3, and $HoVO_3$. The upper panels show the data corresponding to the G-type spin and C-type orbitally ordered low-temperature orthorhombic phase of YVO_3 and $HoVO_3$, wheres the lower panels depict the data corresponding to the C-type spin and G-type orbitally ordered monoclinic phase of YVO_3 and $HoVO_3$. Both data sets originate from Ref. [37]. The data of $GdVO_3$ of Ref. [96] are displayed in the middle panels. They do not show any signatures which can be attributed to a G-type spin ordered phase. Taken from Ref. [96].

5.1.7 Mott-Hubbard excitations in RVO$_3$

We expect two types of electronic excitations in the investigated energy range from 0.75 eV to 5.5 eV: Mott-Hubbard (MH) excitations $|d_i^2 d_j^2\rangle \rightarrow |d_i^1 d_j^3\rangle$ between different vanadium ions i and j and charge-transfer (CT) excitations $|p^6 d^2\rangle \rightarrow |p^5 d^3\rangle$, between the oxygen $2p$ and the vanadium $3d$ level. According to the Zaanen-Sawatzky-Allen scheme, RVO$_3$ belongs to the group of MH insulators where the on-site Coulomb repulsion U is lower than the CT energy Δ. Due to the inversion symmetry on the V site the onsite $d-d$ excitations are not dipole allowed but can yield finite spectral weight by the coupling to phonons. A detailed optical study of the local $d-d$ excitations has been reported by Benckiser *et al.* [18] focusing on the mid- and near-infrared frequency range. In the spectral range relevant for this work local $d-d$ excitations can be neglected because of the overlap with the strongly dipole-allowed MH excitations.
Due to the multiorbital character of RVO$_3$, the final $|d_i^1 d_j^3\rangle$ states of the MH excitations are split into a complex multiplet structure, which is supposed to be reflected in a multi-peak structure of the optical data [8, 10]. Since the splitting between the t_{2g} level and the e_g level amounts to $10\,Dq \approx 2$ eV in RVO$_3$, we may neglect the e_g orbitals for a discussion of the lowest excited states. For the sake of simplicity, we assume cubic symmetry and neglect the crystal-field splitting within the t_{2g} levels of roughly 0.1 eV − 0.2 eV. In the ground state, the t_{2g}^2 configuration shows $^3T_1$ symmetry with spin 1, in agreement with Hund's rule. The excited states $|t_{2g}^1 t_{2g}^3\rangle$ have to be distinguished according to the t_{2g}^3 sector because the t_{2g}^1 configuration always has the same energy. The t_{2g}^3 state splits into four levels $^4A_2$, ^2E, $^2T_1$, and $^2T_2$ with ^2E and $^2T_1$ being degenerate [8, 10, 23]. A sketch of the t_{2g}^2 ground state and the t_{2g}^3 excited states is shown in Fig. 5.9. The energies of these levels amount to $U - 3J_H$ ($^4A_2$), U (^2E,$^2T_1$), and $U + 2J_H$ ($^2T_2$) (see Fig. 5.10) [8,10] with the on-site Coulomb repulsion $U \approx 4$ eV − 5 eV [19,54]. The value of the Hund exchange $J_H \approx 0.55$ eV − 0.7 eV has been determined from the energy of spin-forbidden orbital excitations in YVO$_3$ [18]. The complex spin and orbital ordering phase diagram of RVO$_3$ is supposed to be the origin of a complex temperature dependence of the optical spectra [8, 10]. A change of spin and orbital correlations is expected to be reflected in a characteristic spectral-weight transfer between the individual components of the optical multiplets [10]. The temperature dependence of the individual absorption bands can be understood by considering the spin and orbital selection rules for the electron transfer between neighboring lattice sites (the total spin of the initial and final state has to be equal: $S_z^i = S_z^f$; in cubic symmetry t_{2g} orbitals generally only have overlap with the same t_{2g} orbital on the neighboring lattice site, cf. Sec. 2.6). We will use this concept to analyze the temperature dependence of the experimental data in Sec. 6.3.2.

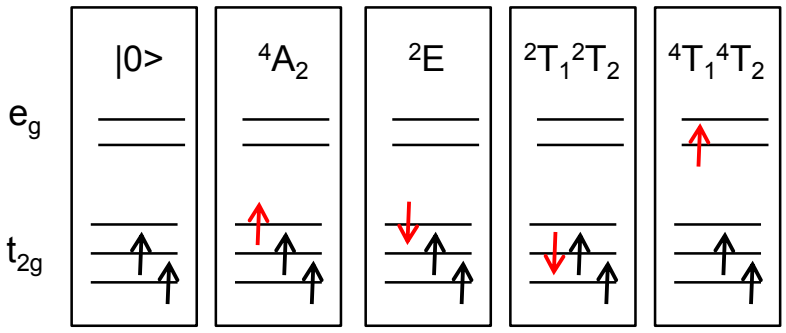

Figure 5.9: Sketch of the t_{2g}^2 ground state multiplet $^3T_1$ of $R\mathrm{VO}_3$ (left) and the t_{2g}^3 multiplets $^4A_2$, ^2E, $^2T_1$, and $^2T_2$ and the lowest $t_{2g}^2 e_g^1$ multiplets $^4T_2$ and $^4T_1$, all corresponding to possible excited states resulting from a MH excitation.

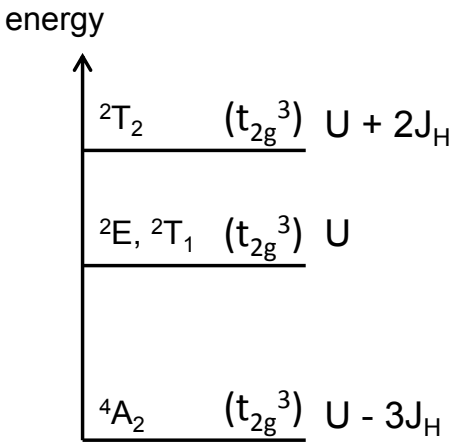

Figure 5.10:
Energy separation between the t_{2g}^3 multiplets $^4A_2$, $[^2E, {}^2T_1]$, and $^2T_2$.

5.1.8 Probing orbital fluctuation by the use of ellipsometry

As discussed in Sec. 5.1.3, different groups have claimed that orbital fluctuations may be strong in the monoclinic phase of $R\mathrm{VO}_3$. The experimental determination of orbital fluctuations is challenging. Our experimental approach is based on theoretical studies performed by Khaliullin, Horsch, Oleś, and Feiner [8, 10]. They study the optical properties of strongly correlated transition-metal oxides on the basis of spin-orbital superexchange models and show that the expected temperature dependence of the optical spectra is strikingly different for scenarios with either strongly fluctuating orbitals or rigid orbital order. In Sec. 2.6 we have seen that the MH excitations are the real counterparts of the virtual hopping processes that constitute the superexchange interactions between neighboring lattice sites. Thus the MH excitations are intimately connected with the spin-spin and orbital-orbital correlation functions. In the case of $R\mathrm{VO}_3$ the multi-orbital superexchange model includes coupled spin and orbital degrees of freedom. Ac-

cording to Refs. [8, 10] the intensity of a MH excitation $\int_0^\infty \sigma_n^{(\gamma)} d\omega$ into a specific multiplet state labeled by n along the cubic axis γ is related to the respective contribution to the effective low-energy superexchange Hamiltonian (Eq. 2.6 on page 13) $H_n^{(\gamma)}(ij)$ via the optical sum rule [10],

$$\frac{a_0 \hbar^2}{e^2} \int_0^\infty \sigma_n^{(\gamma)}(\omega) d\omega = -\pi \left\langle H_n^{(\gamma)}(ij) \right\rangle = -\frac{\pi}{2} K_n^{(\gamma)} \tag{5.1}$$

where a_0 is the distance between magnetic ions. The second equality relates the superexchange energy to the associated kinetic energy $K_n^{(\gamma)}$ via the Hellman-Feynman theorem [10].

Khaliullin, Horsch, Oleś, and Feiner [8, 10] made extensive use of this concept to study the optical properties of strongly correlated transition-metal oxides and determined the expected temperature and polarization dependence of the different multiplet transitions which contribute to the optical conductivity. Khaliullin, Horsch, Oleś, and Feiner [8, 10] specify $H_n^{(\gamma)}(ij)$ in terms of the on-site intraorbital Coulomb interaction energy U, the effective hopping element t of $d - d$ charge excitations between transition-metal ions, and the Hund exchange J_H. They use their results to calculate the optical spectral weights of the MH excitations into the ${}^4A_2$ ($n = 1$), $[{}^2T_1,\ {}^2E]$ ($n = 2$), and ${}^2T_2$ ($n = 3$) multiplets within the ab plane ($\gamma = ab$) and along the c direction ($\gamma = c$) in terms of the kinetic energies $K_n^{(\gamma)}$ based on a mean-field concept for cubic crystal symmetry. Oleś *et al.* [8] calculate the optical spectral weights assuming rigid orbital order with $T_{OO} = \infty$ on the example of LaVO_3 for the phase with C-type spin and G-type orbital order and YVO_3 for the low-temperature phase with G-type spin and C-type orbital order. They apply a mean-field approximation and separate the spin and orbital correlations from each other. The obtained values at $T = 0$ and above the magnetic transition at $T = 0.85J$ ($\approx 300\,\mathrm{K}$) are summarized in table 5.3. The kinetic energy terms are depicted in the left panel of Fig. 5.11 as a function of normalized temperature T/J for the transition into the phase with C-type spin and G-type orbital order. Khalliullin *et al.* [10], on the contrary, allow for quantum effects that go beyond the mean-field theory and include fluctuating orbitals as well as coupled spin-orbital degrees of freedom. They set $T_{OO} = T_N$. The so obtained optical spectral weights for the transition into the phase with C-type spin and G-type orbital order as a function of normalized temperature T/J are shown in right panel of Fig. 5.11.

It has been outlined in Sec. 5.1.3 that orbital quantum fluctuations are expected to be strong along the c axis in the monoclinic phase where orbital fluctuations and FM spin order support each other [14]. Khaliullin, Horsch, Oleś, and Feiner [8, 10] have demonstrated that the temperature evolution of the optical spectral weight of the excitation into the ${}^4A_2$ multiplet for $E \| c$ (which is proportional to $K_1^{(c)}$) gives valuable information about the strength of orbital fluctuations.

	LaVO_3 C-type AFM phase		YVO_3 G-type AFM phase	
	0 K	300 K	0 K	300 K
$-K_1^{(c)}$	1.640	1.181	0.0	0.0
$-K_2^{(c)}$	0.0	0.280	0.586	0.494
$-K_3^{(c)}$	0.0	0.0	0.465	0.392
$-K_1^{(ab)}$	0.219	0.471	0.249	0.471
$-K_2^{(ab)}$	0.961	0.532	0.871	0.532
$-K_3^{(ab)}$	0.436	0.253	0.415	0.253

Table 5.3: Optical spectral weights in terms of the kinetic energies $K_n^{(\gamma)}$ (in units of the superexchange constant $J = \frac{4t^2}{U}$) for the MH excitations into the ${}^4A_2$ ($n=1$), $[{}^2T_1,\ {}^2E]$ ($n=2$), and ${}^2T_2$ ($n=3$) multiplets along the c direction ($K_n^{(c)}$) and within the ab plane ($K_n^{(ab)}$) on the example of LaVO_3 (G-type OO and C-type SO) and YVO_3 (C-type OO and G-type SO) at $T=0$ and above the magnetic transition at $T=0.85\ J$ (≈ 300 K) as obtained by Oleś *et al.* [8] under the assumption of classical orbital order with $T_{OO}=\infty$ in the cubic approximation.

The superexchange Hamiltonian of Eq. 5.1 for this transition ($n=1,\ \gamma=c$) reads [8, 10, 98]:

$$H_1^{(c)} = -\frac{J}{3}R(2+\vec{S}_i\cdot\vec{S}_j)(\frac{1}{4}-\tau_i\cdot\tau_j) \tag{5.2}$$

The orbital pseudospins $T=1/2$ are described by the operators τ_i which are defined by the (initially degenerate) orbital doublet d_{zx} and d_{yz} at site i. Both of them are active along the c axis as there is precisely one electron in these two orbitals at each site i. Here, $(2+\vec{S}_i\cdot\vec{S}_j)$ is the projection operator in the high-spin state for $S=1$ spins [8, 10]. The superexchange constant J is given by $\frac{4t^2}{U}$ and the parameter R is defined as $R=1/(1-3\eta)$ with $\eta=J_H/U$. In order to determine the strength of orbital fluctuations, one has to study the detailed temperature dependence of the spectral weight, which thus is the most interesting quantity. Both results for $K_1^{(c)}$ (taken from Fig. 5.11 of Refs. [10] and [8]) as a function of normalized temperature T/J are displayed in Fig. 5.35 (b) on page 105, see below. We draw a conclusion about the importance of orbital fluctuations in $R\mathrm{VO}_3$ by comparing our experimental results with the predictions for both scenarios, rigid orbital order versus fluctuating orbitals, in Sec. 5.3.3.
Equation 5.2 can also be used to extract the expected total spectral-weight change of the excitation into ${}^4A_2$ for $E \parallel c$ when going from a completely disordered state

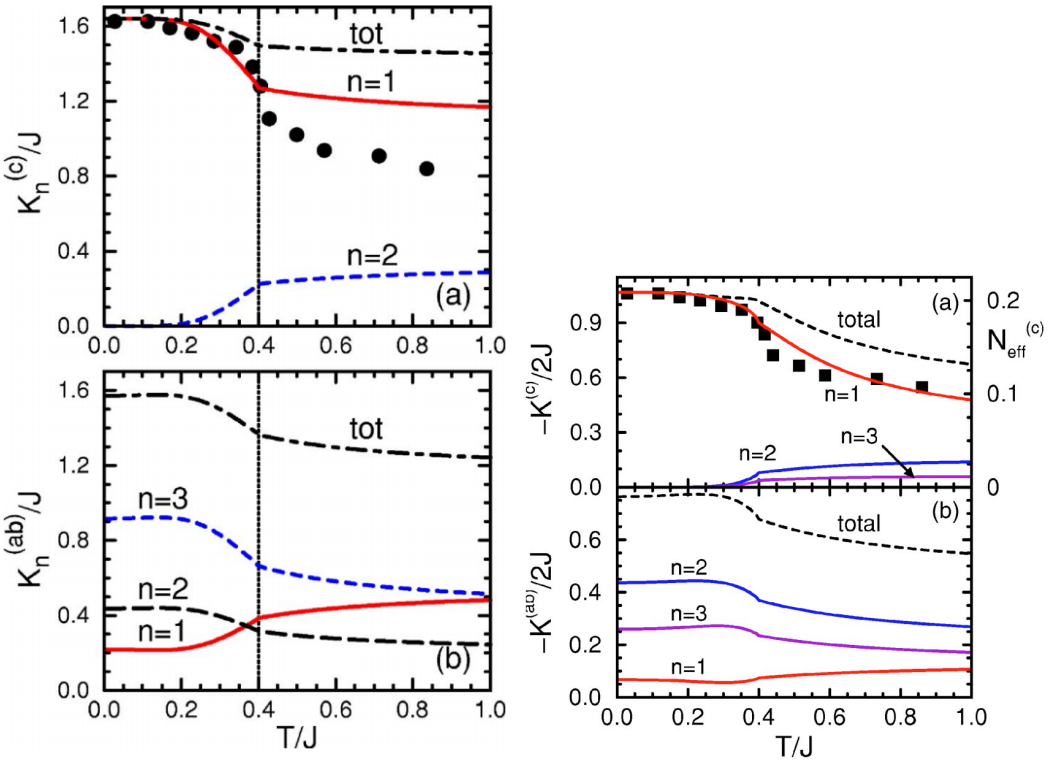

Figure 5.11: Optical spectral weights in terms of the kinetic energies $K_n^{(\gamma)}$ (in units of J (left panels) and $2J$ (right panels), in the left panels $K_n^{(\gamma)}$ are defined with opposite signs to obtain positive quantities) for the MH excitations into the ${}^4A_2$ ($n = 1$), $[{}^2T_1,\ {}^2E]$ ($n = 2$), and ${}^2T_2$ ($n = 3$) multiplets along the c direction ($K_n^{(c)}$) and within the ab plane ($K_n^{(ab)}$), and the total (tot) spectral weights ($\sum_n K_n^{(\gamma)}$) as a function of normalized temperature T/J for the transition into the phase with C-type spin and G-type orbital order. The left panels show the results obtained by Oleś *et al.* [8]. They set $T_N = 0.4\ J$ and assume rigid orbital order with $T_{OO} = \infty$ (the figure has been taken from Ref. [8]). The right panels show the results of Khaliullin *et al.* [10] who assume fluctuating orbitals with $T_N = T_{OO} = 0.4\ J$ (the figure has been taken from Ref. [10]). Both results refer to cubic crystal symmetry. In the upper panels (a) the effective carrier concentration of the double-peak structure between 1 eV and 3 eV in $\sigma_1^c(\omega)$ of LaVO_3 (black circles) as obtained by Miyasaka *et al.* [21] is reproduced (see Sec. 5.3.2) after scaling to match the value of $K_1^{(c)}$ at $T \to 0$.

into the state with fully ordered spins and orbitals, of C and G type, respectively. It amounts to 33 % for the spin part and 50% for the orbital part. Accordingly, multiplication yields an expected total change of spectral weight of approx. 66%. We will compare this value with our experimental result in Sec. 5.3.3 and thereby verify the peak assignment.

5.2 Experimental data

In this section the experimental results obtained on YVO_3, GdVO_3, and CeVO_3 are presented. Variable-temperature measurements have been performed inside the cryostat at an angle of incidence of 70°. All samples were oriented such that the crystallographic axis were parallel to the ellipsometer coordinate system. Consequently, it was sufficient to acquire the ellipsometric variables Ψ_{pp} and Δ_{pp} (cf. Sec. 3.2.1). All accessible Mueller-matrix elements have been obtained at room temperature to check for possible misalignment or depolarization.

5.2.1 Optical conductivity of YVO_3

All accessible Mueller-matrix elements have been acquired for anisotropic YVO_3 for four different orientations, using two different polished sample surfaces, an *ab* plane and an *ac* plane (measurement series 1). The size of the sample surfaces amounts to approx. 6 mm × 6 mm. To obtain the dielectric function ε^γ ($\gamma = a, b, c$) the experimental data is fit by a sum of two Tauc-Lorentz oscillators to describe the data close to the band gap and four Gaussian oscillators at higher energies for $\varepsilon^a(\omega)$ and a sum of one Tauc-Lorentz oscillator and five Gaussian oscillators for $\varepsilon^c(\omega)$ (for temperatures below T_S two Tauc-Lorentz oscillators and four Gaussian oscillators are used to describe $\varepsilon^c(\omega)$). Two of the Gaussian oscillators account for the steep increase of $\varepsilon_2(\omega)$ above $\approx 4.5\,\mathrm{eV}$ (see Fig. 5.13). The parameters of the Tauc-Lorentz and Gaussian oscillators are summarized in tables 5.4 and 5.5 for the data sets at $T = 15\,\mathrm{K}$, 100 K, and 300 K. Figure 5.12 shows an exemplary fit to the measured data at 140 K. The fit describes the measured data very well, yielding an MSE (see Sec. 3.2.4) of approx. 0.9 for $T > T_S$ ($= 77\,\mathrm{K}$) and approx. 1.8 for $T < T_S$. The quality of the fit is remarkable, keeping in mind that the model parameters are simultaneously fit to all accessible Mueller-matrix elements that have been obtained for 4(!) different sample orientations. It turned out that the use of Tauc-Lorentz oscillators for the description of the line shape close to the band gap yields a better fit than a model consisting of Gaussian oscillators alone. A model consisting of Lorentz oscillators is not able to reproduce the line shape of the measured data close to the band gap (see Fig. 5.33 below). In the fit a surface roughness with a thickness ranging from 35 Å to 80 Å depending on the sample surface is assumed. The thickness of the surface layer has been deduced from the transparent region of YVO_3 ($\varepsilon_2(\omega) \approx 0$) below 1.5 eV, as has been described in Sec. 4.2.1. The dielectric function along all three crystallographic directions *a*, *b*, and *c* is plotted in Fig. 5.13. The left panel of Fig. 5.14 shows the optical conductivity $\sigma_1(\omega)$. A close-up view of the multiplet structure below 4.5 eV is presented in the right panel of Fig. 5.14. The data show a striking polarization dependence between the *ab* plane and the *c* axis. Only a very small anisotropy is observed between the *a* and the *b* axis, the main features, including the temperature dependence, are

the same in both directions. The analysis of the anisotropy within the *ab* plane is not the objective of this work, therefore we will not go into further detail.
The main focus of this work is on the determination of the temperature dependence of the optical data. The number of temperature curves turned out to be not enough for a detailed analysis. Particularly, more data is needed close to the spin and orbital ordering temperatures T_N and T_{OO}, respectively, and it is desirable to acquire data at temperatures above room temperature. In the framework of a second measurement series (measurement series 2), the data acquisition was restricted to the ellipsometric variables Ψ_{pp} and Δ_{pp}. As we want to neglect the anisotropy within the *ab* plane, it was sufficient to make use of only one polished sample surface of another sample, an *ac* plane (size of the sample surface 5 mm × 2.5 mm), which has been measured in two different orientations, with the *a* and the *c* axis parallel to the plane of incidence, respectively. To obtain the dielectric function, the same set of oscillators is used in the fit as before. Here, the data below 1.5 eV yield a surface roughness with a thickness of 23 Å that has been included in the fit. Figure 5.15 shows the Tauc-Lorentz and Gaussian oscillators that compose $\varepsilon_2(\omega)$. Figure 5.16 compares the optical conductivity $\sigma_1(\omega)$ of YVO_3 at 140 K as obtained from measurement series 1 and measurement series 2, respectively. The data for the *c* axis agree very well, slightly larger deviations are observed for the data corresponding to the *ab* plane. One reason for the deviations is given by the fact that no *b* axis data has been acquired within measurement series 2. However, the main features of both data sets corresponding to the *ab* plane are the same. The dielectric function $\varepsilon(\omega)$ for various temperatures as obtained in the framework of measurement series 2 is shown in Fig. 5.17. Figure 5.18 displays the optical conductivity $\sigma_1(\omega)$ in the energy range from 1.0 eV to 4.5 eV. In the framework of the second measurement series, data has been acquired only above the structural phase transition temperature T_S at 77 K, as samples tend to break when undergoing the phase transition (see Sec. 5.3.2 below). As we are mainly interested in a detailed T dependence around T_N and T_{OO}, we want to avoid this problem.

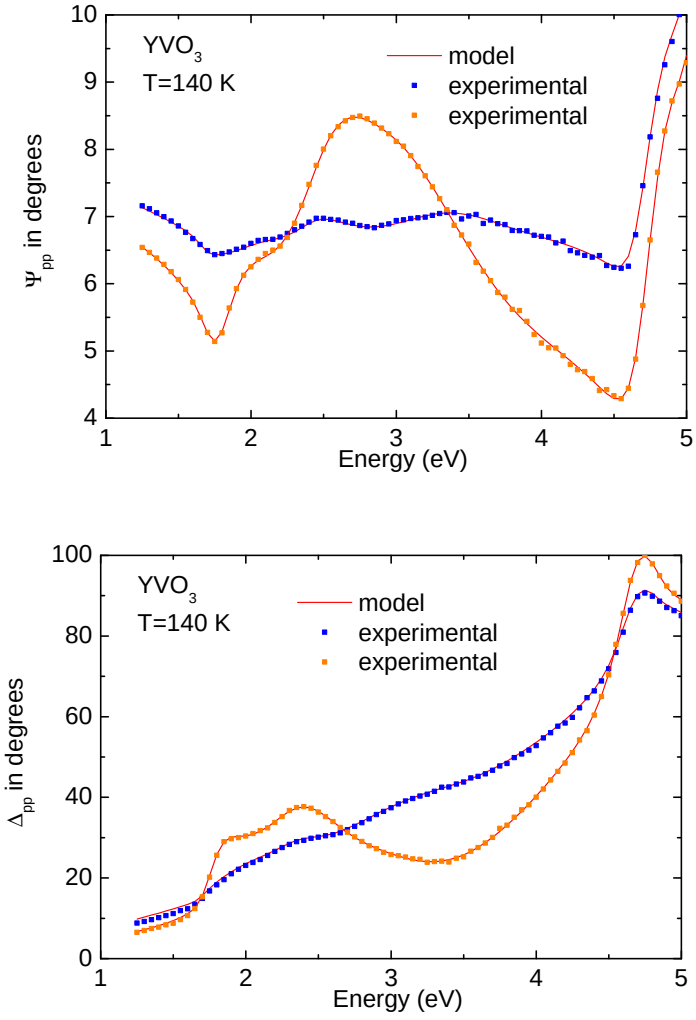

Figure 5.12: Experimentally obtained Ψ_{pp} (top) and Δ_{pp} (bottom) of YVO_3 for two different sample orientations at $T = 140\,\mathrm{K}$ with fit. Data that have been acquired on an ac plane with the c axis parallel to the plane of incidence (orange squares) and on an ab plane with the a axis parallel to the plane of incidence (blue squares) are shown.

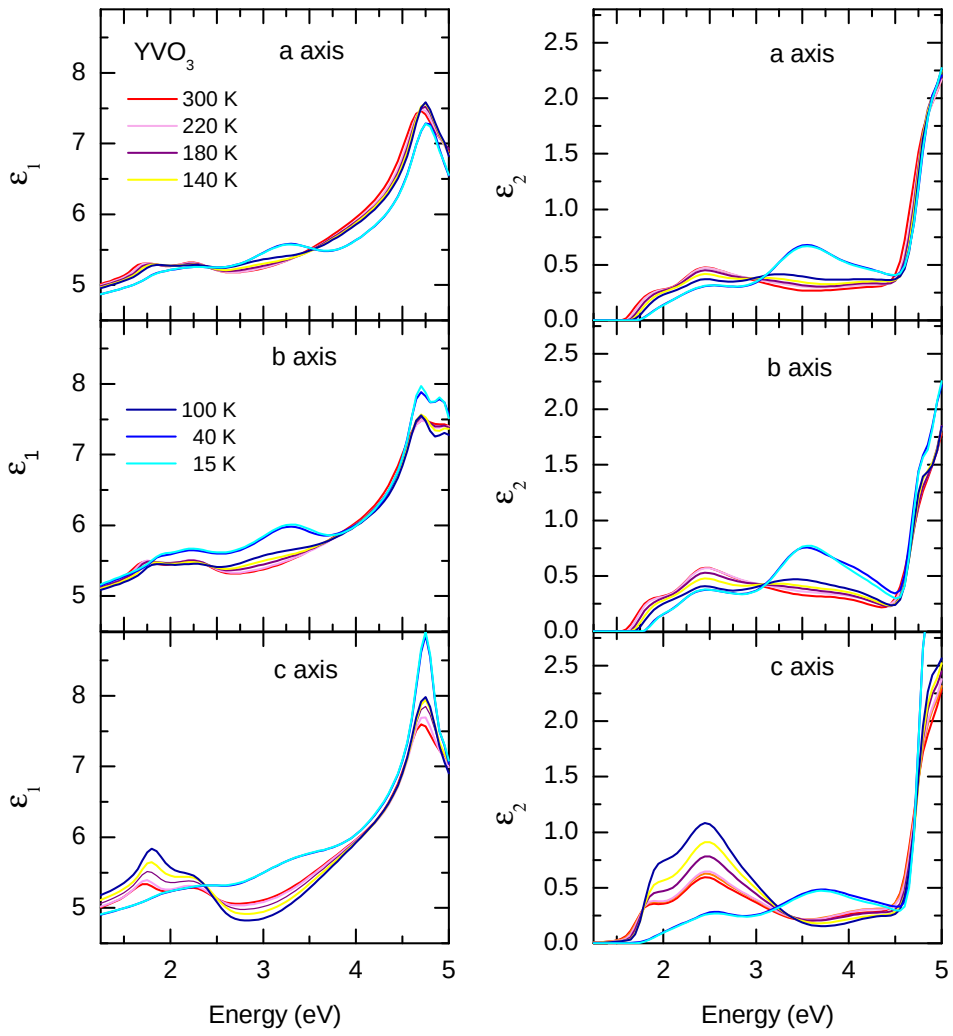

Figure 5.13: Dielectric function $\varepsilon(\omega)$ of YVO_3 for the a, b, and c direction between 1.25 eV and 5.0 eV for different temperatures (measurement series 1).

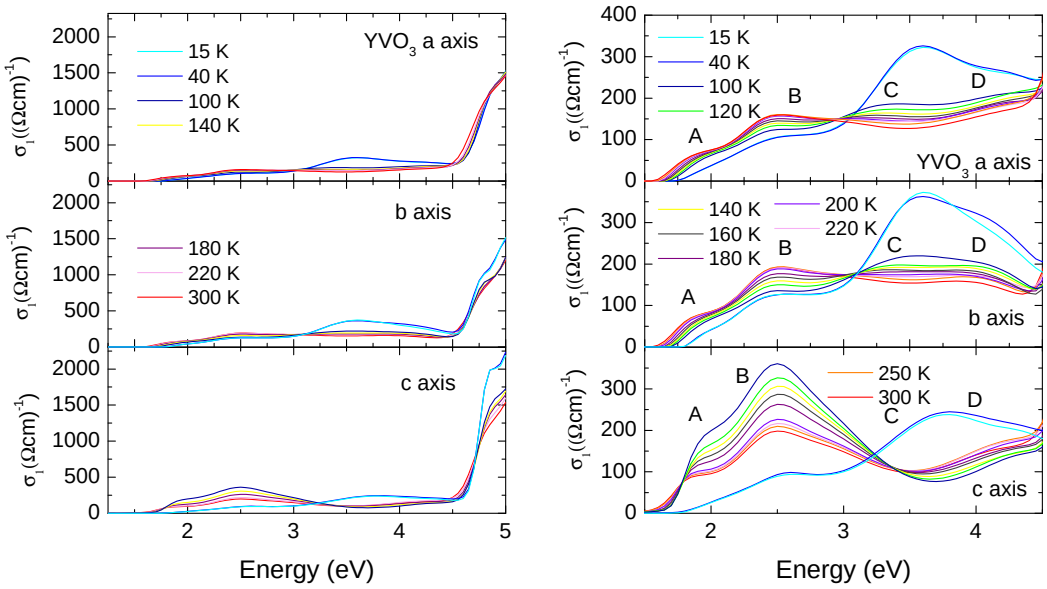

Figure 5.14: Optical conductivity $\sigma_1(\omega)$ of YVO_3 for the a, b, and c direction between 1.25 eV and 5.0 eV (left panel) and a close-up view of the multiplet structure between 1.5 eV and 4.5 eV (right panel) for different temperatures (measurement series 1).

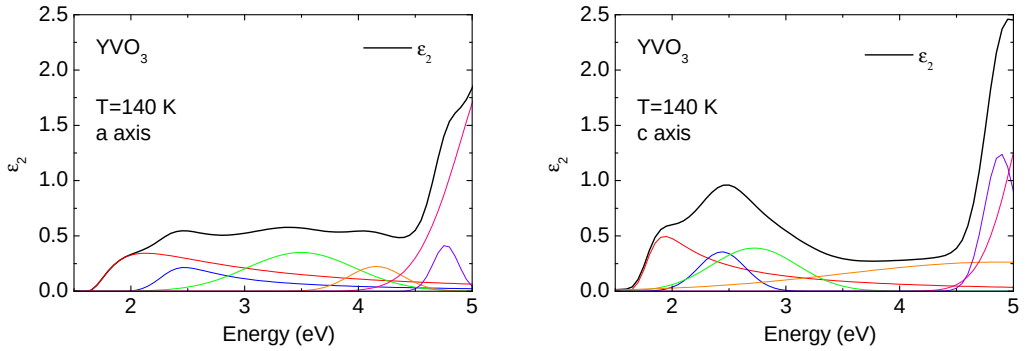

Figure 5.15: The measured data of YVO_3 is best fit by a sum of two Tauc-Lorentz oscillators and four Gaussian oscillators for $\varepsilon_2^a(\omega)$ and one Tauc-Lorentz and five Gaussian oscillators for $\varepsilon_2^c(\omega)$. Two of the Gaussian oscillators describe the steep increase of $\varepsilon_2(\omega)$ above ≈ 4.5 eV. (The data have been obtained within measurement series 2.)

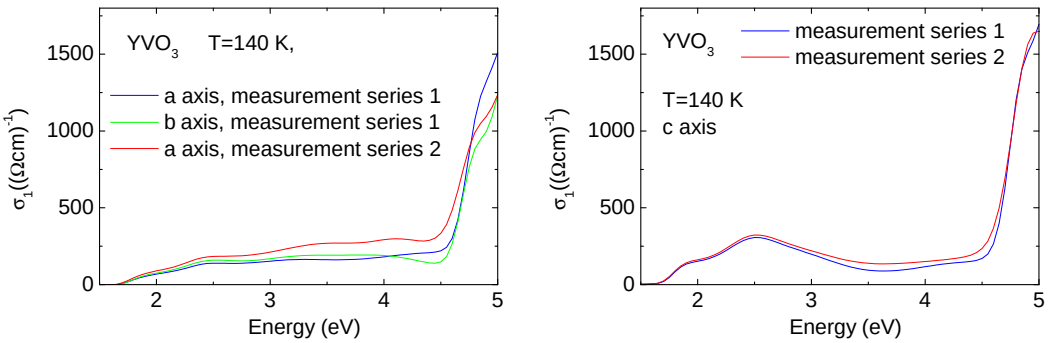

Figure 5.16: Comparison between the optical conductivity $\sigma_1(\omega)$ of YVO_3 obtained within measurement series 1 and measurement series 2 for the ab plane (left panel) and the c axis (right panel). Within measurement series 2 no b axis data have been acquired. Details on the measurements can be found in the text.

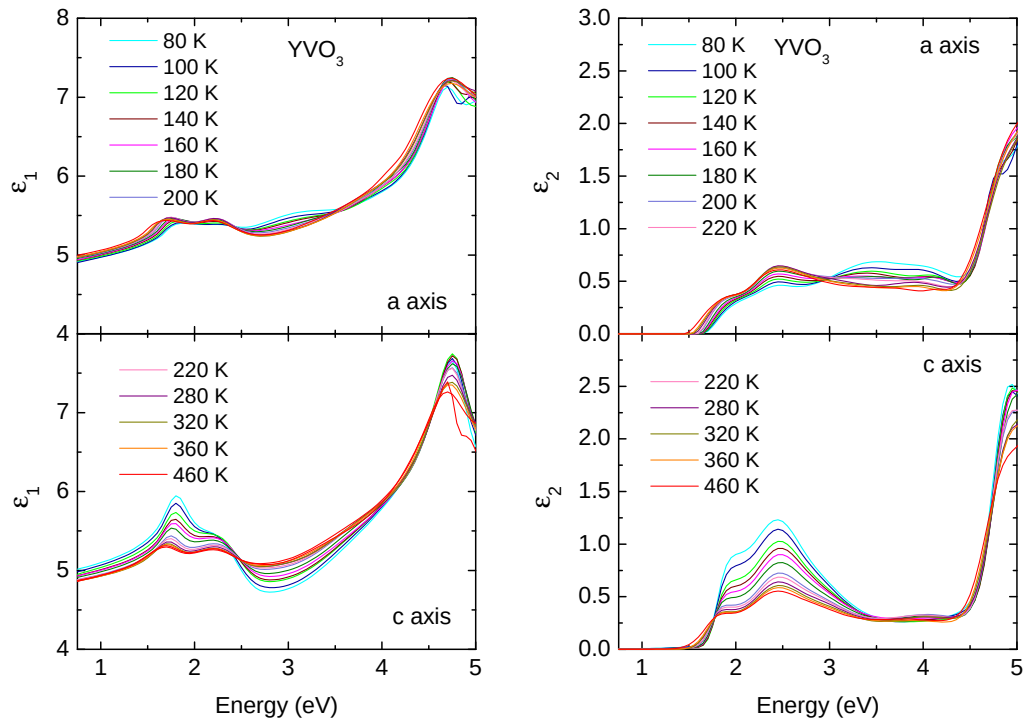

Figure 5.17: Dielectric function $\varepsilon(\omega)$ of YVO_3 for the a and c direction between 0.75 eV and 5.0 eV as obtained from a second measurement series for $T > T_S$ only (measurement series 2). (Not all temperatures are shown for clarity.)

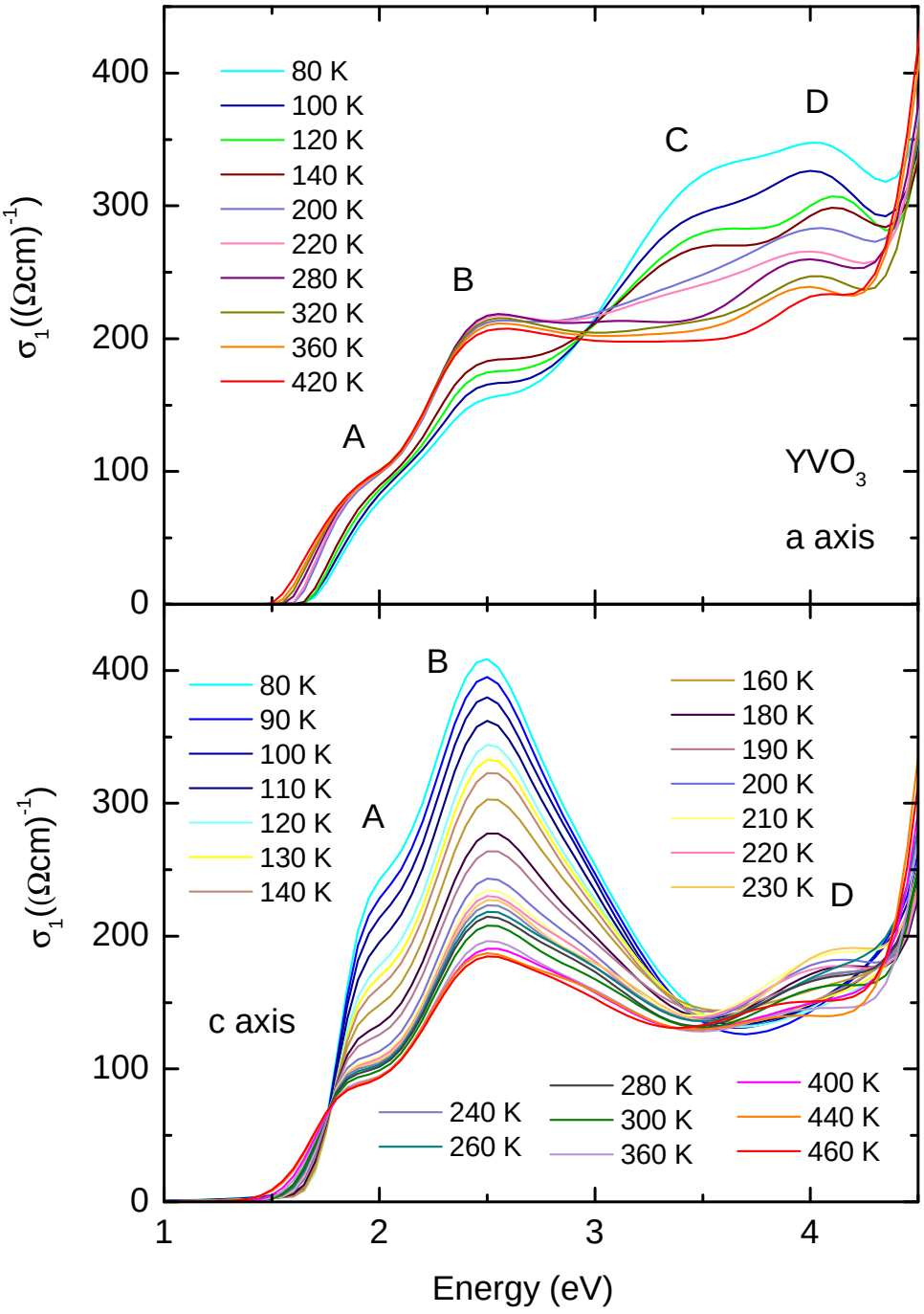

Figure 5.18: Optical conductivity $\sigma_1(\omega)$ of YVO_3 for the a and c direction between 1.0 eV and 4.5 eV as obtained from a second measurement series for $T > T_S$ only (measurement series 2). (Not all temperatures are shown for clarity.)

Table 5.4: Parameters of the fit to the measured data of YVO_3 (measurement series 1) with Gaussian (GA) and Tauc-Lorentz (TL) oscillators (a and b axis). The parameters of the oscillators are defined in Sec. 3.1.5 in Eq. 3.24 and Eq. 3.23, respectively. Apart from the amplitude A of the Gaussian oscillator, which is dimensionless, all parameters are given in eV.

a axis		GA1	GA2	GA3	GA4		TL1	TL2
	ω_0	3.4898	4.2329	4.8797	5.1158	A	4.3248	2.4971
$T = 15\,K$	Br	0.7029	1.3061	0.2989	0.2535	ω_0	1.7624	2.3614
	A	0.3763	0.3617	1.5247	1.9824	γ	0.4353	1.0358
						ω_g	1.7165	1.6651
	ω_0	3.2016	4.2799	4.8001	5.0584	A	7.0268	1.0089
$T = 100\,K$	Br	0.8171	1.6123	0.1941	0.4422	ω_0	1.7526	2.3994
	A	0.1862	0.3083	0.5406	2.1177	γ	0.5245	0.6249
						ω_g	1.6472	1.6155
	ω_0	3.0494	4.4456	4.7719	5.1331	A	12.2301	5.5061
$T = 300\,K$	Br	0.5855	1.4270	0.2999	0.5405	ω_0	1.5525	2.2855
	A	0.0324	0.1825	0.7330	2.1556	γ	0.5379	0.6408
						ω_g	1.6439	1.9723

b axis		GA1	GA2	GA3	GA4		TL1	TL2
	ω_0	3.4834	3.8346	4.7627	5.0759	A	11.8495	6.7074
$T = 15\,K$	Br	0.5673	1.0642	0.1951	0.3778	ω_0	1.7905	2.2238
	A	0.2632	0.4264	0.8976	2.6538	γ	0.4080	0.6110
						ω_g	1.7885	2.0196
	ω_0	3.4478	4.2030	4.7649	5.1536	A	12.9100	0.8399
$T = 100\,K$	Br	1.0790	0.7446	0.2269	0.5163	ω_0	1.6821	2.3995
	A	0.3281	0.1645	0.7474	2.2319	γ	0.4454	0.5733
						ω_g	1.6969	1.5953
	ω_0	3.0109	3.9458	4.7610	5.2184	A	5.9605	3.1006
$T = 300\,K$	Br	0.9089	1.0590	0.3220	0.6190	ω_0	1.7212	2.3611
	A	0.1415	0.1884	0.5606	2.2607	γ	0.4550	0.6824
						ω_g	1.5340	1.7137

Table 5.5: Parameters of the fit to the measured data of YVO_3 (measurement series 1) with Gaussian (GA) and Tauc-Lorentz (TL) oscillators (c axis). See the caption of table 5.4 for the definition of the parameters.

c axis		GA1	GA2	GA3	GA4	GA5		TL1	TL2
	ω_0	3.7313	4.4578	4.8178	5.0646		A	4.8745	0.8722
$T = 15\,K$	Br	0.9905	0.5964	0.1792	0.3916		ω_0	1.7389	2.4927
	A	0.3916	0.1710	1.6280	3.3541		γ	0.6381	0.7608
							ω_g	1.7375	1.5543
	ω_0	2.4446	2.6255	4.4114	4.8293	5.1361	A	14.4352	
$T = 100\,K$	Br	0.4144	0.9777	0.9168	0.2578	0.4638	ω_0	1.8026	
	A	0.2790	0.5400	0.1796	1.2111	2.6678	γ	0.3762	
							ω_g	1.6418	
	ω_0	2.4196	2.6494	4.2180	4.7780	5.1378	A	2.6747	
$T = 300\,K$	Br	0.4031	1.1357	1.2159	0.2473	0.6024	ω_0	1.7648	
	A	0.1465	0.4099	0.2596	0.5506	2.4715	γ	0.3573	
							ω_g	1.4713	

5.2.2 Optical conductivity of $GdVO_3$

The dielectric function $\varepsilon(\omega)$ of anisotropic $GdVO_3$ is deduced from the ellipsometric variables Ψ_{pp} and Δ_{pp}, which have been acquired on a single polished sample surface, an *ac* plane. The surface has been measured in two different orientations, with the *a* and the *c* axis parallel to the plane of incidence, respectively. The fit to the experimental data is based on a model consisting of seven Gaussian oscillators for $\varepsilon_2^a(\omega)$ and $\varepsilon_2^c(\omega)$, respectively, three of them describe the steep increase of $\varepsilon_2(\omega)$ above $\approx 4.5\,\mathrm{eV}$, see Fig. 5.19. The parameters of the Gaussian oscillators for the data sets at 15 K, 280 K, and 460 K are summarized in tables 5.6 and 5.7. The fit is remarkably good, yielding an MSE between 0.6 and 0.9, depending on the temperature. An exemplary fit to the measured data at $T = 130\,\mathrm{K}$ is presented in Fig. 5.20. The noise in the experimental data, which is most pronounced for energies $\gtrsim 3.5\,\mathrm{eV}$, originates from the smallness of the sample. The size of the sample surface amounts to only 3 mm × 2 mm. This leads to a low intensity at the detector as part of the light beam is reflected away from the brass cone which serves as the sample holder (see Fig. 4.6 in Sec. 4.1.3). A surface roughness with a thickness of approx. 25 Å is deduced from the data below 1.5 eV ($\varepsilon_2(\omega) \approx 0$). The dielectric function $\varepsilon(\omega)$ is presented in Fig. 5.21. Figure 5.22 shows the optical conductivity $\sigma_1(\omega)$ in the whole measured energy range from 0.75 eV to 5.5 eV, whereas a close-up view of the multiplet structure below 4.5 eV is presented in Fig. 5.23.

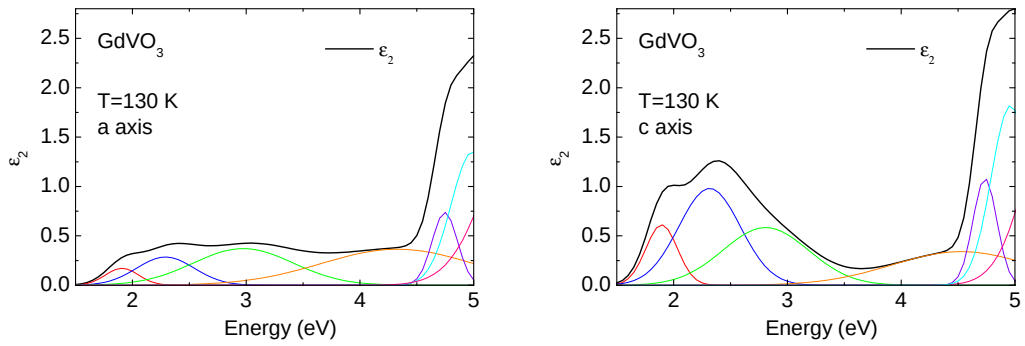

Figure 5.19: The measured data of $GdVO_3$ is best fit by a sum of seven Gaussian oscillators for $\varepsilon_2^a(\omega)$ and $\varepsilon_2^c(\omega)$, respectively. Three of the Gaussian oscillators describe the steep increase of $\varepsilon_2(\omega)$ above $\approx 4.5\,\mathrm{eV}$.

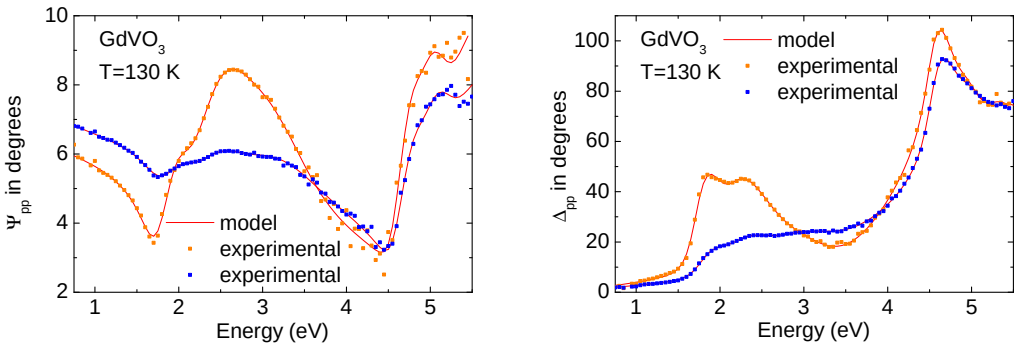

Figure 5.20: Experimentally obtained Ψ_{pp} (left panel) and Δ_{pp} (right panel) of GdVO_3 for two different sample orientations at $T = 130\,\mathrm{K}$. The data have been acquired on an ac plane with the c axis (orange squares) and the a axis (blue squares) parallel the plane of incidence, respectively.

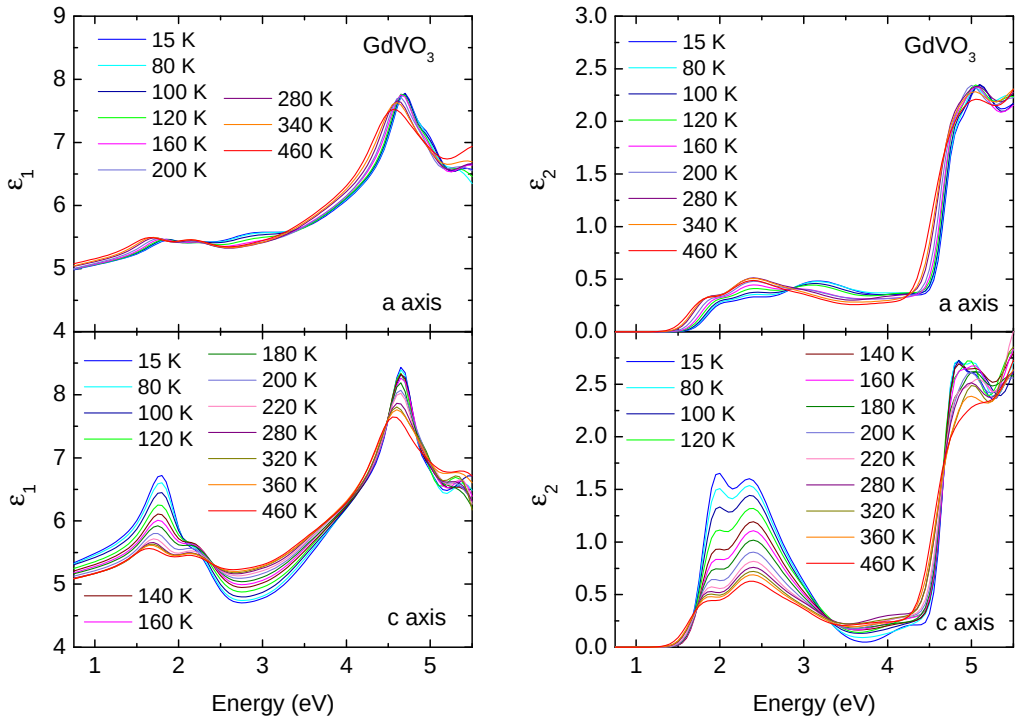

Figure 5.21: Dielectric function $\varepsilon(\omega)$ of GdVO_3 for the a and c direction between 0.75 eV and 5.5 eV for different temperatures. (Not all temperatures are shown for clarity.)

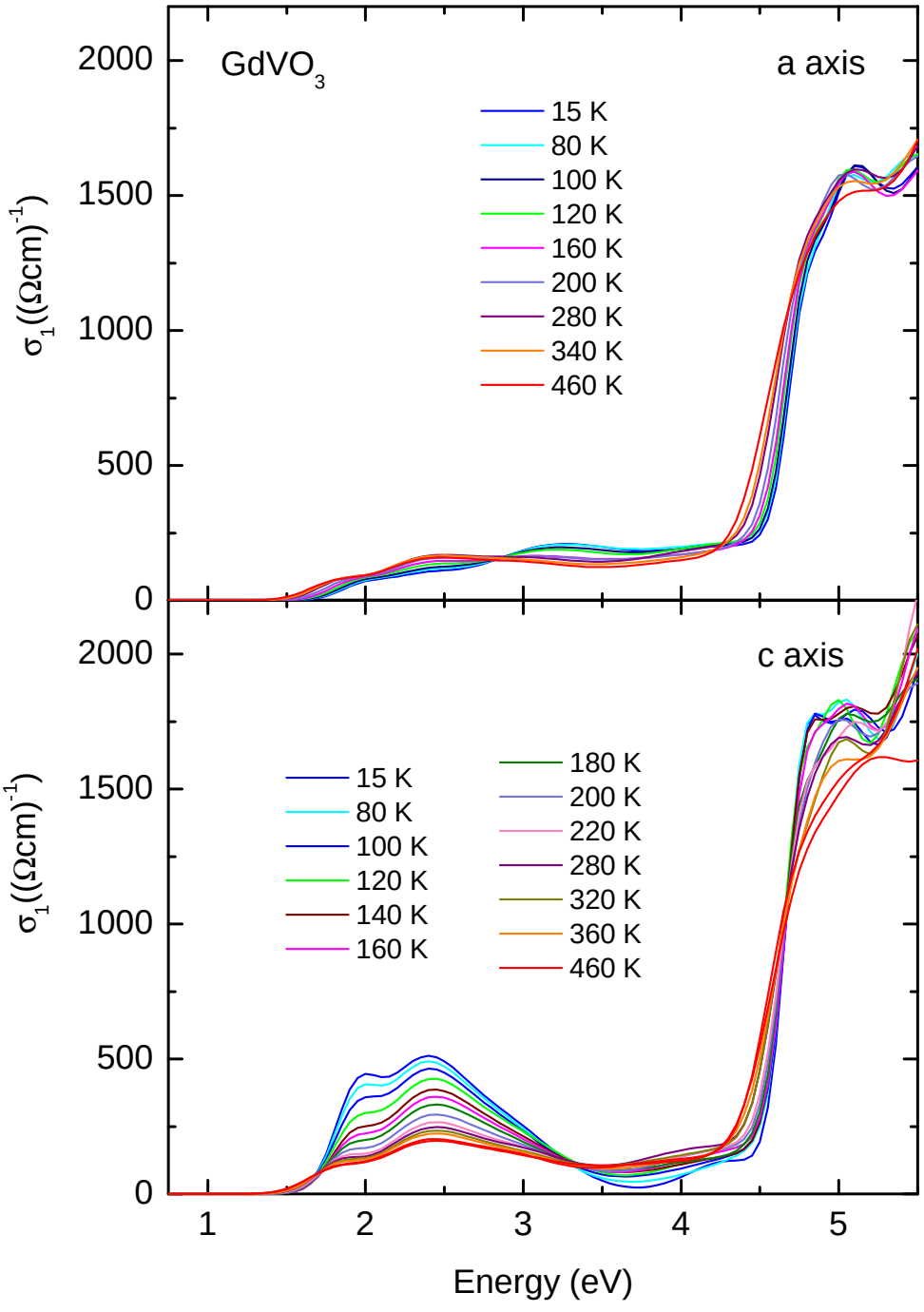

Figure 5.22: Optical conductivity $\sigma_1(\omega)$ of $GdVO_3$ for the a and c direction between 0.75 eV and 5.5 eV for different temperatures. (Not all temperatures are shown for clarity.)

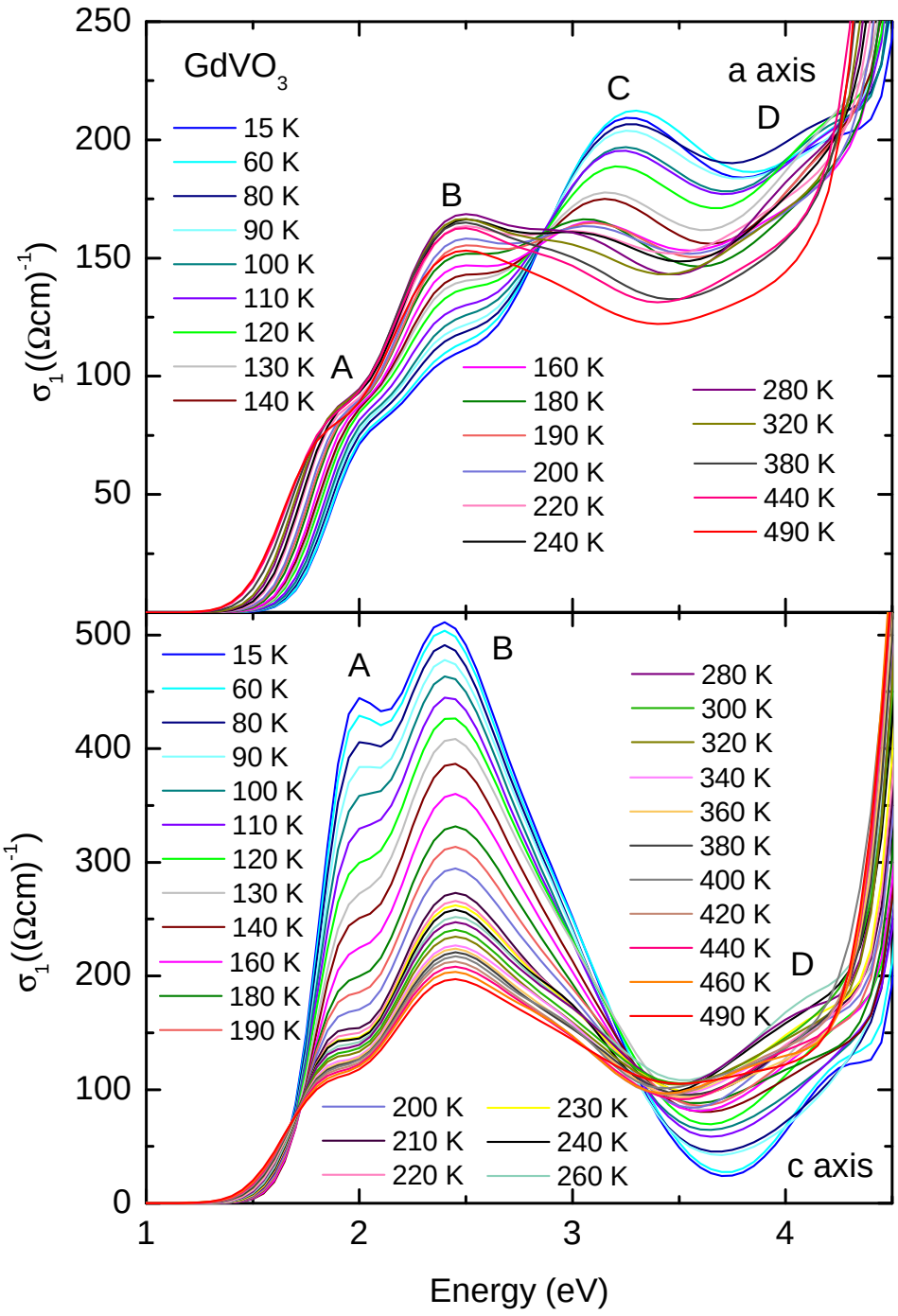

Figure 5.23: Close-up view of the optical conductivity $\sigma_1(\omega)$ of GdVO_3 for the a and c direction between 1.0 eV and 4.5 eV for different temperatures. (Not all temperatures are shown for clarity for $\sigma_1^a(\omega)$.)

Table 5.6: Parameters of the fit to the measured data of $GdVO_3$ with Gaussian (GA) oscillators (a axis). The center energy ω_0, the FWHM Br, and the amplitude A (dimensionless) of the Gaussian oscillators are defined in Sec. 3.1.5 in Eq. 3.24. The parameters ω_0 and Br are given in eV.

a axis		GA1	GA2	GA3	GA4	GA5	GA6	GA7
	w_0	1.9591	2.2886	3.1104	4.266	4.7633	5.0177	5.6048
$T = 15\,\mathrm{K}$	Br	0.3371	0.5461	1.0770	1.1872	0.2348	0.4618	0.9137
	A	0.1469	0.2165	0.4566	0.3270	0.6968	1.4550	2.1601
	w_0	1.8155	2.2796	2.8744	4.1351	4.7019	4.9870	5.7341
$T = 280\,\mathrm{K}$	Br	0.3478	0.6614	0.9839	1.4237	0.3276	0.5399	1.1322
	A	0.2058	0.3583	0.3431	0.3336	0.7200	1.3708	2.4066
	w_0	1.7751	2.2750	2.8725	3.9963	4.6403	4.9515	5.9380
$T = 460\,\mathrm{K}$	Br	0.3955	0.6756	0.9895	1.1972	0.3984	0.6162	1.4307
	A	0.2133	0.3463	0.3210	0.2502	0.5569	1.2767	2.8005

Table 5.7: Parameters of the fit to the measured data of $GdVO_3$ with Gaussian (GA) oscillators (c axis). See the caption of table 5.6 for the definition of the parameters.

c axis		GA1	GA2	GA3	GA4	GA5	GA6	GA7
	w_0	1.9207	2.2867	2.7464	4.2958	4.7567	4.9953	5.5297
$T = 15\,\mathrm{K}$	Br	0.3143	0.6096	0.8880	0.6327	0.2647	0.4127	0.7121
	A	1.0699	1.2013	0.7481	0.2098	1.6203	1.8844	2.6067
	w_0	1.8075	2.3601	2.9867	4.1597	4.6965	4.9581	5.5244
$T = 280\,\mathrm{K}$	Br	0.3357	0.7413	0.6629	1.3884	0.3444	0.4624	0.7541
	A	0.3448	0.7281	0.2887	0.3113	0.9022	1.6643	2.5540
	w_0	1.7794	2.3300	2.8973	3.9895	4.6597	4.9683	5.7258
$T = 460\,\mathrm{K}$	Br	0.4007	0.6933	0.6334	1.6614	0.3745	0.6315	0.8973
	A	0.3100	0.5791	0.2493	0.2385	0.6469	1.6598	2.9444

5.2.3 Optical conductivity of $CeVO_3$

The ellipsometric variables Ψ_{pp} and Δ_{pp} have been obtained for two different orientations of a single crystal of $CeVO_3$. A polished *ac* surface has been measured with the *a* and the *c* axis parallel to the plane of incidence, respectively. To obtain the dielectric function from the measured data, a fit based on four (five) Gaussian oscillators for $\varepsilon^a(\omega)$ ($\varepsilon^c(\omega)$) yields a good result. One (two) oscillators account for the steep increase of $\varepsilon_2^a(\omega)$ ($\varepsilon_2^c(\omega)$) above $\approx 4.5\,\mathrm{eV}$, see Fig. 5.24. The parameters of the Gaussian oscillators for the data sets at 60 K, 250 K, and 490 K are summarized in tables 5.8 and 5.9. The quality of the fit increases with increasing temperature, yielding an MSE that decreases from approx. 2.5 for $T = 60\,\mathrm{K}$ to approx. 1 for $T = 490\,\mathrm{K}$. Figure 5.25 shows an exemplary fit to the measured data at 145 K. Similar to the case of $GdVO_3$, the single crystal of $CeVO_3$ on hand is very small, the size of the sample surface amounts to only $2.5\,\mathrm{mm} \times 1.5\,\mathrm{mm}$. As a result, part of the light beam does not hit the detector as it is reflected away from the sample holder consisting of a brass cone (see Fig. 4.6 in Sec. 4.1.3). The low intensity at the detector leads to the noise in the experimental data, which is especially pronounced in the higher energy region. A surface roughness with a thickness of 60 Å has been deduced from the data below 1.2 eV.
Figure 5.26 displays the dielectric function $\varepsilon(\omega)$. The optical conductivity $\sigma_1(\omega)$ between 0.75 eV and 5.0 eV is shown in Fig. 5.27, whereas a close-view of the multiplet structure below 4.5 eV is displayed in Fig. 5.28.

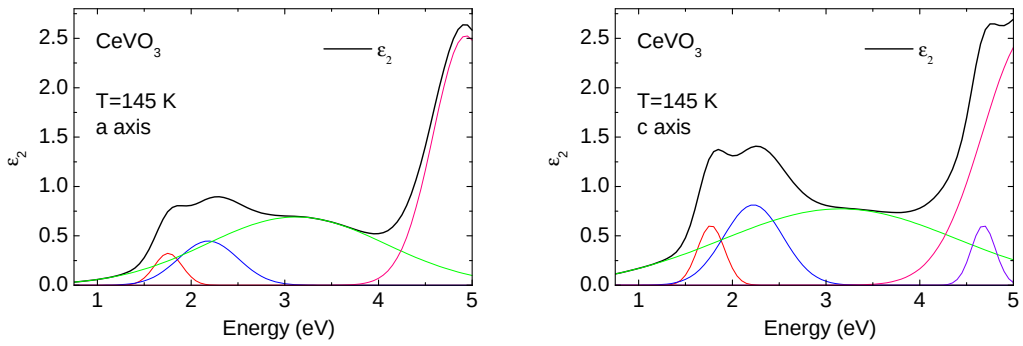

Figure 5.24: The measured data of $CeVO_3$ is best fit by a sum of four Gaussian oscillators for $\varepsilon_2^a(\omega)$ and five Gaussian oscillators for $\varepsilon_2^c(\omega)$. One (two) of the Gaussian oscillators describe(s) the steep increase of $\varepsilon_2^a(\omega)$ ($\varepsilon_2^c(\omega)$) above $\approx 4.5\,\mathrm{eV}$.

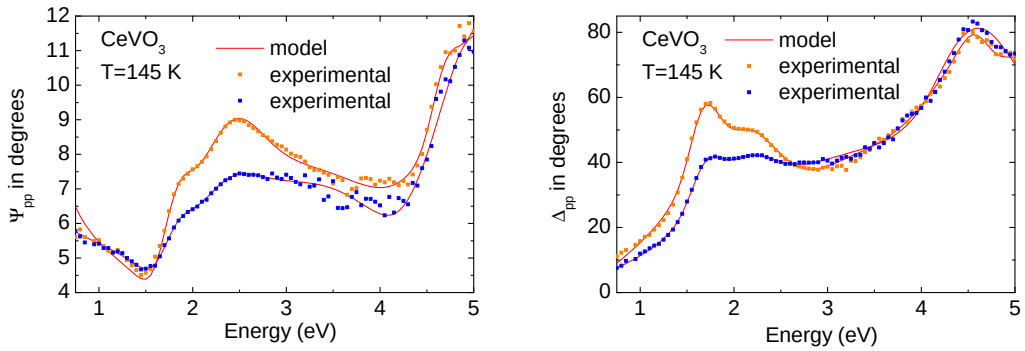

Figure 5.25: Experimentally obtained Ψ_{pp} (left panel) and Δ_{pp} (right panel) of $CeVO_3$ for two different sample orientations at $T = 145\,\mathrm{K}$. The data have been acquired on an ac plane with the c axis (orange squares) and the a axis (blue squares) parallel to the plane of incidence, respectively.

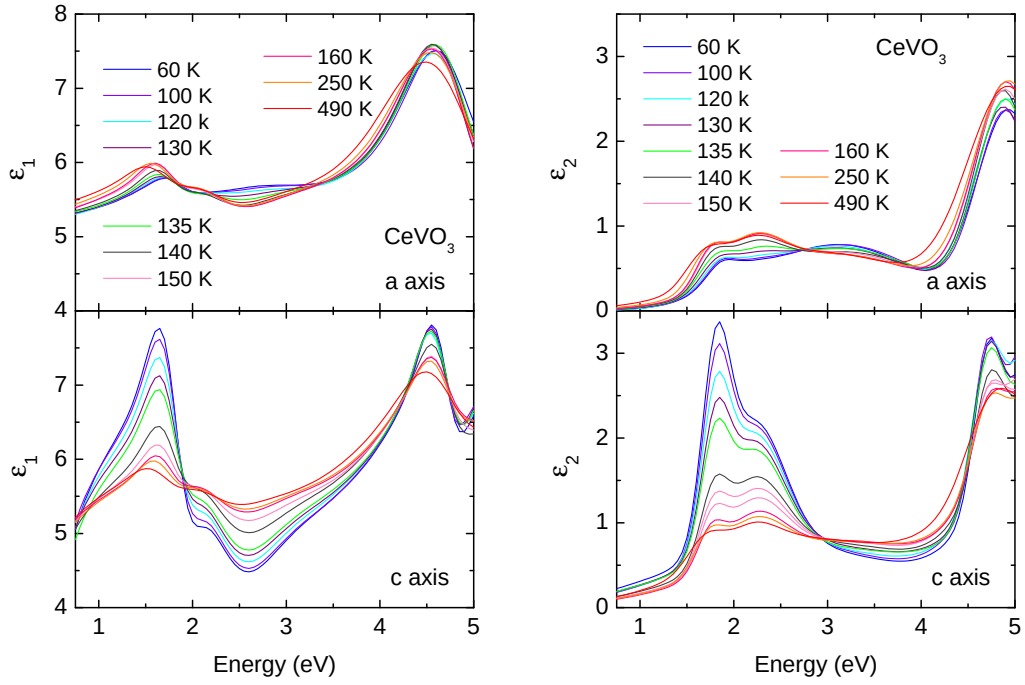

Figure 5.26: Dielectric function $\varepsilon(\omega)$ of $CeVO_3$ for the a and c direction between 0.75 eV and 5.0 eV for different temperatures. (Not all temperatures are shown for clarity.)

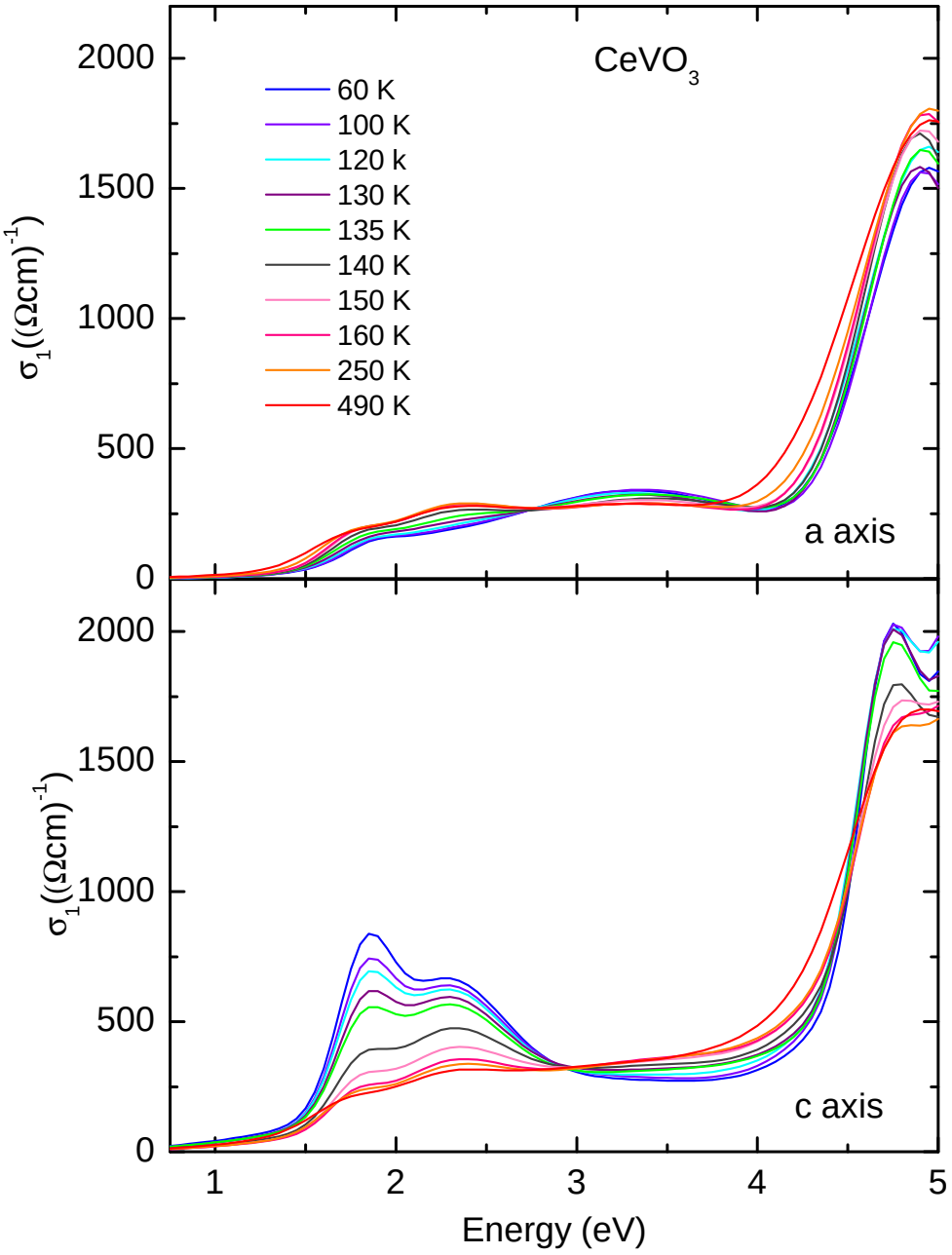

Figure 5.27: Optical conductivity $\sigma_1(\omega)$ of CeVO_3 for the a and c direction between 0.75 eV and 5.0 eV for different temperatures. (Not all temperatures are shown for clarity.)

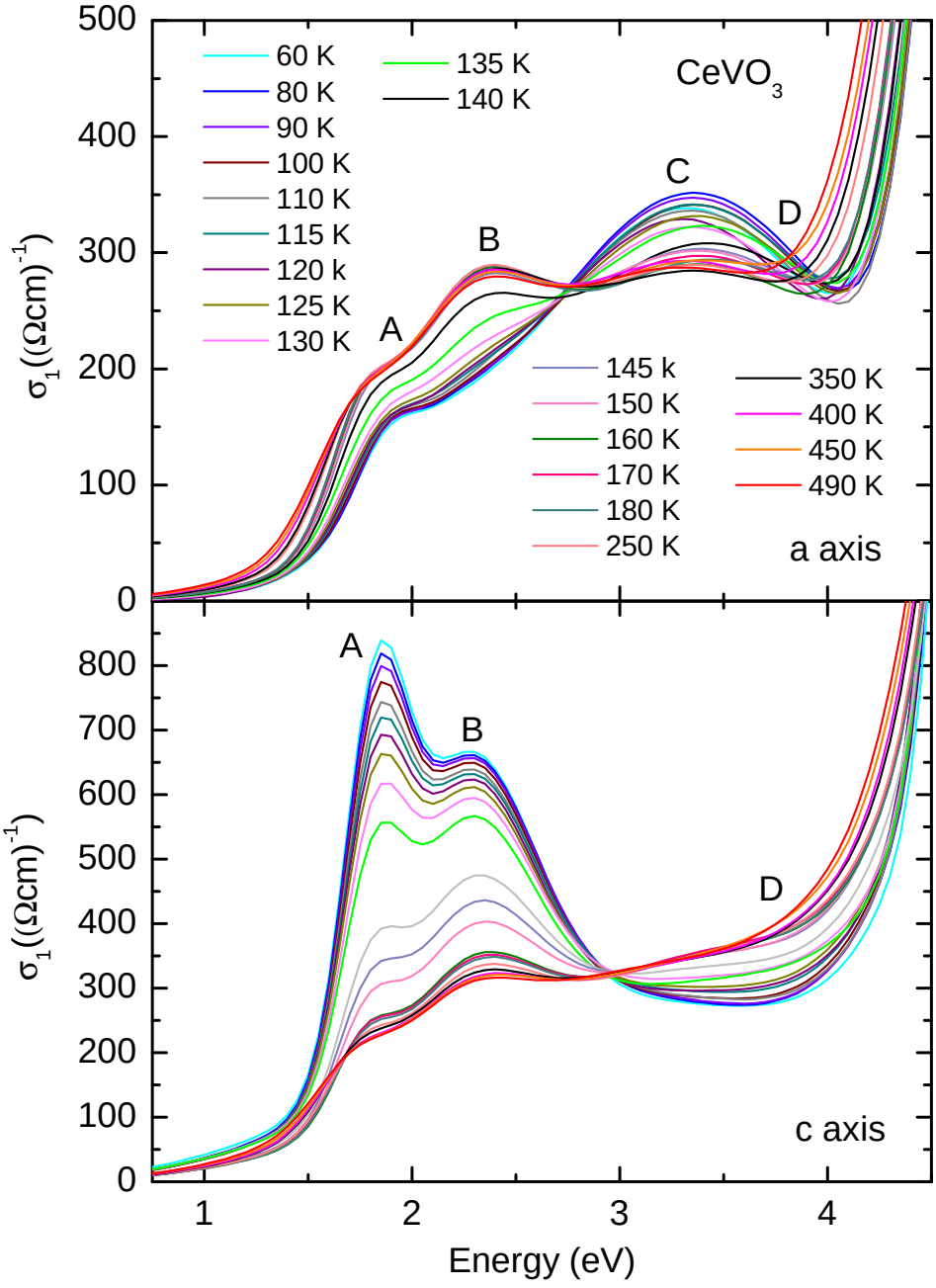

Figure 5.28: Close-up view of the optical conductivity $\sigma_1(\omega)$ of $CeVO_3$ for the a and c direction between 0.75 eV and 4.5 eV for different temperatures.

Table 5.8: Parameters of the fit to the measured data of CeVO_3 with Gaussian (GA) oscillators (a axis). The center energy ω_0, the FWHM Br, and the amplitude A (dimensionless) of the Gaussian oscillators are defined in Sec. 3.1.5 in Eq. 3.24. The parameters ω_0 and Br are given in eV.

a axis		GA1	GA2	GA3	GA4
	ω_0	1.8459	2.0031	3.1121	4.9376
$T = 60\,\mathrm{K}$	Br	0.3276	0.7111	1.9496	0.8037
	A	0.1480	0.2041	0.7822	2.3066
	ω_0	1.7085	2.1893	3.0756	4.9421
$T = 250\,\mathrm{K}$	Br	0.3910	0.7581	2.3021	0.9016
	A	0.3499	0.4600	0.6672	2.6068
	ω_0	1.6728	2.1830	2.9568	4.9369
$T = 490\,\mathrm{K}$	Br	0.4543	0.7147	2.3713	1.0443
	A	0.3329	0.3617	0.6826	2.5505

Table 5.9: Parameters of the fit to the measured data of CeVO_3 with Gaussian (GA) oscillators (c axis). See the caption of table 5.8 for the definition of the parameters.

c axis		GA1	GA2	GA3	GA4	GA5
	ω_0	1.8099	2.2184	2.58301	4.7058	5.9375
$T = 60\,\mathrm{K}$	Br	0.3422	0.7520	2.9387	0.3264	1.7900
	A	2.0768	1.4926	0.7192	1.5316	5.2904
	ω_0	1.7272	2.2034	3.1534	4.6919	5.2837
$T = 250\,\mathrm{K}$	Br	0.3587	0.7506	2.8612	0.3765	1.3601
	A	0.3797	0.4887	0.7770	0.6737	2.3950
	ω_0	1.6907	2.1932	2.6811	4.7380	5.7022
$T = 490\,\mathrm{K}$	Br	0.4283	0.6258	2.3935	0.6172	2.2920
	A	0.3262	0.2829	0.7932	0.8773	2.5003

5.3 Discussion

5.3.1 Multiplet assignment and temperature dependence

The overall behavior of the optical conductivity $\sigma_1(\omega)$ is very similar for YVO_3, $GdVO_3$, and $CeVO_3$ (see Figs. 5.14, 5.22, and 5.27). The main difference is that YVO_3 shows the low-temperature phase with C-type OO below $T_S = 77\,\mathrm{K}$ with a pronounced peak at 3.5 eV. Figure 5.29 compares the optical conductivity of all three compounds at two different temperatures. In all three compounds, the Mott gap is about 1.6 eV to 1.8 eV, in excellent agreement with infrared-transmittance data [18]. Above the gap we observe the MH excitations $|d_i^2 d_j^2\rangle \rightarrow |d_i^1 d_j^3\rangle$. At 4.5 eV, $\sigma_1(\omega)$ steeply rises up to roughly 1500 $(\Omega cm)^{-1}$, corresponding to the onset of CT excitations $|p^6 d^2\rangle \rightarrow |p^5 d^3\rangle$ between the oxygen $2p$ and the vanadium $3d$ level. This general picture is well accepted [21–23, 99, 100]. According to Sec. 5.1.7, we now focus on a consistent assignment of the MH excitations to the t_{2g}^3 multiplets $^4A_2$, $[^2T_1,\ ^2E]$, and $^2T_2$ under the assumption of cubic symmetry, neglecting the crystal-field splitting within the t_{2g} levels. We aim to understand the temperature dependence of the individual absorption bands observed in our measured data on the basis of variations of nearest-neighbor spin-spin and orbital-orbital correlations according to the spin and orbital ordering phase diagram of RVO_3. If the excitation into a certain t_{2g}^3 multiplet is allowed or forbidden strongly depends on polarization and temperature. Figure 5.30 sketches the allowed excitations $|t_{2g,i}^2 t_{2g,j}^2\rangle \rightarrow |t_{2g,i}^1 t_{2g,j}^3\rangle$ in the different ordered phases of RVO_3. To deduce their expected optical spectral weights we make use of table 5.3 on page 73.

The multiplet structure of $\sigma_1(\omega)$ below 4.5 eV constitutes of four absorption peaks at roughly 1.7 eV − 2.2 eV (peak A), 2.3 eV − 2.5 eV (peak B), 2.8 eV − 3.6 eV (peak C), and 3.6 eV − 4.4 eV (peak D) in the a direction, whereas peak C is missing in the c direction. See Figs. 5.14, 5.18, 5.23, 5.28, and 5.29. The modeling of the ellipsometric data uses two oscillators (Tauc-Lorentz or Gaussians, see Figs. 5.15 and 5.19) to describe the line shape of peak B at approx. 2.4 eV in $\sigma_1^c(\omega)$ of YVO_3 and $GdVO_3$. This does not necessarily mean the existence of two microscopically different excitations as the line shape of the absorption band might not be Gaussian or Tauc-Lorentz like but can be dominated by bandstructure effects. Furthermore, peaks C and D (the spectral weight between 3 eV and 4.5 eV) in $\sigma_1^a(\omega)$ are modeled by a single Gaussian oscillator for the data of $CeVO_3$, see Fig. 5.24. This is due to the noise in the experimental data of $CeVO_3$ (see Fig. 5.25), which is especially pronounced in the a axis spectrum in the energy range from 3 eV to 4 eV. The line shape in this energy range is only approximate, the experimental data does not yield enough information to definite determine the parameters of two oscillators.

The lowest multiplet $^4A_2$ is a high-spin state in which the xy, xz, and yz orbitals are occupied by one electron each (see Fig. 5.9 on page 71). Due to the high-spin

character, parallel spins on adjacent sites in the initial state give rise to a larger spectral weight than antiparallel spins. In contrast, the other t_{2g}^3 multiplets [^2E, $^2T_1$] and $^2T_2$ all are low-spin states (see Fig. 5.9), thus, the spectral weight is larger for antiparallel spins. This yields the following clear predictions for the phase with C-type SO [8, 10, 99] in which spins are parallel along the c axis and antiparallel within the ab plane (see Fig. 5.4). (1) The spectral weight of the excitation into the lowest multiplet $^4A_2$ is expected to be larger in σ_1^c than in σ_1^a. (2) With decreasing temperature, spin-spin and orbital-orbital correlations are enhanced, thus, σ_1^c is expected to increase whereas σ_1^a is expected to decrease for the lowest multiplet. (3) The opposite temperature dependence is expected for the higher multiplets. A comparison of these predictions with our data clearly shows that both peaks A and B at $\approx 2.0\,\mathrm{eV}$ and $\approx 2.4\,\mathrm{eV}$, respectively, have to be assigned to the lowest $3d^3$ multiplet $^4A_2$. We observe a spectacular increase of the double-peak structure consisting of peak A and B in σ_1^c when the temperature is lowered below T_{OO} (see Figs. 5.18, 5.23, and 5.28). In opposition, peaks A and B loose spectral weight with decreasing temperature in σ_1^a. The temperature dependence of combined peak A and B in σ_1^c will be discussed in further detail in Sec. 5.3.3 in the context of the investigation of the importance of orbital fluctuations in $R\mathrm{VO}_3$. According to theory [8] (see table 5.3), the excitation into $^4A_2$ in σ_1^a retains a finite transition probability for fully antiferro orbital and spin correlations even in a perfect cubic structure since excitations to a state with $S = 3/2$ and $|S^z| = 1/2$ are possible. This explains the finite spectral weight of peaks A and B in σ_1^a in the C-type spin-ordered phase (see Figs. 5.18, 5.23, and 5.28).

Peak C is located roughly $3J_H$ above peak A in σ_1^a in agreement with the expectations for the [^2E, $^2T_1$] multiplets. The spectral weight of the excitation into [^2E, $^2T_1$] vanishes for parallel spins [8, 10, 99] (see table 5.3) and therefore, peak C is absent in σ_1^c (see Figs. 5.18, 5.23, 5.28, and 5.29). Within the ab plane the excitation into [^2E, $^2T_1$] is expected to gain weight when entering the spin and orbitally ordered phase. This is in agreement with our observation as peak C increases below T_{OO} in σ_1^a (see Figs. 5.18, 5.23, 5.28). The dramatic changes observed at $T_S = 77\,\mathrm{K}$ in YVO_3 (see Fig. 5.14) unambiguously prove that our peak assignment is correct. At T_S, the nearest-neighbor correlations along c change from ferro to antiferro for the spins and vice versa for the orbitals, thus, two adjacent sites show the same orbital occupation below T_S with, e.g., xz occupied on both sites. In this case, according to the orbital selection rule, an excitation into $^4A_2$ requires hopping from xz on one site to yz on a neighboring site, which is forbidden along c in cubic symmetry (see table 5.3), explaining the spectacular suppression of peaks A and B below T_S (see Fig. 5.14). The finite spectral weight at low T is due to deviations from cubic symmetry [22]. At the same time, the antiferromagnetic and ferro-orbital correlation along c strongly allow the transition into the $^2T_1$ multiplet explaining the emergence of peak C below 77 K in the data of YVO_3 (see table 5.3). The strong increase in spectral weight of peak C also

in σ_1^a across $T_S = 77\,\mathrm{K}$ (see Fig. 5.14) cannot be explained on the basis of spin and orbital ordering, as the ordering pattern does not change across the phase transition within the *ab* plane [87]. It most likely originates from the change of the crystal structure across the structural transition since a change of the VO_6 octahedra tilt leads to a modification of the transition probabilities between xz and yz orbitals within the *ab* plane.
The highest t_{2g}^3 multiplet $^2T_2$ is roughly expected at $U + 2J_H$ i.e., $5J_H > 2.7\,\mathrm{eV}$ above the lowest peak. It is thus reasonable to assume that this excitation is located above the onset of CT excitations at 4.5 eV. Peak *D* at $3.6\,\mathrm{eV} - 4.4\,\mathrm{eV}$ lies about $10\,Dq = 1.9\,\mathrm{eV}$ above peaks *A* and *B* and thus can be assigned to the $^4T_2$ multiplet, the lowest $t_{2g}^2 e_g^1$ multiplet ($S = 3/2$). In cubic symmetry, the excitation from a t_{2g} orbital on site i to an e_g orbital on a neighboring site is forbidden, but deviations from cubic symmetry yield a finite spectral weight. The excitation into $^4T_2$ favors parallel spins on neighboring sites and should therefore gain weight in the phase with *C*-type spin order in σ_1^c. However, we observe the opposite temperature dependence (see Figs. 5.18, 5.23, 5.28, and 5.29). A possible explanation could be the overlap with the CT excitations. The CT edge is shifted to higher energies for decreasing temperatures (see Figs. 5.14, 5.22, and 5.27) which leads to a loss of spectral weight between $4.0\,\mathrm{eV} - 4.5\,\mathrm{eV}$. Within the *ab* plane, the excitation into $^4T_2$ remains weakly spin allowed also in the spin-ordered phase since excitations to a state with $S = 3/2$ and $|S^z| = 1/2$ are possible. However, peaks *C* and *D* can hardly be separated from each other in σ_1^a (see Figs. 5.15, 5.19, and 5.24). The increasing weight of peak *C* when entering the spin-ordered phase might also affect the spectral weight of peak *D*. A distinct determination of the individual temperature dependences of peaks *C* and *D* is difficult.
To summarize this section, we present a detailed analysis of the observed absorption bands in terms of different $3d^3$ multiplets. Our peak assignment is consistent with the observed temperature dependence. The assignment of both, peaks *A* and *B* to the high-spin $^4A_2$ multiplet is unambiguous due the only small energetic separation of peaks *A* and *B*, but particularly due to the distinct temperature dependence. An explanation for the double-peak structure of the excitation is given in Sec. 5.4. The temperature dependence of the absorption band observed at approx. 3 eV (peak *C*) in $\sigma_1^a(\omega)$ clearly supports our interpretation in terms of the $[^2E,\ ^2T_1]$ multiplet. The FM spin order along *c* in the *C*-type spin-ordered phase strongly suppresses the excitation into the low-spin multiplet $[^2E,\ ^2T_1]$ in $\sigma_1^c(\omega)$. We suggest that the spectral weight at approx. $3.6\,\mathrm{eV} - 4.4\,\mathrm{eV}$ (peak *D*) originates from the excitations into the lowest $t_{2g}^2 e_g^1$ multiplet $^4T_2$.

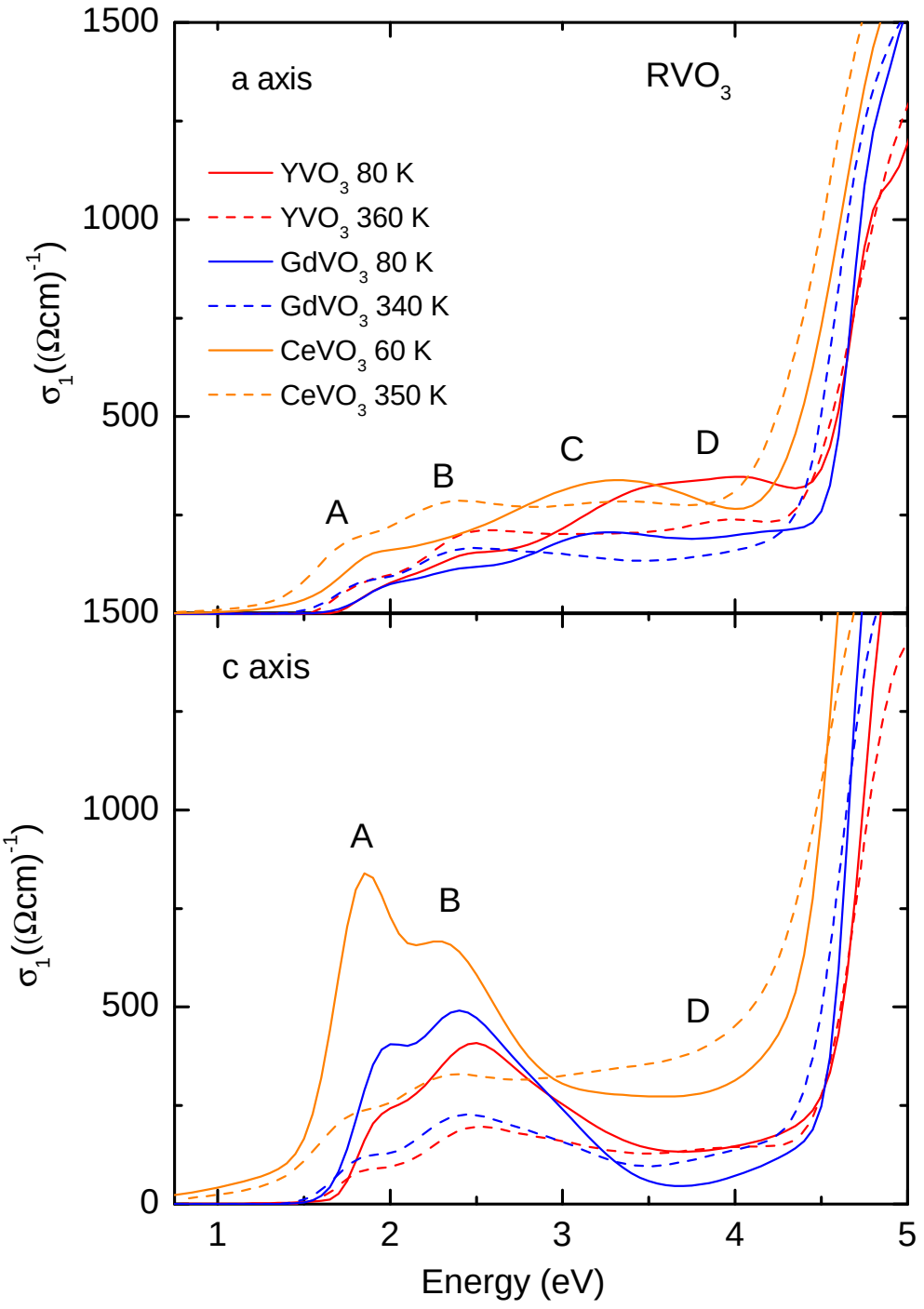

Figure 5.29: Comparison of the optical conductivity $\sigma_1(\omega)$ of YVO_3, GdVO_3, and CeVO_3 for the a and c direction for two different temperatures.

peak	A, B	C	D
multiplet	${}^4A_2$	$[{}^2E, {}^2T_1]$	${}^4T_2$

Table 5.10: The table summarizes the peak assignment.

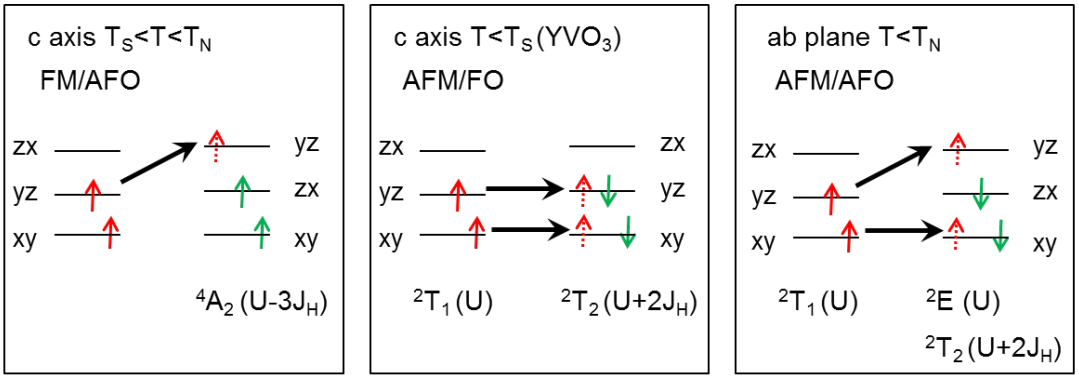

Figure 5.30: Sketch of MH excitations to final t_{2g}^3 multiplets. The allowed excitations in a simple one-electron picture for different spin and orbital ordering patterns are marked by black arrows. The possible final multiplets are indicated below the sketches.

5.3.2 Comparison with literature

We are not the first to acquire temperature-dependent optical data of $R\mathrm{VO}_3$. However, there is a striking disagreement between different experimental data sets existent in the literature, which call for clarification. Miyasaka *et al.* [21] investigated LaVO_3 and YVO_3 by reflectivity measurements and obtained the temperature-dependent optical conductivity from 0.06 eV up to 5 eV by a Kramers-Kronig analysis. Their result is depicted in Fig. 5.31. In agreement with our data, they observe the strongly temperature-dependent double-peak structure (peaks A and B) at around 2 eV for $E \parallel c$. However, the expected jump of the spectral weight at T_S for YVO_3 is missing. Tsvetkov *et al.* [23] report an optical study of the electronic excitations across the MH gap in YVO_3 by the use of ellipsometry, see Fig. 5.32. The interesting behavior of the intermediate temperature phase for $E \parallel c$ is only analyzed at a single temperature $T = 80\,\mathrm{K}$. Here, the strong absorption band consisting of two peaks at around 2 eV is completely absent, whereas the pronounced peak at 3.5 eV, characteristic for the low-temperature phase, is already visible at 80 K. It is not seen at any temperature in Ref. [21]. The data of Miyasaka *et al.* [21] have recently been corrected by reflectivity data of Fujioka *et al.* [22] on YVO_3 and LaVO_3 within the framework of a detailed study focusing on the doping variation of the optical conductivity of $\mathrm{Y}_{1-x}\mathrm{Ca}_x\mathrm{VO}_3$ and $\mathrm{La}_{1-x}\mathrm{Sr}_x\mathrm{VO}_3$. The data of Ref. [22] show the expected jump of the spectral weight at T_S for YVO_3, but both this jump and the temperature dependence above T_S are much smaller than in our data. We attribute this difference to the different experimental techniques. As ellipsometry is a self-normalizing technique, it is much better suited for a precise determination of the temperature dependence than reflectivity measurements with a subsequent Kramers-Kronig analysis.

Conflicting with our assignment, peaks A and B have been attributed to the two lowest multiplets ${}^4A_2$ and $[{}^2E,{}^2T_1]$ in Refs. [21–23]. Between these multiplets, a splitting of $3J_H > 1.5\,\mathrm{eV}$ is expected, which is incompatible with the observed splitting between A and B of only 0.5 eV. In other words, the previous assignment of peaks A and B to two different multiplets yields a nonphysically small value of J_H [99]. Moreover, this scenario is inconsistent with the fact that the spectral weights of peaks A and B show the same temperature dependence, as discussed in Sec. 6.3.2.

Both, the incorrect assignment and the discrepancies of the data can be traced back to problems with the sample temperature. Samples of YVO_3 tend to break at the first-order structural transition at T_S, often leading to a loss of thermal contact [22, 37]. We were able to avoid this problem by very slow cooling. A comparison of our data and the data of Fujioka *et al.* [22] shows that the seemingly contradictory data of Refs. [21] and [23] can be reconciled with each other by taking into account problems with the sample temperature across T_S.

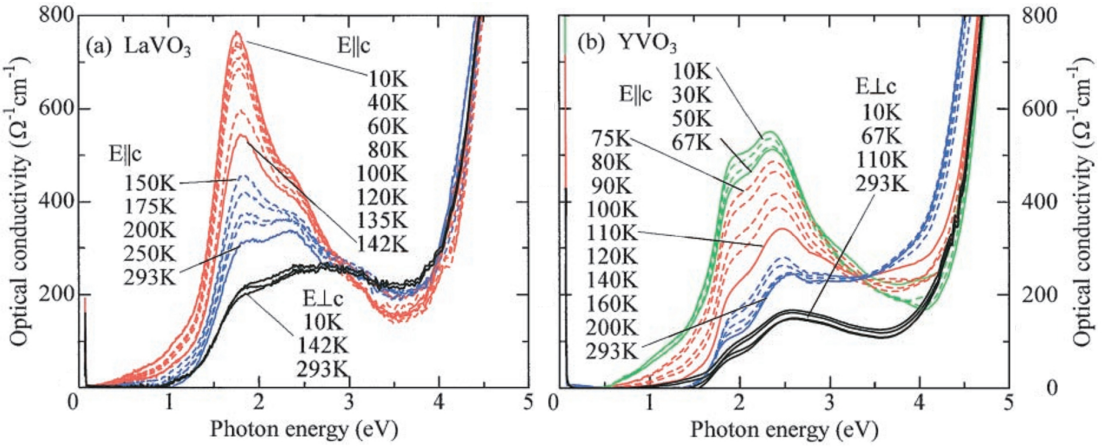

Figure 5.31: Optical conductivity $\sigma_1(\omega)$ of (a) $LaVO_3$ and (b) YVO_3 for $E \parallel c$ and $E \perp c$ as obtained by Miyasaka *et al.* [21] by the use of reflectivity measurements at different temperatures. Taken from Ref. [21].

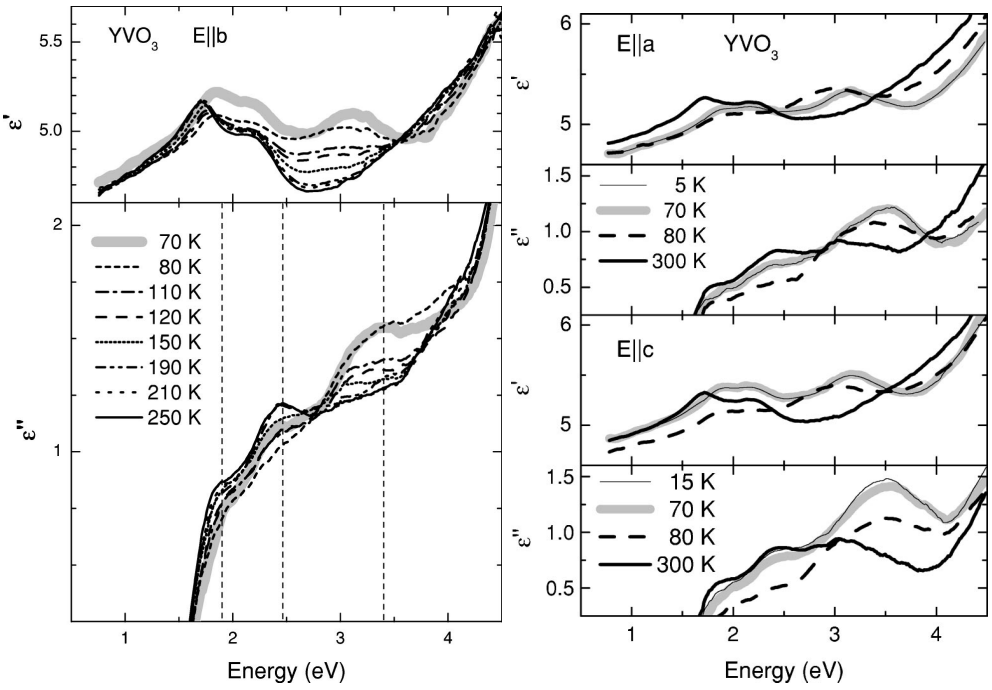

Figure 5.32: Dielectric function $\varepsilon = \varepsilon_1 + i\varepsilon_2$ (here: $\varepsilon = \varepsilon' + i\varepsilon''$) of YVO_3 for the a, b, and c direction as obtained by Tsvetkov *et al.* [23] by the use of ellipsometry at different temperatures. Taken from Ref. [23].

5.3.3 Temperature dependence of the spectral weight: strength of orbital fluctuations

The correct assignment of peaks A and B to the lowest multiplet $^4A_2$ is crucial for the discussion of the role played by orbital fluctuations. As discussed in Sec. 5.1.3 the spectral weight of the $^4A_2$ multiplet in $\sigma_1^c(\omega)$ depends sensitively on spin-spin and orbital-orbital correlations between adjacent sites [8, 10, 99]. For a detailed analysis of the temperature dependence of peaks A and B, we fit the measured data by a sum of Lorentz oscillators (see Sec. 3.1.5). The fit to ε^a (ε^c) is based on four (three) Lorentz oscillators describing peaks A, B, C, and D (peaks A, B, and D;), respectively , see Figs. 5.33 and 5.34. The strong increase of the spectral weight above 4.5 eV attributed to the onset of CT excitations is reproduced in the fit by two Gaussian oscillators. There are no severe correlations between the individual parameters of the Lorentz and Gaussian oscillators, as all entries of the two-parameter correlation function S_{kl} do not exceed the critical value of 0.92 (see Sec. 3.2.4). The fit with Lorentz oscillators is not able to reproduce the line shape of $\varepsilon_2(\omega)$ very well, particularly strong deviations are observed in the energy region of the onset of electronic excitations above the band gap at about 1.6 eV − 1.8 eV, see Figs. 5.33 and 5.34. However, the effective carrier concentration N_{eff} of peaks A and B obtained from the Lorentzian fit parameters is well suited to analyze the changes of spectral weight with temperature. The deviations of the Lorentzian line shape from the precise line shape of $\varepsilon_2(\omega)$ compensate in $N_{eff}(T)$ when restricting the attention to temperature dependent changes of $N_{eff}(T)$. We do not infer the temperature dependence of peaks A and B in $\varepsilon_2^c(\omega)$ from the parameters of the Tauc-Lorentz and Gaussian oscillators, that have been used to deduce the precise line shape of $\varepsilon_2(\omega)$ from the measured data. Due to its asymmetric line shape the Tauc-Lorentz oscillator is not well suited for the determination of the spectral weight of an individual absorption band. Furthermore, the line shape of some absorption bands could best be described by more than one oscillator (see Figs. 5.15, 5.19, and 5.24). In particular, peaks A and B in $\varepsilon_2^c(\omega)$ are modeled by the use of three oscillators for YVO$_3$ and GdVO$_3$. The fit based on Tauc-Lorentz and Gaussian oscillators is thus not necessarily physically meaningful. The right panels of Fig. 5.34 display the sum of the effective carrier concentrations of peaks A and B in $\varepsilon_2^c(\omega)$ for YVO$_3$, GdVO$_3$, and CeVO$_3$, respectively, as deduced from the Lorentzian fit parameters by the use of Eq. 4.4 on page 53. In Fig. 5.35 (a) the sum of the spectral weights of peaks A and B in $\varepsilon_2^c(\omega)$ scaled to one for the lowest temperature on a normalized T axis with $T_N = 1$ is shown.

According to theory (see the discussion of Eq. 5.2 in Sec. 5.1.8), comparing a fully polarized ferromagnetic and G-type orbitally ordered state ($T = 0$) with a disordered orbital and spin state ($T = \infty$), the spectral weight of the excitation into the $^4A_2$ multiplet along c in the later case is reduced to 1/3 from low temperatures to high temperatures. This is valid in any scenario, i.e., it applies to

both rigid orbital order and strong orbital fluctuations. We observe a reduction of spectral weight of approx. 60% (see Fig. 5.35 (a)). This is in good agreement with the theoretical predictions and further proves that our peak assignment is correct. The small deviation can be attributed to a background originating from excitations at higher energies or surface effects.
Figure 5.35 (b) displays two different theoretical results (see Sec. 5.1.8) for $N_{eff}(T)$ of the lowest MH excitation ($^4A_2$ multiplet) along c. The blue line reproduces the result of Oleś *et al.* [8] who assume rigid orbital order with $T_{OO} = \infty$, whereas the red line represents the result of Khaliullin *et al.* [10] who allow for fluctuating orbitals and set $T_N = T_{OO}$ (cf. the discussion in Sec. 5.1.8 and Fig. 5.11 on page 74). The blue line for rigid orbital order shows only the reduction of spectral weight by a factor of 2/3, stemming from the spin part, because it assumes $T_{OO} = \infty$. The key feature of this comparison is not the difference in absolute value but the temperature dependence above the ordering temperature. For rigid orbital order, the spectral weight is nearly constant for $T > T_N$ and exhibits a clear kink right at T_N. In contrast, there is no pronounced effect at T_N for strong quantum fluctuations. The smoking gun for strong fluctuations is a strong temperature dependence far above T_N or T_{OO}, most of the change occurs above the ordering temperature. The comparison of these predictions with our results (shown in Fig. 5.35 (a)) yields the following result: For all compounds we find nearly constant spectral weights above T_{OO}, a clear kink at T_{OO}, and also a kink at T_N. These findings are in excellent agreement with the expectations for rigid orbital order. The fact that the changes above T_{OO} are much smaller than below rules out strong orbital fluctuations in RVO$_3$. The line shape of $N_{eff}(T)$ in the case of CeVO$_3$ agrees particularly well with the predictions for rigid orbital order. This clearly shows that orbital fluctuations are suppressed not only in strongly distorted YVO$_3$ but also for large R ions such as in pseudocubic CeVO$_3$.

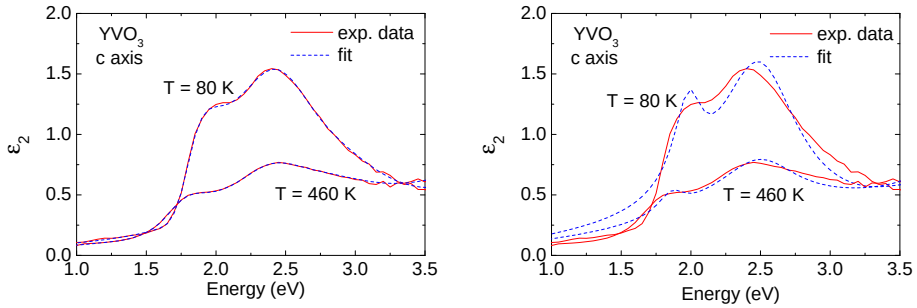

Figure 5.33: Fit to the measured data of YVO$_3$ with Tauc-Lorentz and Gaussian oscillators (left panel), and Lorentz oscillators (right panel). The fit with Lorentz oscillators is only used to analyze the temperature dependence of the spectral weight of the absorption bands.

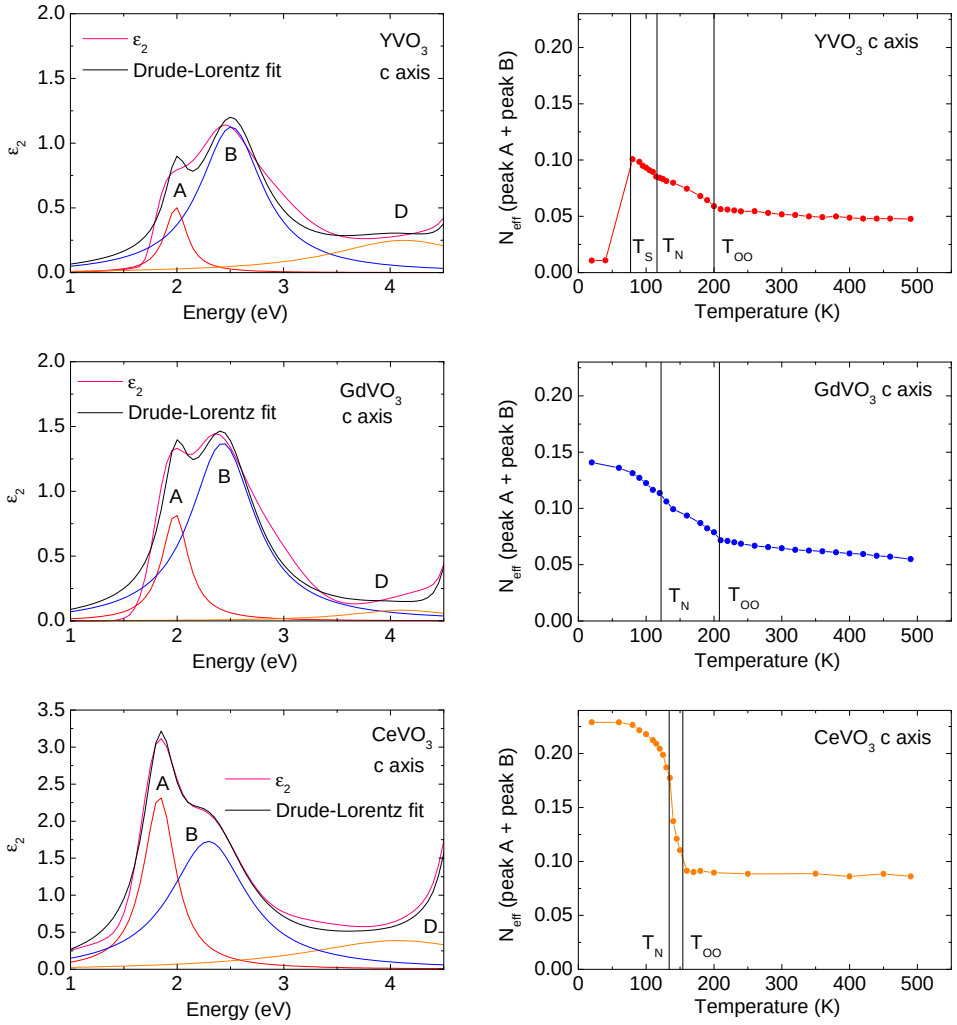

Figure 5.34: Left panels: Result of the Drude-Lorentz fit to the measured data of YVO_3 (upper panel), GdVO_3 (middle panel), and CeVO_3 (lower panel) at $T = 100\,\mathrm{K}$ (black line). The dielectric function $\varepsilon_2^c(\omega)$ is described by a sum of three Lorentz oscillators in the energy range below 4.5 eV, labeled peak A (red line), B (blue line), and D (orange line), respectively. The displayed function ε_2^c (pink line) refers to the result of the fit to the measured data based on Tauc-Lorentz and Gaussian oscillators, that has been discussed in Secs. 5.2.1 – 5.2.3. Right panels: Sum of the effective carrier concentrations N_{eff} of peaks A and B resulting from the Lorentzian fit parameters according to Eq. 4.4 on page 53.

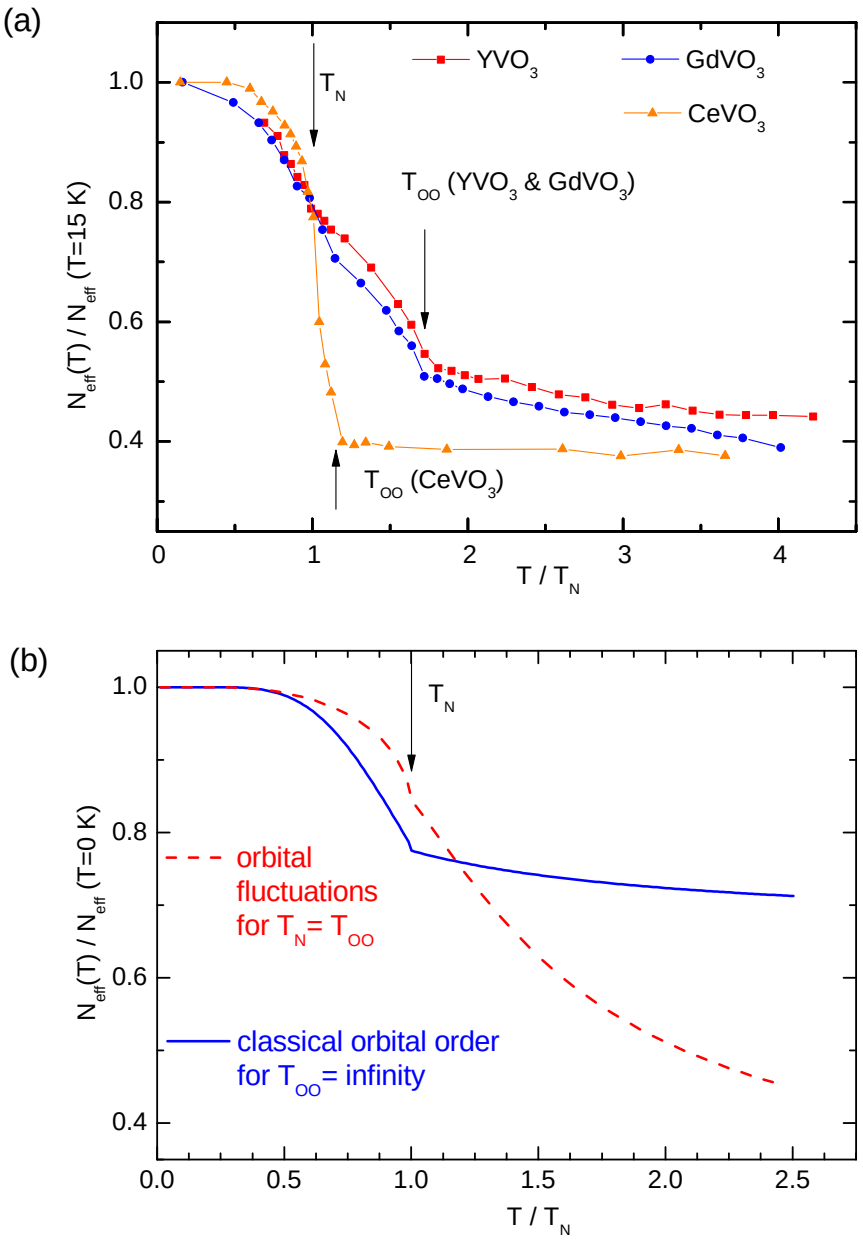

Figure 5.35: (a) Sum of the spectral weights of peaks A and B in $\sigma_1^c(\omega)$ normalized to one for the lowest measured temperature for $GdVO_3$ and $CeVO_3$. For YVO_3, $N_{eff}(T)$ is scaled to equal the value of $N_{eff}[GdVO_3]$ at $T = 80\,K$. (b) Theoretical results for $N_{eff}(T)$ of the lowest MH excitation ($^4A_2$ multiplet) in σ_1^c for strong orbital fluctuations (red, $T_N = T_{OO}$) and rigid orbital order (blue, $T_{OO} = \infty$, i.e., only the reduction of the spin part to 2/3 is taken into account). Reproduced from Refs. [10] and [8] and scaled to one for $T = 0$.

5.4 Observation of an excitonic resonance in $R\mathrm{VO}_3$

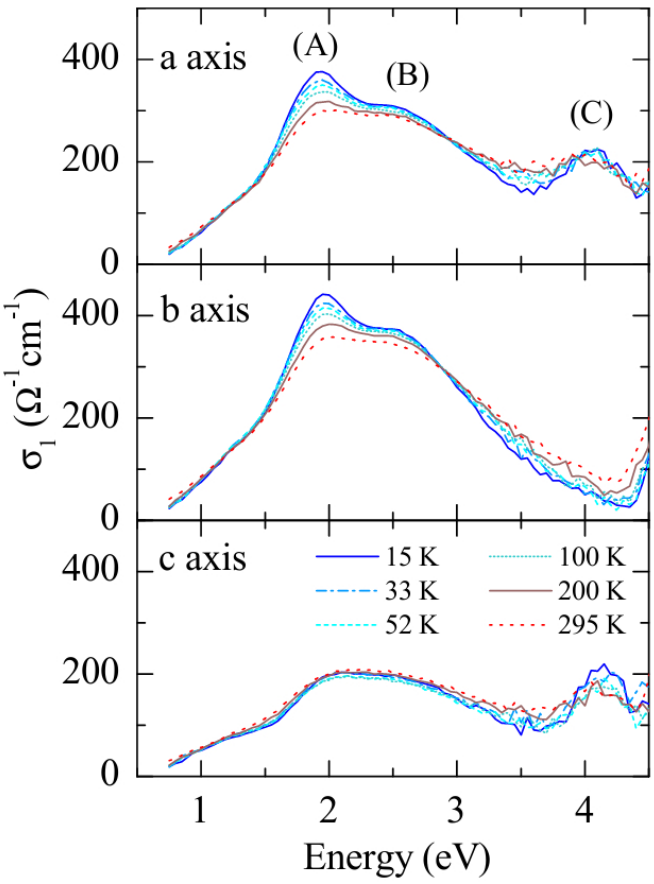

Figure 5.36:
Optical conductivity of $YTiO_3$ in the energy range of the Mott-Hubbard excitations as obtained by Gössling *et al.* [13]. Peak (A) of the double-peak structure $(A)/(B)$ at approx. 2 eV has been interpreted in terms of an excitonic resonance. Taken from Ref. [13].

Finally, we address the double-peak structure A/B of the excitation into the lowest $3d^3$ multiplet. Similar double- and multi-peak structures of the lowest multiplet have been reported for $LaMnO_3$ and $YTiO_3$ (see Fig. 5.36) [11, 13]. The peak splitting has been assigned to either excitonic or band-structure effects, which both have been neglected thus far in our discussion of local multiplets. We propose that peak A is an excitonic resonance, i.e., not a truly bound state below the gap but a resonance within the absorption band. Due to an attractive interaction between a d^3 state in the upper Hubbard band and a d^1 state in the lower Hubbard band, the energy of the resonance (peak A) is less than the energy of peak B, where peak B reflects an excitation to $|d^1 d^3\rangle$ without attractive interaction. In order to substantiate this claim, we discuss results from photoemission spectroscopy (PES) [101, 102] and from band-structure calculations [20, 99, 100].

5.4.1 Literature on photoemission spectroscopy and band structure calculations

Using LDA+U, Fang *et al.* [99] calculated the optical conductivity of LaVO_3 and YVO_3 for different polarizations and for different ordering patterns of spins and orbitals. The results are displayed in Fig. 5.37. The two lowest peaks (called α and β in Ref. [99]) correspond to the two lowest multiplets of our local approach, i.e., to the double-peak A/B and peak C, respectively. Accordingly, the spectral weight of peak α (β) in σ_1^c decreases (increases) in YVO_3 across the phase transition from the intermediate-temperature phase with C-type spin order to the low-temperature phase with G-type spin order, as observed experimentally for peak A/B (C). Peak α is the lowest peak, well separated from the higher-lying excitations, and clearly consists of a single peak only, both for YVO_3 and LaVO_3 [99]. The experimentally observed splitting into peaks A and B is absent in the LDA+U results, which neglect excitonic effects. For the intermediate-temperature phase of YVO_3, Fang *et al.* [99] predict peaks α and β (with β observable for $E \perp c$ only)

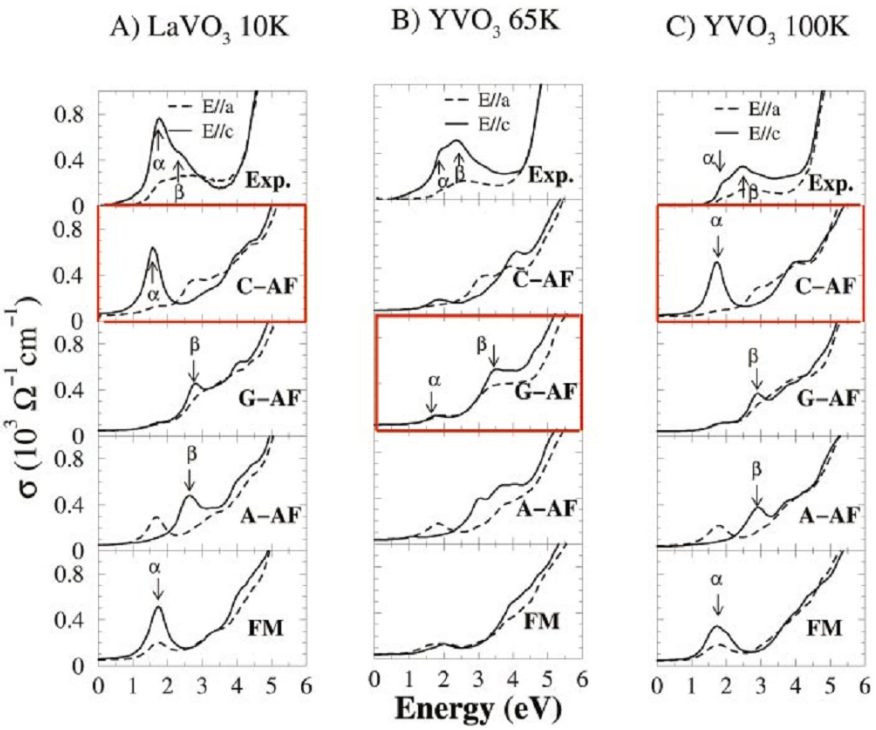

Figure 5.37: LDA+U results of Fang *et al.* [99] for the optical conductivity of YVO_3 at 65 K and 100 K, and of LaVO_3 at 10 K for different magnetic structures. The results for the most stable spin structure are framed in red. Taken from Ref. [99].

at about 1.7 eV and 2.9 eV, respectively, both significantly lower than peaks B and C in experiment, but in LDA+U results, the peak energies depend sensitively on the particular choice of U. Considering only the energies, one may be tempted to assign peaks α and β to peaks A and B, but this is clearly ruled out by the dependence of the spectral weight on both temperature and polarization as well as by the value of J_H, as discussed in Secs. 6.3.2 and 5.3.2. Also the LDA+U study of Solovyev *et al.* [100] reports on the optical conductivity of LaVO_3, the result is displayed in Fig. 5.38. In agreement with the results of Fang *et al.* [99], there is no splitting of the lowest excitation. Solovyev *et al.* [100] find the band gap at 0.7 eV and the CT gap at about 3.5 eV, while the lowest absorption band is peaking at about 1.7 eV. Since both gaps are about 0.7 eV − 1 eV lower than in experiment, we assign the lowest peak from LDA+U at 1.7 eV to peak B in our data. As mentioned above, the peak energy depends sensitively on the choice of U. The LDA+DMFT study of De Raychaudhury *et al.* [20] does not report on the optical conductivity, but it shows the electron-removal and -addition spectra (as measured by PES and inverse PES) for LaVO_3 and YVO_3, see Fig. 5.39. For LaVO_3, the electron-removal spectrum shows contributions from all three t_{2g} orbitals, peaking at about 1.2 eV − 1.4 eV below the Fermi energy E_F [20]. The small splitting reflects the crystal-field splitting within the t_{2g} level. The first peak of the electron-addition spectrum lies at about 1.2 eV above E_F. Neglecting excitonic effects, one may thus expect the first peak in the optical conductivity at about 2.4 eV − 2.6 eV, which is in agreement with peak B. For YVO_3, the electron-removal and -addition spectra peak at about -1.4 eV to -1.5 eV and +1.2 eV, respectively [20], thus, the peak in

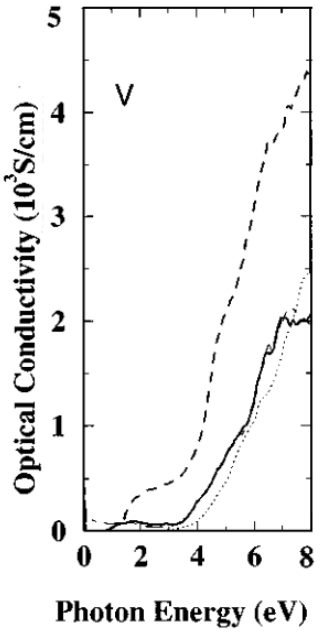

Figure 5.38:
Calculated optical conductivity of LaVO_3 by Solovyev *et al.* [100] using LDA+U. The solid (dotted) line considers only t_{2g} (all $3d$) states. The dashed line shows the experimental results for $\sigma_1(\omega)$ of LaVO_3 at room temperature acquired by Arima *et al.* [57] using reflectivity measurements. Taken from Ref. [100].

the optical conductivity is expected at a slightly larger energy in YVO_3 than in LaVO_3, in agreement with our experiment. The calculated electron-removal and -addition spectra for YVO_3 show small shoulders at about -1.1 eV and +0.7 eV. However, similar features are absent in the calculated spectra of LaVO_3. In strong contrast, peak A in the optical conductivity is much more pronounced in LaVO_3 (see Fig. 5.31 taken from Ref. [21]) than in YVO_3. Our results on YVO_3, GdVO_3, and CeVO_3 show that the strength of peak A in the optical conductivity increases for increasing radius of the rare-earth ion. In summary, band-structure calculations do not provide any explanation for the observed splitting of about 0.5 eV between peaks A and B.

Experimental photoemission spectra of LaVO_3 and YVO_3 show a single peak lying about $1.5\,\mathrm{eV} - 1.8\,\mathrm{eV}$ below E_F [101, 102], see Fig. 5.40. For LaVO_3, the combination of PES and inverse PES has been reported by Maiti and Sarma [101], see Fig. 5.41. The separation between the highest peak below E_F and the lowest peak above E_F amounts to roughly 3 eV, but the inverse PES data were measured with a resolution of only 0.8 eV. These results are in agreement with the LDA+DMFT study of Ref. [20] discussed above. Neither band-structure calculations nor the PES data provide any explanation for the splitting of peaks A and B. Electron-removal and -addition spectra do not reflect excitonic effects in contrast to the optical conductivity. Altogether, this strongly supports an excitonic interpretation of peak A.

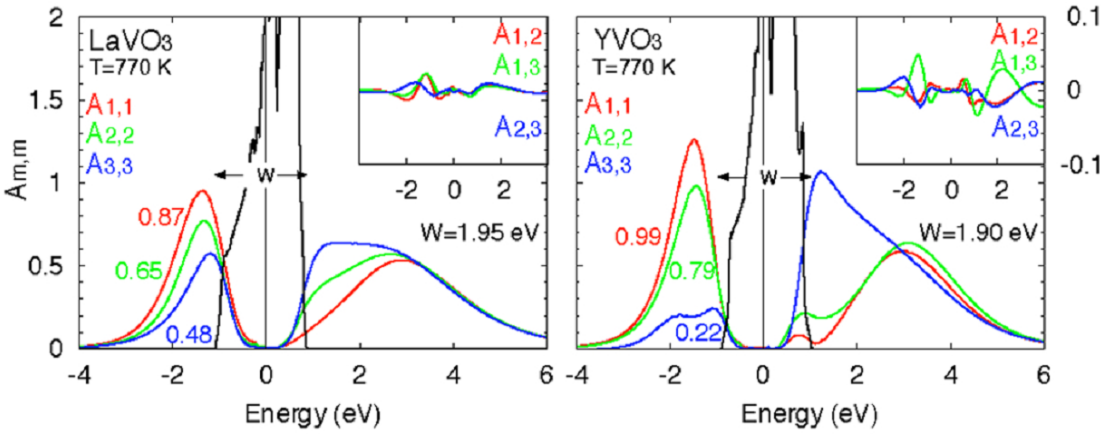

Figure 5.39: LDA+DMFT results of De Raychaudhury *et al.* [20] for the spectral matrix $A_{m,m'}$ of LaVO_3 (left) and YVO_3 (right). $A_{m,m'}$ is given in the crystal-field basis consisting of the different t_{2g} orbitals. The black line refers to the LDA density of states. Taken from Ref. [20].

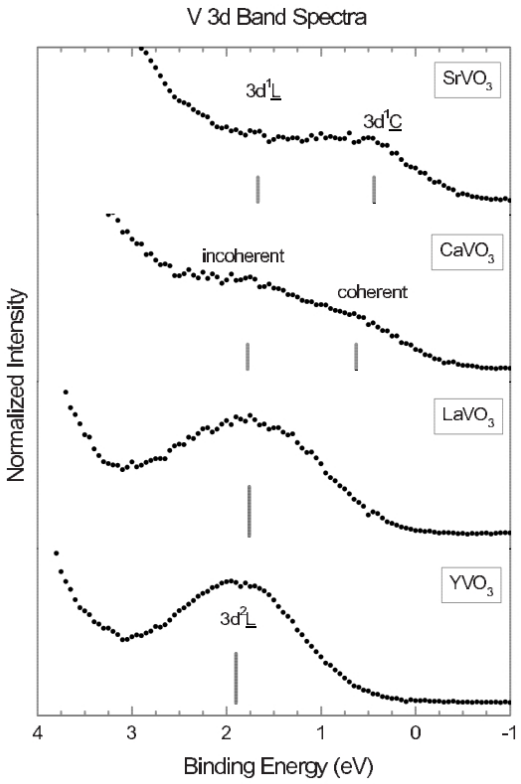

Figure 5.40:
Photoemmision results of Mossanek *et al.* [102] showing the V 3*d* valence band spectra of SrVO_3, CaVO_3, and LaVO_3. Taken from Ref. [102].

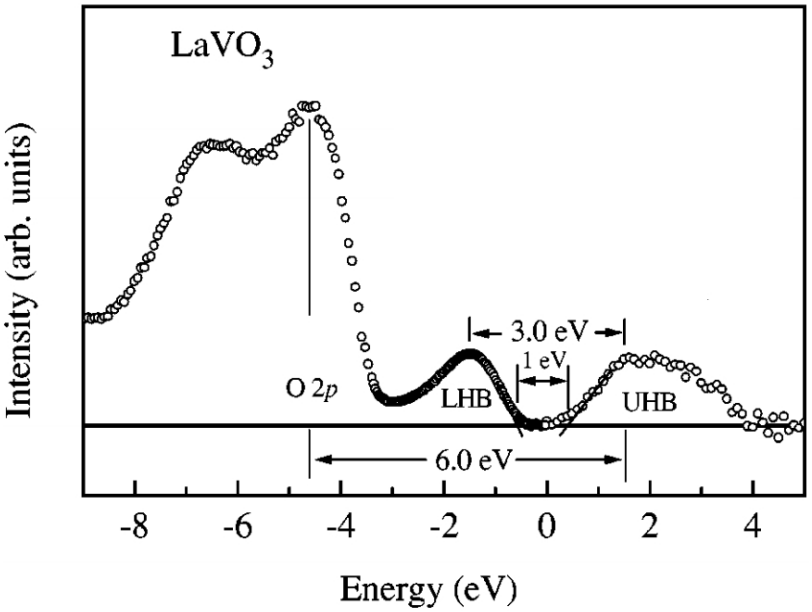

Figure 5.41:
Results of Ref. [101] from ultraviolet PES and inverse PES on LaVO_3. Taken from Ref. [101].

5.4.2 Exciton formation in correlated insulators

The mechanism for exciton formation, i.e. the binding of a particle and a hole, in the upper Hubbard band of correlated insulators has been investigated elaborately by both, experimentalists and theorists [103–111]. While in simple band insulators, exciton formation is driven by a lowering of the Coulomb energy whereas the kinetic energy increases, it is well established that the kinetic energy plays an important role for exciton formation in the case of a 2D Mott insulator with AFM exchange on a square lattice [105,107,110]. Transitions of excitonic origin, that show a significant dispersion, have been observed in the 2D cuprates (e.g. in $\mathrm{LaCuO_4}$, $\mathrm{Sr_2CuO_2Cl_2}$), which can be characterized as being of CT type [104,109–111]. According to the model proposed by Zhang and Ng [105], CT exciton formation results in two spinless Cu sites, a spinless Cu^{1+} ($3d^{10}$, $S = 0$) ion and a neighboring Cu^{2+} ($3d^9$, $S = 1/2$) $-$ O ($2p^5$, $S = 1/2$) hole singlet, which can move freely in the antiferromagnetically ordered $\mathrm{CuO_2}$ (Cu^{2+} $3d^9$, $S = 1/2$) planes, see Fig. 5.42. Exciton formation thus leads to a reduction of the kinetic energy. This mechanism for exciton formation might also be of importance for the understanding of Cooper pair formation in high-T_C superconductors [105, 112–114].
It has been proposed by the authors of Ref. [13] that a similar mechanism for exciton formation operates in the case of antiferro-*orbital* order. In the following, we reproduce the simple argumentation of Ref. [13], that has been applied to the case of the $3d^1$ MH insulator $\mathrm{YTiO_3}$. The actual situation is simplified by considering a 1D model with only two orbitals per site, e.g., yz and zx, for a chain running along the z direction. Hopping is only allowed between orbitals of the same type, it is zero between yz and zx orbitals. The situation is illustrated in Fig. 5.43. The two types of orbitals are denoted by circles and squares, occupied orbitals are represented by black and gray symbols, whereas empty symbols refer to empty orbitals. The occupation of yz and zx orbitals alternates in the antiferro-orbital ordered ground state (see Fig. 5.43 (a)). The empty orbitals are higher in energy because of, e.g., the ligand-field splitting. Figure 5.43 (b) exemplifies an excitation from the lower to the upper Hubbard band, i.e. $|d^1d^1\rangle \rightarrow |d^2d^0\rangle$ in $\mathrm{YTiO_3}$. Site 2 is empty while site 3 is doubly occupied. Figures 5.43 (c) and (d) illustrate the motion of the double occupancy to sites 4 and 5, respectively. Since hopping is only allowed within the same type of orbitals, on sites 3 and 4 the orbitals of higher energy are occupied (gray symbols in Fig. 5.43). Consequently, a trace of orbitally excited states emerges and the bandwidth is reduced from the bare bandwidth $\sim t$ to the energy scale of the orbital excitations, corresponding to an increase in kinetic energy. The trace of the excited orbitals can be healed out if the hole accompanies the double occupancy, i.e., by the formation of an exciton (dashed line in Fig. 5.43). The exciton can thus hop on a larger energy scale than the hole or the double occupancy alone. The antiferro-orbital order does not constrain the motion of the exciton, in other words, exciton formation results in

a gain of kinetic energy.
An exciton in a Mott-Hubbard insulator is referred to by the term *Hubbard exciton*. To sum up, a Hubbard exciton denotes a bound state of a doubly occupied site and an empty site that moves in the background of singly occupied sites.

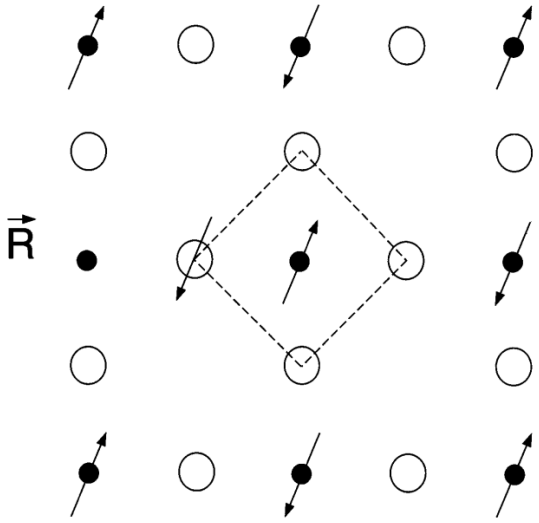

Figure 5.42:
Mechanism of exciton formation in 2D cuprates as proposed by Zhang and Ng [105]. The O atoms are denoted by open circles, the Cu atoms are denoted by full circles, the arrows refer to the spins of holes. Exciton formation results in a spinless Cu^{1+} site (which is empty in a hole picture) and a spin singlet which is formed by one hole on the O ligands and another hole on the centered Cu^{2+} ion. Taken from Ref. [105].

5.4.3 Hubbard exciton in $R\mathrm{VO}_3$

The situation that has been outlined above can be applied to the antiferro-orbital order of $R\mathrm{VO}_3$ both within the ab plane and along c in the monoclinic phase below T_{OO} with C-type spin and G-type orbital order. Here, the hopping of either a single d^3 state or a single d^1 state leaves a trace of orbitally excited states whereas the motion of a bound state is not hindered by the antiferro-orbital background. In $R\mathrm{VO}_3$, the ratio $\mathrm{SW}_A/\mathrm{SW}_B$ (see Fig. 5.44) of the spectral weights of peaks A and B in σ_1^c strongly increases from $R = \mathrm{Y}$ via Gd to Ce. Interestingly, this ratio also depends sensitively on the temperature, but only below the orbital-ordering temperature T_{OO} (see Fig. 5.44). Below T_{OO}, the spectral weights of both peaks A and B increase, but this increase is much more pronounced for the excitonic peak A. This clearly demonstrates the significant role played by orbital order for exciton formation in the MH insulators $R\mathrm{VO}_3$. It follows from Hund's rule that the kinetic energy is assumed to play a more significant role for the formation of Hubbard excitons in the case of parallel spin alignment, which justifies that peak A is much more pronounced in σ_1^c compared to σ_1^a, especially below the spin-ordering transition at T_N.
This scenario is further supported by Novelli *et al.* [115]. They performed pump-probe spectroscopic measurements on YVO_3 in the energy range from 1.65 eV to

2.75 eV, covering the frequency range of peaks A and B. They make use of our static ellipsometric data on YVO_3 to analyze the pump-induced time-dependent changes of the spectral weight of peak A and peak B in $\sigma_1^c(\omega)$ separately, and disentangle thermal and nonthermal contributions. Figure 5.45 displays the nonthermal contributions to the pump-driven spectral weight variations at $t = 50 \pm 30ps$ (well beyond the electronic relaxation) at different equilibrium temperatures. The central result is the observation of a direct transfer of spectral weight between peaks A and B (named HE (Hubbard exciton) and SP ("single-particle" band), respectively, in Ref. [115]), i.e., a conservation of the total spectral weight. This confirms the claim, that both excitations correspond to the same multiplet and corroborates the excitonic nature of peak A. It is evident from Fig. 5.45 that photo-induced spectral-weight transfer from peak A to peak B only takes place below the orbital ordering temperature T_{OO} and is further increased below T_N in the C-type spin ordered phase. This can be recognized as a further clear indication for the importance of the kinetic energy contribution to exciton formation. The spectral weight loss of peak A after the pump excitation is explained in terms of the pump-induced spin disorder. Novelli *et al.* [115] argue that spin disorder suppresses the kinetic energy gain of the excitonic resonance, leading to a spectral-weight transfer from excitonic peak A to peak B (for a detailed discussion, see Ref. [115]). It is further interesting to note that only peak B contributes to the fast response ($t < 3$ ps), whereas the spectral weight of peak A seems to be unchanged within the first few picoseconds after the pump excitation. This gives further evidence that only peak B is of single-particle origin since the excitonic band has more of a localized character and consequently is not expected to be perturbed immediately after the event of the pump [115].

To summarize this section, results from band-structure calculations and photoemission spectroscopy do not give any explanation for the splitting of peaks A and B. We thus suggest that peak A has to be interpreted in terms of an excitonic resonance in the upper Hubbard band, i.e. a bound state of a doubly occupied site and an empty site. The temperature dependence of our data clearly substantiates the importance of the kinetic energy for Hubbard exciton formation. While the motion of either a single d^3 state or a single d^1 state is hindered by the antiferro-orbital ordered background, a bound state can move around freely, which leads to a reduction of the kinetic energy.

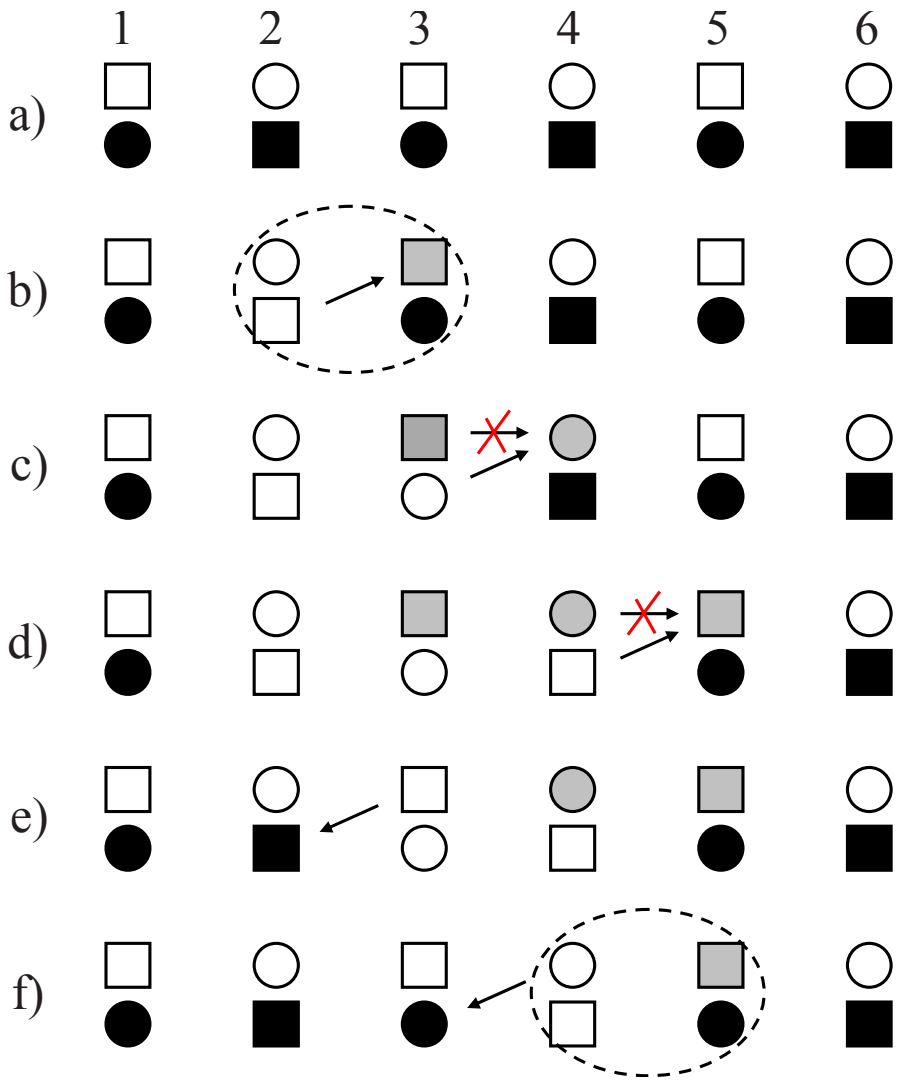

Figure 5.43: Simple sketch of the formation and propagation of a Hubbard exciton (dashed line) as suggested in Ref. [13]. Here, two types of orbitals (illustrated by circles and squares, e.g., yz and zx orbitals) per site are considered. According to the orbital selection rule, hopping is only allowed between orbitals of same type. Full (open) symbols represent occupied (empty) orbitals. (a) Antiferro-orbital ordered ground state. (b) Formation of a hole and a double occupancy on sites 2 and 3, respectively. (c) – (f) Motion of the hole, the double occupancy, or the exciton. More details are given in the text. Taken from Ref. [13].

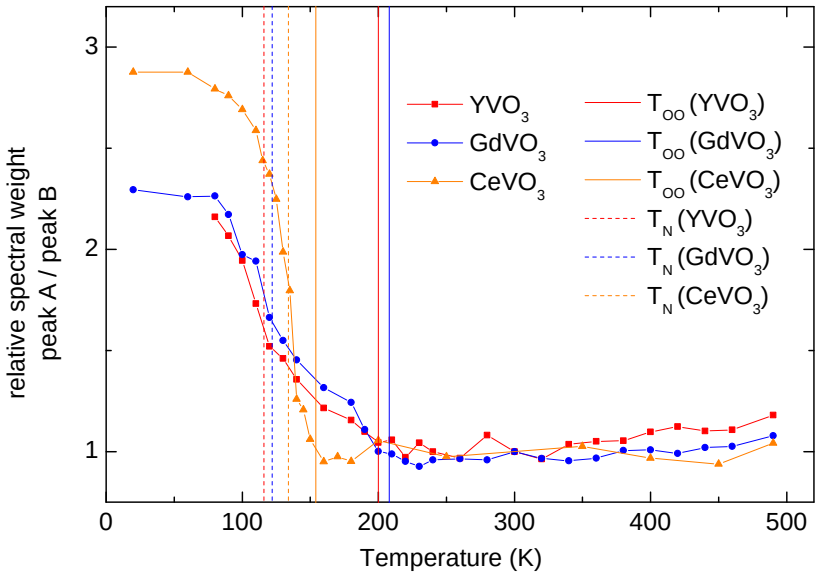

Figure 5.44: Ratio of the spectral weights of peaks A and B in $\sigma_1^c(\omega)$, normalized to the value at 300 K.

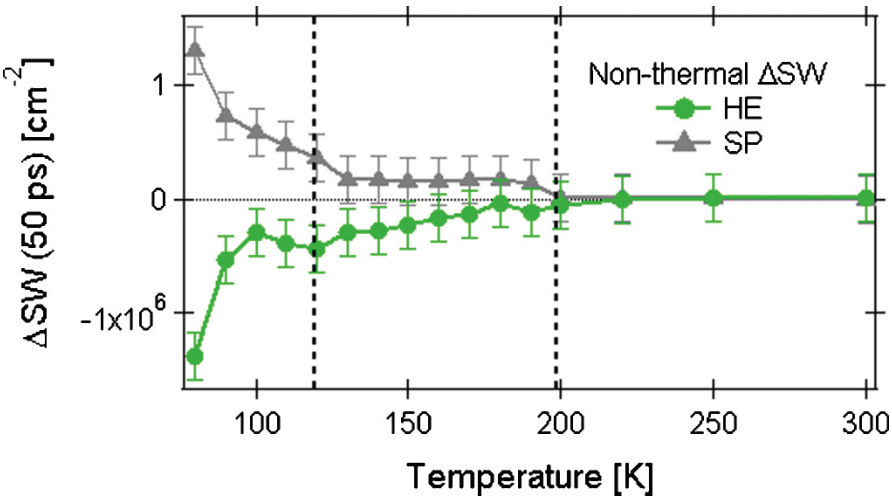

Figure 5.45: Nonthermal spectral-weight changes of peaks A (green circles) and B (gray triangles) in σ_1^c of YVO_3, named HE (Hubbard exciton) and SP ("single-particle"), respectively, that result from time-domain spectroscopic data obtained by Novelli *et al.* [115] at different equilibrium temperatures. The error bars were estimated from the fitting. Taken from Ref. [115].

5.5 Conclusion

We present a detailed analysis of the temperature dependence of the optical conductivity $\sigma_1(\omega)$ of YVO_3, GdVO_3, and CeVO_3 in the energy range from 0.75 eV to 5.0 eV for temperatures ranging from 15 K to 490 K. The steep increase of the optical conductivity above 4.5 eV is attributed to the onset of charge-transfer excitations, while the multiplet structure below 4.5 eV clearly reflects the multiplet splitting of the $3d^3$ final states of Mott-Hubbard excitations. We derive a peak assignment that consistently explains the temperature dependence of our data on the basis of nearest-neighbor spin-spin and orbital-orbital correlations and we thereby solve the controversies concerning the optical data of YVO_3 reported in the literature. A comparison of our data with a theory based on a low-energy spin-orbital superexchange Hamiltonian leads us to the conclusion that orbital fluctuations can not be strong in $R\mathrm{VO}_3$. The Mott-Hubbard excitation into the lowest $3d^3$ multiplet shows a pronounced double-peak structure, which we attribute to an excitonic resonance, i.e. not a truly bound state below the gap but a resonance within the absorption band. The distinct temperature dependence of the double-peak structure clearly indicates that not only the Coulomb attraction between a doubly occupied site and an empty site but also the kinetic energy plays an important role for exciton formation in Mott-Hubbard insulators.

6 Ellipsometry on $LaSrFeO_4$

The chapter on hand presents the ellipsometric studies of the compound $LaSrFeO_4$. The chapter is structured as follows. In Sec. 6.1 a motivation is given for the optical investigations on $LaSrFeO_4$ and the crystal and electronic structure is shortly introduced. The experimental data is then presented in Sec. 6.2. In Sec. 6.3 the expected multiplet splitting of Mott-Hubbard and charge-transfer absorption bands is discussed, then it is turned to the peak assignment and finally the analysis of the temperature dependence of the Mott-Hubbard excitations is presented. The chapter ends with a conclusion in Sec. 6.4.

6.1 The compound $LaSrFeO_4$

6.1.1 Motivation

The compound $LaSrFeO_4$ can be characterized as a correlated insulator with $3d^5$ electron configuration on the Fe^{3+} sites. As discussed in Sec. 2.7, one distinguishes between two kinds of correlated insulators, depending on the relative size of the on-site Coulomb interaction energy U and the charge-transfer (CT) energy Δ between the highest occupied oxygen $2p$ band and the transition-metal $3d$ band [52]. In a CT insulator with $U > \Delta$, the charge gap is formed between O $2p$ and the upper Hubbard band (UHB). In contrast, Mott-Hubbard (MH) insulators show $U < \Delta$, and the states closest to the Fermi level predominantly have transition-metal character, see Fig. 2.9 in Sec. 2.7. Compounds with intermediate-size transition metals such as Fe or Mn are close to the transition between CT systems and MH systems. Here, the hybridization between the ligand O $2p$ and the transition metal $3d$ bands plays an important role. Particularly, the character of Mn^{3+} has been discussed controversially. On the basis of optical data, both $LaMnO_3$ and $LaSrMnO_4$ have been interpreted either as of CT type [57, 59, 117–119] or of MH type [11, 12, 120–123] while recently a dual nature of the optical gap has been proposed [124]. This controversy arises due to the strong hybridization between the Mn $3d$ and the O $2p$ states. Figure 6.1 displays a sketch of a correlated insulator for the different cases, $U \gg \Delta$, $U \gtrsim \Delta$, and $U \ll \Delta$. Early on, Mizokawa and Fujimori [54] pointed out that $U > \Delta$ in $LaMnO_3$, but that the highest occupied O $2p$ band shows a large admixture of $3d$ character. It has been emphasized in Ref. [12] (see also the Phd thesis of A. Gössling [43]) that the symmetry of the

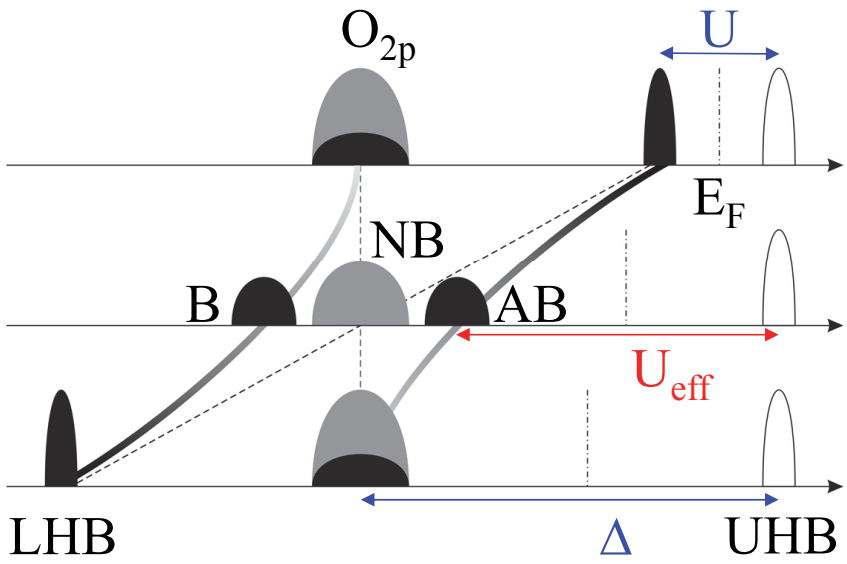

Figure 6.1: Sketch of a Mott-Hubbard insulator (top row, $U \ll \Delta$) and of a charge-transfer insulator (bottom row, $U \gg \Delta$) for a single half-filled $3d$ orbital and degenerate O $2p$ orbitals. The black dashed line depicts the increase of U from top to bottom, E_F depicts the Fermi level (dash-dotted). Due to hybridization, one has to distinguish bonding (B), non-bonding (NB), and anti-bonding (AB) bands. For $U \gtrsim \Delta$, the highest occupied anti-bonding band may still be classified as the lower Hubbard band with symmetry properties derived from the $3d$ character, yielding an effective value $U_{\text{eff}} < \Delta$ (cf. Fig. 1 in Ref. [12] and Fig. 2 in Ref. [56]). [116]

highest occupied, strongly hybridized band is determined by the $3d$ band, which is essential for the optical selection rules and thus for a quantitative analysis of the optical data. It has been suggested that the manganites can be viewed as *effective* Mott-Hubbard systems, where an effective Coulomb interaction energy U_{eff} has to be considered, which is strongly renormalized by hybridization (see Fig. 6.1). This scenario is supported by recent measurements on transition-metal difluorides MF_2 using x-ray emission spectroscopy [56]. Due to the element selectivity of this technique, the contribution of the transition-metal lower Hubbard band (LHB) to the highest occupied states can be revealed even for $U > \Delta$.

At first sight, the situation is more transparent in the case of the ferrites $RFeO_3$ with trivalent Fe ions. Compared to the $3d^4$ manganites, the stability of the high-spin $3d^5$ state of Fe^{3+} gives rise to a comparably large energy of MH excitations of roughly $U + 4J_H$, where J_H denotes the intra-atomic Hund exchange. Indeed, these compounds commonly are identified as CT systems [54, 57, 117, 125]. How-

ever, the case of layered $LaSrFeO_4$ is still under discussion. $LaSrFeO_4$ has also been interpreted as a CT insulator based on optical reflectivity data measured up to 36 eV at room temperature with in-plane polarization of the electric field [126]. In contrast, Omata *et al.* [127] conclude from their resonant photoemission data that the valence band in $LaSrFeO_4$ is formed by a mixture of Fe $3d$ and O $2p$ states. Thus they characterize $LaSrFeO_4$ as an intermediate type CT and MH insulator, but they also mention that the states at the valence band edge mainly show O $2p$ character.

The aim of this chapter is to gain further insight into the character of $LaSrFeO_4$ by analyzing the optical conductivity $\sigma_1(\omega)$. Due to the layered structure of $LaSrFeO_4$, $\sigma_1(\omega)$ is expected to show a pronounced anisotropy. The anisotropy of the optical spectra can be used to disentangle MH excitations and CT excitations. The distinction between MH and CT excitations is still a valid classification scheme even in the presence of hybridization since the hybridized states retain their original symmetry and thus follow the same selection rules. As discussed in Refs. [12] and [43] for the case of $LaSrMnO_4$, MH excitations only contribute to σ_1^a, i.e. for polarization of the electric field within the 2D layer, but not to σ_1^c. This reflects that $Fe - Fe$ hopping between adjacent FeO_2 layers is negligible. On the contrary, CT excitations are observed in both, $\sigma_1^a(\omega)$ and $\sigma_1^c(\omega)$, as each Fe site is surrounded by an oxygen octahedron.

Additionally, the temperature dependence of the spectral weight is investigated. As discussed in Secs. $2.6 - 2.7$, CT and MH excitations generally show different spin and orbital selection rules and only the spectral weight of the MH excitations is expected to be strongly affected by a change of the nearest-neighbor spin-spin and orbital-orbital correlation functions [8–13,49,99]. It has been discussed in Sec. 5 that the spectral weight of the lowest absorption band in $\sigma_1^c(\omega)$ of $3d^2$ $R\mathrm{VO}_3$ increases by a factor of $2 - 3$ due to the ordering of spins and orbitals, in agreement with theoretical expectations. Also in $LaMnO_3$ and $LaSrMnO_4$ pronounced changes of the spectral weight with temperature have been observed, which can be attributed to changes of the spin-spin correlations [11,12]. This clearly demonstrates the *effective* MH character of these systems. However, the behavior of the $3d^1$ MH insulators $YTiO_3$ and $SmTiO_4$ is still puzzling in this context [13]. Temperature dependent ellipsometric data of $YTiO_3$ and $SmTiO_4$ have been acquired by A. Gössling, see Refs. [13, 43]. In $YTiO_3$, the spectral weight of the lowest MH excitation is expected to change by 25 % between the paramagnetic and the ferromagnetic state [8]. However, the increase around the ordering temperature T_C amounts to only 5 %, while, at the same time, larger changes are observed up to 300 K [13]. Due to the three-dimensional character of the magnetic order, these larger changes far above T_C cannot be explained by a change of the spin-spin correlations. In the G-type antiferromagnet $SmTiO_3$, spin ordering is expected to suppress the spectral weight of the lowest MH excitation by about 50 % for all crystallhographic directions [8], but the observed effects are again much smaller

and show even the wrong sign along the b and the c axis [13]. This behavior has been attributed to small changes of the orbital occupation [13]. It is important to quantify the possible strength of other effects such as excitonic contributions, the thermal expansion of the lattice, or bandstructure effects. In this context, layered $LaSrFeO_4$ with its stable $3d^5$ state is an interesting candidate for a reference system. Long-range antiferromagnetic spin order sets in at $T_N = 366\,\mathrm{K}$ [69, 128, 129] thus one expects only very small changes of the spin-spin and orbital-orbital correlation functions below room temperature.

Thus far, not much is known about the optical spectra of $LaSrFeO_4$. Room temperature data has been obtained by the means of diffuse reflectance on powdered samples [130] and by reflectivity measurements on single crystals [126, 131] but only for in-plane polarization of the electric field.

6.1.2 Structure, spins, and orbitals

The compound $LaSrFeO_4$ crystallizes in the single-layered perovskite structure of K_2NiF_4 with tetragonal symmetry $I4/mmm$. The Fe^{3+} ions are octahedrally coordinated by oxygen ions, building perfect FeO_2 square planes with $180°$ $Fe-O-Fe$ bonds. The lattice constants at room temperature are $a = 3.8744(1)\,\text{Å}$ and $c = 12.7134(3)\,\text{Å}$ [69]. Nominally, there are five electrons in the $3d$ shell per Fe^{3+} site. In the high-spin ground state, these five electrons yield a total spin of $5/2$. Antiferromagnetic order has been observed below $T_N = 366\,\mathrm{K}$ [69, 128]. The crystal and magnetic structure is visualized in Fig. 6.2. Our crystals do not exhibit any evidence for an additional magnetic phase transition [69]. In cubic approximation, the $3d$ level is split into the lower-lying t_{2g} and the higher-lying e_g levels. The magnitude of the $t_{2g} - e_g$ splitting $\Delta_{t2g-eg} = 10\,Dq$ is mainly determined by the $Fe-O$ bond lengths, it can be estimated to be roughly $10\,Dq = 1.0\,\mathrm{eV} - 1.5\,\mathrm{eV}$ in $LaSrFeO_4$ [12, 132]. The FeO_6 octahedra show a sizable tetragonal distortion with $Fe-O$ bond lengths of $1.9354\,\text{Å}$ in the plane and $2.1486\,\text{Å}$ perpendicular to it at $10\,\mathrm{K}$ [69]. Therefore, the t_{2g} manifold is split into the lower-lying doublet e'_g (yz and zx) and the higher-lying b_{2g} (or xy) level. At the same time, the e_g level splits into a_{1g} ($3z^2-r^2$) and b_{1g} (x^2-y^2), where the energy of the former is significantly reduced compared to the energy of the latter. In $LaSrMnO_4$, these splittings have been determined from optical data, yielding $\Delta_{t2g}(d^4) = 0.2\,\mathrm{eV}$ and $\Delta_{eg}(d^4) = 1.4\,\mathrm{eV}$ [12]. For $LaSrFeO_4$, a similar value of Δ_{t2g} is expected, but the value of Δ_{eg} is expected to be smaller, since Δ_{eg} is enhanced in $LaSrMnO_4$ due to the additional Jahn-Teller splitting of the singly occupied e_g level, which is evident from the larger value of c/a. It has to be emphasized that the pronounced elongation of the octahedra in $LaSrFeO_4$ gives rise to a sizeable value of Δ_{eg}, even in the absence of a Jahn-Teller contribution. The results below yield $\Delta_{eg} \approx 0.8\,\mathrm{eV}$.

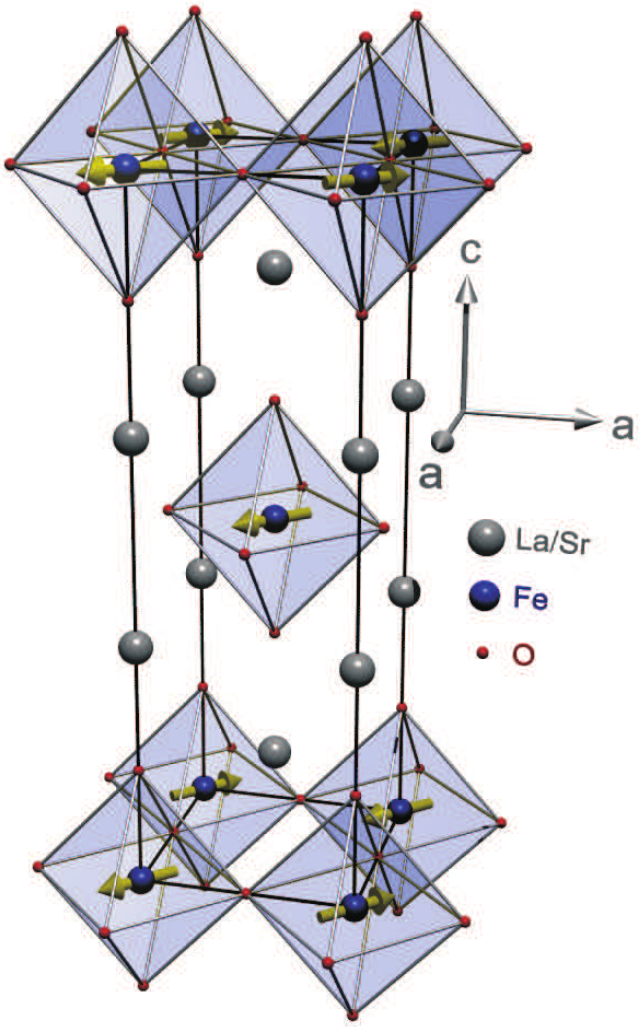

Figure 6.2: Tetragonal unit cell and visualization of the magnetic structure of $LaSrFeO_4$. Taken from Ref. [69].

6.2 Experimental data

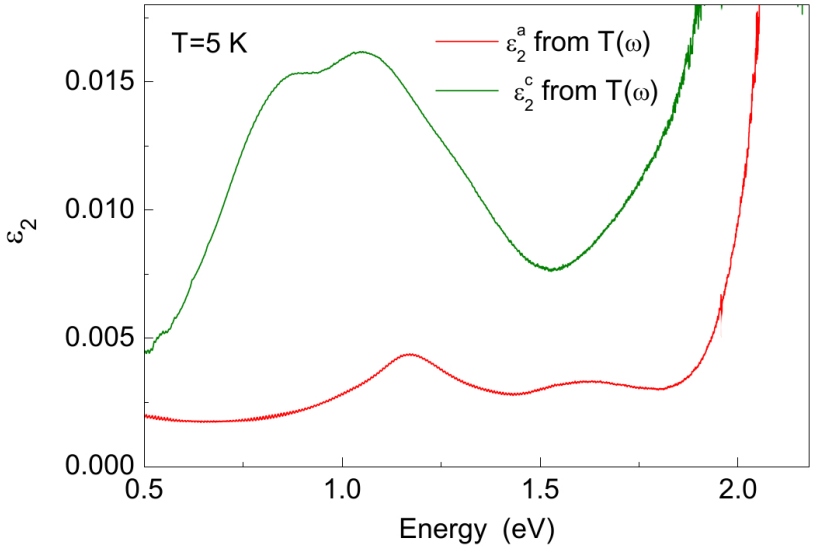

Figure 6.3: The dielectric function $\varepsilon_2(\omega)$ below the charge gap as determined from transmittance measurements on a single crystal with a thickness of 39 μm.

Measurements of the ellipsometric variables Ψ_{pp} and Δ_{pp} have been performed on a polished ac surface in two different orientations, with the a and c axis parallel to the plane of incidence, respectively, for temperatures from 15 K to 250 K. The ellipsometric measurements have been performed by K. Shportko. The dielectric functions $\varepsilon^a(\omega)$ and $\varepsilon^c(\omega)$ are obtained by fitting the measured data of both orientations simultaneously with a series of Gaussian oscillators for $\varepsilon_2(\omega)$. In the analysis a finite surface roughness is taken into account. The properties of the surface are determined in a frequency range where the investigated bulk sample is transparent, i.e., $\varepsilon_2(\omega) \approx 0$. To determine the suitable energy range, it is made use of infrared transmittance data between 0.5 eV and 2.5 eV which have been acquired by L. Fels. The transmittance measurements have been performed with a Fourier-transform spectrometer (Bruker IFS 66/v) on a single crystal which was polished to a thickness of 39 μm. The observed interference fringes are used to determine the refractive index n, which in turn allows the determination of $\varepsilon_2(\omega)$ from the transmittance. The results are displayed in Fig. 6.3. These data show only very weak parity- and spin-forbidden local crystal-field excitations between 0.5 eV and 2.0 eV, thus $\varepsilon_2(\omega) \approx 0$ is a valid approximation below 2 eV. Using this result for the analysis of the low-energy ellipsometry data yields a surface roughness with a

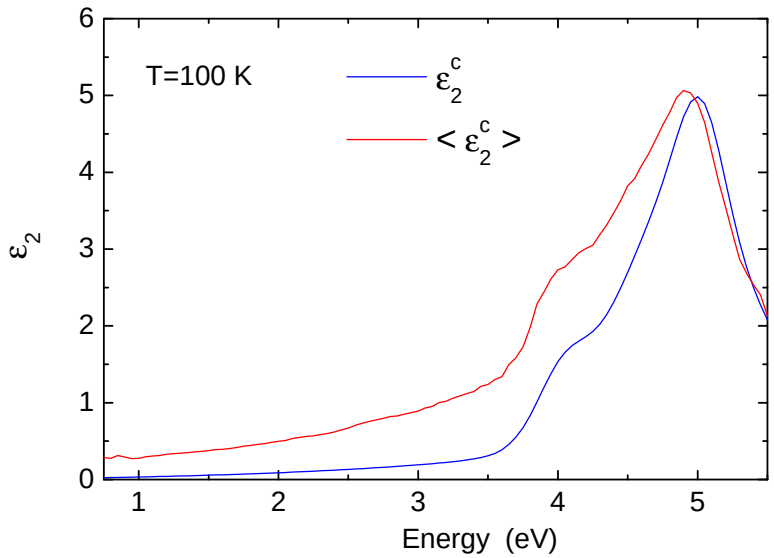

Figure 6.4: Comparison of the dielectric function ε_2^c and the pseudo-dielectric function $< \varepsilon_2^c >$ of $LaSrFeO_4$ at $T = 15\,K$. For the former, a surface roughness of 6 nm has been taken into account. The pseudo-dielectric function $< \varepsilon_2^c >$ results from the measurement on an *ac* surface with the *c* axis parallel to the plane of incidence (cf. Sec. 3.2.2).

thickness of approx. 6 nm. In Fig. 6.4 the resulting $\varepsilon_2^c(\omega)$ is compared to the so-called pseudo-dielectric function $< \varepsilon_2^c >$, which is obtained by direct inversion of the measured Ψ_{pp} and Δ_{pp} values obtained from the measurement on the *ac* plane with the *c* axis parallel to the plane of incidence, cf. Sec. 3.2.2. Figure 6.4 shows that the overall features are well reproduced by $< \varepsilon_2^c >$, but large discrepancies are observed below the onset of strong absorption at about 3.5 eV, where $< \varepsilon_2^c >$ shows a spurious background. The transmittance data prove that this background is an artefact present only in $< \varepsilon_2^c >$ which has to be accounted for by assuming a finite surface roughness in the data modeling. It has to be pointed out that a similar feature has been observed in optical data of $BiFeO_3$ published by Pisarev *et al.* [125] where only the pseudo-dielectric functions are discussed.
The resulting dielectric function $\varepsilon(\omega) = \varepsilon_1^l + i\varepsilon_2^l$ $(l = a, c)$ of $LaSrFeO_4$ from 1.5 eV to 5.5 eV is displayed in Fig. 6.5. The real part of the optical conductivity $\sigma_1^l(\omega)$ is shown in Fig. 6.6. Figure 6.7 displays the different Gaussian oscillators that compose $\varepsilon_2(\omega)$ in the fit. The Gaussian fit parameters are summarized in tables 6.2 and 6.3 at the end of this chapter. Overall, the data agree with the room-temperature data of $\sigma_1^a(\omega)$ reported in Refs. [126, 131]. Thus far, data for $\sigma_1^c(\omega)$ has not been reported, a striking anisotropy between $\sigma_1^a(\omega)$ and $\sigma_1^c(\omega)$ is found in

our data. Both $\sigma_1^a(\omega)$ and $\sigma_1^c(\omega)$ show a strong absorption band at $4\,\mathrm{eV} - 5.5\,\mathrm{eV}$. However, in $\sigma_1^a(\omega)$ an additional peak is found at 3 eV and the shoulder at 3.8 eV is much more pronounced. In the following it is argued that the latter two features correspond to MH excitations.

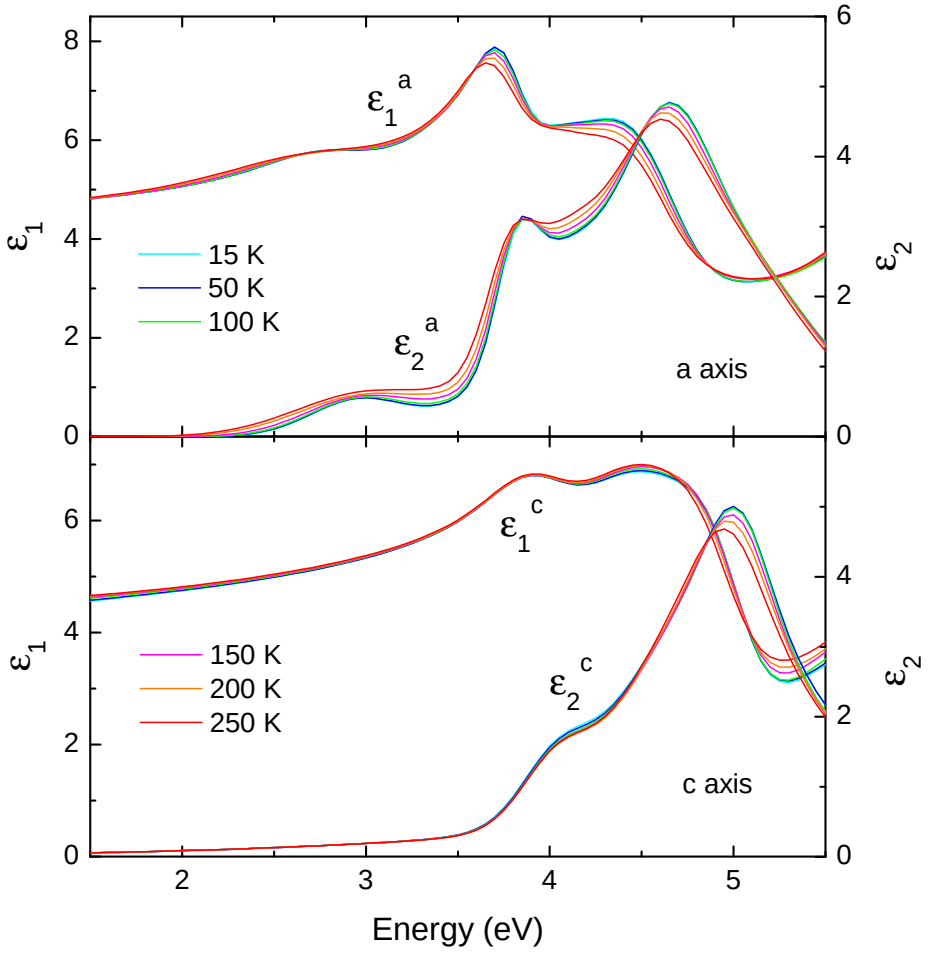

Figure 6.5: Dielectric function $\varepsilon(\omega)$ of $LaSrFeO_4$ for the a and c direction for temperatures between 15 K and 250 K.

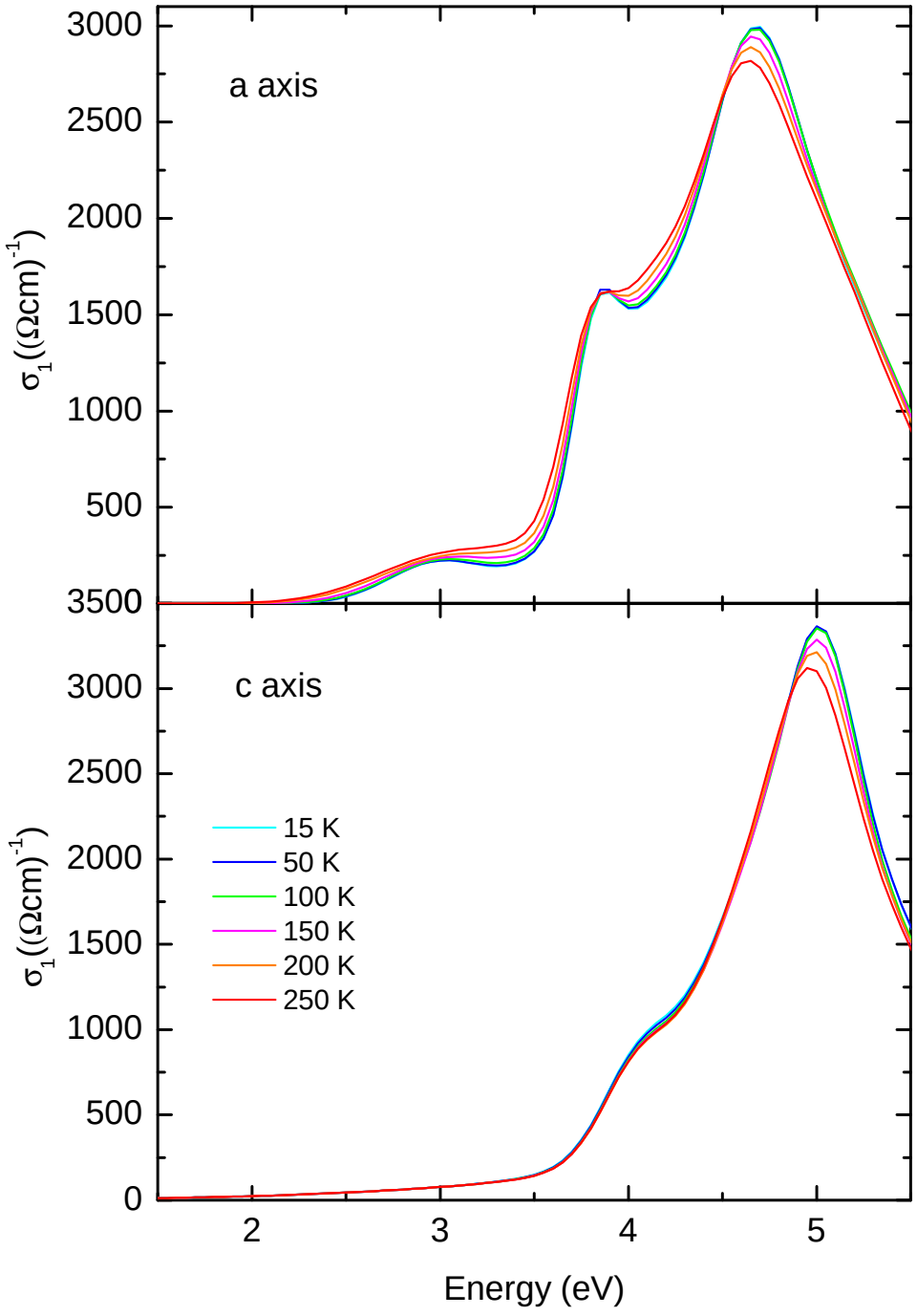

Figure 6.6: Optical conductivity $\sigma_1(\omega)$ of $LaSrFeO_4$ for the a and c direction for temperatures between 15 K and 250 K.

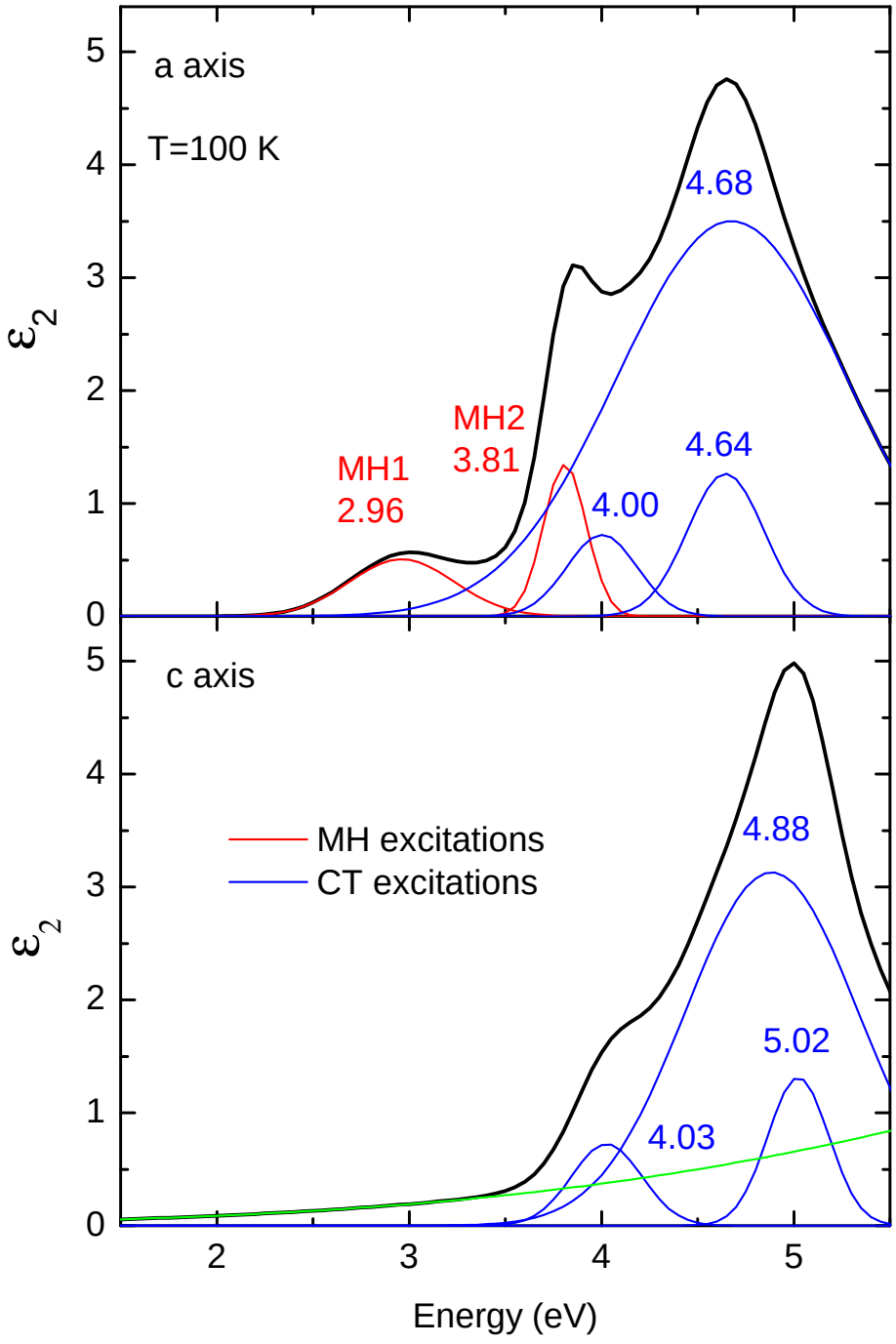

Figure 6.7: The measured data is best fit by a sum of five Gaussian oscillators for ε_2^a and three Gaussian oscillators for ε_2^c, plus an additional oscillator (green) outside the measured range that accounts for higher lying excitations as well as for the small values of absorption below 3.5 eV in ε_2^c.

6.3 Discussion

6.3.1 Charge-transfer and Mott-Hubbard excitations

The observed absorption bands can be assigned to MH and CT excitations. The role played by local crystal-field (i.e., valence-conserving $3d^5 \rightarrow 3d^{5,*}$) excitations can be neglected in our analysis of the ellipsometry data. In $LaSrFeO_4$ they are forbidden both by the parity and by the spin selection rule. Accordingly, they show a very small spectral weight with typical values of $\sigma_1 < 10\,(\Omega\mathrm{cm})^{-1}$ [133, 134]. Their signatures are visible in the transmittance data below the charge gap, see Fig. 6.3.

First, we focus on the physics of CT excitations, which result from the transfer of an electron from a ligand O $2p$ orbital to a Fe $3d$ orbital, $|3d^5\,2p^6\rangle \rightarrow |3d^6\,2p^5\rangle$. Pisarev *et al.* [125] present a detailed theoretical analysis of the CT excitations for undistorted FeO_6 octahedra. The highest occupied O states are of non-bonding character with symmetry $t_{1g}(\pi)$, $t_{2u}(\pi)$, $t_{1u}(\pi)$, and $t_{1u}(\sigma)$. Their relative energies are determined by, e.g., the different Madelung energies of $2p(\pi)$ and $2p(\sigma)$ orbitals and by the $2p(\pi) - 2p(\pi)$ overlap [125]. The $t_{1g}(\pi)$ level is expected to be the highest in energy. Quantum-chemistry calculations [125] for $LaFeO_3$ predict that $t_{2u}(\pi)$, $t_{1u}(\pi)$, and $t_{1u}(\sigma)$ are lower by 0.8 eV, 1.8 eV, and 3 eV, respectively. The lowest unoccupied states are the anti-bonding $t_{2g}(\pi)$ and $e_g(\sigma)$ orbitals with hybrid Fe $3d -$ O $2p$ character, and these are split by $\Delta_{t2g-eg} = 10\,Dq$. According to the parity selection rule, the even-even (from g type to g type) transitions from the $t_{1g}(\pi)$ level at the top of the O band to the unoccupied $t_{2g}(\pi)$ and $e_g(\sigma)$ orbitals are forbidden. Additionally, the matrix elements for transitions from π to σ levels vanish for a single octahedron, thus only π-π and σ-σ transitions give rise to strong absorption. In summary, the onset of CT excitations is governed by the dipole-forbidden transition $t_{1g}(\pi) \rightarrow t_{2g}(\pi)$, followed by the strong dipole-allowed transitions $t_{2u}(\pi) \rightarrow t_{2g}(\pi)$ and $t_{1u}(\pi) \rightarrow t_{2g}(\pi)$. The next transition $t_{1u}(\sigma) \rightarrow e_g(\sigma)$ is roughly 2 eV higher in energy due to the splitting between $t_{2g}(\pi)$ and $e_g(\sigma)$ on the one hand and between $2p(\pi)$ and $2p(\sigma)$ states on the other hand. Thus in cubic approximation there are only two strong excitations in the energy range relevant to us. For the layered structure of $LaSrFeO_4$, one has to expect additional splittings. However, the large splitting Δ_{eg} of the e_g level is not important for the lowest CT excitations, which correspond to an electron transfer into the $t_{2g}(\pi)$ level.

Let us now address the MH excitations, which result from the transfer of an electron between neighboring Fe sites i and j via the σ or π bonding of the ligand O $2p$ orbital, $|3d_i^5\,3d_j^5\rangle \rightarrow |3d_i^4\,3d_j^6\rangle$. Starting from the cubic approximation, the initial $3d^5$ state has ${}^6A_1$ symmetry, corresponding to the $(2S+1) = 6$-fold degenerate $t_{2g}^3 e_g^2$ high-spin state (see Fig. 6.8 (a)). According to the orbital selection rule, there is no overlap between t_{2g} and e_g orbitals on neighboring sites due to the

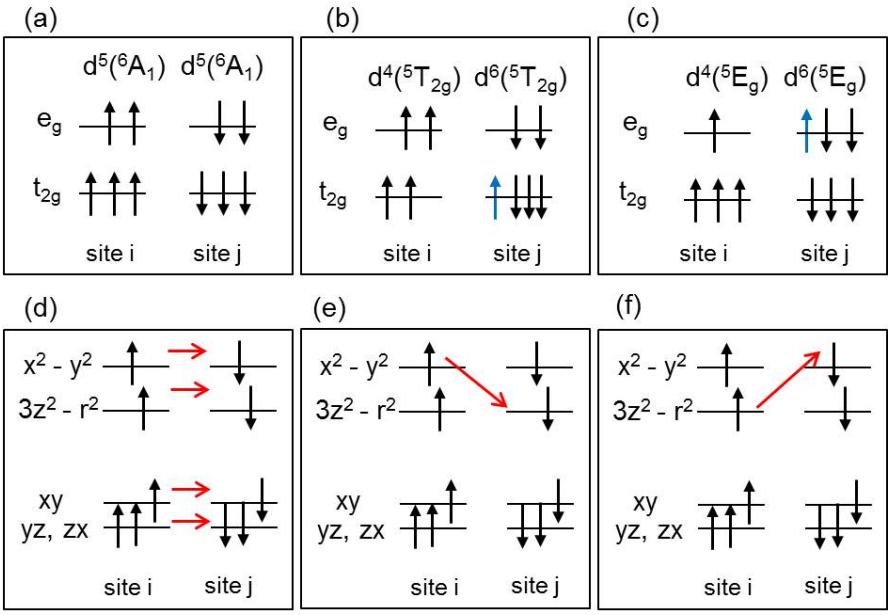

Figure 6.8: Sketch of (a) the initial state $|3d_i^5\, 3d_j^5\rangle$ and (b,c) the final states $|3d_i^4\, 3d_j^6\rangle$ of the MH excitations in cubic approximation. In layered $LaSrFeO_4$ with tetragonal crystal symmetry, three MH peaks are expected in σ_1^a. They correspond to (d) an electron transfer between orbitals of the same type, energy E, (e) a transfer from x^2-y^2 to $3z^2-r^2$, energy $E-\Delta_{eg}$, and (f) a transfer from $3z^2-r^2$ to x^2-y^2, energy $E+\Delta_{eg}$.

undistorted 180° bonds in $LaSrFeO_4$. From the $[^6A_{1g}(d^5);\, ^6A_{1g}(d^5)]$ initial state one can reach the final states $[^5T_{2g}(t_{2g}^2, e_g^2);\, ^5T_{2g}(t_{2g}^4, e_g^2)]$ (corresponding to an electron transfer between t_{2g} orbitals, see Fig. 6.8 (b)) and $[^5E_g(t_{2g}^3, e_g^1);\, ^5E_g(t_{2g}^3, e_g^3)]$ (corresponding to an electron transfer between e_g orbitals, see Fig. 6.8 (c)). All reachable $3d^4$ and $3d^6$ states have total spin $S=2$. The spectral weight of these transitions therefore strongly depends on the nearest-neighbor spin-spin correlations [8, 10, 49], favoring antiparallel alignment of spins on neighboring sites (see Fig. 6.8), as given in the antiferromagnetically ordered state below $T_N = 366\,\mathrm{K}$. Since the orbital quantum number is preserved in the transition (cf. Figs. 6.8 (b) and 6.8 (c)), both excitations have approximately the same energy[1]. As a consequence, only one MH peak is expected in the optical spectra in the cubic approximation.

However, deviations from cubic symmetry play an important role in the tetragonal structure of $LaSrFeO_4$. First of all, the matrix elements for MH excita-

[1]Here, it is neglected that the value of $10\,Dq$ $(3d^n)$ depends on the number n of electrons.

Table 6.1: Matrix elements for MH excitations between nearest-neighbor Fe sites along the x direction as given by the Slater-Koster table [135]. The electron transfer takes place via the σ or π bonding of the ligand O $2p$ orbital. The orbital character changes only for excitations from x^2-y^2 to $3z^2-r^2$ or vice versa (third column), in all other cases the orbital character is preserved. According to Ref. [135], the relation $V_{pd\sigma} = V_{pd\pi} \cdot \sqrt{3}$ holds true.

x^2-y^2	$3z^2-r^2$	$x^2-y^2/3z^2-r^2$	xy	yz	zx
$\frac{3}{4}V_{pd\sigma}^2$	$\frac{1}{4}V_{pd\sigma}^2$	$-\frac{\sqrt{3}}{4}V_{pd\sigma}^2$	$V_{pd\pi}^2$	0	$V_{pd\pi}^2$

tions between different FeO_2 layers can be neglected, thus MH excitations do not contribute to $\sigma_1^c(\omega)$. Second, lifting the degeneracy in particular of the e_g level enhances the number of observable absorption bands in $\sigma_1^a(\omega)$. An e_g splitting $\Delta_{eg} = \Delta[(x^2-y^2) - (3z^2-r^2)]$ on the order of 1 eV is expected due to the elongation of the FeO_6 octahedra, as discussed in Sec. 6.1.2. In the following, the much smaller spitting Δ_{t2g} within the t_{2g} levels is neglected. It will be shown that Δ_{eg} is crucial in order to pull the lowest MH absorption band below the onset of CT excitations. The matrix elements for nearest-neighbor $Fe-Fe$ transitions are summarized in table 6.1. Due to the undistorted 180° bonds of $LaSrFeO_4$, these hopping processes conserve the orbital character. The single exception is the finite overlap between $3z^2-r^2$ on site i and x^2-y^2 on a neighboring site. One thus expects three different MH peaks (referred to as MH1, MH2, and MH3 in the following) in $\sigma_1^a(\omega)$ with energy separation Δ_{eg}: (1) The electron transfer from x^2-y^2 to $3z^2-r^2$ (MH1, see Fig. 6.8 (e)). (2) The excitation from any orbital on site i to an orbital of the same type on the neighboring site (MH2, see Fig. 6.8 (d)). This excitation is expected at an energy of Δ_{eg} above MH1. The individual contributions have approximately the same energy because the orbital quantum number is preserved[2]. (3) The excitation from $3z^2-r^2$ to x^2-y^2 (MH3, see Fig. 6.8 (f)). This excitation is expected at an energy of $2\Delta_{eg}$ above MH1. The matrix elements of table 6.1 are used to calculate the relative spectral weight of the MH peaks. Summing up the individual contributions one finds that the spectral weight of MH1 and MH3 is identical, whereas the spectral weight of MH2 is expected to be 3.8 times larger.

[2]Again, it is neglected that the value of $10\,Dq$ ($3d^n$) depends on the number n of electrons.

6.3.2 Peak assignment

A first tool to distinguish CT and MH excitations is the spectral weight. In transition-metal oxides, typical values of $\sigma_1(\omega)$ are of a few $1000\,(\Omega\mathrm{cm})^{-1}$ for CT excitations but only a few $100\,(\Omega\mathrm{cm})^{-1}$ for MH excitations (cf. Sec. 5 on pseudocubic vanadates and Refs. [12, 13, 57]). The difference is due to the fact that the matrix elements are of first order in the Fe − O hopping amplitude for CT excitations and of second order for MH excitations. To further disentangle CT excitations and MH excitations, the observed anisotropy can be used. In layered $LaSrFeO_4$, MH excitations do not contribute to $\sigma_1^c(\omega)$ since the interlayer Fe − Fe hopping is strongly suppressed.
The strong absorption band observed at $4\,\mathrm{eV} - 5\,\mathrm{eV}$ in $\sigma_1^c(\omega)$ clearly has to be attributed to CT excitations. The analysis of the ellipsometric data uses three Gaussian oscillators to describe the line shape, see Fig. 6.7. This does not imply the existence of three microscopically different excitations since the line shape of the absorption band is not necessarily Gaussian but reflects bandstructure effects. The analysis of the a-axis data requires three very similar oscillators, in particular with a similar spectral weight. The peak energies differ by up to 0.4 eV for the two crystallographic directions, which most probably reflects the different on-site energies of apical and in-plane O ions. This band at $4\,\mathrm{eV} - 5\,\mathrm{eV}$ is attributed to the two strong dipole-allowed CT excitations $t_{2u}(\pi) \rightarrow t_{2g}(\pi)$ and $t_{1u}(\pi) \rightarrow t_{2g}(\pi)$ (in cubic approximation, see discussion in Sec. 6.3.1). The splitting between these two excitations is expected to be about 1 eV according to quantum-chemistry calculations for $LaFeO_3$ [125]. In $LaSrFeO_4$, the next higher-lying peak is observed at about 7 eV in the in-plane data of Refs. [126, 131]. This large energy difference to the peak at 5 eV supports the interpretation that both $t_{2u}(\pi) \rightarrow t_{2g}(\pi)$ and $t_{1u}(\pi) \rightarrow t_{2g}(\pi)$ contribute to the absorption band between 4 eV and 5 eV. Note that both excitations correspond to a transfer to a $3d$ $t_{2g}(\pi)$ state, and that the crystal-field splitting of the $t_{2g}(\pi)$ level is expected to be only small, about 0.2 eV (see Sec. 6.1.2). Moreover, the matrix elements for transitions into the t_{2g} manifold do not differ very strongly between a and c, even for an elongated octahedron, in contrast to the matrix elements for transitions into the $x^2 - y^2$ orbital. The similar spectral weights along a and c between 4 eV and 5 eV therefore support this assignment.
The a-axis data show two additional features at 3.0 eV and 3.8 eV, see Figs. 6.6 and 6.7. For the feature at 3.0 eV, both its lower spectral weight with $\sigma_1^a(3\,\mathrm{eV})$ peaking at about $250\,(\Omega\mathrm{cm})^{-1}$ and the observed anisotropy support an interpretation in terms of a MH excitation. Moreover, the splitting between the two lowest MH excitations is expected to be roughly $\Delta_{eg} \approx 1\,\mathrm{eV}$ (see Fig. 6.8), in very good agreement with the difference of 0.8 eV between the observed peak energies of 3.0 and 3.8 eV. The third MH excitation is expected roughly $2\Delta_{eg}$ above the lowest one, i.e., within the strong CT band. As far as the relative spectral weight is con-

cerned, one roughly expects a factor of 3.8 between the two lowest MH excitations (see Sec. 6.3.1). Experimentally, the spectral weight of MH1 and MH2 is rather similar. However, the simple estimate does not take into account hybridization effects and is based on a local approach. Furthermore, an accurate determination of the experimentally observed relative spectral weight of MH1 and MH2 is rather difficult due to the overlap with the much stronger CT excitations, see also the discussion in Sec. 6.3.3 below.

At first sight, it is unexpected that the lowest absorption band is of MH type because the $3d^5$ configuration is stabilized by the intra-atomic Hund exchange J_H. In cubic approximation, a first rough estimate of the MH excitation energy yields $U+4J_H$ with $4J_H \approx 3\,\mathrm{eV}$. This is much larger than in the $3d^4$ manganites, for which one expects $U-J_H$. However, MH1 in the layered structure of $LaSrFeO_4$ corresponds to a transfer from x^2-y^2 to $3z^2-r^2$, thus it is Δ_{eg}^{Fe} lower in energy than in cubic approximation. In comparison, the lowest MH excitation in $LaSrMnO_4$ requires the opposite transfer from $3z^2-r^2$ to x^2-y^2, raising the excitation energy to $E_{Mn} = U - J_H + \Delta_{eg}^{Mn}$. In $LaSrMnO_4$, this MH excitation is observed at $E_{Mn} \approx 2\,\mathrm{eV}$ [12]. We thus expect MH1 in $LaSrFeO_4$ at about $E(\mathrm{MH1}) \approx E_{Mn} + 5J_H - \Delta_{eg}^{Fe} - \Delta_{eg}^{Mn}$, i.e., roughly at $3\,\mathrm{eV} - 4\,\mathrm{eV}$. Here, the slight increase of U from Mn to Fe is neglected, but it is also neglected that the $3d^4$ and $3d^6$ states relevant for the MH1 excitation both are Jahn-Teller active (cf. Fig. 6.8 (d)), which reduces $E(\mathrm{MH1})$. Moreover, these estimates neglect the effect of hybridization depicted schematically in Fig. 6.1. Therefore, the assignment of the peak at 3.0 eV to MH1 appears feasible.

However, alternative scenarios have to be discussed, too. As outlined in Sec. 6.3.1, the lowest CT excitation $t_{1g}(\pi) \rightarrow t_{2g}(\pi)$ is dipole-forbidden and expected at about 0.8 eV below the lowest dipole-allowed CT excitation. Firstly, the spectral weight of the peak at 3 eV is too large for a dipole-forbidden excitation, and secondly, only a modest anisotropy of this excitation is expected. Possibly, this dipole-forbidden excitation may explain the small but finite values of $\sigma_1^c(\omega)$ between 2 eV and 3.5 eV. In a further scenario, the peak at 3.0 eV may be interpreted as a CT exciton. Note that this peak is lying at about 0.5 eV below the CT absorption edge and that a truly bound state with such a large binding energy is very unlikely. Again, it is not obvious why such an exciton should show a pronounced anisotropy. Moreover, an exciton with such a large binding energy is expected to show a larger spectral weight and a smaller line width.

Summarizing this section, strong evidence has been found that the lowest dipole-allowed absorption band in $LaSrFeO_4$ is of MH type, which is made possible by the strong splitting Δ_{eg} caused by the layered structure and by the Fe $3d-$O $2p$ hybridization. It has to be added that in $LaSrFeO_4$ the energy of the lowest *dipole-forbidden* CT excitation may be comparable to the energy of MH1. Furthermore, the MH excitation from x^2-y^2 at site i to a t_{2g} orbital on a neighboring site is lower in energy than MH1, but the matrix element for this excitation vanishes. It

should be emphasized that this results do not disagree with the common interpretation that non-layered ferrites belong to the class of CT insulators. The different character can be explained by the absence of a large Δ_{eg} in the non-layered compounds. Pisarev *et al.* [125] studied the optical properties of a series of different ferrites with trivalent Fe ions. Many of these compounds show a shoulder in the vicinity of the onset of strong CT absorption, which has been attributed to the parity-forbidden excitation $t_{1g}(\pi) \rightarrow t_{2g}(\pi)$ [125]. The peak observed at 3.0 eV in $LaSrFeO_4$ is much too strong for such a dipole-forbidden excitation. However, our results suggest that MH excitations may not be neglected for a quantitative analysis of the non-layered ferrites, they may for instance provide a better explanation for a shoulder close to the absorption edge than the dipole-forbidden excitation discussed above.

6.3.3 Temperature dependence

We have seen in Sec. 5 that in the case of the pseudocubic vanadates the temperature dependence of the spectral weight of MH excitations allows to study the temperature dependence of nearest-neighbor spin-spin and orbital-orbital correlations. As discussed in the motivation of this chapter (Sec. 6.1.1) the temperature dependence of MH excitations has also attracted a lot of interest for other transition-metal compounds [8–13, 49, 99]. In $LaSrFeO_4$ one expects that the temperature dependence of nearest-neighbor spin-spin and orbital-orbital correlations is only small below 300 K. Actually, the spin-spin correlations change only gradually even above the ordering temperature due to the two-dimensional character [13]. This ferrite thus may serve as a reference compound to study the role of other effects such as the thermal expansion of the lattice or bandstructure effects.

As expected, the MH excitations at 3.0 eV and 3.8 eV show only a modest temperature dependence, see the upper panel of Fig. 6.6. According to the fit using Gaussian oscillators (see Fig. 6.7), the spectral weight of MH2 at 3.8 eV changes only by about 10 % between 5 K and 250 K, see Fig. 6.9. At the same time, the peak width increases by about 15 %, and the peak frequency decreases by about 1 %. For the peak MH1 at 3.0 eV, a quantitative analysis is more challenging. Both the spectral weight and the width of the Gaussian oscillator depicted in Fig. 6.7 increase strongly with temperature, while the frequency of the oscillator increases by about 1 % from 5 K to 250 K. As mentioned above, there is not necessarily a one-to-one correspondence between the Gaussian oscillators and the microscopic excitations with different line shapes, which is corroborated by the unexpected behavior of the oscillator parameters such as the hardening of the frequency with increasing temperature. This gives clear evidence that the change of MH1 is covered by the temperature-induced smearing of the much stronger CT excitations. To determine the temperature dependence of MH1 more reliably, MH1 is sepa-

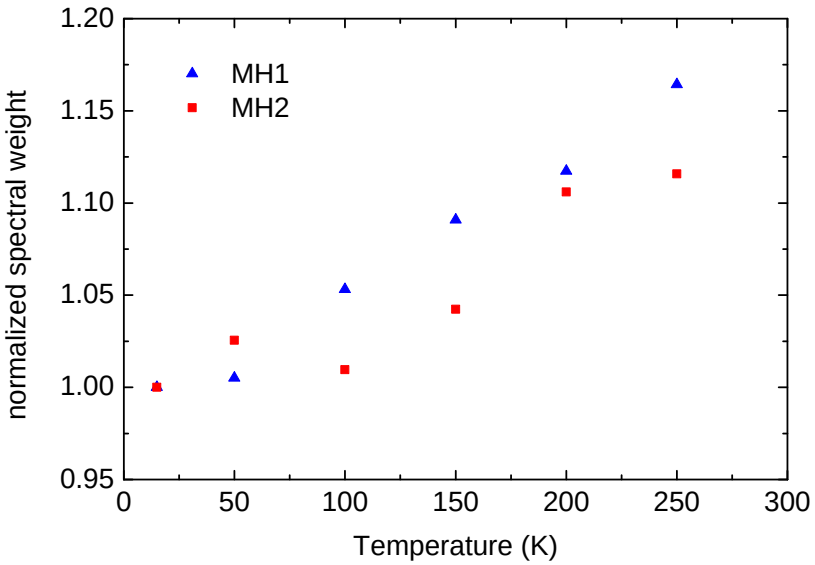

Figure 6.9: Temperature dependence of the normalized spectral weight of MH1 and MH2 in $\sigma_1^a(\omega)$ of $LaSrFeO_4$.

rated from the higher-lying excitations by fitting ε_2^a in the range $0.75\,\text{eV} - 3.75\,\text{eV}$ simultaneously by an exponential function and a Gaussian oscillator (see Fig. 6.10). The former accounts for the CT band edge and its shift with temperature, the latter describes the remaining spectral weight below the CT edge. With this procedure an increase of the spectral weight of MH1 of merely 15 % between 15 K and 250 K has been found, see Fig. 6.9. Obviously, also this value has to be taken with care, since it depends strongly on the line shape assumed for the onset of the CT absorption band. In fact, the opposite trend is expected, namely a reduction of spectral weight with increasing temperature as the a axis lattice constant increases from 3.8709(1) Å to 3.8744(1) Å between 10 K and room temperature [69]. An increased $\text{Fe} - \text{O}$ distance should result in a reduction of the Fe $3d - \text{O}$ $2p$ overlap which in turn should reduce the spectral weight of both MH and CT excitations.

It has to be concluded that an accurate determination of the temperature dependence of the spectral weight of the MH excitations is a difficult task in $LaSrFeO_4$ due to the overlap with the much stronger CT excitations. A clear separation of strong CT excitations and weaker MH excitations is an obvious prerequisite in order to reliably determine the spectral weight of the latter. However, it can safely be concluded that the thermal expansion of the lattice has only a modest impact on the spectral weight of MH excitations below room temperature.

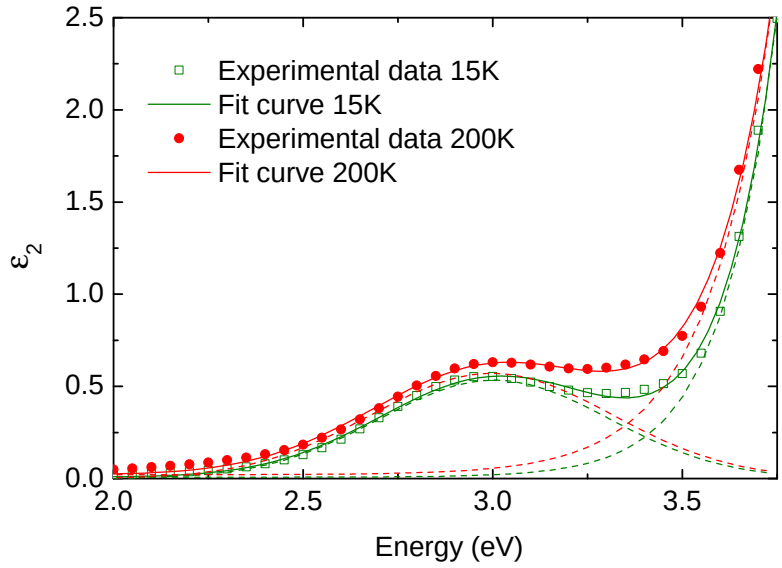

Figure 6.10: Solid lines: Fit of the excitation MH1 at 3.0 eV and of the CT band edge by using a Gaussian oscillator and an exponential function (depicted by dashed lines). The temperature dependence clearly is dominated by the change of the band edge.

Table 6.2: Parameters of the fit to the measured data with Gaussian oscillators (a axis). The center energy ω_0 and the FWHM Br of the Gaussian oscillators are defined in Sec. 3.1.5 in Eq. 3.24. Both parameters are given in eV. The effective carrier concentration N_{eff} of a Gaussian oscillator is introduced in Sec. 4.2.3 in Eq. 4.7.

a axis		MH1	MH2	CT1	CT2	CT3	background
	N_{eff}	0.042	0.062	0.058	0.14	1.05055	–
$T = 15\,\mathrm{K}$	ω_0	2.96	3.82	4.00	4.65	4.68	–
	Br	0.60	0.26	0.43	0.48	1.40	–
	N_{eff}	0.042	0.064	0.058	0.135	1.06	–
$T = 50\,\mathrm{K}$	ω_0	2.95	3.81	4.01	4.65	4.68	–
	Br	0.61	0.25	0.43	0.47	1.40	–
	N_{eff}	0.045	0.063	0.058	0.128	1.08	–
$T = 100\,\mathrm{K}$	ω_0	2.96	3.81	4.00	4.65	4.68	–
	Br	0.64	0.26	0.43	0.47	1.40	–
	N_{eff}	0.052	0.065	0.058	0.12	1.08	–
$T = 150\,\mathrm{K}$	ω_0	2.97	3.80	4.01	4.63	4.67	–
	Br	0.72	0.27	0.43	0.46	1.39	–
	N_{eff}	0.064	0.069	0.059	0.094	1.09	–
$T = 200\,\mathrm{K}$	ω_0	2.98	3.79	4.02	0.44	4.66	–
	Br	0.84	0.28	0.43	0.47	1.37	–
	N_{eff}	0.073	0.070	0.059	0.079	1.098	–
$T = 250\,\mathrm{K}$	ω_0	2.99	3.78	4.02	4.60	4.64	–
	Br	0.90	0.30	0.43	0.43	1.36	–

Table 6.3: Parameters of the fit to the measured data with Gaussian oscillators (c axis). See the caption of table 6.2 for the definition of the parameters.

c axis		MH1	MH2	CT1	CT2	CT3	background
$T = 15\,\mathrm{K}$	N_{eff}	–	–	0.059	0.78	0.12	461.85
	ω_0	–	–	4.03	4.89	5.02	10.42
	Br	–	–	0.43	1.09	0.38	7.62
$T = 50\,\mathrm{K}$	N_{eff}	–	–	0.059	0.78	0.11	9.96
	ω_0	–	–	4.02	4.89	5.02	10.42
	Br	–	–	0.43	1.08	0.37	7.62
$T = 100\,\mathrm{K}$	N_{eff}	–	–	0.059	0.76	0.12	9.96
	ω_0	–	–	4.02	4.88	5.02	10.42
	Br	–	–	0.43	1.06	0.37	7.62
$T = 150\,\mathrm{K}$	N_{eff}	–	–	0.059	0.74	0.11	9.96
	ω_0	–	–	4.02	4.88	5.01	10.42
	Br	–	–	0.43	1.05	0.39	7.62
$T = 200\,\mathrm{K}$	N_{eff}	–	–	0.059	0.75	0.096	9.96
	ω_0	–	–	4.02	4.89	4.99	10.42
	Br	–	–	0.43	1.04	0.38	7.62
$T = 250\,\mathrm{K}$	N_{eff}	–	–	0.059	0.75	0.084	9.96
	ω_0	–	–	4.02	4.88	4.96	10.42
	Br	–	–	0.43	1.03	0.39	7.62

6.4 Conclusion

We present a detailed analysis of the optical conductivity of layered $LaSrFeO_4$ for temperatures ranging from 15 K to 250 K in the frequency range from 0.5 eV to 5.5 eV by the use of spectroscopic ellipsometry in combination with transmittance measurements. We make use of infrared transmittance data from 0.5 eV to 2.5 eV to reliably determine the energy range with $\varepsilon_2 \approx 0$. This information is needed for the determination of the surface properties of the bulk single crystal, which have to be included in the modeling of the ellipsometric data.
A multipeak structure is observed in both $\sigma^a(\omega)$ and $\sigma^c(\omega)$, which we attribute to Mott-Hubbard and charge-transfer excitations. To disentangle both types of excitation, we take advantage of the anisotropy of the optical spectra. Due to the layered structure of $LaSrFeO_4$, Mott-Hubbard excitations are expected to contribute to $\sigma_1^a(\omega)$ only. A further tool to distinguish both types of excitations is their difference in spectral weight. We present a consistent assignment of all absorption bands. The data gives strong evidence that the lowest dipole-allowed excitation is of Mott-Hubbard type. This is against expectations at first sight, as the $3d^5$ electron configuration of Fe^{3+} is particularly stable due to the intra-atomic Hund exchange J_H. We argue that the lowest Mott-Hubbard excitation is pulled below the onset of the charge-transfer excitations because of Fe $3d-$O $2p$ hybridization and particularly the large splitting of the e_g orbital in the tetragonal structure, which partially compensates this large intra-atomic exchange contribution. These results are in agreement with recent studies of non-layered ferrites. Here, the splitting of the e_g level is absent which justifies the identification as charge-transfer insulators.
We further demonstrate that the spectral weight of the Mott-Hubbard excitations in $LaSrFeO_4$ shows only a weak dependence on temperature, which can be attributed to the fact that spin-spin and orbital-orbital correlations between nearest neighbors do not vary strongly below room temperature in this high-spin $3d^5$ compound with a Néel temperature of $T_N = 366$ K. This is in contrast to other transition-metal compounds such as RVO_3 (see Sec. 5) and $LaMnO_3/LaSrMnO_4$ [11,12], where pronounced changes of the nearest-neighbor spin-spin and/or orbital-orbital correlations lead to a strong temperature dependence of the spectral weight of the Mott-Hubbard excitations. However, a detailed analysis of the temperature dependence of the Mott-Hubbard excitations in $LaSrFeO_4$ turned out to be rather difficult due to the overlap with the much stronger charge-transfer excitations.

7 Ellipsometry on cobaltates

Cobaltates show a large number of interesting physical properties. The most prominent examples are unconventional superconductivity, that has been observed in two-dimensional CoO_2 layers if they are separated by a thick insulating layer of Na ions and H_2O molecules [136], and giant magnetoresistance, that has been reported for the mixed Co^{3+} and Ni^{3+} perovskite-type compound $(RE)Ni_{0.3}Co_{0.7}O_3$ [137]. The physics of cobaltates has further attracted a lot of research interest because of the spin-state issue, in particular the spin state of the Co^{3+} ions with $3d^6$ electron configuration in a cubic crystal field behaves as an additional degree of freedom. It has been shown that different spin states lie energetically close for a $3d^6$ electron configuration in an octahedral surrounding [35]. The crystal-field splitting $10\,Dq$ competes with the on-site Hund exchange. If the former is dominant, the nonmagnetic low-spin (LS) state ($S = 0,\ t_{2g}^6 e_g^0$) is realized, whereas the Hund exchange favors the magnetic high-spin (HS) state ($S = 2,\ t_{2g}^4 e_g^2$). Also the intermediate-spin (IS) state ($S = 1,\ t_{2g}^5 e_g^1$) has been discussed as a possible spin state of the Co^{3+} ions. It might become energetically favorable due to band-structure effects [24] or large distortions [138, 139]. The experimental observation of unexpected behavior of various physical parameters has often been attributed to a spin-state transitions of the Co^{3+} ions [25, 70, 140, 141].
Undoped $LaCoO_3$ shows a pseudocubic perovskite crystal structure. It can be characterized as a nonmagnetic insulator at low temperatures ($T \lesssim 25\,\mathrm{K}$), while the Sr-doped compounds $La_{1-x}Sr_xCoO_3$ are ferromagnets with a resistivity ρ that exhibits metallic behavior for doping concentrations $x \gtrsim 0.18$ [70]. The magnetic susceptibility of $LaCoO_3$ shows unusual behavior above $T \approx 25\,\mathrm{K}$, which has been discussed in terms of a thermal population of higher spin states from a LS ground state, the spin-state transition is absent in the Sr-doped compounds for doping concentrations $x \gtrsim 0.125$ [142]. In undoped $EuCoO_3$, the spin-state transition is shifted to a much higher temperature [25].
For the layered cobaltates $La_{2-x}Sr_xCoO_4$ and $La_{2-x}Ca_xCoO_4$ indications for both, a thermally-induced and a doping-induced spin-state transition are discussed in the literature (see references below).
The excitations across the band gap that are observed in optics are expected to be sensitive to the spin state of the Co^{3+} ions. As the cobaltates are classified into the group of charge-transfer (CT) insulators, the lowest electronic excitation has the form of an electron transfer from the oxygen $2p$ shell to the Co $3d$ shell [57, 143–145]. Whereas a LS Co^{3+} state fully blocks the excitation to the

Co^{3+} t_{2g} shell, CT excitations to the Co^{3+} t_{2g} shell should yield finite spectral weight in the case of a Co^{3+} HS configuration. A temperature-induced or doping-induced spin-state transition should therefore be well visible in optics. However, temperature-dependent reflectivity data of $LaCoO_3$ hardly vary across the spin-state transition [27].
A detailed doping- and temperature-dependent ellipsometric analysis of the optical conductivity of both, the pseudocubic perovskites $RCoO_3$ (R = rare earth ion) and the single-layered compounds $La_{2-x}Sr_xCoO_4$ and $La_{2-x}Ca_xCoO_4$ is still missing. Here, we present optical data of $LaCoO_3$, $EuCoO_3$, $La_{2-x}Sr_xCoO_4$ ($x = 0, 0.33, 0.45, 0.5, 0.9$), and $La_{1.5}Ca_{0.5}CoO_4$ for temperatures ranging from 15 K to 490 K. The data has been acquired by the use of ellipsometry for energies from 0.07 eV to 5.5 eV for $LaCoO_3$ and 0.75 eV to 5.5 eV (or 5.0 eV) for all other compounds. Applying optical investigations, we aim to shine further light on the hugely debated spin-state issue from a different point of view.
This chapter is organized as follows: In the first section the physics of cobaltates is briefly discussed, focusing in particular on the spin-state issue. The ellipsometric data is presented in the second section. Finally, a discussion of the results follows in the third section and the chapter ends with a conclusion.

7.1 The compounds

7.1.1 The compounds $LaCoO_3$ and $EuCoO_3$

Structural properties

$LaCoO_3$ crystallizes in a nearly cubic perovskite structure. A small rhombohedral distortion has been observed. Compared to the ideal cubic perovskite structure, the crystal is distorted along the [111] direction of the cubic unit cell [146]. The rhombohedral unit cell is twice as large as the cubic cell, the rhombohedral lattice constants run along the face diagonals [110] of the cubic cell, as can be seen in Fig. 7.1. The rhombohedral lattice parameters have been determined to be $\alpha_{rhom} = 60.8°$ and $a_{rhom} = 5.379$ Å [25], the lattice parameter a_{rhom} is related to the one of the cubic cell a_c by $a_{rhom} \approx \sqrt{2}a_c$. The space group of $LaCoO_3$ at room temperature has been determined to be $R\bar{3}c$ [25, 146–148]. Maris *et al.* [149] conclude from their high-resolution single-crystal x-ray diffraction data that $LaCoO_3$ shows a small monoclinic distortion, that could be induced by a collective Jahn-Teller effect for temperatures $20\,K \leq T \leq 300\,K$ and propose the subgroup $I2/a$ of $R\bar{3}c$. Kobayashi *et al.* [148] have shown that the rhombohedral distortion is reduced with increasing temperature, at about 1610 K a structural phase transition of second order is reported to take place with an adoption of the ideal cubic structure. Also the space group $R\bar{3}$ has been discussed for temperatures $T \gtrsim 650\,K$ [146,150]. However, the small distortions away from the cubic arrangement do not

play an important role for our optical investigations.
The substitution of the La^{3+} ions by the smaller Eu^{3+} ions leads to an increased chemical pressure. As a consequence, the cell volume is reduced by about 6 % (from 56 Å^3 in $LaCoO_3$ to 52.75 Å^3 in $EuCoO_3$) [25] and the symmetry is reduced to orthorhombic with space group *Pnma*. The lattice parameters of $EuCoO_3$ amount to $a = 5.370$ Å, $b = 5.255$ Å, and $c = 7.477$ Å [25].

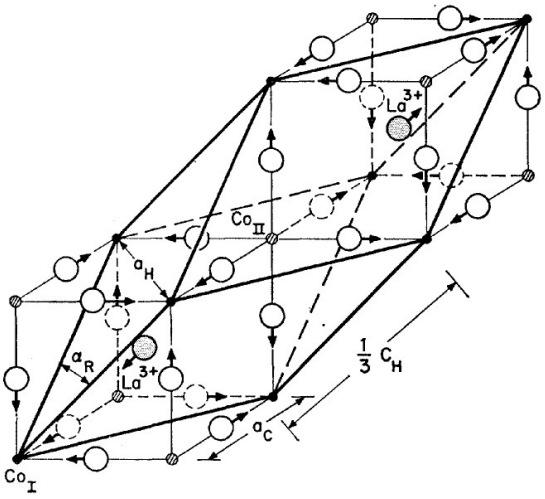

Figure 7.1: Rhombohedral unit cell of $LaCoO_3$. The parameter of a pseudocubic unit cell a_c, the parameters of a hexagonal unit cell a_H and c_H, and the rhombohedral angle α_R are marked. Taken from Ref. [146].

Magnetic and electrical properties

The electrical properties of $LaCoO_3$ and $EuCoO_3$ are determined by the open $3d$ shell of the Co^{3+} ion that comprises six electrons and is surrounded by an O^{2-} octahedron. The crystal field of the oxygen ions splits the $3d$ level into the lower lying t_{2g} orbitals and the higher lying e_g orbitals. See the discussion in Sec. 2.2.1 and Fig. 2.4.
In the ground state, $LaCoO_3$ and $EuCoO_3$ show insulating behavior. The resistivity $\rho(T)$ of $La_{1-x}Eu_xCoO_3$ is shown in Fig. 7.2. One observes an activation-type behavior $\rho \propto \exp(\Delta_{act}/T)$ below 400 K. The activation energy of $LaCoO_3$ amounts to $\Delta_{act} \simeq 1200\,\mathrm{K} \approx 0.1\,\mathrm{eV}/k_B$. Above $\backsimeq 400$ K a steep drop is observed in the resistivity curve of $LaCoO_3$, which is discussed in the literature in terms of an insulator-to-metal transition occurring at $T_{IM} \approx 480$ K [25, 27, 151]. The resistivity of $LaCoO_3$ above T_{IM} amounts to about 1 mΩ cm, which is characteristic for

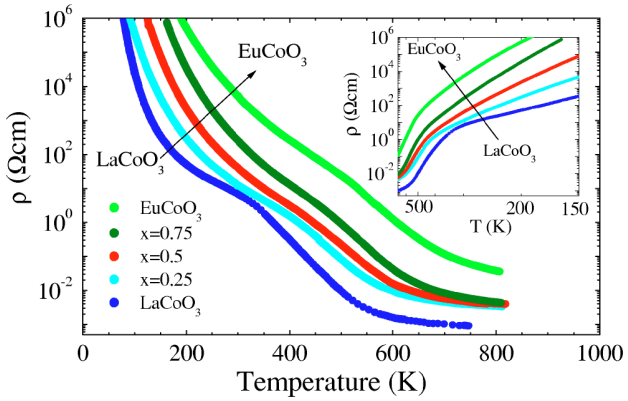

Figure 7.2: Electrical resistivity of $La_{1-x}Eu_xCoO_3$ as function of temperature for different values of the doping concentration x. The data on a reciprocal temperature scale is depicted in the inset. Taken from Ref. [25].

a fairly poor metal [25, 27, 70, 152–154]. For increasing Eu content the resistivity ρ is drastically enhanced. This can be explained by the increasing distortion of the crystal structure away from a cubic perovskite structure. The hopping probability of the charge carriers is reduced in $EuCoO_3$ due to the strong deviations of the $Co-O-Co$ bond angles from 180° [25]. As a consequence, the activation energy Δ_{act} of $EuCoO_3$ exceeds the one of $LaCoO_3$ by about a factor of 3 [25]. The insulator-to-metal transition is shifted to $T_{IM} \approx 600\,\mathrm{K}$ in $EuCoO_3$, the shift of T_{IM} is thus much less pronounced than the one of Δ_{act}. Further evidence for the insulator-to-metal transition in $LaCoO_3$ comes from optical conductivity data [27]. With increasing temperature, the absorption edge is significantly shifted to lower energies starting at around 400 K [27]. The insulator-to-metal transition in $LaCoO_3$ is also evident from anomalies in the specific heat and thermal expansion around T_{IM} [155, 156].

The magnetic susceptibility $\chi(T)$ of $La_{1-x}Eu_xCoO_3$ is depicted in Fig. 7.3. It shows quite unusual behavior. The increase of $\chi(T)$ towards lowest temperatures has been ascribed to magnetic impurities and/or oxygen nonstoichiometries [25, 147, 151, 157]. It is quite established that the nonmagnetic behavior of $LaCoO_3$ at low temperatures can be attributed to the Co^{3+} LS ground state (LS: $S = 0$, $t_{2g}^6 e_g^0$). The rise of the magnetic susceptibility above about 25 K and the maximum at about 100 K have been ascribed to a spin-state transition [25, 158]. The spin-state transition is not a phase transition in the thermodynamic sense [158]. Neither the thermal expansion nor the specific heat of $LaCoO_3$ show a pronounced anomaly at a specific temperature, they rather just show a broad Schottky-type anomaly [25, 158]. The spin-state transition corre-

sponds to a thermal population of higher spin states, the HS (HS: $S = 2$, $t_{2g}^4 e_g^2$) or the IS (IS: $S = 1$, $t_{2g}^5 e_g^1$) state, while the LS state stays the state of lowest energy. Also structural parameters are reported to change across the spin-state transition [141].
The maximum in $\chi(T)$ is continuously reduced and shifted to higher temperatures for increasing doping concentration x, indicating that the spin-state transition is shifted to a higher temperature in $EuCoO_3$. The enhanced crystal-field splitting in $EuCoO_3$ caused by the stronger chemical pressure is assumed to stabilize the LS state [25].
In the lower panel of Fig. 7.3 a background is substracted from the raw susceptibility data to focus on the Curie susceptibility of the Co^{3+} ions. One further observes a shoulder in the $\chi(T)$ data of $LaCoO_3$ around the metal-insulator transition. Like T_{IM} deduced from the $\rho(T)$ data this shoulder shifts to higher temperatures for increasing x [25]. However, compared to the significant shift of the spin-state transition temperature, the shift of T_{IM} is very moderate, indicating that the insulator-to-metal and the spin-state transition occur independently of each other [25].

The Co^{3+} spin-state issue of $LaCoO_3$

The spin state of the Co^{3+} ions has attracted researchers interest since the 1950s [159, 160]. As discussed in the introduction, the spin state of the $3d^6$ electron configuration of the Co^{3+} ions is subject to a competition between the crystal-field (CF) splitting Δ_{CF} between the t_{2g} and the e_g level and the on-site Hund exchange. The Tanabe-Sugano-Kamimura diagram of a d^6 system, which presents the energies of the different d^6 mulitplets in a cubic crystal field as a function of the crystal-field splitting, is depicted in Fig. 7.4 [35] (cf. Sec. 2.2.2). The state of lowest energy for a rather weak crystal field is the ${}^5T_{2g}$ multiplet ($S = 2$, $t_{2g}^4 e_g^2$), which is usually referred to as the HS state. It is 15-fold degenerate (5-fold spin and 3-fold orbital). For an increasing strength of the crystal field, the ${}^1A_{1g}$ multiplet ($S = 0$, $t_{2g}^6 e_g^0$) becomes lower in energy at some point. The ${}^1A_{1g}$ multiplet, which is not degenerate, is the so-called LS state. Another low-energy multiplet is the ${}^3T_{1g}$ multiplet ($S = 1$, $t_{2g}^5 e_g^1$), it is 9-fold degenerate (3-fold spin and 3-fold orbital) and is usually referred to as the IS state [35]. The ${}^3T_{2g}$ multiplet (3-fold spin and 3-fold orbital degeneracy) is another IS state ($S = 1$) with $t_{2g}^5 e_g^1$ electron configuration, but it lies higher in energy due to the Coulomb interaction. The LS, IS, and HS configurations are sketched in Fig. 7.5. According to the multiplet calculation of a $3d^6$ electron configuration in a cubic crystal field, the IS state can never be the ground state, see Fig. 7.4. This can be understood on the basis of the following simple argumentation. Assuming an energy loss of Δ_{CF} for each electron occupying the e_g level and an energy gain of J_H for each electron pair with parallel spins, the different spin configurations have the following energies:

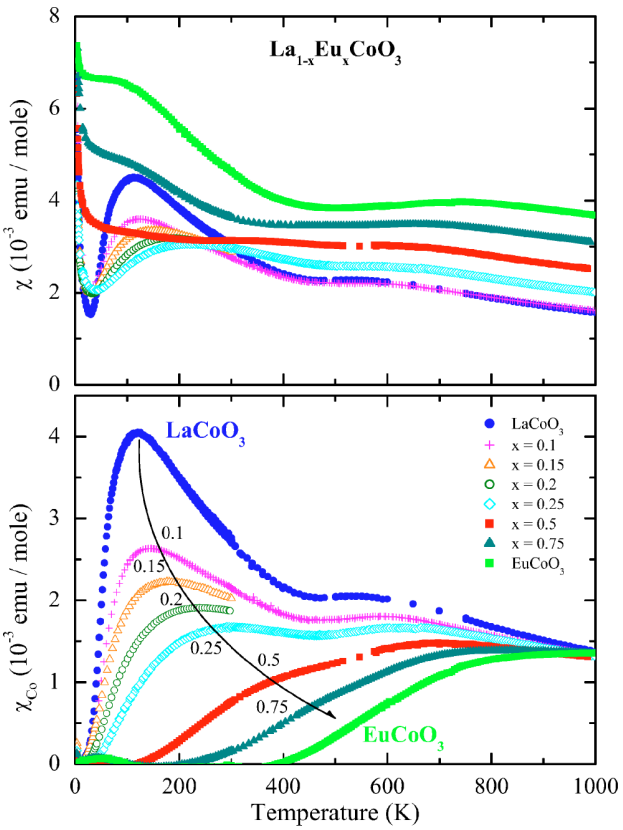

Figure 7.3: The upper panel shows the magnetic susceptibility of $La_{1-x}Eu_xCoO_3$. The contribution from the van Vleck susceptibility of the Eu^{3+} ions becomes more dominant with increasing doping concentration. The lower panel shows the susceptibility of the Co^{3+} ions. A background susceptibility has been substracted from the raw data that consists of a Curie-Weiss contribution caused by magnetic impurities and/or oxygen nonstoichiometry, the van Vleck susceptibility of both the Co^{3+} and the Eu^{3+} ions, and a contribution caused by the diamagnetism of the core electrons. Taken from Ref. [25].

$E_{LS} = -6J_H$, $E_{IS} = -7J_H + \Delta_{CF}$ and $E_{HS} = -10J_H + 2\Delta_{CF}$. Figure 7.6 shows the energies of the different multiplets as a function of Δ_{CF}/J_H in a purely ionic picture. However, in a realistic picture both effects, spin-orbit coupling and hybridization between the O $2p$ and the Co $3d$ bands, which are neglected in this simple ionic picture, might play an important role.
In agreement with crystal-field theory, early publications suggest a scenario of a thermal population of Co^{3+} HS states to explain the steep increase observed in

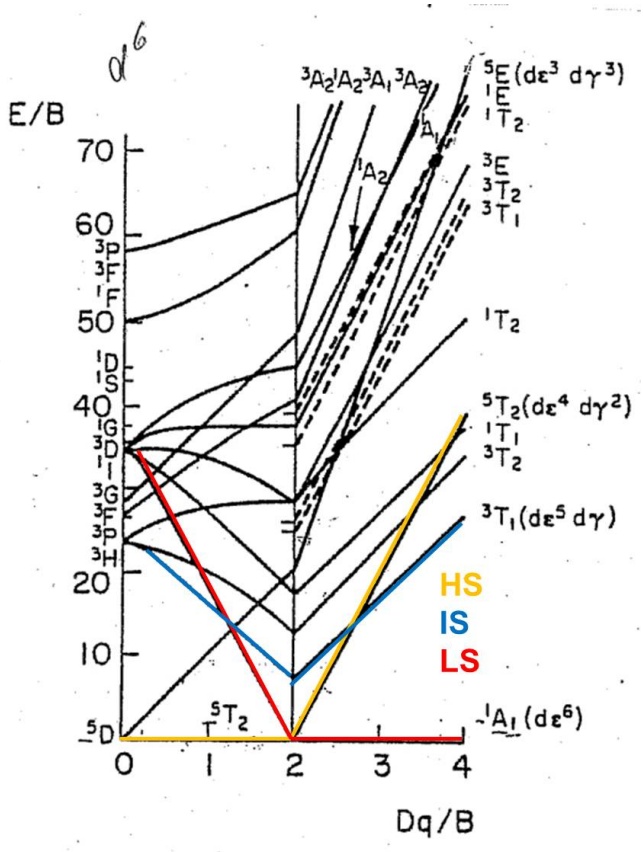

Figure 7.4: Tanabe-Sugano-Kamimura diagram of a d^6 system (cf. Sec. 2.2.2). The HS ($^5T_{2g}$), IS ($^3T_{1g}$), and LS ($^1A_{1g}$) states are marked in orange, blue, and red, respectively. Taken from Ref. [35].

the magnetic susceptibility $\chi(T)$ of $LaCoO_3$ starting at about 25 K. In this scenario the LS state remains the state of lowest energy [146, 151, 161–163]. In 1996, Korotin *et al.* [24] published local-density approximation plus Hubbard U band-structure calculations (LDA+U) that demonstrate that the hybridization between the Co e_g and O $2p$ levels may stabilize the IS state. However, e_g orbital ordering is needed in the IS state as this state is calculated to be a metal otherwise [24]. Many publications followed that attribute the spin-state transition to a thermal population of the IS state [149, 157, 164–166].
It has been pointed out by Zobel *et al.* [158] and Baier *et al.* [25] that particularly the magnetic susceptibility $\chi(T)$ of $LaCoO_3$ below T_{IM} can only be consistently described in a scenario assuming a thermal population of a state with a magnetic moment of 1, referred to as the IS state [25, 158]. The fit to the measured susceptibility data yields a g-factor of ≈ 2.2 and an energy splitting between the LS and the thermally populated state of approx. 180 K, the fit to the susceptibility data

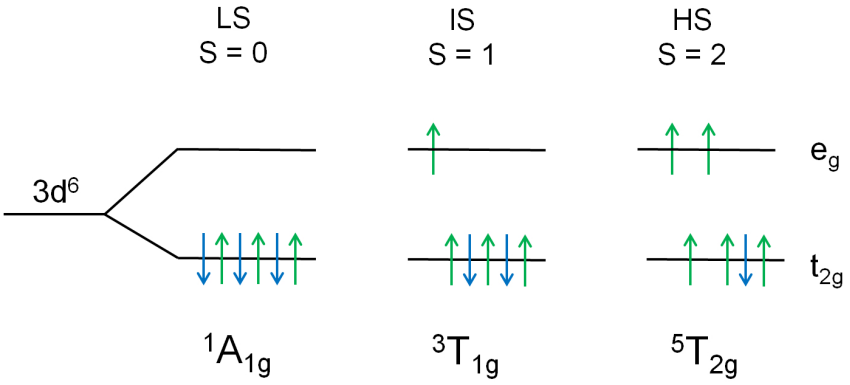

Figure 7.5: The low-spin (LS), intermediate-spin (IS), and high-spin (HS) $3d^6$ electron configuration of a Co^{3+} ion in a cubic crystal field. The $^1A_{1g}$, $^3T_{1g}$, and $^5T_{2g}$ multiplets are the lowest multiplets with spin $S = 0$, $S = 1$, and $S = 2$, respectively [35].

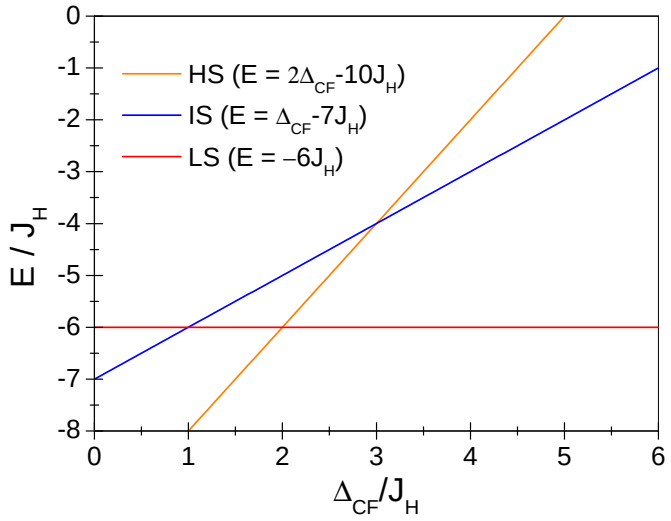

Figure 7.6: Sketch of the energies of the LS state ($^1A_{1g}$ multiplet with $S = 0$, $t_{2g}^6 e_g^0$), the IS state ($^3T_{1g}$ multiplet with $S = 1$, $t_{2g}^5 e_g^1$), and the HS state ($^5T_{2g}$ multiplet with $S = 2$, $t_{2g}^4 e_g^2$) as a function of the crystal-field splitting Δ_{CF} between the t_{2g} and the e_g level. The crystal field splitting is scaled by J_H.

of $EuCOO_3$ yields a energy splitting of approx. 2200 K [25]. A model assuming a thermal population of a state with a magnetic moment of 2 overestimates the experimentally observed value of $\chi(T)$ at 100 K significantly [25, 158]. In agreement with Korotin *et al.* [24], the populated IS state is found to show no orbital degeneracy. The lifting of the orbital degeneracy is attributed to the Jahn-Teller effect, which is active for partially filled e_g orbitals [25, 149, 158]. The susceptibility data of $EuCoO_3$ can be slightly better described with a model assuming an IS state which is three-fold orbital degenerate. As the spin-state transition occurs at a much higher temperature in $EuCoO_3$, it is speculated that the Jahn-Teller effect of the IS state is suppressed by thermal fluctuations and/or the elevated charge-carrier density above T_{IM} [25, 167]. Zobel *et al.* [158] and Baier *et al.* [25] further observe an interesting scaling behavior between the magnetic susceptibility $\chi(T)$ and the thermal expansion $\alpha(T)$ of $LaCoO_3$. They obtain a good description within a scenario of a thermal population of the IS state without orbital degeneracy. Figure 7.7 shows the result of Kriener [167] for the occupation number of the LS and the thermally populated IS state of $LaCoO_3$ and $EuCoO_3$ as a function of temperature. According to this simple calculation, the population of the IS state amounts to $\backsimeq 70\%$ in $LaCoO_3$ ($T_{IM} \backsimeq 480$ K), while it amounts to only $\backsimeq 7\%$ in $EuCoO_3$ ($T_{IM} \backsimeq 600$ K) at the metal-insulator transition temperature [25, 167]. For $T \to 1000$ K the magnetic susceptibility $\chi(T)$ approaches a similar value of 1.4×10^{-3} emu/mole for all doping concentrations x in $La_{1-x}Eu_xCoO_3$, indicating that the spin state at $T \gtrsim 1000$ K is independent of x [25].
Further evidence for a thermal population of the IS state comes from infrared spectroscopy on $LaCoO_3$ [157]. An anomalous splitting of the phonon modes and a variation of their intensity has been reported to occur with the spin-state transition. It has been attributed to a Jahn-Teller splitting of the e_g orbitals, which is characteristic for the IS state [157]. Changes of the phonon modes across the spin-state transition, that have been attributed to a collective Jahn-Teller effect of the IS states, have also been detected in Raman spectroscopy [164]. Indications for a Jahn-Teller distortion come further from the analysis of powder and single crystal x-ray diffraction data. An alternation of short and long $Co-O$ bonds in the ab plane has been observed giving evidence for orbital ordering [149]. As the distortions increase with temperature, it has been concluded that a thermal activation of the IS state takes place. Also a pair density function analysis of pulsed neutron data give evidence for a Jahn-Teller effect characteristic for an IS state [165]. In addition, the thermal expansion $\alpha(T)$ of $LaCoO_3$ gives clear evidence for the population of higher spin states starting at $T \approx 25$ K. The anomalous increase above 25 K can be attributed to increasing $Co-O$ distances coming along with the population of e_g levels [25, 158]. Saitoh *et al.* [166] perform a cluster-model analysis of their photoemission and x-ray absorption data and obtain the best description within a scenario of thermally populated IS states from a LS ground state.

Soft x-ray absorption spectroscopy (XAS) and magnetic circular dichroism (MCD) studies performed by Haverkort *et al.* [26] have changed the discussion of the spin-state issue considerably. They seem to solve the spin-state issue of $LaCoO_3$. A good description of the data is obtained by the use of a configuration-interaction cluster model within a scenario of an inhomogeneous mixture of LS and thermally excited HS states. The model accounts for spin-orbit coupling and includes the full atomic multiplet theory and hybridization between Co $3d$ and O $2p$ bands. The effective activation energy from the LS to the HS state is found to change with temperature, it increases from 20 meV $\approx 230\,\mathrm{K}\cdot k_B$ at 50 K to 80 meV $\approx 930\,\mathrm{K}\cdot k_B$ at 650 K. This leads to a significantly reduced population of the HS state at higher temperatures. Consequently, the difference in occupation numbers of higher spin states between $LaCoO_3$ and $EuCoO_3$ at the metal-insulator transition is not as drastic as in the LS/IS scenario with fixed activation energy as assumed in Fig. 7.7. Haverkort *et al.* [26] point out that spin-orbit coupling plays an important role in $LaCoO_3$. The spin-orbit coupling partly lifts the 15-fold degeneracy of the HS state. The resulting states of different energy have a pseudo total momentum of $\tilde{\mathrm{J}}$=1, 2, or 3, where the triplet with $\tilde{\mathrm{J}}$= 1 has the lowest energy. This state has $L_z = 0.6$ and $S_z = 1.3$. Haverkort *et al.* [26] emphasize that it is consequently not surprising that this three-fold degenerate HS state with S_z close to one has been wrongly identified with the IS state within many investigations. Haverkort *et al.* [26] strictly rule out the IS state scenario because it is incompatible with the large orbital momentum deduced from the MCD data. Also electron spin resonance data [168,169] and inelastic neutron scattering data [170] give clear evidence that the lowest-energy excited state from the LS ground state is the spin-orbit split triplet of ${}^5T_{2g}$. A g-factor of approx. $3-3.5$ is found, which cannot be ascribed to an IS state. This finding is in disagreement with the result of Zobel *et al.* [158] and Baier *et al.* [25], who deduced a g-factor of approx. 2.2 from the fit to their susceptibility data. However, the susceptibility data can well be described within a scenario of g-factor of approx. $3-3.5$ and a thermal population of the spin-orbit split HS state with a magnetic moment of 1, when a temperature-dependent activation energy is assumed. Also various other experimental findings can be well explained within this picture. The fit to the XAS and MCD data of Haverkort *et al.* [26] yields a larger $10\,Dq$ for the LS Co^{3+} sites ($10\,Dq = 0.7$ eV) than for the HS sites ($10\ Dq = 0.5$ eV). This confirms the finding of Zobel *et al.* [158] of the anomaly of the coefficient of thermal expansion at the spin-state transition. Furthermore, a recent combined extended x-ray absorption fine structure and neutron pair distribution function analysis performed by Sundararm *et al.* [171] confirms the LS/HS scenario. Sundararm *et al.* [171] conclude from their analysis that the Jahn-Teller distortions of $LaCoO_3$ reported in Ref. [149], that led the authors of Ref. [149] to the conclusion of an IS state scenario, can only be small.

In conclusion, it has to be pointed out that many publications assigned the spin-state transition to a thermal population of the IS state instead of the HS state

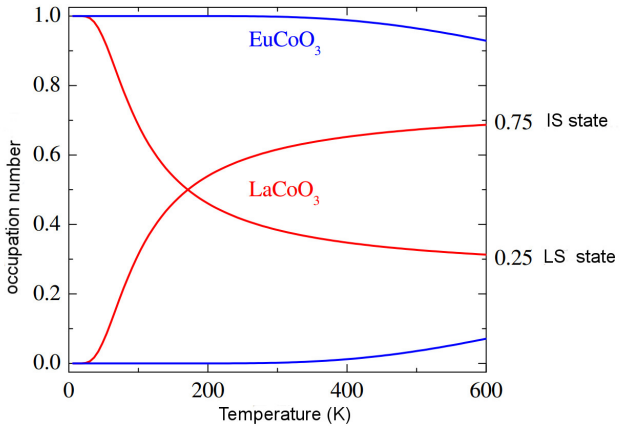

Figure 7.7: Calculated occupation numbers of the LS and IS state for $LaCoO_3$ (red) and $EuCoO_3$ (blue) as a function of temperature by Kriener [167]. The curves have been calculated by use of the thermodynamic distribution function assuming an energy splitting between the LS and the IS state of approx. 200 K for $LaCoO_3$ and approx. 2300 K for $EuCoO_3$. Taken from Ref. [167].

from the LS ground state. They assumed the activation energy to be independent of temperature. If one allows for a temperature dependent activation energy, the experimentally observed behavior of the magnetic susceptibility can well be described within the LS/HS scenario. Furthermore, various publications such as, e.g., Refs. [157, 164] come to the conclusion of a thermal population of the IS state based on their observation of individual Jahn-Teller distorted octahedra. However, these interpretations have to be regarded with care. A distinction between a scenario of individual Jahn-Teller distorted octahedra or a scenario consisting of a mixture of larger HS (which might also be distorted to some extend) and smaller LS octahedra might be challenging.

Metal-insulator transition of $La_{1-x}Eu_xCoO_3$

As obvious from both, electrical resistivity data and optical conductivity data, $LaCoO_3$ shows an insulator-to-metal transition at around 480 K [25, 27]. As opposed to the spin-state transition, the metal-insulator transition is a real phase transition in the thermodynamic sense, as being revealed by an anomaly in the specific heat around T_{IM} [155]. With increasing x in $La_{1-x}Eu_xCoO_3$, the shift of the metal-insulator transition to higher temperatures is much less pronounced than the shift of the spin-state transition [25]. This indicates that both transitions occur independently of each other and the metal-insulator transition is not affected by the population of higher spin states of the Co^{3+} ions [25]. Its origin

is still discussed controversially. Many different scenarios have been proposed. Korotin *et al.* [24] attributed the spin-state transition to a thermal population of IS states with e_g orbital ordering on the basis of their LDA+U calculations and proposed that the insulator-to-metal transition at around 480 K in $LaCoO_3$ can be attributed to a melting of this orbital order. The resulting IS state without orbital order is calculated to be a metal [24]. In the LS/IS scenario, a melting of the Jahn-Teller distortion in the metallic phase which re-establishes the orbital degeneracy of the IS state could also explain the enhanced susceptibility close to T_{IM} [25, 158, 167]. It has furthermore been suggested that ferromagnetic (FM) correlations above T_{IM} are responsible for the observed increase of $\chi(T)$ at the metal-insulator transition [25, 27]. This has been proposed in analogy to hole-doped $La_{1-x}Sr_xCoO_3$, where the ground state can be characterized as being metallic with FM correlations for doping concentrations $x \gtrsim 0.18$ [70]. However, the Co^{3+} compound $LaCoO_3$, although showing more or less metallic behavior above T_{IM}, is hardly comparable to the mixed Co^{3+} and Co^{4+} compounds, where the ferromagnetism has been explained by a double exchange between Co^{3+} and Co^{4+} ions. Other explanations for the rise of the magnetic susceptibility close to T_{IM} include scenarios that are based on three different spin-states [141, 166, 172]. A population of the IS state at the spin-state transition and the HS state around the metal-insulator transition has been proposed [172]. A good description of $\chi(T)$ within these scenarios requires a temperature dependence of the energies of the IS and the HS state [172]. A comparison between temperature-dependent optical conductivity data of $LaCoO_3$ and doping dependent optical conductivity data of $La_{1-x}Sr_xCoO_3$ reveals a strong similarity [27]. The authors of Ref. [27] thus suggest, that the thermally induced insulator-to-metal transition can be characterized as a Mott transition of a correlated electron system [27,152]. Various other scenarios have been proposed to explain the metal-insulator transition, e.g. the closing of the energy gap between the occupied t_{2g} states and unoccupied e_g states [173], or a thermal population of e_g states. The latter has been suggested on the basis of the observation of an increasing $Co-O$ bond length around T_{IM} [146].

7.1.2 The compounds $La_{2-x}Sr_xCoO_4$ and $La_{2-x}Ca_xCoO_4$

Structural properties

The compounds $La_{2-x}Sr_xCoO_4$ and $La_{2-x}Ca_xCoO_4$ crystallize in the single-layered K_2NiF_4-type perovskite structure. An orthorhombic distortion away from the tetragonal K_2NiF_4-type structure has been observed already at room temperature for the parent compound La_2CoO_4 The orthorhombic unit cell of La_2CoO_4 is depicted in Fig. 7.8. The degree of orthorhombic distortion can be reduced by hole doping. Cwik [42] has shown that it is fully suppressed at room temperature beyond a doping concentration of $x = 0.3$ in the compounds $La_{2-x}A_xCoO_4$ with

A = Ca, Sr, or Ba. The orthorhombic distortion can be described by a rotation and tilting of the corner-sharing CoO_6 octahedra, which is due to an ionic size mismatch. The phase-transition temperature from the high-temperature tetragonal (HTT) phase with space group *I4/mmm* to the low-temperature orthorhombic (LTO) phase with space group *Bmab* decreases upon increasing doping concentration x. The Sr-doped compound $La_{1.7}Sr_{0.3}CoO_4$, for instance, enters the LTO phase only below 227 K [174], while the half-doped compound $La_{1.5}Sr_{0.5}CoO_4$ is reported to retain its tetragonal structure down to lowest temperatures [175]. Indications for a phase transition into a new low-temperature tetragonal phase (LTT) taking place at $T = 135$ K have been reported by Ref. [176] for the parent compound La_2CoO_4, whereas no indications for a LTT phase have been found for $La_{1.7}Sr_{0.3}CoO_4$ in Ref. [42]. The observed behavior of the doped cobaltates is very similar to the phase diagram of the isostructural compounds $La_{2-x}Sr_xNiO_4$ and $La_{2-x}Sr_xCuO_4$.
The lattice parameters of the compounds relevant for this work are summarized in table 7.1.

Magnetic and electrical properties

Let us now focus on the magnetic properties of $La_{2-x}Sr_xCoO_4$ and $La_{2-x}Ca_xCoO_4$. The parent compound La_2CoO_4 is an antiferromagnetic (AFM) insulator with $T_N = 275$ K [176], similar to the isostructural compounds La_2CuO_4 and La_2NiO_4. A sketch of the spin arrangements in the CoO_2 planes of La_2CoO_4 as proposed by Cwik [42] is shown in Fig. 7.9. The spins show an AFM nearest-neighbor coupling within the CoO_2 planes with a spin moment that lies within the planes. Short-range AFM spin order has been reported to set in below ~ 130 K in $La_{1.7}Sr_{0.3}CoO_4$ [42]. The spin correlations in $La_{1.7}Sr_{0.3}CoO_4$ are similar to the arrangements observed in the parent compound La_2CoO_4. Commensurate spin order is not lost in the compound with the relative high doping concentration of $x = 0.3$ [42]. In contrast, commensurate spin order is destroyed already at a doping concentration of $x = 0.024$ and $x = 0.135$ in $La_{2-x}Sr_xCuO_4$ and $La_{2-x}Sr_xNiO_4$, respectively [177–179]. The high stability of the AFM ordered phase observed in $La_{2-x}Sr_xCoO_4$ is believed to be a consequence of the high charge localization being reflected in the high electrical resistivity [28] (see below).

Further hole doping beyond $x > 0.3$ suppresses long-range magnetic order and a spin-glass phase is realized at low temperatures [42]. For doping levels $x > 0.3$ short-range incommensurate spin ordering has been observed [42]. The incommensurate modulation vector increases nearly linearly with the doping concentration x. This is similar to the case of doped cuprates and nickelates. The linear dependence has been attributed to a stripe phase, i.e. the doping induced TM^{3+} ions (TM = Cu, Ni, Co) are grouped into stripes that separate the AFM ordered spins of the TM^{2+} ions. While the stripe ordering is lost above a Sr concentration as low

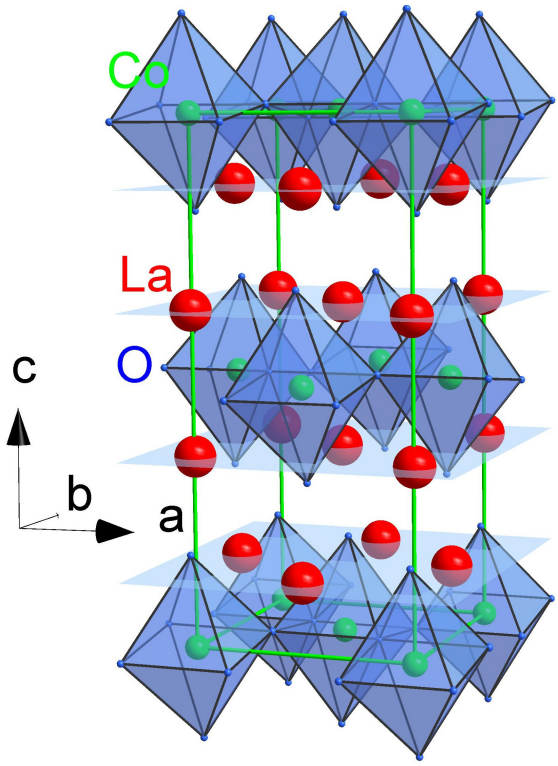

Figure 7.8: Orthorhombic unit cell of La_2CoO_4 at room temperature (space group *Bmab*). Compared to the tetragonal layered perovskite structure (space group *I4/mmm*), the CoO_6 octahedra are tilted and rotated. Taken from Ref. [42].

doping x	a (Å)	b(Å)	c(Å)	space group	Ref.
0	5.521(3)	5.486(3)	12.631(5)	*Bmab*	[30]
0.3	3.8556(1)	3.8556(1)	12.6499(5)	*I4/mmm*	[42]
0.45	3.8458(1)	3.8458(1)	12.5934(2)	*I4/mmm*	[42]
0.5 (Sr)	3.8392(1)	3.8392(1)	12.5345(5)	*I4/mmm*	[42]
0.5 (Ca)	3.8299(1)	3.8299(1)	12.3949(3)	*I4/mmm*	[42]
0.9	3.8109(1)	3.8109(1)	12.4837(2)	*I4/mmm*	[42]

Table 7.1: Lattice parameters of $La_{2-x}Sr_xCoO_4$ and $La_{1.5}Ca_{0.5}CoO_4$ at room temperature as deduced by Cwik [42] (for $x > 0$) from x-ray diffraction data on single crystals.

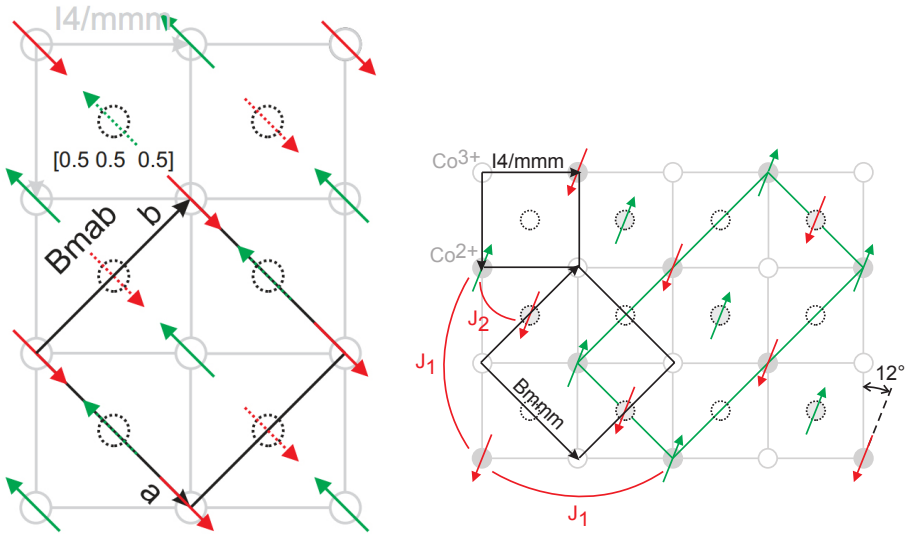

Figure 7.9: Left panel: Spin-ordering pattern of La_2CoO_4 in *Bmab* notation. Dashed circles indicate Co^{2+} ions of an adjacent CoO_2 layer. Right panel: Spin-ordering and checkerboard charge-ordering pattern of magnetic Co^{2+} and nonmagnetic Co^{3+} ions within the *ab* plane of the tetragonal unit cell (in *I4/mmm* notation) of $La_{1.5}Sr_{0.5}CoO_4$ as proposed by Cwik [42]. The positions of the Co ions in the adjacent CoO_2 layer are indicated by dashed circles. The symmetry of the charge-order unit cell is *Bmmm*, the magnetic unit cell is shown in green. The in-plane and out-of-plane AFM exchange couplings are denoted by J_1 and J_2, respectively. Both figures are taken from Ref. [42].

as ≈ 0.14 in the cuprates, it persists up to a Sr concentration of ≈ 0.6 and ≈ 0.5 in layered cobaltates and nickelates, respectively [174, 178–180]. In $La_{2-x}Sr_xNiO_4$ and $La_{2-x}Sr_xCuO_4$ the stripe phase is reported to be most stable near $x = 1/3$ and $x = 1/8$, respectively [178, 179]. In the cobaltates, the half-doped compound $La_{1.5}Sr_{0.5}CoO_4$ exhibits the most robust charge and spin order with a maximum in the spin- and charge-order correlation lengths ($\xi_{ab}^{charge} \approx 26\,\text{Å}$, $\xi_c^{charge} \approx 8\,\text{Å}$, and $\xi_{ab}^{spin} \approx 70\,\text{Å}$, $\xi_c^{spin} \approx 10\,\text{Å}$) and the highest spin-freezing temperature ($T_S \approx 30\,\text{K}$) [174, 181]. For $x = 0.5$ the Co^{2+} and Co^{3+} ions show a checkerboard-like ordering pattern. Short-range checkerboard-like charge ordering is reported to set in below $T_C = 825\,\text{K}$ [175]. The charge-ordering temperature $T_C = 825\,\text{K}$ of $La_{1.5}Sr_{0.5}CoO_4$ is extremely high compared to similar systems, e.g. charges order at $T_C = 217\,\text{K}$ in $La_{0.5}Sr_{1.5}MnO_4$ [182] and $T_C = 480\,\text{K}$ in $La_{1.5}Sr_{0.5}NiO_4$ [180]. The huge difference between the charge-ordering temperature and the spin-ordering temperature in $La_{1.5}Sr_{0.5}CoO_4$ suggests that both phenomena are independent of each other [181].

The magnetic ordering in $La_{1.5}Sr_{0.5}CoO_4$ has been reported to be nearly commensurate, Fig. 7.9 depicts a sketch of the spin-order and charge-order arrangement that has been proposed by Cwik *et al.* [42,174]. They conclude from their neutron scattering data a pattern of ordered $S = 3/2$ Co^{2+} HS ions and nonmagnetic Co^{3+} ions. The magnetic Co^{2+} ions are claimed to show an effective AFM coupling via next-nearest neighbor bonds $Co^{2+} - O - Co^{3+} - O - Co^{2+}$ and a weak coupling between nearest Co^{2+} neighbors of adjacent CoO_2 layers. The phase diagram of $La_{2-x}Sr_xCoO_4$ as obtained by Cwik *et al.* [174] is shown in Fig. 7.10.
Checkerboard-like charge order has also been observed in the half-doped Ca compound $La_{1.5}Ca_{0.5}CoO_4$ with correlation lengths that are five times longer ($\xi_{ab}^{charge} \approx 115\,\text{Å}$ and $\xi_c^{charge} \approx 59\,\text{Å}$) than in the Sr-doped counterpart [183]. In addition, $La_{1.5}Ca_{0.5}CoO_4$ shows long-range magnetic order below $T_S \approx 50\,\text{K}$ [184] (or $T_S \approx 8\,\text{K}$ according to Ref. [30]) with correlation length $\xi_{ab}^{spin} = 195\,\text{Å}$ and $\xi_c^{spin} = 22\,\text{Å}$. Horrigane *et al.* [184] explain their neutron scattering data on $La_{1.5}Ca_{0.5}CoO_4$ by a magnetic four-domain model, considering two types of AFM ordering patterns and a twin structure of their single crystal.
The in- and out-of-plane resistivities ρ_{ab} and ρ_c of $La_{2-x}Sr_xCoO_4$ as obtained by Benomar *et al.* [185] for $0.4 \leq x \leq 0.8$ are shown in Fig. 7.11. La_2CoO_4 and $LaSrCoO_4$ are categorized into the group of CT insulators. $La_{2-x}Sr_xCoO_4$ shows insulating or semiconducting behavior at least for doping concentrations $0.0 \leq x \leq 1.5$ [186]. For $0.4 \leq x \leq 0.7$ it shows insulating behavior with an activation energy of $\sim 500\,\text{meV}$ ($\approx 5800\,\text{K}\cdot k_B$). The highest magnitude of ρ_{ab} is observed for the half-doped compound, ρ_{ab} is significantly reduced beyond a doping concentration of $x = 0.7$. It has to be pointed out that the magnitude of ρ_{ab} in $La_{2-x}Sr_xCoO_4$ is significantly larger than in various isostructural compounds (e.g. an activation energy of $\sim 70\,\text{meV}$ has been reported for $LaSrMnO_4$ [126]). The highly insulating behavior can be explained by the spin-blockade mechanism which is active in $La_{2-x}Sr_xCoO_4$. It is discussed in the next section (Sec. 7.1.2) together with the spin-state degree of freedom of the Co^{3+} ion.

The Co^{3+} spin-state issue of $La_{2-x}Sr_xCoO_4$ and $La_{2-x}Ca_xCoO_4$

The layered cobaltates $La_{2-x}Sr_xCoO_4$ and $La_{2-x}Ca_xCoO_4$ contain both, Co^{3+} ions with electron configuration $3d^6$ and Co^{2+} ions with electron configuration $3d^7$ in a ratio of $x/(1-x)$. While it is well established that the $3d^7$ configuration of the Co^{2+} ions shows the HS electron configuration ($S = 3/2$, $t_{2g}^5 e_g^2$, the lowest HS state corresponds to the $^4T_{1g}$ multiplet in cubic symmetry) [28,29,139], see Fig. 7.53 on page 198, the spin state of the Co^{3+} $3d^6$ ions is widely disputed. The HS, IS, and LS electron configuration of a Co^{3+} ion in a tetragonal crystal field is depicted in Fig. 7.54 on page 199. The Co^{3+} spin state of the mixed $Co^{2+} - Co^{3+}$ compounds $La_{2-x}Sr_xCoO_4$ and $La_{2-x}Ca_xCoO_4$ has been extensively investigated.

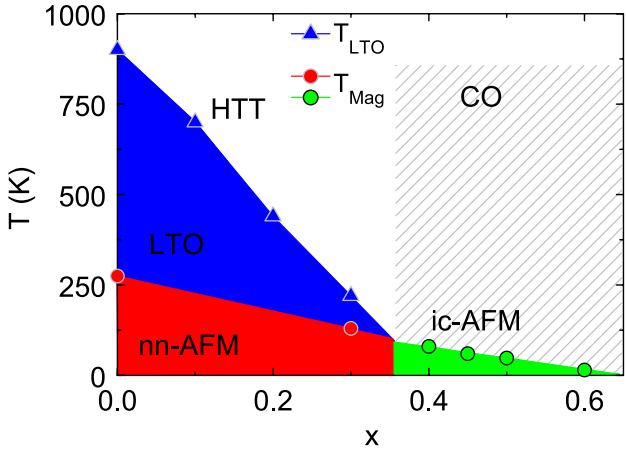

Figure 7.10: Phase diagram of $La_{2-x}Sr_xCoO_4$ as proposed by Cwik *et al.* [174]. Taken from Ref. [174].

Wang *et al.* [31] propose that there are two doping-induced spin-state transitions in $La_{2-x}Sr_xCoO_4$ in the doping range $0.0 < x < 1.1$ on the basis of their unrestricted Hartree-Fock calculations. According to Ref. [31] an AFM HS state is realized for $x < 0.39$ which transforms into a FM HS state for $x > 0.39$, while an HS/LS ordered state is proposed to set in at $x = 0.52$.
In the framework of their neutron scattering study on $La_{1.5}Sr_{0.5}CoO_4$ revealing $Co^{2+} - Co^{3+}$ checkerbord-like charge order, Zaliznyak *et al.* [175, 181] proposed that the Co^{3+} ions in the half-doped Sr compound are in an IS state which is nonmagnetic due to quenching by strong planar anisotropy. This is in contrast to more elaborate neutron scattering studies performed by Cwik [42]. He finds alternating smaller $Co^{3+}O_6$ and larger $Co^{2+}O_6$ octahedra, the $Co^{3+}O_6$ octahedra are found to be not Jahn-Teller active. He proposes the Co^{3+} LS state to be realized in $La_{1.5}Sr_{0.5}CoO_4$ at room temperature. Horigane *et al.* [183], who detected the checkerboard-like $Co^{2+} - Co^{3+}$ charge ordering in $La_{1.5}Ca_{0.5}CoO_4$ by the use of neutron and resonant x-ray scattering, suggested a mixed IS/HS state of the Co^{3+} ions in the half-doped Ca compound with the help of their fluorescence spectra and magnetic susceptibility data. Indications for magnetic scattering intensities that may originate from Co^{3+} spin order are found in elastic neutron diffraction data [184]. The authors of Ref. [184] thus propose that the Co^{3+} ions realize the magnetic HS state in $La_{1.5}Ca_{0.5}CoO_4$.
Moritomo *et al.* [28] study the spin-state properties of $La_{2-x}Sr_xCoO_4$ ($0.4 \leq x \leq 1.0$) by measuring magnetic and transport properties in the temperature range from 100 K to 300 K and applying a Curie-Weiss analysis of the magnetic susceptibility. While they confirm that the Co^{2+} ions are in a HS state, they claim that

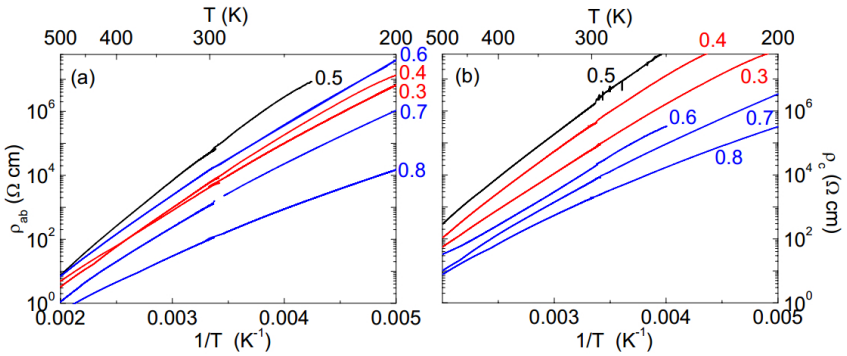

Figure 7.11: Arrhenius plot of the DC electrical resistivity of $La_{2-x}Sr_xCoO_4$. The in-plane component ρ_{ab} of the resistivity is shown in (a), the out-of-plane component ρ_c is shown in (b). The experimental data have been acquired by Benomar [185]. Taken from Ref. [42].

a spin-state transition takes place on the Co^{3+} ions from the HS ($x \leq 0.6$) to the IS state ($x \geq 0.8$) [28]. Their claim is based on the fact that the effective magnetic moment drops from $3.4\,\mu_B$ to $2.6\,\mu_B$ with increasing doping level x beyond $x = 0.7$, at the same time they observe a significant decrease of the Weiss temperature and the in-plane resistivity ρ_{ab} (at 400 K) [28]. They point out that the Co^{3+} IS state supports the e_g electron transfer between Co^{3+} and Co^{2+} and thereby triggers a FM superexchange in competition with the original AFM superexchange, which explains the reduction of the Weiss temperature. NMR measurements support this result [187].
However, Hollmann *et al.* [188] question the results of Moritomo *et al.* [28] as they claim that the application of a Curie-Weiss analysis is not appropriate in the compounds $La_{2-x}Sr_xCoO_4$ with rather strong spin-orbit coupling. They investigate the spin state of $La_{2-x}Sr_xCoO_4$ ($0.5 \leq x \leq 0.8$) by the use of magnetic susceptibility data for temperatures up to 1000 K together with a multiplet calculation [29]. In agreement with Moritomo *et al.* [28], their data support the HS state for Co^{2+} ions. But they conclude from the observed anisotropy and temperature dependence that the Co^{3+} ions are in the LS state at low temperatures, while higher spin states are thermally populated at higher temperatures. The excited states are either HS or IS states, both states cannot be distinguished by the use of magnetic susceptibility data. The activation energy between the spin states is determined to be around 2000 K. This is much higher than the activation energy reported for the pseudocubic compound $LaCoO_3$. This is in agreement with structural data. For $LaCoO_3$ the $Co-O$ bond length has been determined to be 1.91 Å, whereas the in-plane bond length of the Co^{3+} ions in $La_{1.5}Sr_{0.5}CoO_4$ is reported to be only 1.89 Å [42]. The increased crystal field in the layered compound is thus expected to

stabilize the LS state. The temperature dependence of the infrared-active phonon modes in $La_{1.5}Sr_{0.5}CoO_4$ and $La_{1.5}Ca_{0.5}CoO_4$ detected by Lee *et al.* [32] also gives evidence for a population of higher spin states above $T \approx 400\,\mathrm{K}$ and $T \approx 600\,\mathrm{K}$ for the Sr-doped and Ca-doped compound, respectively. Taking into account structural data of Refs. [42,181,181], which exhibit a huge increase of the c-axis lattice constant above 400 K, Lee *et al.* [32] conclude that the populated state is the IS state as the e_g^1 electron configuration favors an elongation of the CoO_6 octahedra. The susceptibility data of Hollmann *et al.* [188] at lower temperatures ($T < 400\,\mathrm{K}$) for $0.3 \leq x \leq 0.8$ indicate that the ground state of Co^{3+} must be the LS state at least for $x \geq 0.4$. The structural data acquired by Cwik [42] reveal a spectacular drop of the c-axis lattice parameter beyond $x = 0.45$ in $La_{2-x}Sr_xCoO_4$, which is due to a decrease of the elongation of the CoO_6 octahedra. It is attributed to a doping-induced spin-state transitions from a HS Co^{3+} to a LS Co^{3+} state.
Wu and Burnus [139] use local spin density approximation plus Hubbard U calculations (LSDA+U) to shed light on the controversies regarding the spin state of Co^{3+} in $La_{1.5}Sr_{0.5}CoO_4$. For their calculations they made use of the structural data reported in Ref. [42] and included also spin-orbit coupling and the multiplet effect. Their analysis strongly suggests that Co^{3+} realizes the LS state, in agreement with Hollmann *et al.* [188]. An IS configuration lies higher in energy by 122 meV ($\approx 1400\,\mathrm{K} \cdot k_B$) and further gives rise to strong in-plane FM correlations and an out-of-plane magnetism, both in strong disagreement with experimental observations [188]. Also the HS Co^{3+} state lies higher in energy by 310 meV ($\approx 3600\,\mathrm{K} \cdot k_B$) and it can further be ruled out as it would result in strong HS Co^{3+} – HS Co^{2+} AFM coupling, in disagreement with the observed spin freezing temperature of $T_S \approx 30\,\mathrm{K}$.
These findings are also strongly supported by an x-ray absorption spectroscopy study performed by Chang *et al.* [189]. They demonstrate that the Co^{3+} LS state must be realized in $La_{1.5}Sr_{0.5}CoO_4$, both at room temperature and below the spin freezing temperature. They furthermore show that a scenario of charge-ordered HS Co^{2+} and LS Co^{3+} ions naturally explains many of the observed remarkable properties of $La_{1.5}Sr_{0.5}CoO_4$. The high charge-ordering temperature $T_C = 825\,\mathrm{K}$ and the extremely insulating behavior can be attributed to the so called spin-blockade mechanism [30, 189, 190]: The $Co^{3+} - Co^{2+}$ electron hopping is remarkably suppressed as it results in a pair of wrong spin states, costing a huge amount of energy, see Fig. 7.12. This further explains the rapid suppression of the AFM spin order in the doped compounds compared to the parent compound La_2CoO_4 [30, 174]. The strong charge localization is further stabilized by the extreme e_g occupation difference between LS Co^{3+} ($t_{2g}^6 e_g^0$) and HS Co^{2+} ($t_{2g}^5 e_g^2$), resulting in hugely different $Co-O$ distances. Additionally, Chang *et al.* [189] outline that the lowest unoccupied band of the LS Co^{3+} ions has almost pure $3z^2 - r^2$ character (the e_g splitting between $3z^2 - r^2$ and $x^2 - y^2$ amounts to $\approx 0.7\,\mathrm{eV}$). Since $3z^2 - r^2$ has only small overlap with the in-plane O $2p_{xy}$ band, the bandwidth of the conduction

band is significantly reduced compared to e.g. cuprate, nickelate, and manganite compounds (where the $x^2 - y^2$ orbital forms the conduction band), which further contributes to the highly insulating character of $La_{1.5}Sr_{0.5}CoO_4$.
It has to be pointed out that the IS state can indeed safely be ruled out on the basis of various theoretical studies. It can only be stabilized for a huge $t_{2g} - e_g$ splitting beyond $\approx 2\,\text{eV}$, which is much larger than the actual splitting of $\approx 0.7\,\text{eV}$ in $La_{1.5}Sr_{0.5}CoO_4$ [30, 138, 139, 189].
Jia *et al.* [190] theoretically confirm the scenario of a Co^{3+} LS state as proposed by Refs. [139] and [189] also for the Ca-doped compound $La_{1.5}Ca_{0.5}CoO_4$ by the use of the full-potential linearized augmented plane-wave method [190]. The Co^{3+} LS state is further confirmed by neutron scattering experiments on $La_{1.5}Sr_{0.5}CoO_4$ performed by Helme *et al.* [191].
Also the spin state of the pure Co^{3+} compound $LaSrCoO_4$ has been investigated. Intuitively, one would expect that the IS state is lowest in energy due to the elongation of the CoO_6 octahedra in these layered systems and the resulting splitting of the e_g level [28, 138, 192–194]. Furthermore, the effective magnetic moment of the IS state $\mu_{eff} = 2.8\,\mu_B$ is in good agreement with the measured value of $\mu_{eff} = 2.6\,\mu_B$ [28]. However, the experimental data have to be regarded with care. The crystal growers of our institute in Cologne made the experience that it is extremely challenging to produce single crystals of $LaSrCoO_4$. On the basis of unrestricted Hartree-Fock calculation under the assumption of a cubic crystal field, Wang *et al.* [79] propose a mixture of LS and HS states being realized in $LaSrCoO_4$. Besides his theoretical investigations on the half-doped compound $La_{1.5}Sr_{0.5}CoO_4$, Wu [138] also performed LSDA+U calculations to study the spin state of the pure Co^{3+} system $LaSrCoO_4$, again including the multiplet effect, spin-orbit coupling, and accounting for the tetragonal distorted crystal structure. A comparison of his results with experimental data confirms the findings of Wang *et al.* [79] claiming that the HS/LS mixed state has the lowest energy. A HS/LS mixed state yields $\mu_{eff} \approx 2.7\,\mu_B$ which agrees also well with the measured value of $\mu_{eff} \approx 2.6\,\mu_B$ [28, 138]. A mixed Co^{3+} HS/LS state leads to a competition between AFM and FM interactions in $LaSrCoO_4$. High-spin Co^{3+} neighbors favor AFM coupling, on the contrary, fluctuations between neighboring HS Co^{3+} and LS Co^{3+} ions lead to ferromagnetism [30]. This is in agreement with the simultaneous observation of FM and AFM features in the magnetic susceptibility in Ref. [28].
Recent near-edge x-ray absorption fine structure measurements performed by Merz *et al.* [30] on $La_{2-x}Ca_xCoO_4$ ($x = 0,\ 0.5,\ 1,\ 1.5$) give clear evidence for the following spin-state scenario: In La_2CoO_4 all Co^{2+} ions are in the HS state. In $La_{1.5}Sr_{0.5}CoO_4$ the Co^{2+} HS state and the Co^{3+} LS state is realized, while in $LaSrCoO_4$ 55 % of the Co^{3+} ions are in the LS and the other 45% are in the HS state. The findings of Merz *et al.* [30] on the Ca-doped compound are thus in agreement with the studies of Refs. [29, 139, 188, 189, 191] on the Sr-doped counterpart.

To conclude, the most probable ground state of the Co^{3+} ions in the layered compound $La_{2-x}Sr_xCoO_4$ with doping levels $0.4 \lesssim x \lesssim 0.8$ is the LS state ($S = 0$) [29, 30, 42, 139, 188–191], while higher spin states might be populated at higher temperatures above $T \approx 500\,\mathrm{K}$, as suggested by Hollmann *et al.* [29]. For doping concentrations $x \gtrsim 0.8$ a mixed HS/LS state might be realized [79,138], while Cwik [42] speculates that a HS Co^{3+} scenario might be possible for doping concentrations $x < 0.4$.

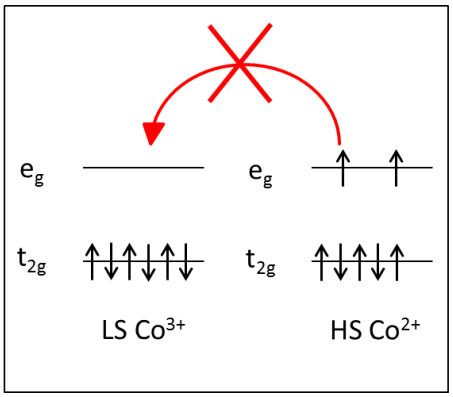

Figure 7.12:
The spin-blockade mechanism: The transfer of an electron from a HS Co^{2+} ion to a LS Co^{3+} ion would result in energetic unfavorable spin configurations.

7.2 Experimental data

In this section the ellipsometric data is presented. First, we briefly discuss the acquisition and analysis of the various data sets. An exemplary plot of the experimentally acquired data on $La_{1.55}Sr_{0.45}CoO_4$ at 15 K with fit is shown in Fig. 7.13. The MSE of the fit to the data amounts to 1.5. A summary of the information on the data acquisition and analysis of the various measured cobaltate samples can be found in table 7.2 on page 189 at the end of this section.

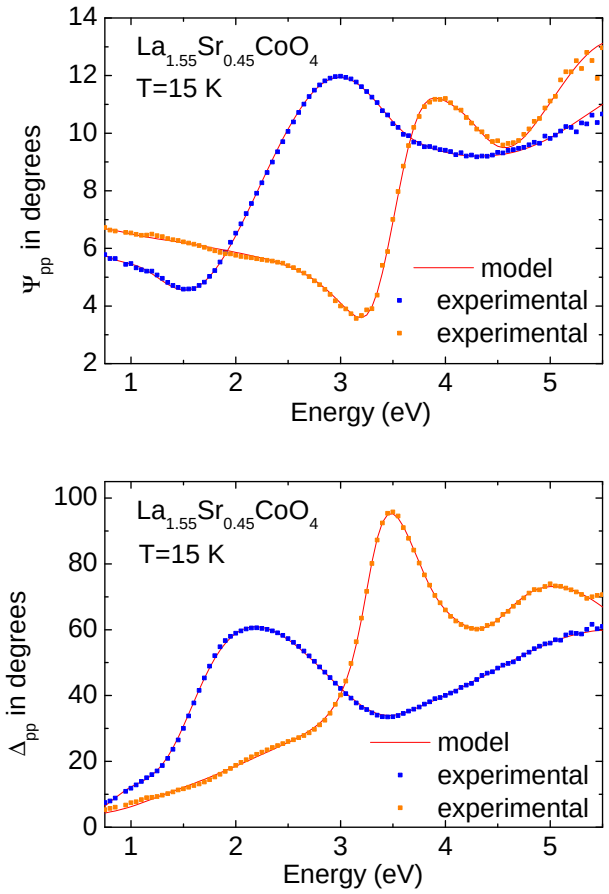

Figure 7.13: Experimentally obtained Ψ_{pp} (top) and Δ_{pp} (bottom) on $La_{1.55}Sr_{0.45}CoO_4$ for two different sample orientations at $T = 15\,\mathrm{K}$. Data that has been acquired on an *ac* plane with the *a* axis lying in the plane of incidence (blue squares) and the *c* axis lying in the plane of incidence (orange squares) are shown.

7.2.1 Optical conductivity of $LaCoO_3$ and $EuCoO_3$

- $LaCoO_3$

  The ellipsometric variables Ψ_{pp} and Δ_{pp} have been acquired on a polished sample surface of pseudocubic $LaCoO_3$ with a diameter of about 4 mm. In the energy range from 0.75 eV to 5.5 eV covered by the VIS/UV ellipsometer at hand in Cologne, data has been acquired inside the cryostat at an angle of incidence of 70° for temperatures ranging from 15 K to 490 K. The data is fitted with 6 Gaussian oscillators, see Fig. 7.14. The parameters of the oscillators are summarized in Figs. 7.20 and 7.21. In the fit, a surface roughness with a thickness of 10 Å is assumed. The fit to the data is very good, it yields an MSE of about $0.4 - 0.8$. The dielectric function $\varepsilon(\omega)$ of $LaCoO_3$ is depicted in Fig. 7.15, Fig. 7.16 shows the optical conductivity $\sigma_1(\omega)$. As the data show an interesting temperature dependence between 40 K and 80 K, additional measurements have been performed in this temperature range in small steps of 5 K. Since these data has been taken within a second measurement series (measurement series 2), the absolute values of the resulting $\varepsilon_2(\omega)$ and $\sigma_1(\omega)$ are slightly different, see Fig. 7.17. The difference can be attributed to surface effects. Therefore, the additional data between 40 K and 80 K are not shown in Figs. 7.15 and 7.16, but referred to in the discussion.
  The optical conductivity of $LaCoO_3$ at lower energies between 0.07 eV and 0.65 eV has been acquired with the help of an IR ellipsometer at the University of California San Diego. The low-temperature measurements have been performed at an angle of incidence of 60°. Unfortunately, the cryostat did not allow for measurements above room temperature. The IR data is fitted together with the data at higher energies. The resulting dielectric function $\varepsilon(\omega)$ and the optical conductivity $\sigma_1(\omega)$ are shown in Figs. 7.18 and 7.19, respectively. The parameters of the Gaussian oscillators used in the fit to the IR data are embedded in Figs. 7.20 and 7.21.

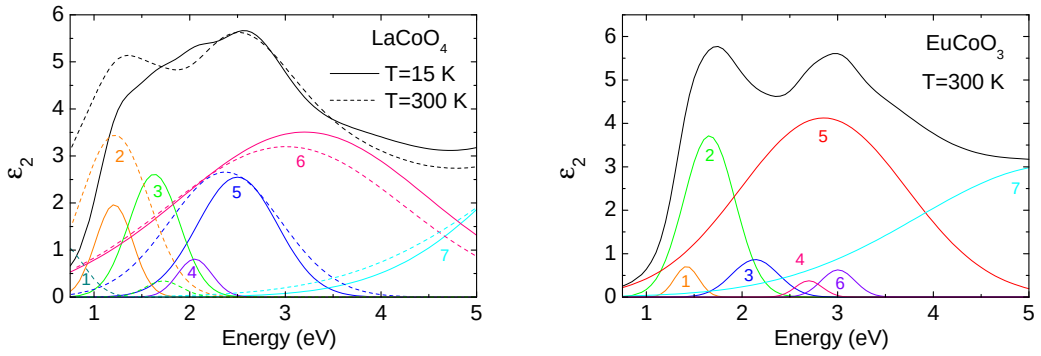

Figure 7.14: Left panel: The model for the dielectric function of $LaCoO_3$ is based on a sum of six Gaussian oscillators. The oscillators describing ε_2 at 15 K are represented by solid lines, whereas the oscillators describing ε_2 at 300 K are represented by dashed lines. While the Gaussian oscillator at ≈ 0.7 eV (peak 1) describing the low-energy spectral weight is missing for low temperatures below 80 K, an additional oscillator is needed at ≈ 2 eV (peak 4) for $T < 80$ K. Right panel: The model for the dielectric function of $EuCoO_3$ is based on a sum of seven Gaussian oscillators.

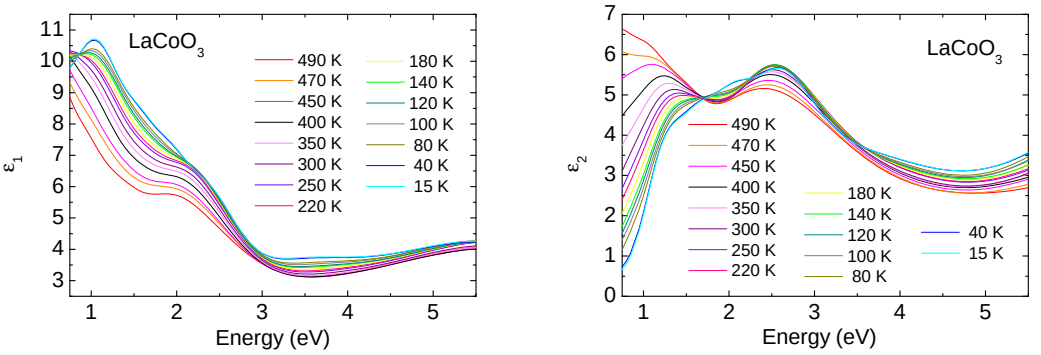

Figure 7.15: Dielectric function $\varepsilon(\omega)$ of $LaCoO_3$ between 0.75 eV and 5.5 eV for temperatures ranging from 15 K to 490 K.

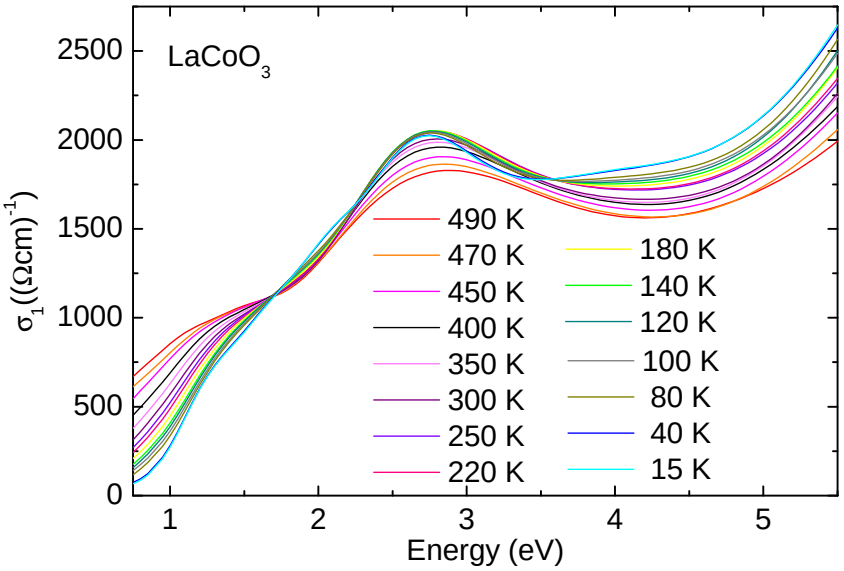

Figure 7.16: Optical conductivity $\sigma_1(\omega)$ of $LaCoO_3$ between 0.75 eV and 5.5 eV for temperatures ranging from 15 K to 490 K.

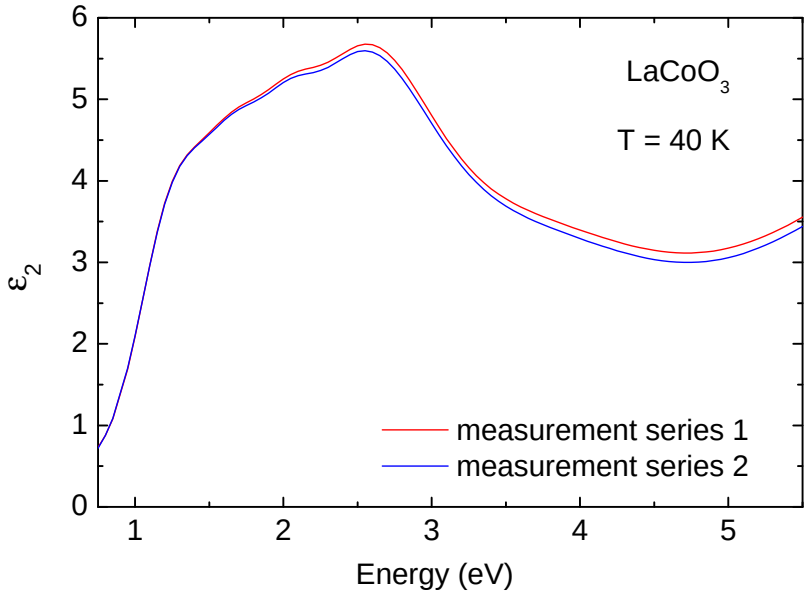

Figure 7.17: Dielectric function $\varepsilon_2(\omega)$ of $LaCoO_3$ at $T = 40$ K resulting from two different measurement series.

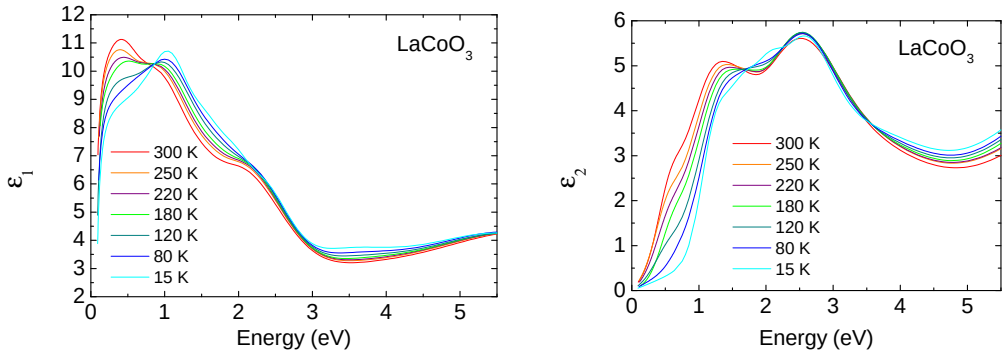

Figure 7.18: Dielectric function $\varepsilon(\omega)$ of $LaCoO_3$ for different temperatures below 300 K. Additional data has been acquired down to energies of 0.07 eV by the use of an IR ellipsometer.

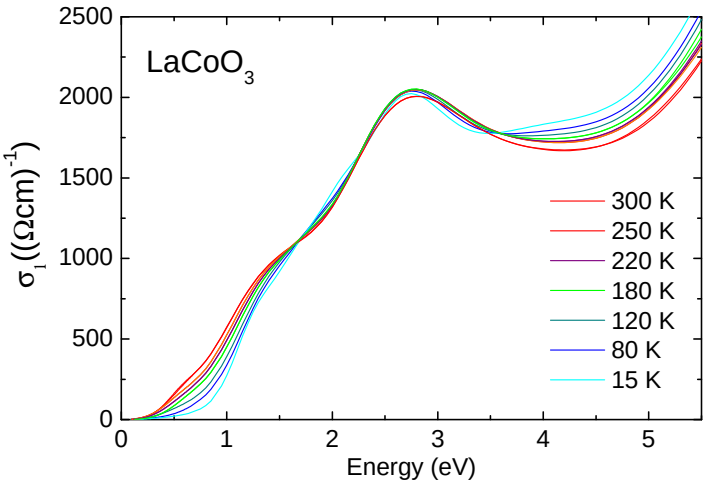

Figure 7.19: Optical conductivity $\sigma_1(\omega)$ of $LaCoO_3$ for different temperatures below 300 K. Additional data has been acquired down to energies of 0.07 eV by the use of an IR ellipsometer.

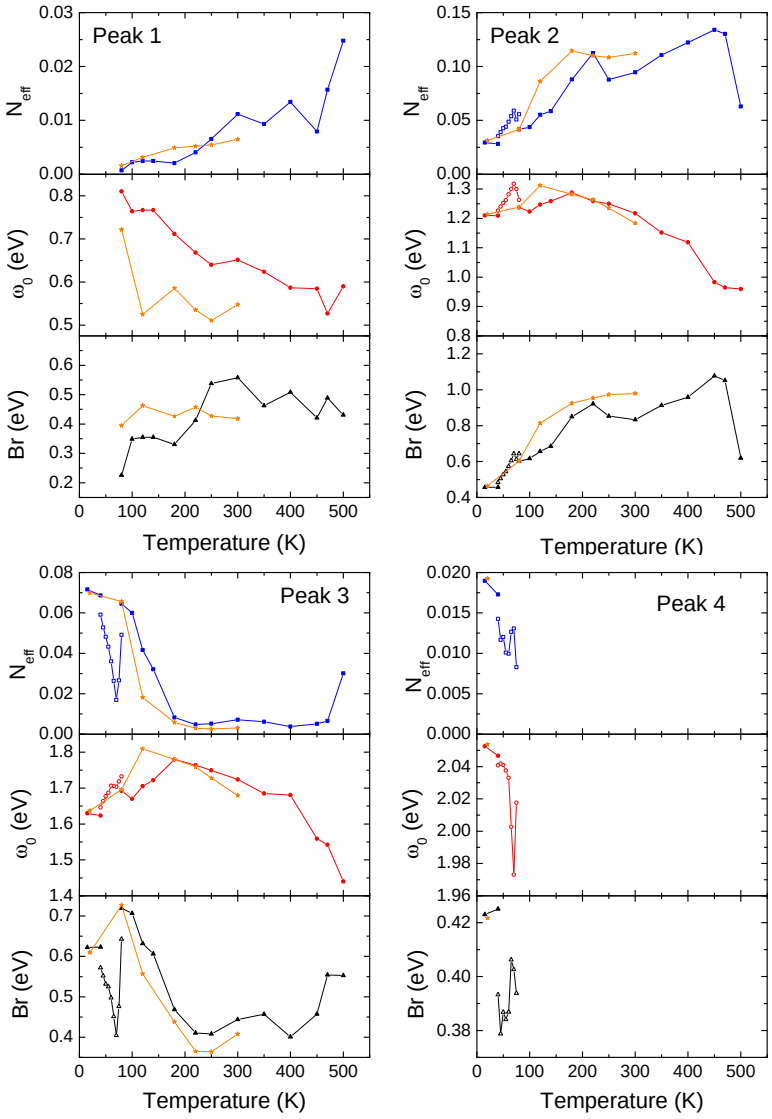

Figure 7.20: Results of the fit to the measured data of $LaCoO_3$ with Gaussian oscillators. The parameters of the Gaussian oscillators are defined in Sec. 3.1.5 (Eq. 3.24). The effective carrier concentration N_{eff} (as defined in Eq. 4.6 in Sec. 4.2.3), the center energy ω_0, and the FWHM Br are shown as a function of temperature. The four panels refer to the four oscillators with the lowest energies. The full symbols (blue, red, and black) represent the best fit parameters that result from the fit to the VIS/UV data alone, the full orange symbols represent the best fit parameters that result from the fit to both data sets, VIS /UV and IR data. The open symbols (blue, red, and black) are the best fit parameters to data that has been taken within another measuring cycle (for temperatures $40\,\mathrm{K} \leq T \leq 80\,\mathrm{K}$). The Gaussian oscillators corresponding to peaks $1-4$ are visualized in Fig. 7.14. See the main text for details.

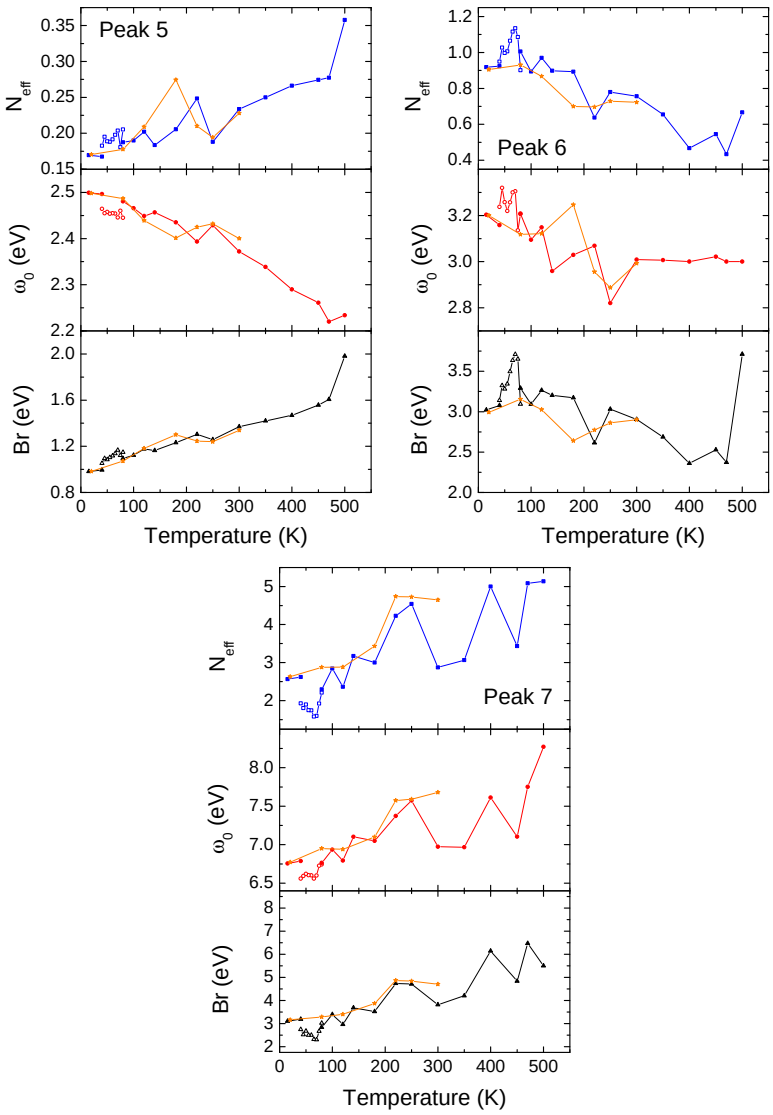

Figure 7.21: Results of the fit to the measured data of $LaCoO_3$ with Gaussian oscillators. The three panels refer to the three oscillators with the highest energies. See the caption of Fig. 7.20 for more information.

- $EuCoO_3$

  The ellipsometric variables Ψ_{pp} and Δ_{pp} have been acquired on a polished sample surface of pseudocubic $EuCoO_3$ with a diameter of approx. 4 mm in the energy range from 0.75 eV to 5.0 eV for temperatures ranging from 15 K to 490 K. The angle of incidence was 70°. The fit to the measured data is based on seven Gaussian oscillators, a surface roughness with a thickness of 10 Å is assumed. The fit to the data yields an MSE of $0.3 - 0.5$. The dielectric function $\varepsilon(\omega)$ of $EuCoO_3$ is shown in Fig. 7.22, the optical conductivity $\sigma_1(\omega)$ is shown in Fig. 7.23. The parameters of the Gaussian oscillators are summarized in Figs. 7.24 and 7.25.

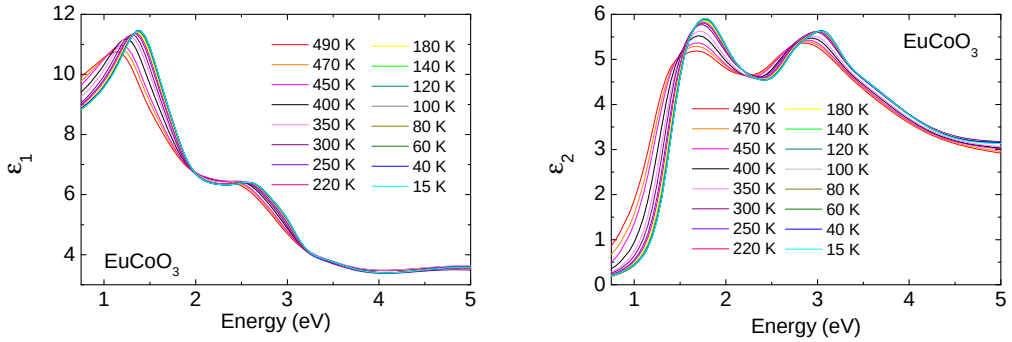

Figure 7.22: Dielectric function $\varepsilon(\omega)$ of $EuCoO_3$ between 0.75 eV and 5.0 eV for temperatures ranging from 15 K to 490 K.

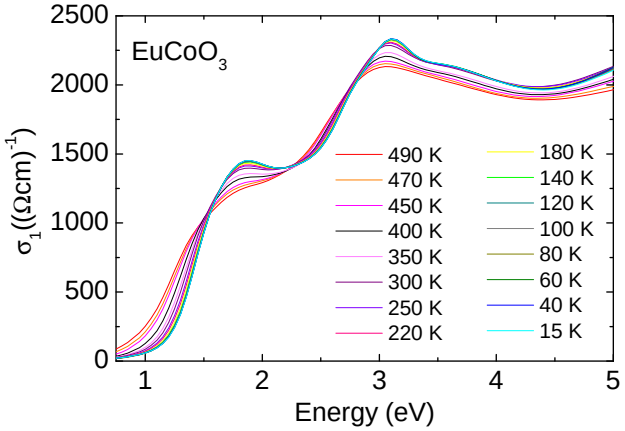

Figure 7.23: Optical conductivity $\sigma_1(\omega)$ of $EuCoO_3$ between 0.75 eV and 5.0 eV for temperatures ranging from 15 K to 490 K.

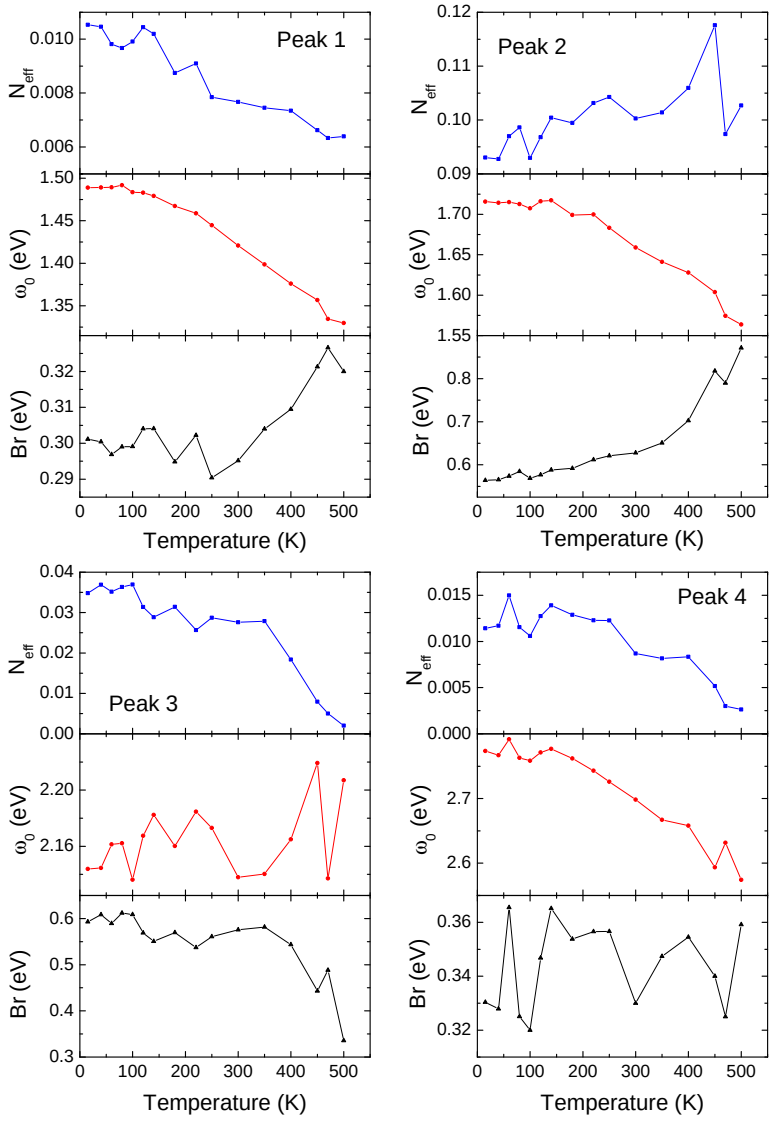

Figure 7.24: Results of the fit to the measured data of $EuCoO_3$ with Gaussian oscillators. The parameters of the Gaussian oscillators are defined in Sec. 3.1.5 (Eq. 3.24). The effective carrier concentration N_{eff} (as defined in Eq. 4.6 in Sec. 4.2.3), the center energy ω_0, and the FWHM Br are shown as a function of temperature. The four panels refer to the four oscillators with the lowest energies. The Gaussian oscillators corresponding to peaks $1-4$ are visualized in Fig. 7.14. See the main text for details.

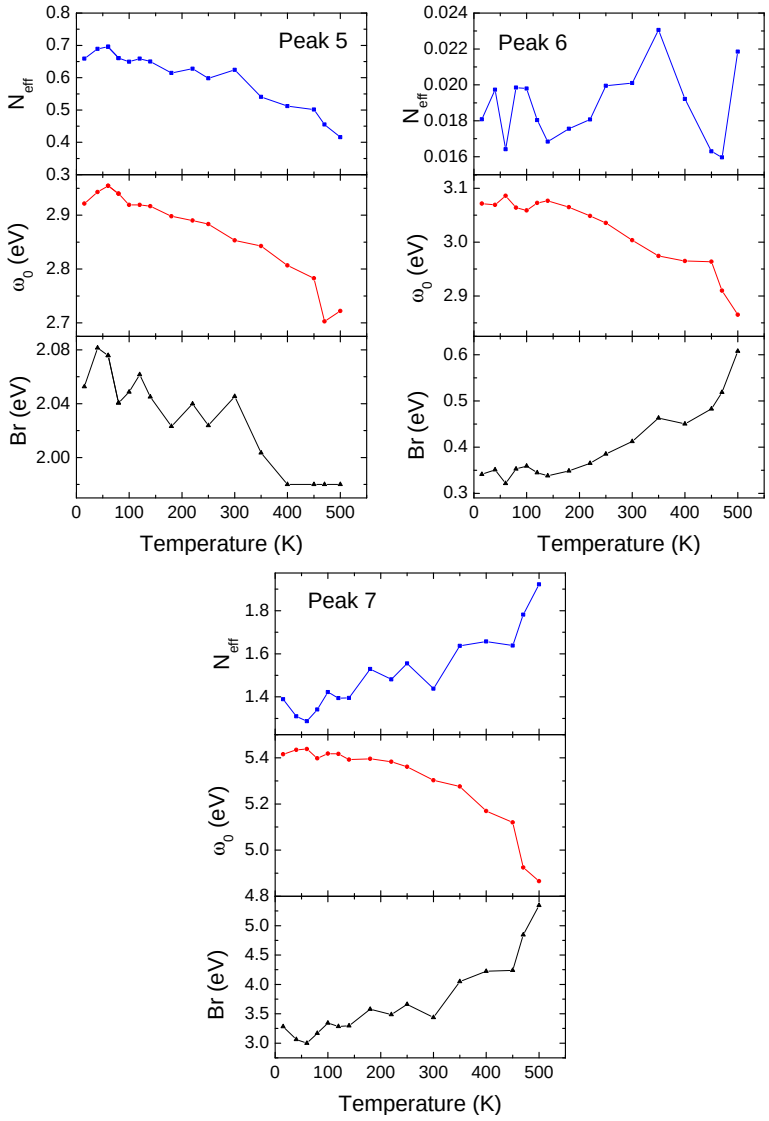

Figure 7.25: Results of the fit to the measured data of $EuCoO_3$ with Gaussian oscillators. The three panels refer to the three oscillators with the highest energies. See the caption of Fig. 7.24 for the definition of the parameters and Fig. 7.14 for the visualization of the Gaussian oscillators.

7.2.2 Optical conductivity of $La_{2-x}Sr_xCoO_4$ (x = 0, 0.33, 0.45, 0.5, and 0.9) and $La_{1.5}Ca_{0.5}CoO_4$

The measurements on layered cobaltates have all been performed with the help of the VIS/UV ellipsometer at hand in Cologne, that covers the frequency range from 0.75 eV to 5.5 eV. The data have been taken inside the cryostat for temperatures ranging from 15 K to 490 K at an angle of incidence of 70°. Details on the data acquisition and analysis of the various data sets are discussed below.

- La_2CoO_4

  All accessible Mueller-matrix elements have been acquired for La_2CoO_4. The data used for the fit have been taken on a polished *ac* surface (the *a* axis refers to the *a* axis of a tetragonal unit cell, space group *I4/mmm*). Measurements have been performed in two different orientations, with the tetragonal *a* axis and the *c* axis parallel to the plane of incidence, respectively. The fit to the measured data is based on three Gaussian oscillators for ε^a and four Gaussian oscillators for ε^c. In the fit a surface roughness with a thickness of 30 Å is assumed. The MSE amounts to $0.6 - 1.2$. Figure 7.26 shows the dielectric function $\varepsilon^\gamma(\omega)$ ($\gamma = a, c$), Fig. 7.27 presents the optical conductivity $\sigma_1^\gamma(\omega)$ of La_2CoO_4. It is important to note that the *a* axis spectra refer to the *a* axis of a tetragonal unit cell. The parameters of the Gaussian oscillators are summarized in Figs. 7.37 and 7.38. Additional data have been acquired on an *ab* plane with the *a* axis of the tetragonal unit cell and the *a* axis of the orthorhombic unit cell (space group *Bmab*) lying parallel to the plane of incidence, respectively. The difference of both data sets lies within the experimental error, which proves that there is no observable optical anisotropy within the *ab* plane. This data is not used for the final fit, as it covers far less different temperatures.

- $La_{2-x}Sr_xCoO_4$, $x = 0.33,\ 0.45$, and 0.5

  The dielectric function $\varepsilon^\gamma(\omega)$ ($\gamma = a, c$) of anisotropic $La_{2-x}Sr_xCoO_4$ ($x = 0.33,\ 0.45$, and 0.5) is deduced from the ellipsometric variables Ψ_{pp} and Δ_{pp}, which have been acquired on a single polished sample surface, an *ac* plane. The *ac* plane has been measured in two different orientations, with the *a* and the *c* axis lying parallel to the plane of incidence, respectively (again, the *a* axis refers to the *a* axis of a tetragonal unit cell with space group *I4/mmm*). The fit is based on four Gaussian oscillators for both, ε^a and ε^c, see Fig. 7.28. A surface roughness with a thickness of 30 Å is assumed in the fit. The MSE of the fits does not exceed 1.5, it mostly is on the order of 0.5. The resulting dielectric functions $\varepsilon^\gamma(\omega)$ ($\gamma = a, c$) are presented in Figs. 7.29 ($x = 0.33$), 7.31 ($x = 0.45$), and 7.33 ($x = 0.5$). Figures 7.30, 7.32, and 7.34 show the optical conductivity $\sigma_1^\gamma(\omega)$. The parameters of the

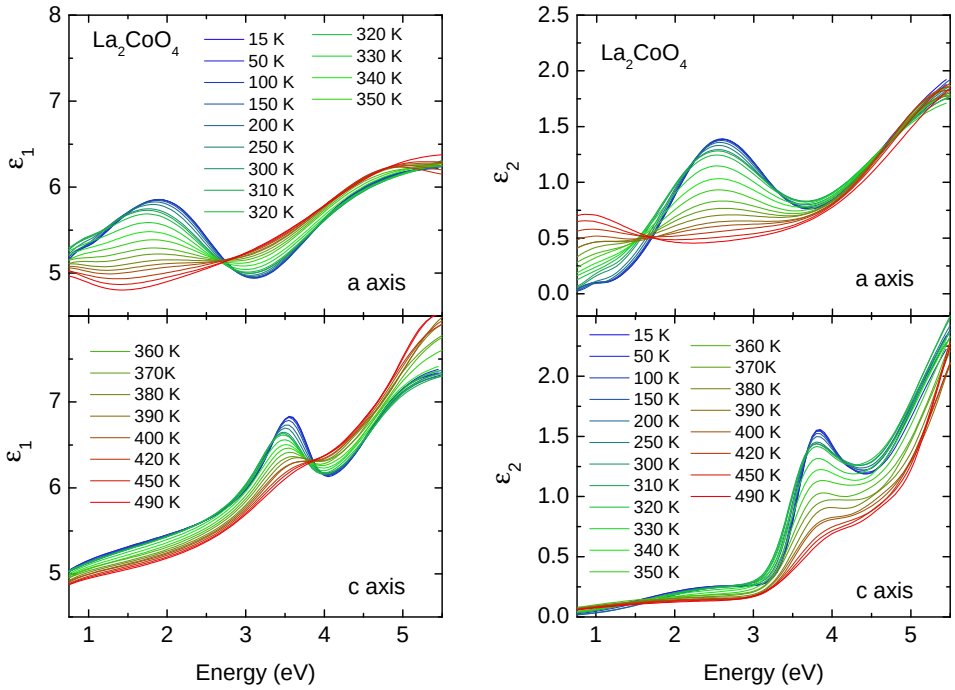

Figure 7.26: Dielectric function $\varepsilon(\omega)$ of La_2CoO_4 for the a and c direction between 0.75 eV and 5.5 eV for different temperatures ranging from 15 K to 490 K.

Gaussian oscillators are summarized in Figs. 7.37 and 7.38. The diameters of the sample surfaces amount to:
$x = 0.3:$ 6 mm; $x = 0.45:$ 4 mm; $x = 0.5:$ 5 mm

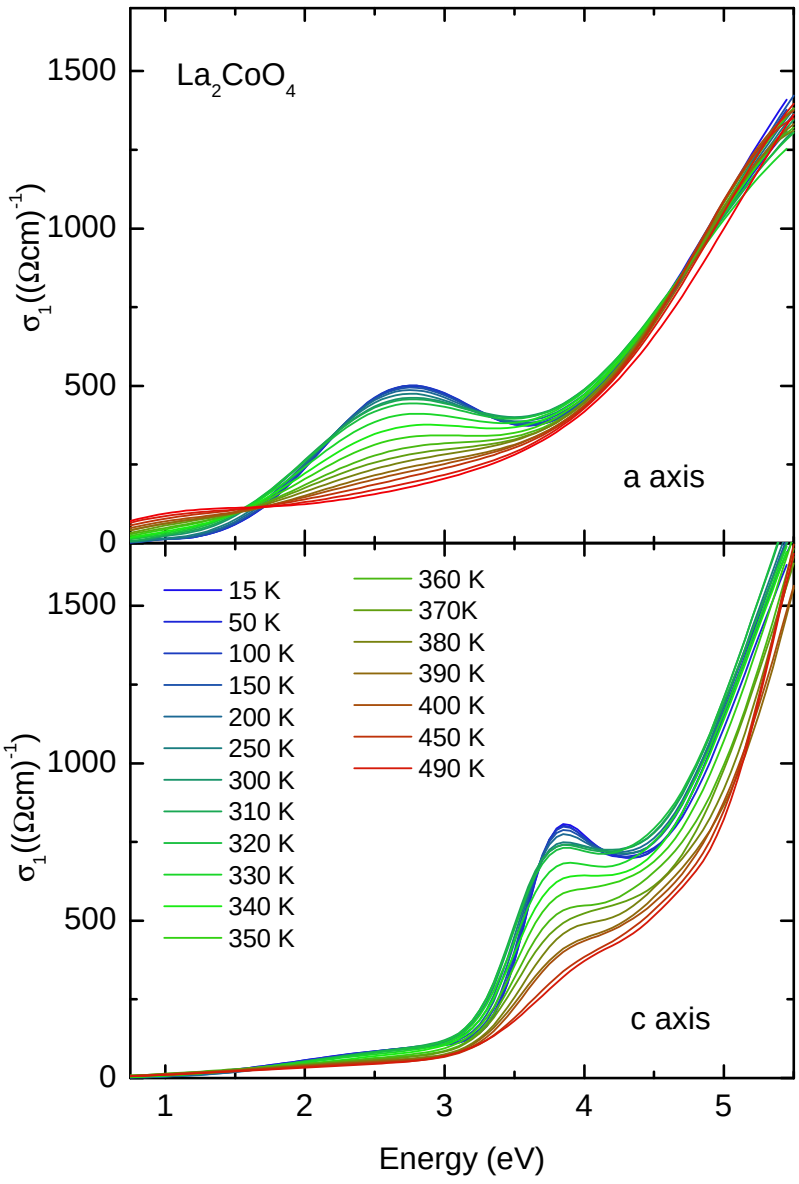

Figure 7.27: Optical conductivity $\sigma_1(\omega)$ of La_2CoO_4 for the a and c direction between 0.75 eV and 5.5 eV for temperatures ranging from 15 K to 490 K.

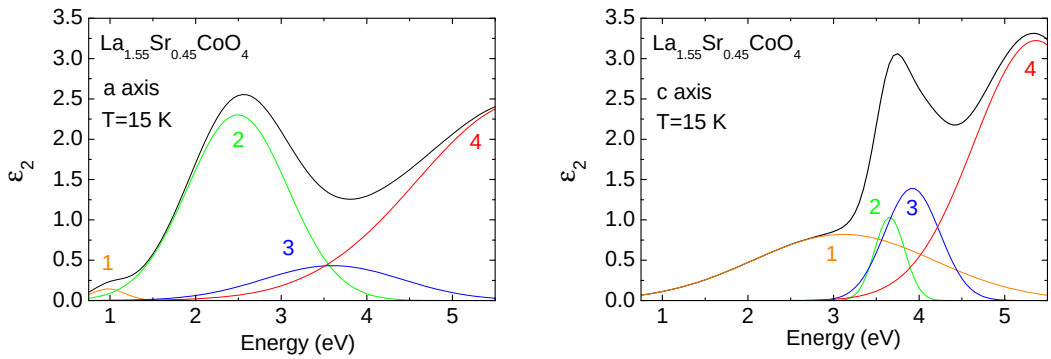

Figure 7.28: The model for the dielectric function of $La_{1.55}Sr_{0.45}CoO_4$ is based on a sum of four Gaussian oscillators for the a and c axis, respectively.

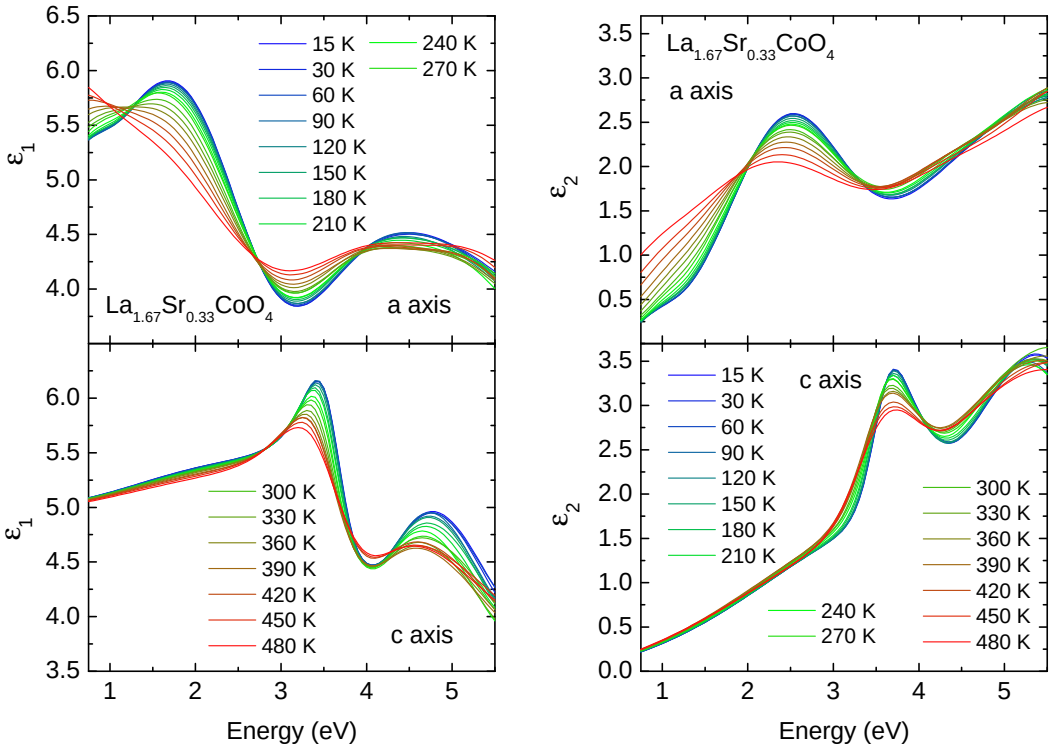

Figure 7.29: Dielectric function $\varepsilon(\omega)$ of $La_{1.67}Sr_{0.33}CoO_4$ for the a and c direction between 0.75 eV and 5.5 eV for different temperatures ranging from 15 K to 480 K.

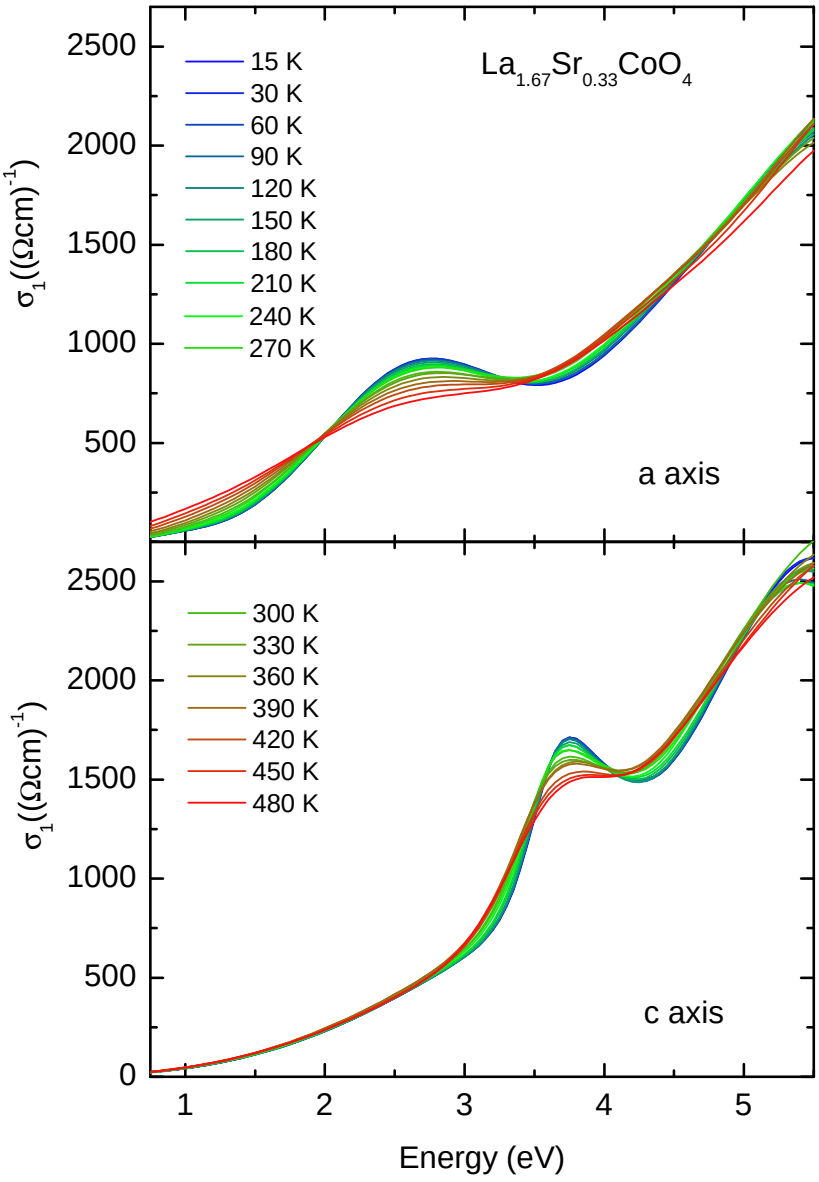

Figure 7.30: Optical conductivity $\sigma_1(\omega)$ of $La_{1.67}Sr_{0.33}CoO_4$ for the a and c direction between 0.75 eV and 5.5 eV for temperatures ranging from 15 K to 480 K.

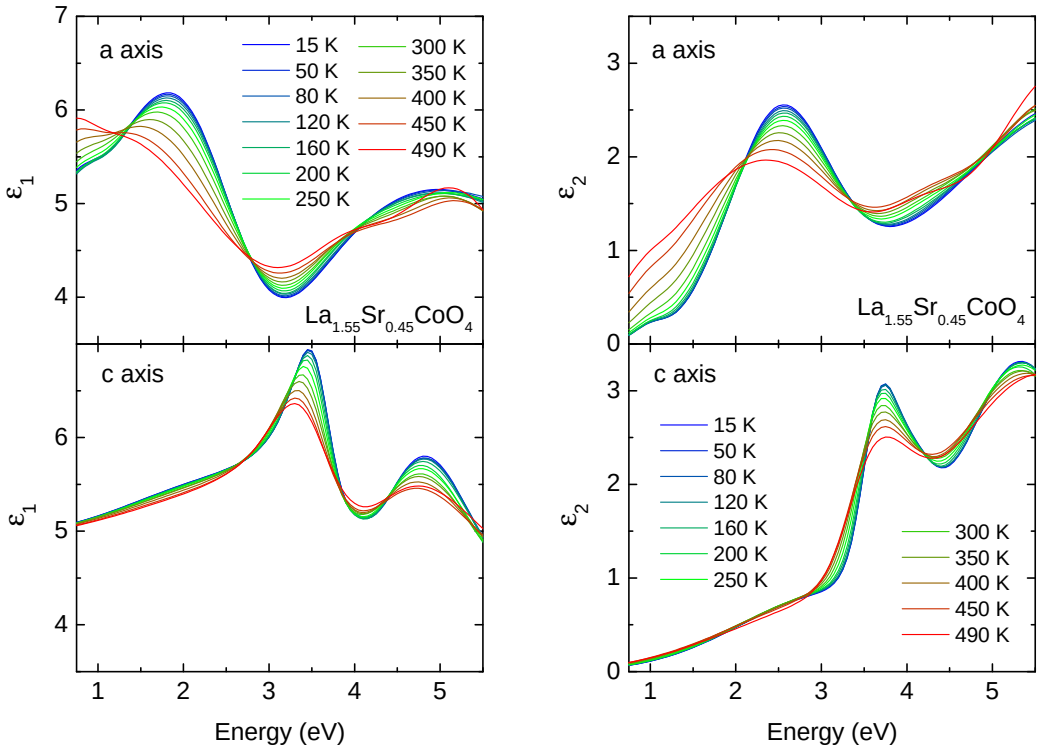

Figure 7.31: Dielectric function $\varepsilon(\omega)$ of $La_{1.55}Sr_{0.45}CoO_4$ for the a and c direction between 0.75 eV and 5.5 eV for different temperatures ranging from 15 K to 490 K.

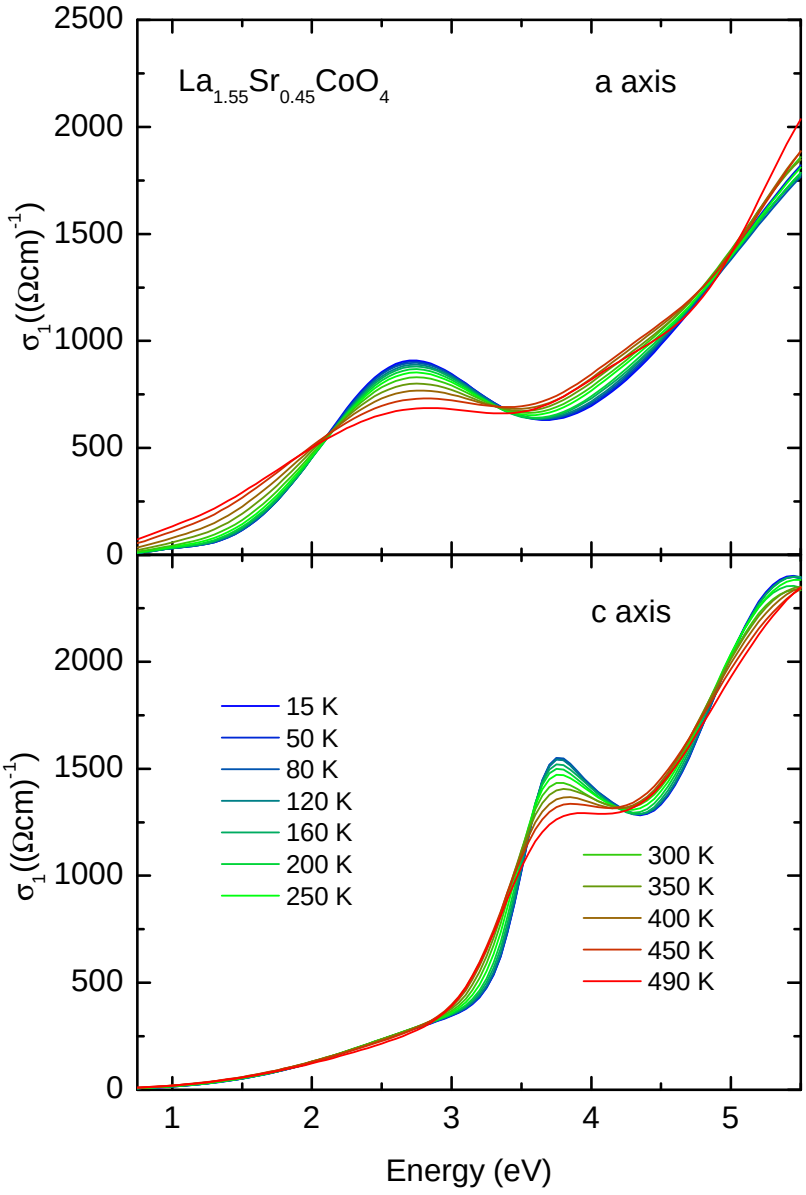

Figure 7.32: Optical conductivity $\sigma_1(\omega)$ of $La_{1.55}Sr_{0.45}CoO_4$ for the a and c direction between 0.75 eV and 5.5 eV for temperatures ranging from 15 K to 490 K.

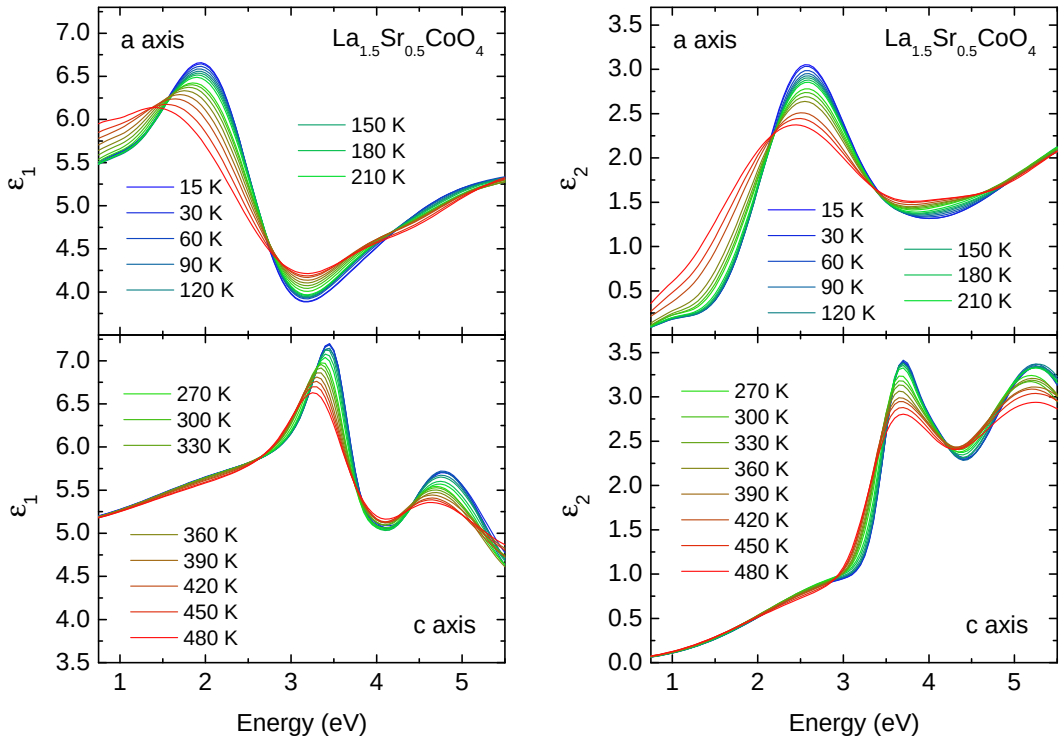

Figure 7.33: Dielectric function $\varepsilon(\omega)$ of $La_{1.5}Sr_{0.5}CoO_4$ for the a and c direction between 0.75 eV and 5.5 eV for different temperatures ranging from 15 K to 480 K.

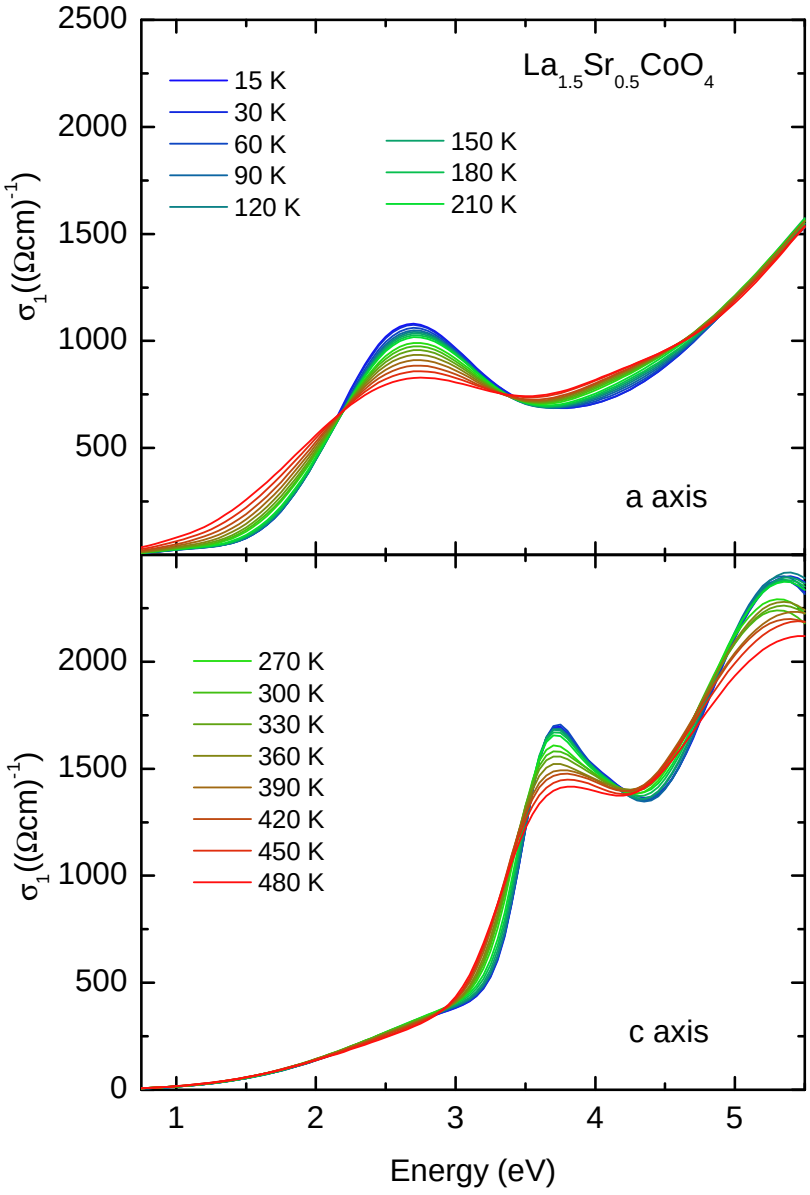

Figure 7.34: Optical conductivity $\sigma_1(\omega)$ of $La_{1.5}Sr_{0.5}CoO_4$ for the a and c direction between 0.75 eV and 5.5 eV for temperatures ranging from 15 K to 480 K.

- $La_{1.5}Ca_{0.5}CoO_4$

  The ellipsometric variables Ψ_{pp} and Δ_{pp} have been acquired on two different polished sample surfaces of $La_{1.5}Ca_{0.5}CoO_4$, an ab plane (size of the sample surface: approx. 3 mm × 3 mm) and an ac plane (size of the sample surface: approx. 4 mm × 2 mm) (a corresponding to the a axis of the tetragonal unit cell). Each surface has been measured in two different orientations with the a and b axis of the ab plane and the a and c axis of the ac plane parallel to the plane of incidence, respectively. In the fit to the experimental data, a surface roughness with a thickness of 30 Å is assumed. Four Gaussian oscillators are used to describe both, ε^a and ε^c. The fit is remarkably good, yielding an MSE of 1.5 to 3.5, depending on temperature. The MSE is slightly higher compared to the fit to the data of $La_{2-x}Sr_xCoO_4$ ($x = 0.33,\ 0.45,\ 0.5$) because for $La_{1.5}Ca_{0.5}CoO_4$ the oscillator model is fitted to four different data sets simultaneously (in the case of $La_{2-x}Sr_xCoO_4$ with $x = 0.3,\ 0.45$, and 0.5, only two data sets were available). The dielectric function $\varepsilon^\gamma(\omega)$ ($\gamma = a, c$) of $La_{1.5}Ca_{0.5}CoO_4$ is presented in Fig. 7.35, the optical conductivity $\sigma_1^\gamma(\omega)$ is shown in Fig. 7.36. The parameters of the Gaussian oscillators are summarized in Figs. 7.37 and 7.38.

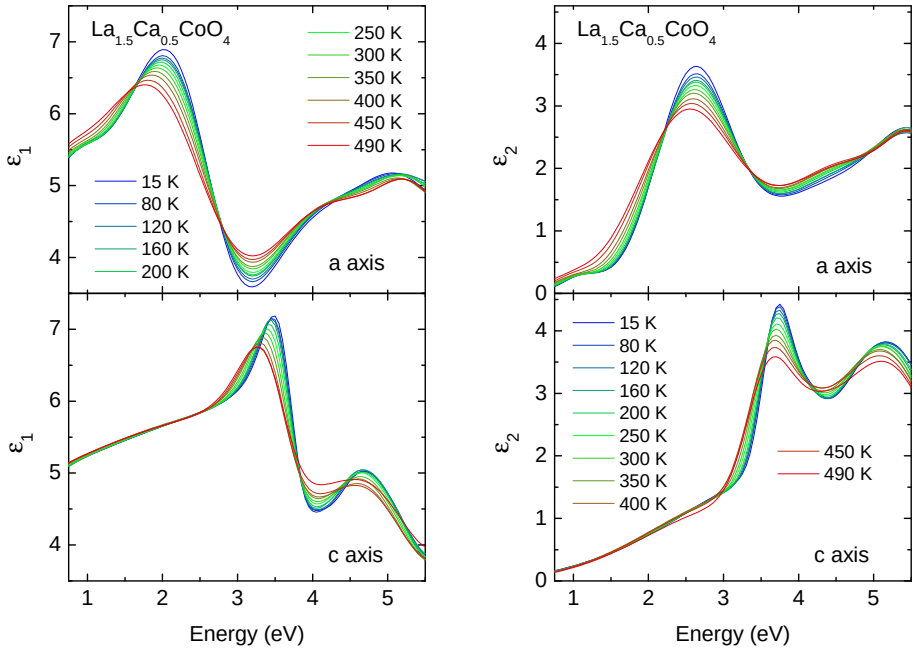

Figure 7.35: Dielectric function $\varepsilon(\omega)$ of $La_{1.5}Ca_{0.5}CoO_4$ for the a and c direction between 0.75 eV and 5.5 eV for different temperatures ranging from 15 K to 490 K.

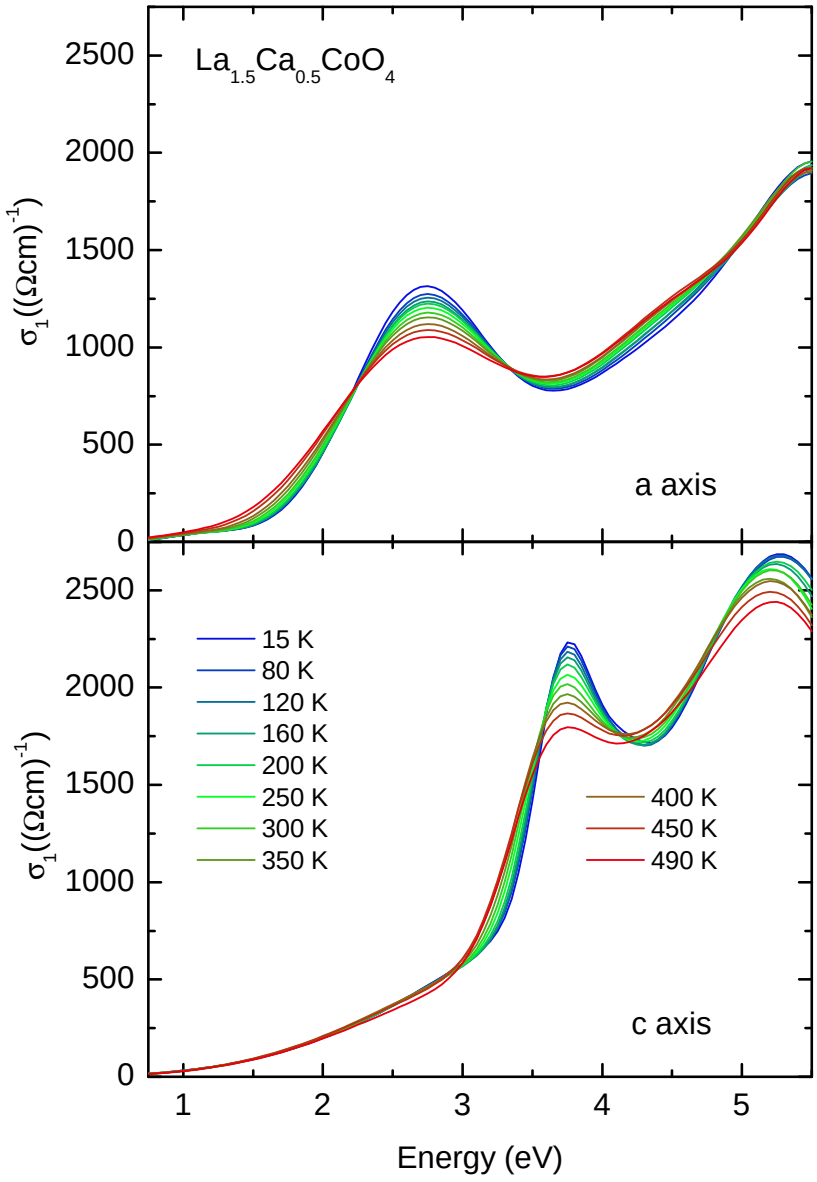

Figure 7.36: Optical conductivity $\sigma_1(\omega)$ of $La_{1.5}Ca_{0.5}CoO_4$ for the a and c direction between 0.75 eV and 5.5 eV for temperatures ranging from 15 K to 490 K.

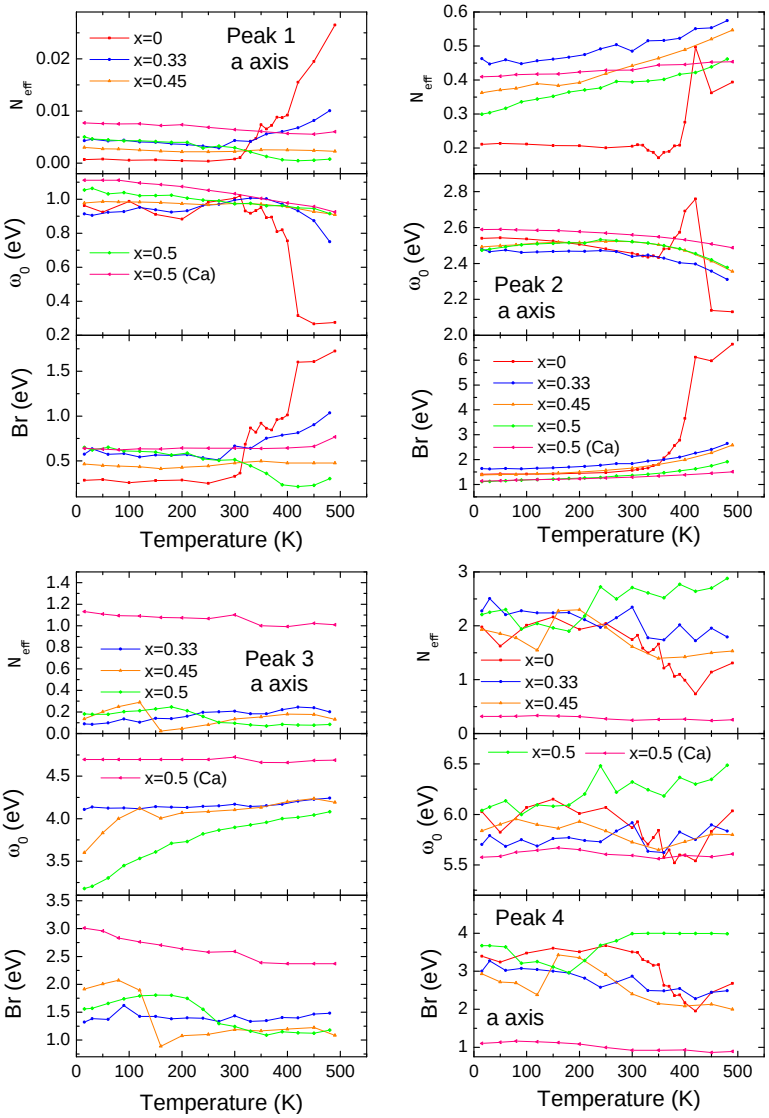

Figure 7.37: Results of the fit to the measured data of $La_{1-x}Sr_xCoO_4$ ($x = 0,\ 0.33,\ 0.45$, and 0.5) and $La_{1.5}Ca_{0.5}CoO_4$ with Gaussian oscillators. The parameters describing ε_2^a are shown. The parameters of the Gaussian oscillators are defined in Sec. 3.1.5 (Eq. 3.24). The effective carrier concentration N_{eff}, the center energy ω_0, and the FWHM Br are shown as a function of temperature. N_{eff} follows from the parameters of the Gaussian oscillators by the use of Eq. 4.7 (in Sec. 4.2.3). The Gaussian oscillators corresponding to peaks $1-4$ are visualized in Fig. 7.28.

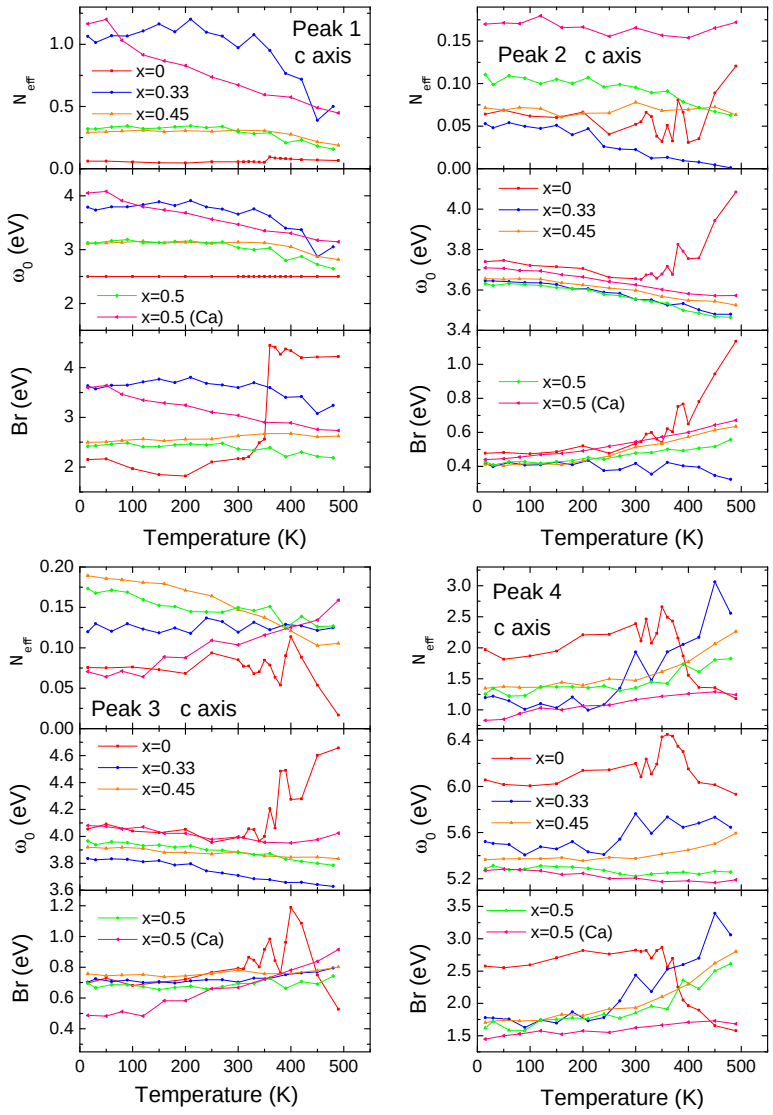

Figure 7.38: Results of the fit to the measured data of $La_{1-x}Sr_xCoO_4$ ($x = 0,\ 0.33,\ 0.45$, and 0.5) and $La_{1.5}Ca_{0.5}CoO_4$ with Gaussian oscillators. The parameters describing ε_2^c are shown. The Gaussian oscillators corresponding to peaks $1-4$ are visualized in Fig. 7.28. See the caption of Fig. 7.37 for the definition of the parameters.

- $La_{1.1}Sr_{0.9}CoO_4$

  The dielectric function $\varepsilon^{\gamma}(\omega)$ $(\gamma = a, c)$ of anisotropic $La_{1.1}Sr_{0.9}CoO_4$ is deduced from the ellipsometric variables Ψ_{pp} and Δ_{pp}, that have been acquired on two different polished sample surfaces, an ab and an ac plane (a corresponding to the a axis of the tetragonal unit cell). Each surface has been measured in one orientation. The ab plane (ac plane) has been measured with the a axis (c axis) being parallel to the plane of incidence. The fit to the experimental data is based on a model consisting of six (four) Gaussian oscillators for the a axis (c axis), see Fig. 7.39, and a surface roughness with a thickness of 30 Å. The MSE of the fits amounts to approx. 1.6. The experimental data originating from the measurement of the ac plane is very noisy, especially for energies $E \geq 3.5\,\mathrm{eV}$. The noise is due to the smallness of the sample. The size of the sample surface amounts to only approx. 1 mm $\times$ 2 mm. This leads to a low intensity at the detector, as part of the beam of light is reflected away from the brass cone, which serves as the sample holder (see Fig. 4.6 in Sec. 4.1.3). The dielectric function $\varepsilon^{\gamma}(\omega)$ $(\gamma = a, c)$ is presented in Fig. 7.40, Fig. 7.41 shows the optical conductivity $\sigma_1^{\gamma}(\omega)$. The parameters of the Gaussian oscillators are summarized in Figs. 7.42, 7.43, and 7.44.

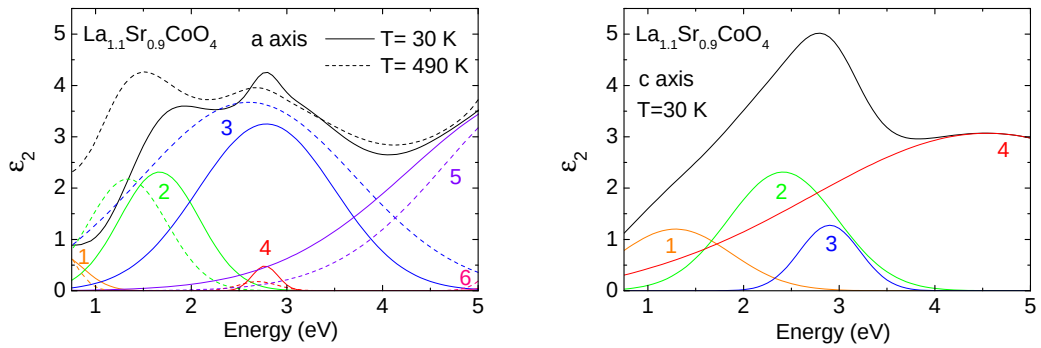

Figure 7.39: The model for the dielectric function of $La_{1.1}Sr_{0.9}CoO_4$ is based on a sum of six (four) Gaussian oscillators for the a (c) axis. For the a axis, the oscillators at two temperatures are shown as the fits differs considerably.

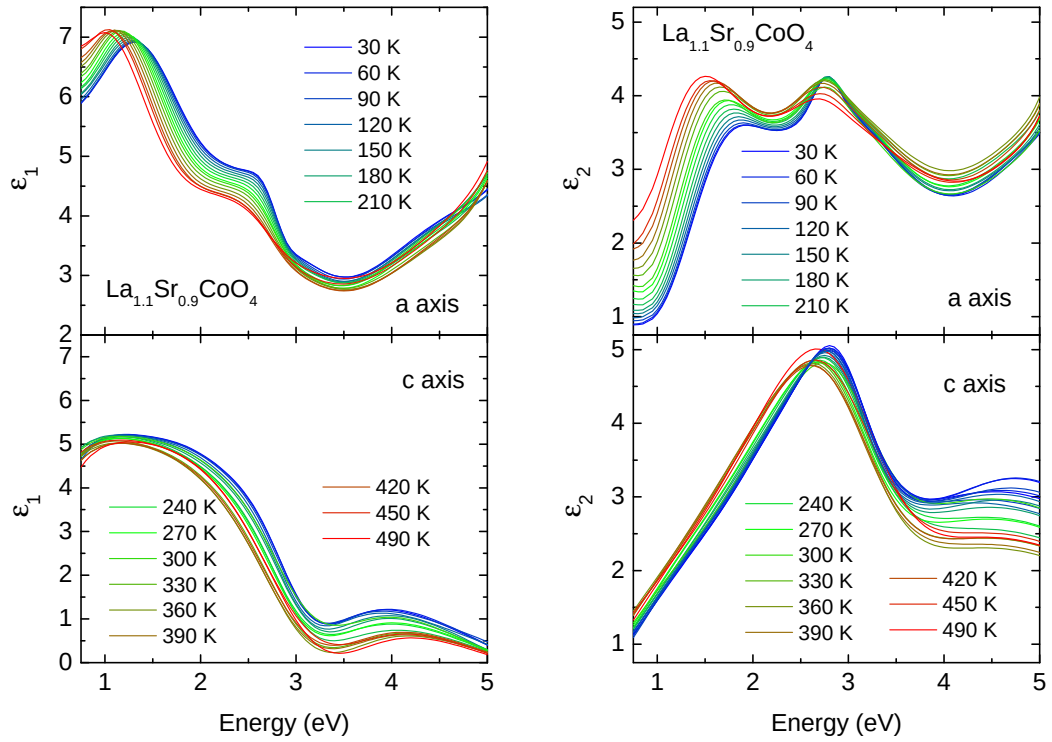

Figure 7.40: Dielectric function $\varepsilon(\omega)$ of $La_{1.1}Sr_{0.9}CoO_4$ for the a and c direction between 0.75 eV and 5.0 eV for different temperatures ranging from 30 K to 490 K.

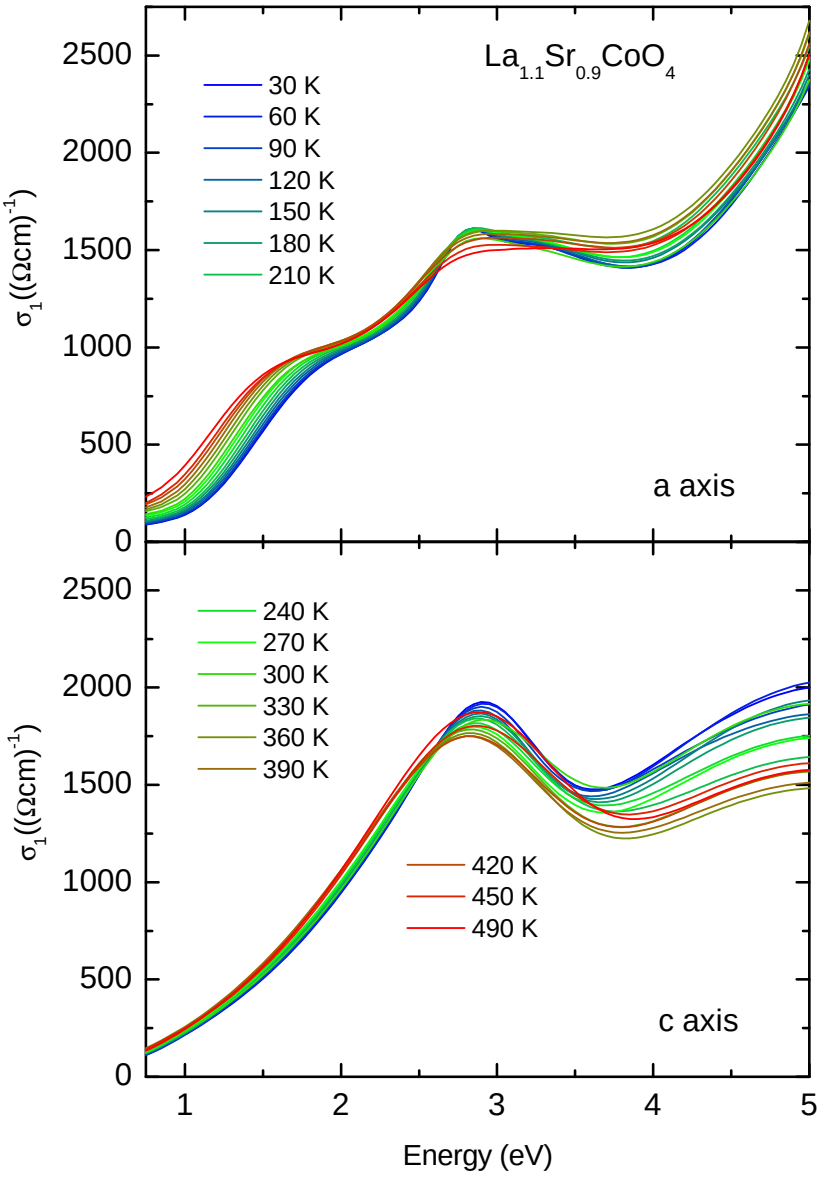

Figure 7.41: Optical conductivity $\sigma_1(\omega)$ of $La_{1.1}Sr_{0.9}CoO_4$ for the a and c direction between 0.75 eV and 5.0 eV for temperatures ranging from 30 K to 490 K.

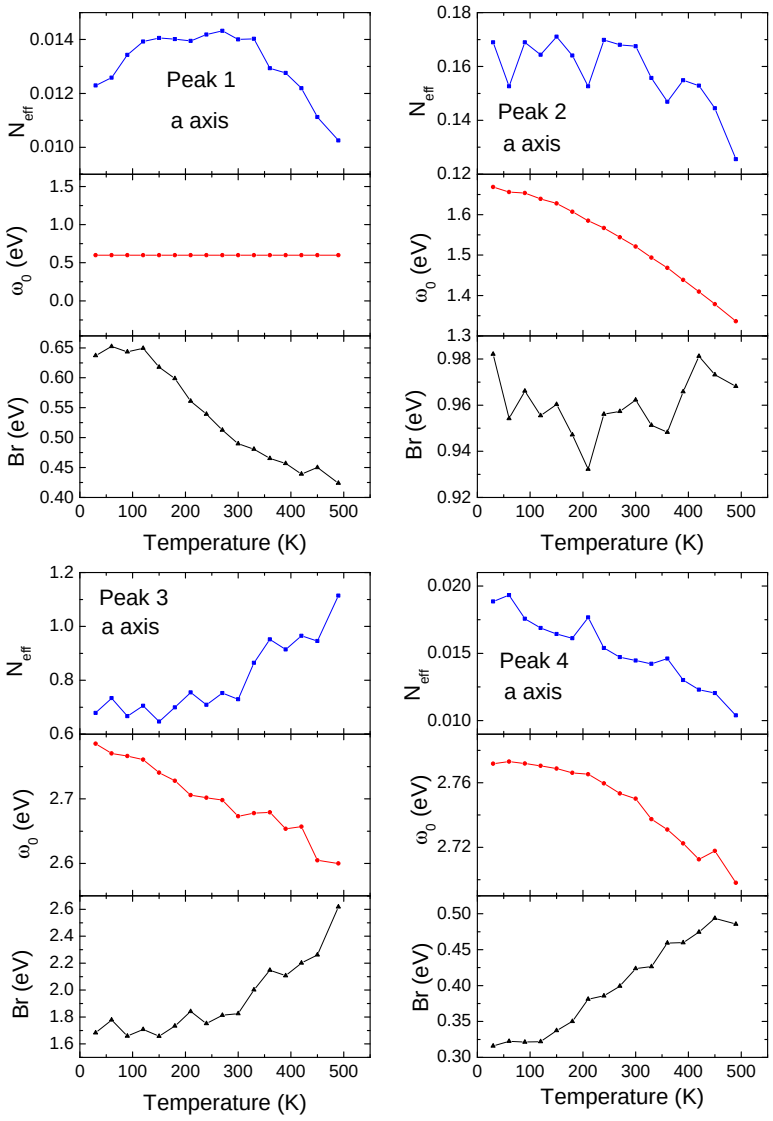

Figure 7.42: Results of the fit to the measured data of $La_{1.1}Sr_{0.9}CoO_4$ with Gaussian oscillators. The parameters describing ε_2^a are shown. The four panels refer to the four oscillators with the lowest energies. The Gaussian oscillators corresponding to peaks $1-4$ are visualized in Fig. 7.39. See the caption of Fig. 7.37 for the definition of the parameters.

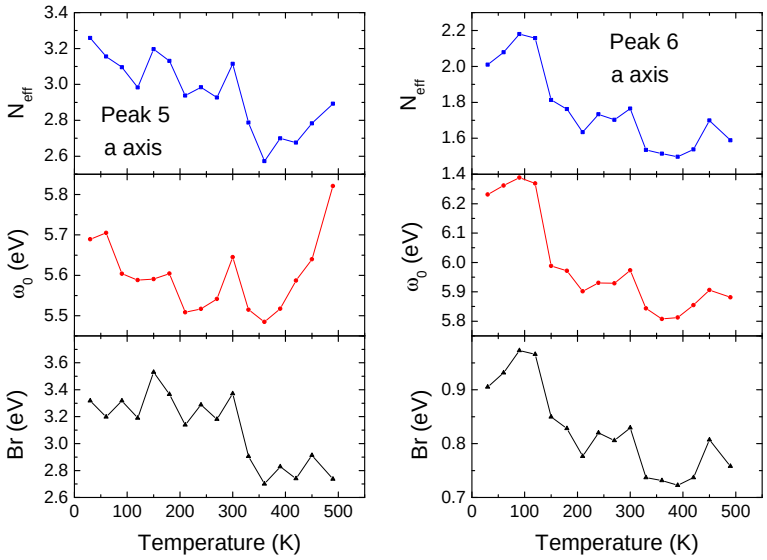

Figure 7.43: Results of the fit to the measured data of $La_{1.1}Sr_{0.9}CoO_4$ with Gaussian oscillators. The parameters describing ε_2^a are shown. The two panels refer to the two oscillators with the highest energies. The Gaussian oscillators corresponding to peaks 5 and 6 are visualized in Fig. 7.39. See the caption of Fig. 7.37 for the definition of the parameters.

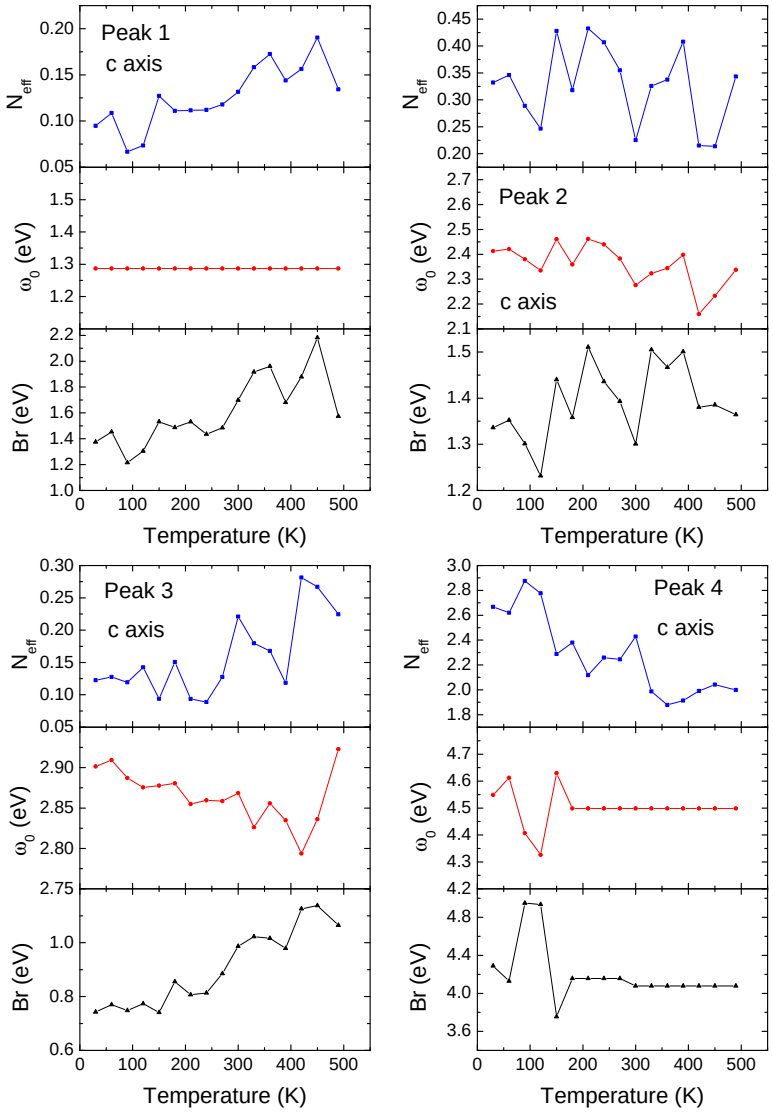

Figure 7.44: Results of the fit to the measured data of $La_{1.1}Sr_{0.9}CoO_4$ with Gaussian oscillators. The parameters describing ε_2^c are shown. The Gaussian oscillators corresponding to peaks $1-4$ are visualized in Fig. 7.39. See the caption of Fig. 7.37 for the definition of the parameters.

compound	size of the sample	orientation	surface	MSE of the fit	number of oscillators
$LaCoO_3$	diameter 4 mm		10Å	$0.4-0.8$	6
$EuCoO_3$	diameter 4 mm		10Å	$0.3-0.5$	7
La_2CoO_4	diameter 5 mm	ac ab	30Å	$0.6-1.2$	3 (a axis) 4 (c axis)
$La_{1.67}Sr_{0.33}CoO_4$	diameter 6 mm	ac	30Å	$0.3-0.6$	4 (a axis) 4 (c axis)
$La_{1.55}Sr_{0.45}CoO_4$	diameter 4 mm	ac	30Å	$0.9-1.5$	4 (a axis) 4 (c axis)
$La_{1.5}Sr_{0.5}CoO_4$	diameter 5 mm	ac	30Å	$0.3-0.6$	4 (a axis) 4 (a axis)
$La_{1.5}Ca_{0.5}CoO_4$	3 mm × 3 mm 4 mm × 2 mm	ab ac	30Å	$1.5-3.5$	4 (a axis) 4 (c axis)
$La_{1.1}Sr_{0.9}CoO_4$	1.5 mm × 2.5 mm 1 mm × 2 mm	ab ac	30Å	$0.3-0.6$	6 (a axis) 4 (c axis)

Table 7.2: Information on the data acquisition and analysis of the measured cobaltate samples.

7.3 Discussion

7.3.1 Results on $LaCoO_3$ and $EuCoO_3$

$LaCoO_3$ and $EuCoO_3$ can be characterized as CT insulators [57, 143–145, 166]. One therefore expects the lowest interband excitation from the O $2p$ band to the Co $3d$ band. As discussed in Sec. 7.1.1, it is well established that the Co^{3+} ions with $3d^6$ electron configuration realize the LS state in the ground state. In the LS state, the t_{2g} level is fully occupied, while the e_g level is empty, see Fig. 7.5 on page 146. Charge-transfer excitations can therefore only take place between the O $2p$ band and the e_g level. A Co^{3+} IS or HS state, on the contrary, allows for CT excitations to both, the t_{2g} level and the e_g level. We therefore expect that a thermal population of higher spin states from a Co^{3+} LS state is well visible in the optical spectra. Surprisingly, optical data of $LaCoO_3$ published by Tokura *et al.* [27] do hardly vary across the spin-state transition between 9 K and 293 K, see Fig. 7.45. These data have been acquired by the use of reflectivity measurements with a subsequent Kramers-Kronig analysis. Also valence-band photoemission and x-ray absorption spectra acquired on $LaCoO_3$ show only small changes across the spin-state transition [166]. The calculated spectra obtained on the basis of a cluster model, on the other hand, are considerably different for an initial LS or HS state [166].

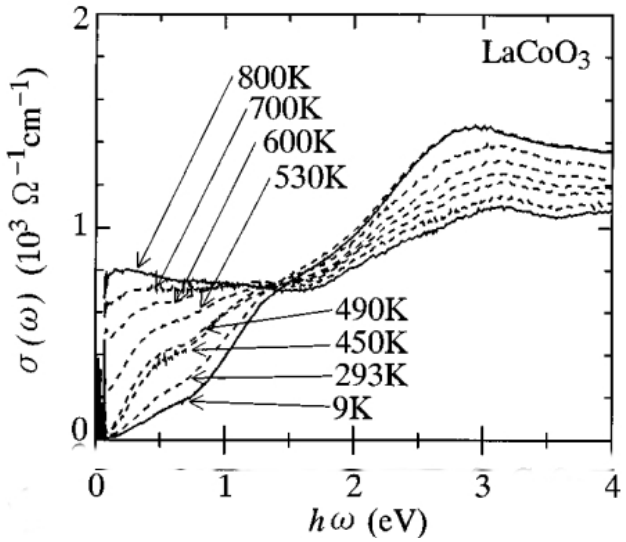

Figure 7.45:
Optical conductivity of $LaCoO_3$ as obtained by Tokura *et al.* [27] by the use of reflectivity measurements with a subsequent Kramers-Kronig analysis. Taken from Ref. [27].

We have made the experience that ellipsometry is very well suited for a detailed analysis of the temperature dependence. The optical conductivity $\sigma_1(\omega)$ of $LaCoO_3$ and $EuCoO_3$ is shown in Figs. 7.16 and 7.23, respectively. Figure 7.46 compares the optical conductivity of $LaCoO_3$ and $EuCoO_3$ at 15 K, 300 K, and 470 K. The spectra of both compounds show strong similarities. One observes rather complex spectra, the fit to the measured data is based on a large number of Gaussian oscillator (six Gaussian oscillators are needed to describe ε_2 of $LaCoO_3$, while seven Gaussian oscillators are needed to describe ε_2 of $EuCoO_3$, see Fig. 7.14). At first sight, one does not see pronounced changes of the optical conductivity of $LaCoO_3$ across the spin-state transition temperature. In agreement with the observation of Tokura *et al.* [27], the optical conductivity of $LaCoO_3$ gains spectral weight at low energies around 1 eV for increasing temperature. This can be recognized as a signature of the metal-insulator transition taking place at $T \approx 480$ K. The fit to the measured data of $LaCoO_3$ describes the spectral weight at low energies by a Gaussian oscillator at around 0.7 eV, which gains weight with increasing temperatures and is completely absent for temperatures below 80 K, see Figs. 7.14 and 7.20. Our MIR ellipsometric data reveals that a finite energy gap is still present at $T = 300$ K, see Fig. 7.19. Unfortunately, it was not possible to acquire MIR data at higher temperatures. The value of $\sigma_1(\omega)$ at 1 eV at low temperatures is lower in our data than in the data of Tokura *et al.* [27] (our data: σ_1 (1 eV,15 K)$\approx$ 250 $(\Omega\text{cm})^{-1}$, Tokura *et al.* [27] : σ_1(1 eV, 9 K)$\approx$ 400 $(\Omega\text{cm})^{-1}$), which demonstrates that we succeed in a better description of the band gap. Furthermore, our data show a subtle peak structure at approx. 2 eV at lower temperatures, which is absent in the data of Tokura *et al.* [27] (see discussion below).

Due to the complexity of the spectra of $LaCoO_3$ and $EuCoO_3$, a detailed assignment of the observed absorption bands in terms of CT excitations $|2p^6 3d^6\rangle \rightarrow |2p^5 3d^7\rangle$ seems difficult. Nevertheless, to gain information about the $3d^7$ final states, we consider the Tanabe-Sugano-Kamimura diagram of a d^7 system, see Fig. 7.47. If the Co^{3+} ions realize the LS state, CT excitations are only possible in states with $S = 1/2$, according to Fig. 7.47 the $3d^7$ final states with the lowest energies are the ^2E, the $^2T_1$, and the $^2T_2$ multiplet. On the other hand, if the Co^{3+} ions realize the HS state, excitations are only possible in states with $S = 3/2$. In this case, the $3d^7$ final states with the lowest energies are the $^4T_1$ and the $^4T_2$ multiplet. We can read off the relevant value of Dq/B for $LaCoO_3$ from the Tanabe-Sugano-Kamimura diagram of the d^6 system (Fig. 7.4). For competing HS and LS states, Dq/B amounts to approx. 2. It can be seen from the Tanabe-Sugano-Kamimura diagram of the d^7 system (Fig. 7.47), that for $Dq/B \approx 2$ the energies of both, the ^2E and the $^4T_1$ multiplet, and the ($^2T_1$, $^2T_2$) and the $^4T_2$ multiplet are very similar. This might offer an explanation for the similarity of the optical spectra of $LaCoO_3$ for temperatures below and above the spin-state transition temperature. However, more elaborate theoretical investigations are

necessary to fully understand the optical spectra. The optical spectra of $LaCoO_3$ and $EuCoO_3$ might be dominated by the oxygen $2p$ bands. Furthermore, strong hybridization between the oxygen $2p$ bands and the Co $3d$ bands are assumed to play an important role in $LaCoO_3$ and $EuCoO_3$. Particularly the hybridization between the Co e_g states and O $2p$ states is assumed to be very strong [144, 166].

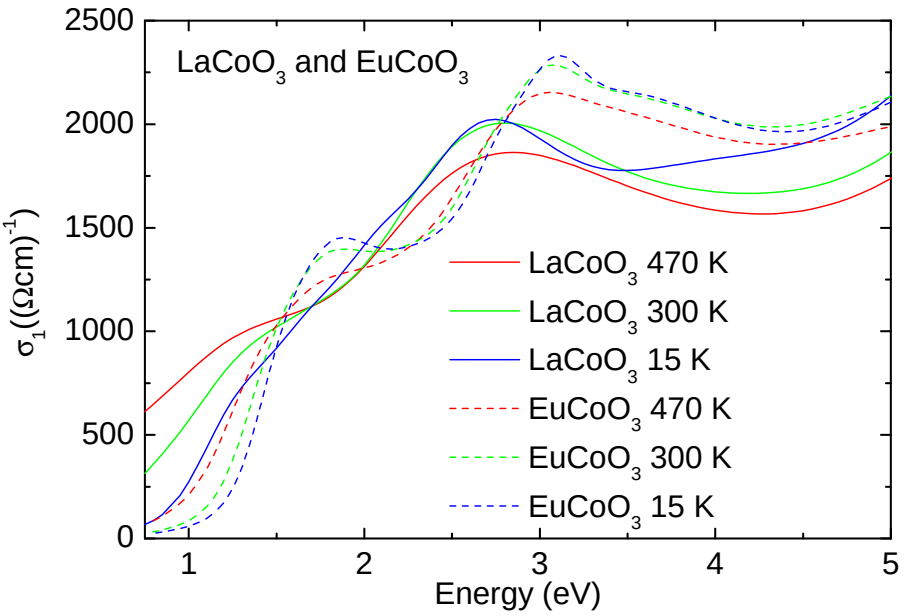

Figure 7.46: Comparison of the optical conductivity $\sigma_1(\omega)$ of $LaCoO_3$ and $EuCoO_3$ at 15 K, 300 K, and 470 K.

We conduct further investigations of the temperature dependence of the optical spectra of $LaCoO_3$ and $EuCoO_3$ with the aim to detect signatures of the spin-state transition in the data of $LaCoO_3$. Close inspection of the temperature dependence of the optical conductivity $\sigma_1(\omega)$ of $LaCoO_3$ and $EuCoO_3$ reveals some important differences, see Fig. 7.46 and also Figs. 7.16 and 7.23. While $\sigma_1(\omega)$ of $EuCoO_3$ shows two pronounced peak structures at around 1.7 eV and 3 eV, that show the expected broadening with increasing temperature, $\sigma_1(\omega)$ of $LaCoO_3$ shows some peculiarities. The value of the optical conductivity $\sigma_1(\omega)$ of $LaCoO_3$ at around 2 eV shows a particular decrease with increasing temperature, which is particularly pronounced between 40 K and 150 K, indicating a correlation with the spin-state transition. Figure 7.48 presents the detailed temperature dependence of the optical conductivity $\sigma_1(\omega)$ of $LaCoO_3$ between 40 K and 80 K. The distinct temperature dependence of $\sigma_1(\omega)$ of $LaCoO_3$ at around 2 eV becomes obvious from Figs. 7.49

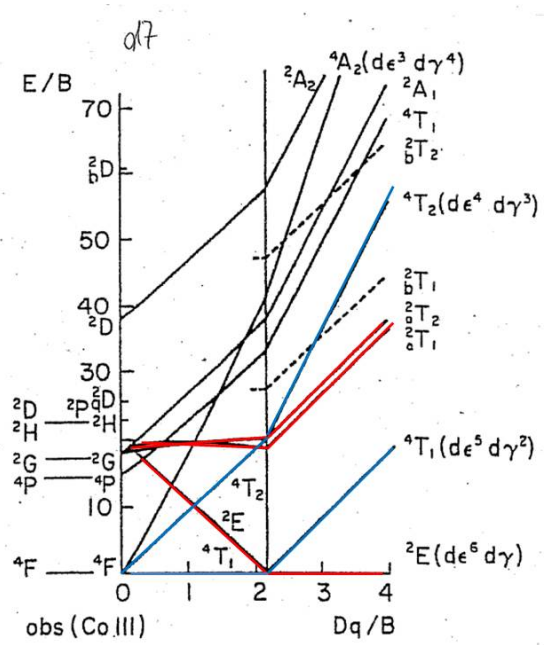

Figure 7.47: Tanabe-Sugano-Kamimura diagram of a d^7 system (cf. Sec. 2.2.2). If the Co^{3+} $3d^6$ ions realize the LS state, possible Co^{2+} $3d^7$ final states of CT excitations have $S = 1/2$. The corresponding multiplets with the lowest energies ^2E, $^2T_1$, and $^2T_2$ are marked in red. If the Co^{3+} ions realize the HS state, possible $3d^7$ final states have $S = 3/2$. The corresponding multiplets with the lowest energies $^4T_1$ and $^4T_2$ are marked in blue. Taken from Ref. [35].

and 7.50, where the values of $\sigma_1(\omega)$ of $LaCoO_3$ at 2 eV and $EuCoO_3$ at 1.85 eV are plotted as a function of temperature [1]. In the fit to the measured data of $LaCoO_3$, the absorption band at 2 eV is described by a Gaussian oscillator (peak 4 in Figs. 7.14 and 7.20), which is only present for temperatures below 80 K, see Figs. 7.14 and 7.20. Also the neighboring oscillator at approx. 1.7 eV (peak 3 in Figs. 7.14 and 7.20) looses significant weight with increasing temperature. The jump of the parameters of peak 3 (see Fig. 7.20, in particular Br and N_{eff}) between 75 K and 80 K is an artifact of the fit. As oscillator peak 4 is missing for $T \geqslant 80$ K, peak 3 compensates part of its weight. However, it is very obvious from Figs. 7.16 and 7.48, that the pronounced peak structure at 2 eV is absent above $T = 80$ K.
Furthermore, the optical conductivity of $LaCoO_3$ shows interesting behavior around 3.2 eV, see Figs. 7.16, 7.46, and 7.48. The value of the optical conductivity $\sigma_1(\omega)$

[1] For $EuCoO_3$ the value of $\sigma_1(\omega)$ at $\omega = 1.85$ eV is plotted as this value amounts to the position of the local maximum of $\sigma_1(\omega)$, for $LaCoO_3$, where no local maximum is present around $\omega = 2$ eV in $\sigma_1(\omega)$, the peculiar behavior becomes most obvious around $\omega = 2$ eV.

of $LaCoO_3$ at 3.2 eV is plotted as a function of temperature in Fig. 7.49. For comparison, the corresponding value of the optical conductivity $\sigma_1(\omega)$ of $EuCoO_3$ is shown in Fig. 7.50, here $\sigma_1(3.5\,\text{eV})$ does not show this peculiar behavior [2]. Close inspection of the line shape of $\sigma_1(\omega)$ around 3 eV (see Figs. 7.16, 7.46, and 7.48) gives the impression that an absorption band is present at approx. 3.2 eV, that shows an unusual decreasing peak frequency for decreasing temperature. This subtle softening of the peak frequency with decreasing temperature is visible up to 300 K, for higher temperatures the broadening of the underlying broad absorption band is dominant and leads to a degrease of $\sigma_1(3.2\,\text{eV})$ with increasing temperature. The fit to the measured data with Gaussian oscillators describes the spectral weight around 3 eV by two largely overlapping broad oscillators at approx. 2.2 eV − 2.5 eV and at approx. 3 eV, denoted as peak 5 and peak 6, respectively, in Figs. 7.14 and 7.21. Peak 5 shows the usual hardening of the peak energy and decreasing width with decreasing temperature. The unexpected behavior of the line shape of $\sigma_1(\omega)$ around 3.2 eV becomes most obvious from the parameters of peak 6. The width of peak 6 decreases upon increasing temperatures by nearly 15% between 15 K and 470 K, see Fig. 7.21.

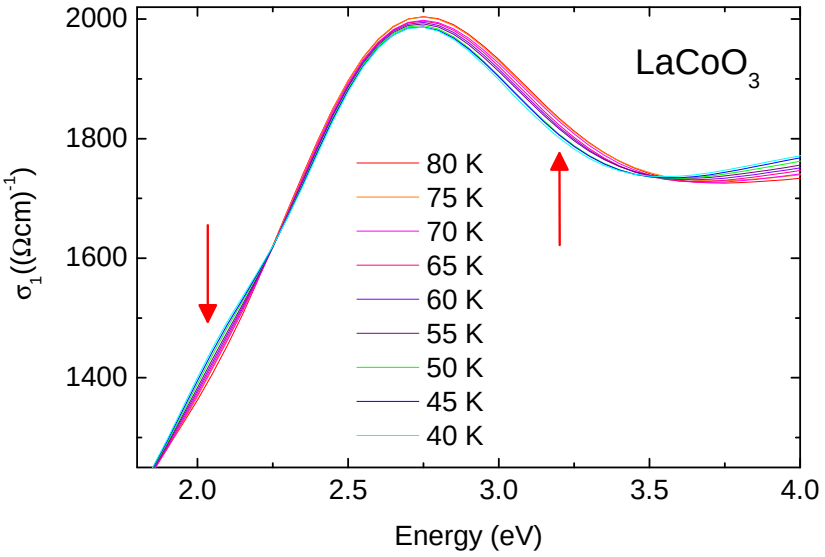

Figure 7.48: Optical conductivity $\sigma_1(\omega)$ of $LaCoO_3$ between 40 K and 80 K.

[2] The value of $\sigma_1(\omega)$ of $EuCoO_3$ is considered at a higher energy ($\omega = 3.5\,\text{eV}$) for $EuCoO_3$ than for $LaCoO_3$ ($\omega = 3.2\,\text{eV}$), because the maximum of $\sigma_1(\omega)$ around 3 eV is shifted to higher energies by 0.3 eV in $EuCoO_3$ ($\sigma_1^{max}(\omega)$ is located at $\omega \approx 3.1\,\text{eV}$) compared to $LaCoO_3$ (σ_1^{max} is located at $\omega \approx 2.8\,\text{eV}$).

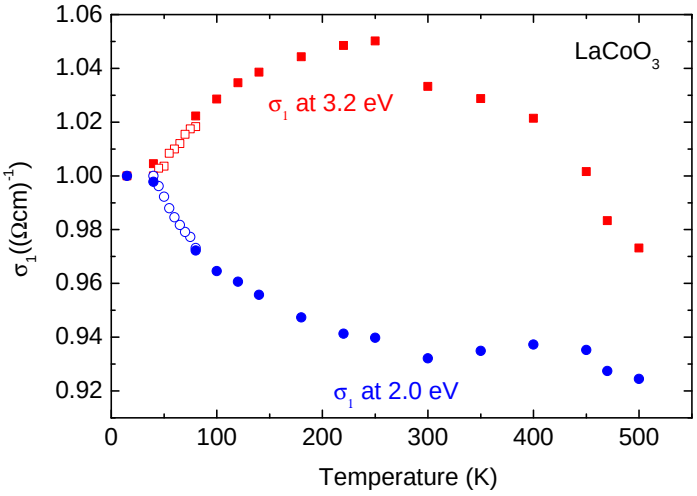

Figure 7.49: Value of the optical conductivity of $LaCoO_3$ at 2 eV (blue circles) and 3.2 eV (red squares) normalized to one at the lowest measured temperature. The open symbols refer to data that has been obtained within measurement series 2.

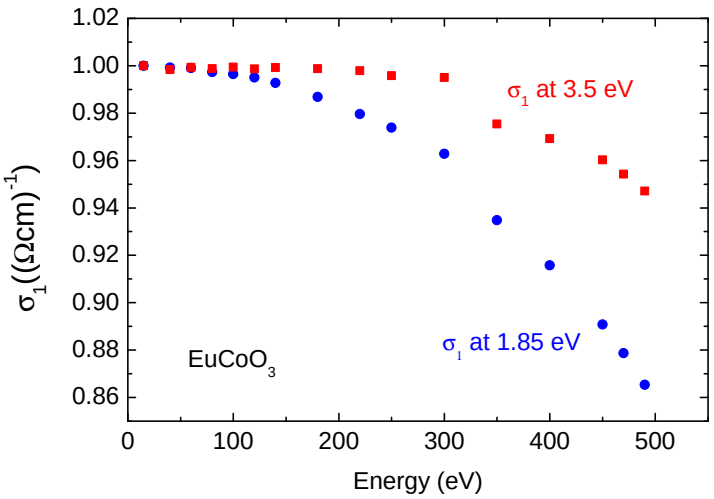

Figure 7.50: Value of the optical conductivity of $EuCoO_3$ at 1.85 eV (blue circles) and 3.5 eV (red squares) normalized to one at the lowest measured temperature.

To conclude, due to the high quality of our data, we succeed in revealing some interesting peculiarities in the temperature dependence of the optical conductivity of $LaCoO_3$, that are not visible in the data of Tokura *et al.* [27]. As these peculiarities are absent in the data of $EuCoO_3$, we attribute them to signatures of the spin-state transition.

7.3.2 Results on $La_{2-x}Sr_xCoO_4$ (x = 0, 0.33, 0.45, 0.5, 0.9) and $La_{1.5}Ca_{0.5}CoO_4$

Optical data of $La_{2-x}Sr_xCoO_4$ and $La_{2-x}Ca_xCoO_4$ are rare in the literature. Room-temperature reflectivity data of $La_{2-x}Sr_xCoO_4$ for $E \parallel ab$ are available in Ref. [195] for doping concentrations $x = 0.0$, 0.5, and 0.8, see Fig. 7.51, and in Ref. [126] for doping concentration $x = 1$. Temperature-dependent optical data of $La_{1.5}Sr_{0.5}CoO_4$ and $La_{1.5}Ca_{0.5}CoO_4$ for temperatures up to 850 K have been published by Lee *et al.* [32], but only for $E \parallel ab$. The data have been obtained by reflectivity measurements with a subsequent Kramers-Kronig analysis. The data are shown in Fig. 7.52. However, the authors of Ref. [32] do not give a detailed explanation of the origin of the observed absorption peaks. Furthermore, we have experienced that ellipsometry is much better suited for a precise analysis of the temperature dependence. In the following, we will discuss our ellipsometric data of layered cobaltates and compare them with the data existent in the literature.

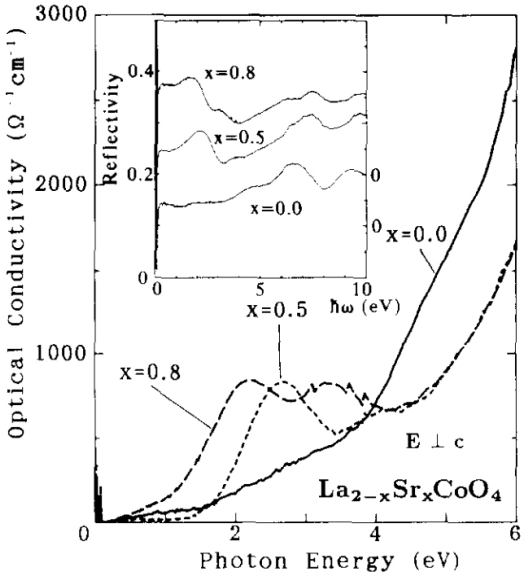

Figure 7.51:
Optical conductivity of $La_{2-x}Sr_xCoO_4$ ($x = 0.0$, 0.5, and 0.8) for $E \parallel ab$ as obtained by Uchida *et al.* [195] by the use of reflectivity measurements with a subsequent Kramers-Kronig analysis. Taken from Ref. [195].

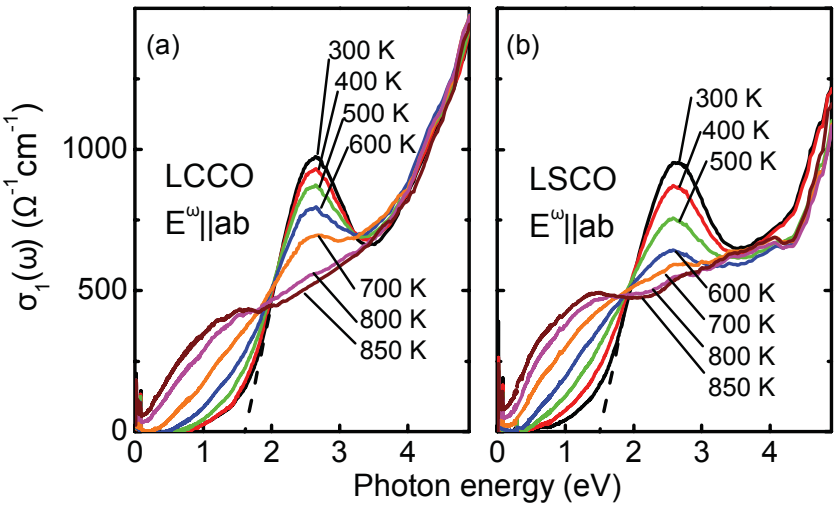

Figure 7.52: Optical conductivity of (a) $La_{1.5}Ca_{0.5}CoO_4$ and (b) $La_{1.5}Sr_{0.5}CoO_4$ for $E \parallel ab$ for various temperatures as obtained by Lee *et al.* [32] by the use of reflectivity measurements with a subsequent Kramers-Kronig analysis. Taken from Ref. [32]

Electron configuration

The CoO_6 octahedra of the layered compounds are significantly elongated. The out-of-plane bond lengths $Co^{2+} - O_{apical}$ and $Co^{3+} - O_{apical}$ of the half-doped Sr compound $La_{1.5}Sr_{0.5}CoO_4$ amount to 2.190 Å and 2.075 Å, respectively, and the in-plane bond lengths $Co^{2+} - O_{basal}$ and $Co^{3+} - O_{basal}$ have been determined to be 1.954 Å and 1.888 Å, respectively [42]. In a one-electron picture the $3d$ orbitals thus order, from lowest to highest energy: xz/yz, xy, $3z^2 - r^2$, $x^2 - y^2$ [138]. The HS Co^{2+} $t_{2g}^5 e_g^2$ electron configuration is sketched in Fig. 7.53. According to Wu *et al.* [139], the crystal field splitting between xz/yz and xy is on the order of 30 meV, the HS Co^{2+} configuration has one t_{2g} hole in the xy orbital [139]. The Co^{3+} LS ion has a closed t_{2g} shell (electron configuration t_{2g}^6) with a splitting between xz/yz and xy of about 70 meV. The splitting is enhanced for Co^{3+} compared to Co^{2+} due the smaller $Co - O$ bond length in the former [139]. In the Co^{3+} HS configuration two electrons are promoted to the e_g level, resulting in the electron configuration $t_{2g}^4 e_g^2$ with spin $S = 2$. The Co^{3+} IS state has one electron in the e_g shell, which resides in the $3z^2 - r^2$ orbital, due to the $3z^2 - r^2/x^2 - y^2$ splitting of the e_g manifold of 0.7 eV [139, 189]. The IS configuration has one hole in the t_{2g} level. In a one-electron picture one would expect the hole to reside in the xy orbital. However, Wu and Burnus [139] have pointed out that the multiplet effect and the spin-orbit coupling play a significant role for the IS state. Due to the stronger

Coulomb repulsion between $3z^2 - r^2$ and xz/yz than between $3z^2 - r^2$ and xy, the hole rather resides in the xz/yz level. The degeneracy of the partially filled xz/yz level is then lifted by spin-orbit coupling, resulting in the following electron configuration of the IS state: $t_{2g}^3 xy^1 (xz + iyz)^1 (3z^2 - r^2)^1$ [139]. A sketch of the Co^{3+} LS, IS, and HS electron configuration in the crystal field of the tetragonally distorted O_6^{2-} octahedra is shown in Fig. 7.54.

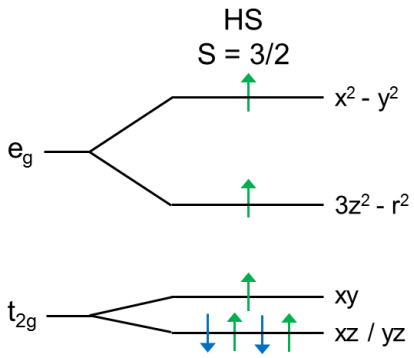

Figure 7.53: Sketch of the HS electron configuration ($S = 3/2$) of the $3d^7$ Co^{2+} ion in the crystal field of the elongated O_6^{2-} octahedra of the layered compounds. The t_{2g} band is split into the lower-lying xz/yz level and the higher-lying xy level, the magnitude of the splitting amounts to 30 meV [139]. The e_g band is split into the lower-lying $3z^2 - r^2$ level and the higher-lying $x^2 - y^2$ level, which are both singly occupied.

Peak assignment

Our spectra for $E \parallel ab$ of the compounds $La_{1.5}Sr_{0.5}CoO_4$ and $La_{1.5}Ca_{0.5}CoO_4$ are generally in good agreement with the results of Lee *et al.* [32] and Uchida *et al.* [195], see Figs. 7.52 and 7.51. The broad absorption band around 2.5 eV is clearly visible in all data sets. For $La_{1.1}Sr_{0.9}CoO_4$, our spectra for $E \parallel ab$ reveal a splitting of the broad absorption band into two bands at around 1.5 eV and 2.7 eV, this observation is in agreement with the one of Uchida *et al.* [195] on $La_{1.2}Sr_{0.8}CoO_4$ and the one of Moritomo *et al.* [126] on $LaSrCoO_4$. However, the spectrum for $E \parallel ab$ of La_2CoO_4 of Uchida *et al.* [195] differs from our result. While the broad band around 2.5 eV is not visible in the room-temperature data of Uchida *et al.* [195], we do observe this broad band around 2.5 eV in the data corresponding to $T = 300$ K, but find its suppression at higher temperatures starting at $T \gtrsim 320$ K.

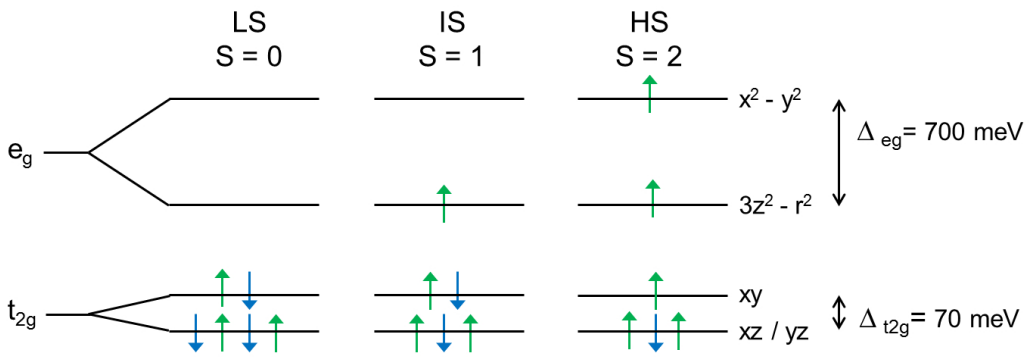

Figure 7.54: Sketch of the LS ($S = 0$), IS ($S = 1$), and HS ($S = 2$) electron configuration of the $3d^6$ Co^{3+} ion in the crystal field of the elongated O_6^{2-} octahedra of the layered compounds. The t_{2g} band is split into the lower lying xz/yz level and the higher lying xy level and the e_g band is split into the lower lying $3z^2 - r^2$ level and the higher lying $x^2 - y^2$ level. The t_{2g} splitting Δ_{t2g} amounts to 70 meV, the e_g splitting Δ_{eg} has been calculated to be 0.7 eV [139]. Simply considering the sequence of the energy levels one would expect the t_{2g} hole of the IS state to be located in the higher lying xy level, however, Wu and Burnus [139] have pointed out that the multiplet effect plays an important role for the IS state electron configuration. The t_{2g} hole resides in the lower lying xz/yz level rather than in the higher lying xy level due to the stronger Coulomb repulsion between $3z^2 - r^2$ and xz/yz than between $3z^2 - r^2$ and xy [139].

As already discussed in Sec. 7.1.2, Wu *et al.* [138,139] performed density-functional calculations using the LSDA+U for the mixed Co^{2+}/Co^{3+} system $La_{1.5}Sr_{0.5}CoO_4$ and the pure Co^{3+} system $LaSrCoO_4$. Within their calculations they include the multiplet effect and spin-orbit coupling and further account for the strong tetragonal distortion of the CoO_6 octahedra. As discussed above, they conclude Co^{3+} to be in the LS state in $La_{1.5}Sr_{0.5}CoO_4$ and in a HS/LS mixed state in $LaSrCoO_4$. The Co^{2+} ions of $La_{1.5}Sr_{0.5}CoO_4$ are assumed to be in a HS state. The spectra obtained by Wu *et al.* [138, 139] are shown in Figs. 7.55 and 7.56. They will be used for the peak assignment.

To compare the data of the compounds with different doping concentrations x, Figs. 7.57, 7.58, and 7.59 show the optical conductivity $\sigma_1(\omega)$ of $La_{2-x}Sr_xCoO_4$ ($x = 0, 0.33, 0.45, 0.5, 0.9$), $La_{1.5}Ca_{0.5}CoO_4$ and $LaCoO_3$ for $T = 15\,K$, $300\,K$, and $490\,K$, respectively.

Let us first focus on the spectra of the *ab* plane. In σ_1^{ab} one observes a pronounced peak at around 2.5 eV for the layered compounds with $x \leq 0.5$ (see Figs. 7.57 – 7.59 and also Figs. 7.27, 7.30, 7.32, 7.34, and 7.36). The main features of the fits to the measured data of the layered compounds with $x \leq 0.5$ are similar. In the fits, the pronounced peak at around 2.5 eV is modeled mainly by a Gaussian oscillator, see Fig. 7.28. The fits further consist of two Gaussian oscillators at higher energies, that account for the pronounced increase of $\sigma_1^{ab}(\omega)$ above 4 eV (for the undoped compound La_2CoO_4 one Gaussian oscillator suffices). In addition, a small Gaussian oscillator is used to model a small feature in the data at around 1 eV. The parameters of the Gaussian oscillators are presented in Fig. 7.37. The Gaussian oscillators are denoted peak 1 to 4 according to their energetic position, see Figs. 7.28 and 7.37, the oscillator around 2.5 eV is peak 2.
In the following, the peaks are assigned to CT excitations O $2p^6$ $Co^{3+}3d^6 \rightarrow$ O $2p^5$ $Co^{2+}3d^7$ and O $2p^6$ $Co^{2+}3d^7 \rightarrow$ O $2p^5$ $Co^{1+}3d^8$ using the results of Wu *et al.* [138, 139] (Figs. 7.55 and 7.56). The broad absorption band around 2.5 eV is assigned to two distinct excitations, involving both, HS Co^{2+} and LS Co^{3+} sites. The lowest in-plane optical excitation is expected from the O_{basal} $2p$ orbital. The O_{basal} $2p$ density of states of $La_{1.5}Sr_{0.5}CoO_4$ is shown in the lower panel of Fig. 7.55 (O1 $2p$, green line). The density of states of the different $3d$ orbitals of the HS Co^{2+} and the LS Co^{3+} ions are presented in the upper and middle panel of Fig. 7.55, respectively. The xy orbital of the HS Co^{2+} ions is only partially filled. It is located approx. 2 eV above the Fermi level. As it yields finite overlap with O_{basal} $2p$, the broad absorption band around 2.5 eV is assigned to the excitation from O_{basal} $2p$ to the HS Co^{2+} xy orbital. In addition, also the unoccupied e_g orbitals $x^2 - y^2$ and $3z^2 - r^2$ of the LS Co^{3+} ions yield finite overlap with O_{basal} $2p$, they are also located approx. 2 eV above the Fermi level. We thus propose that the excitation from O_{basal} $2p$ to LS Co^{3+} $x^2 - y^2$ and $3z^2 - r^2$ gives a second contribution to the broad peak for the doped compounds. This interpretation is in agreement with the one suggested by Wu and Burnus [139] on the basis of the room-temperature reflectivity data published by Uchida *et al.* [195] where the broad peak at around 2.5 eV is also clearly visible, see Fig. 7.51.
As opposed to the partially filled xy orbital of the HS Co^{2+} ions, the $x^2 - y^2$ and $3z^2 - r^2$ orbitals of the LS Co^{3+} ions are unoccupied. As a consequence excitations to $x^2 - y^2$ and $3z^2 - r^2$ of LS Co^{3+} are possible in both spin channels and thus the spectral weight of the broad peak should increase with increasing doping concentration. The upper panel of Fig. 7.60 presents the local maximum value of the optical conductivity $\sigma_1^{ab}(\omega)$ around 2.5 eV. Indeed, it is seen from the upper panel of Fig. 7.60 and also from Fig. 7.57 that the peak height of the absorption band around 2.5 eV is reduced when reducing the Sr doping from $x = 0.5$ over $x = 0.33$ to $x = 0$. We calculated the spectral weight of the broad band by making use of the parameters of peak 2 of the fit with Gaussian oscillators, see Fig. 7.37. In agreement with our expectations, the spectral weight is considerably

smaller for the undoped compound La_2CoO_4 compared to the doped compounds (for $T \lesssim 400\,\mathrm{K}$, for higher temperatures see the discussion of the temperature dependence in Sec. 7.3.2). But we do not observe an increasing spectral weight for increasing doping concentration x for the compounds with $x > 0$. It is however highly questionable if the spectral weight calculated from the parameters of the Gaussian oscillator peak 2 is physically meaningful. The broad absorption band around 2.5 eV is assigned to two distinct excitations, although it is modeled by a single Gaussian oscillator in the fit. Peak 2 has further considerable overlap with the higher lying peak 3. The energetic position of peak 3 and therefore also the overlap with peak 2 varies with doping concentration (see Fig. 7.37). Particularly, the spectral weight of the compound with $x = 0.33$ exceeds the one of the compounds with $x = 0.45$ and $x = 0.5$ because the Gaussian oscillator peak 2 is much broader for this compound (see Fig. 7.37).
Above 4 eV, a pronounced increase of $\sigma_1^{ab}(\omega)$ is observed. This strong absorption could be attributed to the CT excitation from O_{basal} $2p$ to the partially filled e_g orbitals of the HS Co^{2+} ions. The density of states of the down spin channel of $x^2 - y^2$ and $3z^2 - r^2$ peaks at about $3.5\,\mathrm{eV} - 5\,\mathrm{eV}$ above the Fermi level in $La_{1.5}Sr_{0.5}CoO_4$, see upper panel of Fig. 7.55. However, within this picture a decreasing spectral weight with increasing doping concentration x is expected, which is not observed. The spectral weight above 4 eV could further originate from CT excitations from O_{basal} $2p$ bands that lie $2\,\mathrm{eV} - 4\,\mathrm{eV}$ below the Fermi level to the LS Co^{3+} e_g orbitals and the HS Co^{2+} xy orbital. In this case an increasing spectral weight with increasing doping concentration is expected. In agreement, the spectral weight above 4 eV is reduced in the pure Co^{2+} compound La_2CoO_4 compared to the compounds with $x > 0$.
The spectra of the layered compound with doping concentration $x = 0.9$ look significantly different. The pronounced peak in the ab plane spectra at around 2.5 eV of the compounds with doping concentration $x \leq 0.5$ is split into two bands at around 1.5 eV and 2.7 eV, see Fig. 7.39. A similar peak structure is visible in the room-temperature reflectivity data of $La_{1.2}Sr_{0.8}CoO_4$ and $LaSrCoO_4$ in Refs. [195] and [126], respectively, see Fig. 7.51. This change of the optical spectra supports the claim of Wu [138] of a doping-induced spin-state transition in $La_{2-x}Sr_xCoO_4$ from a Co^{3+} LS configuration in $La_{1.5}Sr_{0.5}CoO_4$ to a mixed Co^{3+} HS/LS state in the pure Co^{3+} compound $LaSrCoO_4$. Wu's result [138] for the density of states of the Co $3d$ and O $2p$ orbitals within a mixed Co^{3+} HS/LS scenario of $LaSrCoO_4$ is presented in Fig. 7.56. We propose that the absorption band around 2.7 eV in σ_1^{ab} of $La_{1.1}Sr_{0.9}CoO_4$ corresponds to the broad band around 2.5 eV of the compounds with $x \leq 0.5$, it can be assigned to the CT excitation from the O_{basal} $2p$ orbital to the $x^2 - y^2$ and $3z^2 - r^2$ orbitals of the LS Co^{3+} ions, while the contribution of the CT excitation from O_{basal} $2p$ to the HS Co^{2+} xy orbital should be rather small due to the only small content of Co^{2+} in $La_{1.1}Sr_{0.9}CoO_4$. In agreement with Wu [138], we assign the peak at about 1.5 eV to the CT excitations from the O_{basal}

$2p$ orbital to the partially filled xy and $xz-iyz$ orbitals of the HS Co^{3+} ions, which are located about 0.9 eV above the Fermi level [138] (see Fig. 7.56).
Within the fit with Gaussian oscillators to the measured data of $La_{1.1}Sr_{0.9}CoO_4$ (see Fig. 7.39), the absorption band at about 1.5 eV is described by a Gaussian oscillator with $N_{eff} \approx 0.33$ (peak 2), while the band at about 2.7 eV is described by a broad Gaussian oscillator with $N_{eff} \approx 1.4 - 2.4$ (peak 3) and an additional small oscillator with $N_{eff} \approx 0.03$ (peak 4). See Figs. 7.42 and 7.43 for the parameters of the oscillators. The line shape of ε_2^{ab} is further described by a small Gaussian oscillator at 0.6 eV (peak 1, $N_{eff} \approx 0.013$), and two Gaussian oscillators at higher energies accounting for the spectral weight above 4 eV (peak 5 and 6).

Let us now focus on the c axis spectra. The spectra of the layered compounds with doping concentrations $x \leq 0.5$ show a pronounced peak at 3.5 eV− 4 eV in $\sigma_1^c(\omega)$ (see Figs. 7.57 − 7.59 and also Figs. 7.27, 7.30, 7.32, 7.34, and 7.36). Along c, the $2p$ orbitals of O_{apical} have finite overlap with the $3d$ orbitals of the Co ions. The density of states of the O_{apical} $2p$ orbitals is shown in the lower panel of Fig. 7.55 for $La_{1.5}Sr_{0.5}CoO_4$ (red line: O_{apical} of the Co^{3+} ions (O2a), blue line: O_{apical} of the Co^{2+} ions (O2b), the density of states is different for Co^{3+} and Co^{2+} as the $Co-O$ distances are not the same). It can be seen from the lower panel of Fig. 7.55 that the O_{apical} $2p$ density of states is shifted to lower energies compared to the O_{basal} $2p$ density of states. The pronounced absorption at 3.5 eV − 4 eV is assigned to the CT excitation from the O_{apical} $2p$ band to the empty LS Co^{3+} $3z^2 - r^2$ orbital, whereas the overlap between O_{apical} $2p$ and the empty LS Co^{3+} $x^2 - y^2$ orbital is zero along c for perfect 180° bonds. The peak at 3.5 eV − 4 eV is also clearly visible in the spectra of the pure Co^{2+} compound La_2CoO_4, although its peak height is significantly reduced, see Fig. 7.57. Therefore, an excitation involving the Co^{2+} $3d$ orbitals must also give a contribution to the peak. Let us consider the upper panel of Fig. 7.55, where the density of states of the HS Co^{2+} $3d$ orbitals is shown. It can be seen that only the xy orbital and the $x^2 - y^2$ orbital, which do not yield overlap with O $2p$ along c, have finite density of states above the Fermi level at energies relevant for the peak at 3.5 eV − 4 eV. The $3z^2 - r^2$ orbital does overlap with O $2p$ along c, finite density of states can only be found at approx. 4.5 eV above the Fermi level, which is too high to account for the absorption at about 3.5 eV − 4 eV. However, the t_{2g} crystal-field splitting between xy and xz/yz is only on the order of 30 meV in Co^{2+}, as a consequence the spin-orbit coupling plays an important role and mixes the xy and xz/yz levels [139]. Therefore, excitations to empty t_{2g} states of Co^{2+} can well account for the peak at about 3.5 eV − 4 eV in $\sigma_1^c(\omega)$ of La_2CoO_4. Furthermore, due to the deviation of the bond angles from 180° in the orthorhombic distorted crystal structure of La_2CoO_4, excitations to the xy and the $x^2 - y^2$ orbitals along c might give a small contribution to the peak at 3.5 eV − 4 eV.
Below the pronounced peak at 3.5 eV − 4 eV finite structureless spectral weight

is observed in the optical conductivity, see Fig. 7.57. It is probably due to the smearing out of the O $2p$ bands. Above about 4.5 eV, $\sigma_1(\omega)$ steeply increases. This higher lying absorption could be ascribed to the CT excitation from O_{apical} $2p$ to the HS Co^{2+} $3z^2 - r^2$ orbital or to CT excitations from lower lying O_{apical} $2p$ bands to the LS Co^{3+} $3z^2 - r^2$ orbital.
In the fit to the measured data, four Gaussian oscillators are used to describe $\varepsilon_2^c(\omega)$, see Fig. 7.28. A broad Gaussian oscillator accounts for the pronounced spectral weight below 3 eV (peak 1), two Gaussian oscillators describe the peak at about 3.5 eV − 4 eV (peak 2 and 3) and the fourth oscillator models the spectral weight above ≈ 4.5 eV. See Fig. 7.38 for the parameters of the Gaussian oscillators. However, the different oscillators overlap significantly, we therefore do not expect the parameters of the individual oscillators to have a significant physical meaning.
We now consider the c axis spectra of the compound $La_{1.1}Sr_{0.9}CoO_4$, which differ significantly form the spectra of the compounds with $x \leq 0.5$. A broad peak is observed at about 1.5 eV − 3.5 eV (see Figs. 7.57 − 7.59 and also 7.41), which is modeled in the fit to the measured data by three Gaussian oscillators (peak 1 − 3 in Fig. 7.39). It can be assigned to the excitations from the broad O_{apical} $2p$ bands to the HS Co^{3+} $xz - iyz$ orbital at lower, and the LS Co^{3+} $3z^2 - r^2$ orbital at somewhat higher energy, see Fig. 7.56. A fourth Gaussian oscillator is used in the fit to account for the spectral weight above 4 eV. See Fig. 7.44 for the parameters of the Gaussian oscillators. Due to huge overlap between the individual absorption bands, we do not expect the parameters of the Gaussian oscillators to be physically meaningful.

To summarize this section, we have found a consistent peak assignment in terms of CT excitations from the O $2p$ bands to the different Co^{2+} and Co^{3+} $3d$ orbitals, making use of the calculated density of states published by Wu and Burnus [138, 139]. The polarization dependence of the data is mostly due to the different energetic positions of the O_{basal} $2p$ and O_{apical} $2p$ bands. Our doping dependent analysis of the layered cobaltates reveals, that the spectra look significantly different for a Co^{3+} LS and a Co^{3+} HS configuration. The spectra of the mixed Co^{3+} LS/HS system $La_{1.1}Sr_{0.9}CoO_4$ differ significantly from the spectra of the Co^{3+} LS systems $La_{2-x}Sr_xCoO_4$ with $x \leqslant 0.5$, both for $E \parallel ab$ and $E \parallel c$. It is therefore surprising, that the changes across the spin-state transition are only small in the three dimensional system $LaCoO_3$. It becomes obvious from Figs. 7.57 − 7.59, that the spectra of $La_{1.1}Sr_{0.9}CoO_4$ and $LaCoO_3$ look similar, in particular for $E \parallel ab$. This is in agreement with the expectations at higher temperatures, when both systems contain Co^{3+} LS and Co^{3+} HS ions. However, $LaCoO_3$ is assumed to be a pure Co^{3+} LS system at lowest temperatures. It is possible that the spectra of the pseudocubic perovskites and the layered compounds are dominated by the structure of the oxygen $2p$ bands.

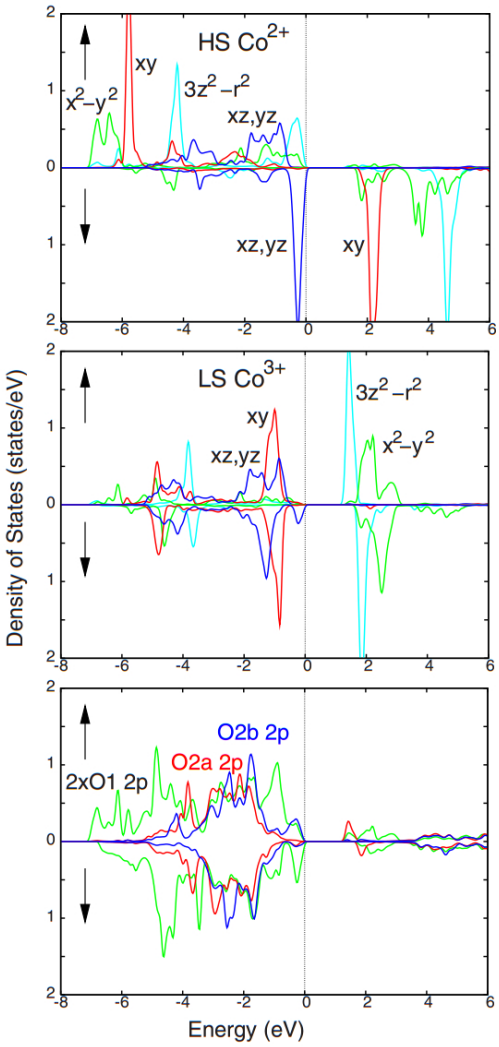

Figure 7.55: Density of states (DOS) of the Co^{2+} HS / Co^{3+} LS ground state of $La_{1.5}Sr_{0.5}CoO_4$ as obtained by Wu and Burnus [139] by the use of LSDA+U calculations including spin-orbit coupling and the multiplet effect. The upper panel shows the DOS of the HS Co^{2+} 3d orbitals, the middle panel shows the DOS of the LS Co^{3+} 3d orbitals, and in the lower panel the DOS of the O 2p orbitals is shown (green line: O_{basal} 2p DOS (O1), red line: O_{apical} 2p DOS belonging to the $Co^{3+}O_6^{2-}$ octahedra (O2a), blue line: O_{apical} 2p DOS belonging to the $Co^{2+}O_6^{2-}$ octahedra (O2b)). The HS Co^{2+} configuration $t_{2g}^5 e_g^2$ with a t_{2g} hole on the xy orbital is sketched in Fig. 7.53 , the LS Co^{3+} configuration t_{2g}^6 with a closed t_{2g} shell is sketched in Fig. 7.54. The Fermi level is located at $E = 0$. Taken from Ref. [139].

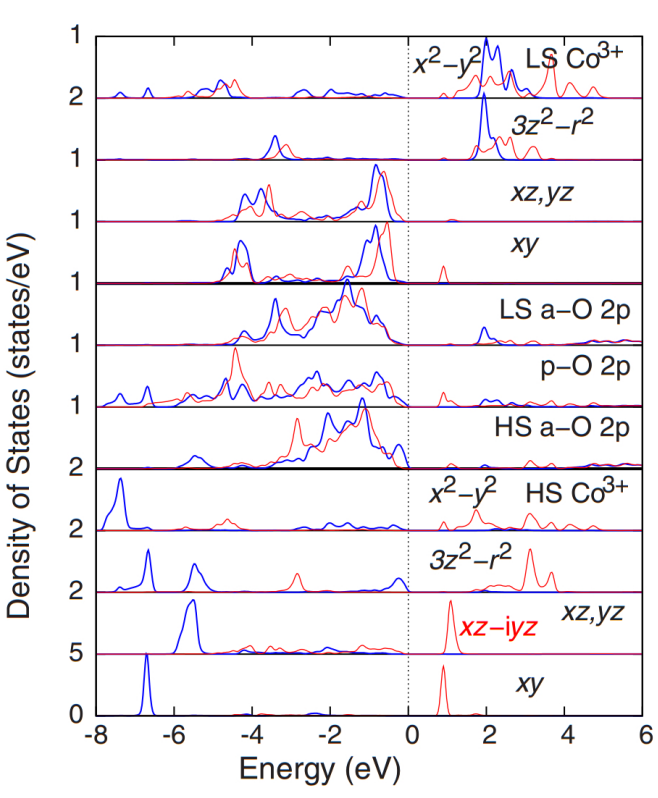

Figure 7.56: Density of states (DOS) of the Co^{3+} HS / Co^{3+} LS mixed ground state of $LaSrCoO_4$ as obtained by Wu [138] by the use of LSDA+U calculations which include spin-orbit coupling and the multiplet effect. Upper panels: DOS of the LS Co^{3+} $3d$ orbitals, middle panels: O_{apical} $2p$ DOS belonging to the Co^{3+}LS O_6^{2-} octahedra (LS a-O $2p$), O_{basal} $2p$ DOS (p-O $2p$) and O_{apical} $2p$ DOS belonging to the Co^{3+}HS O_6^{2-} octahedra (HS a-O $2p$), lower panels: DOS of the HS Co^{3+} $3d$ orbitals. Blue (red) lines correspond to the up (down) spin. Taken from Ref. [138].

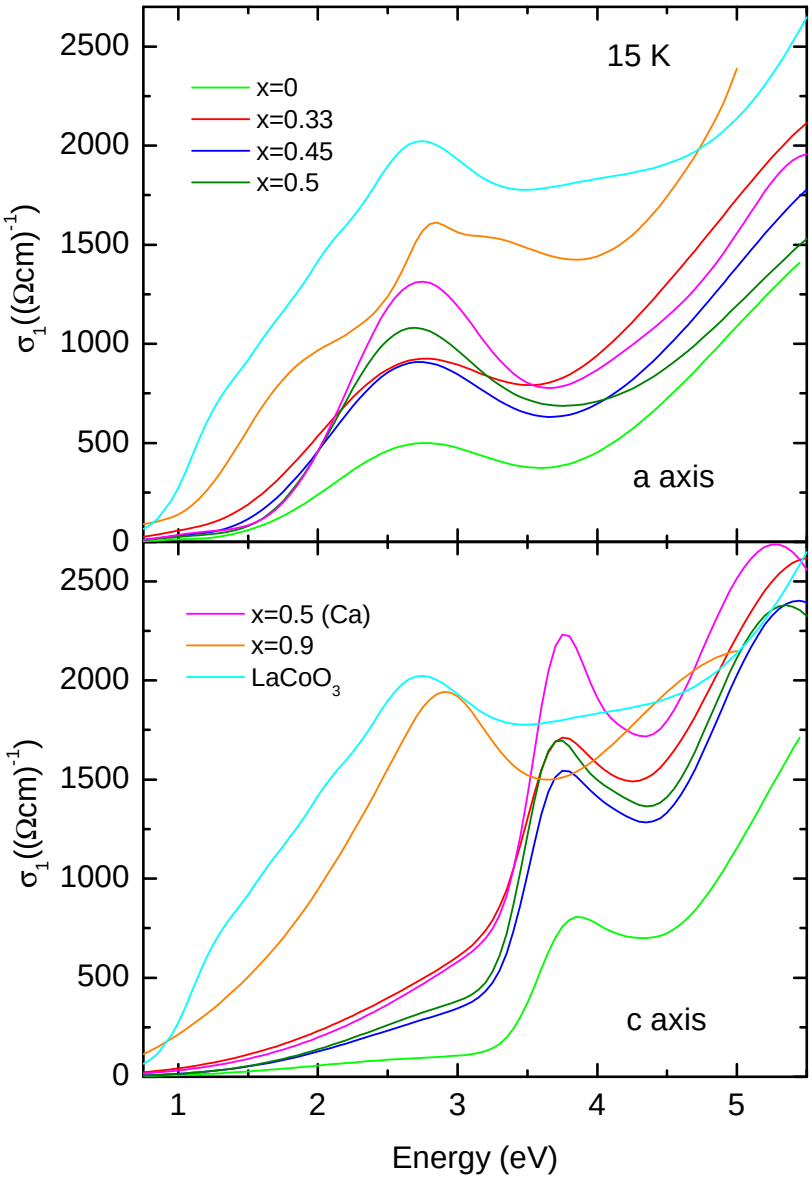

Figure 7.57: Optical conductivity $\sigma_1(\omega)$ of $La_{2-x}Sr_xCoO_4$ (x =0, 0.33, 0.45, 0.5, 0.9), $La_{1.5}Ca_{0.5}CoO_4$, and $LaCoO_3$ for $T = 15\,\mathrm{K}$ ($T = 30\,\mathrm{K}$ for $x = 0.9$).

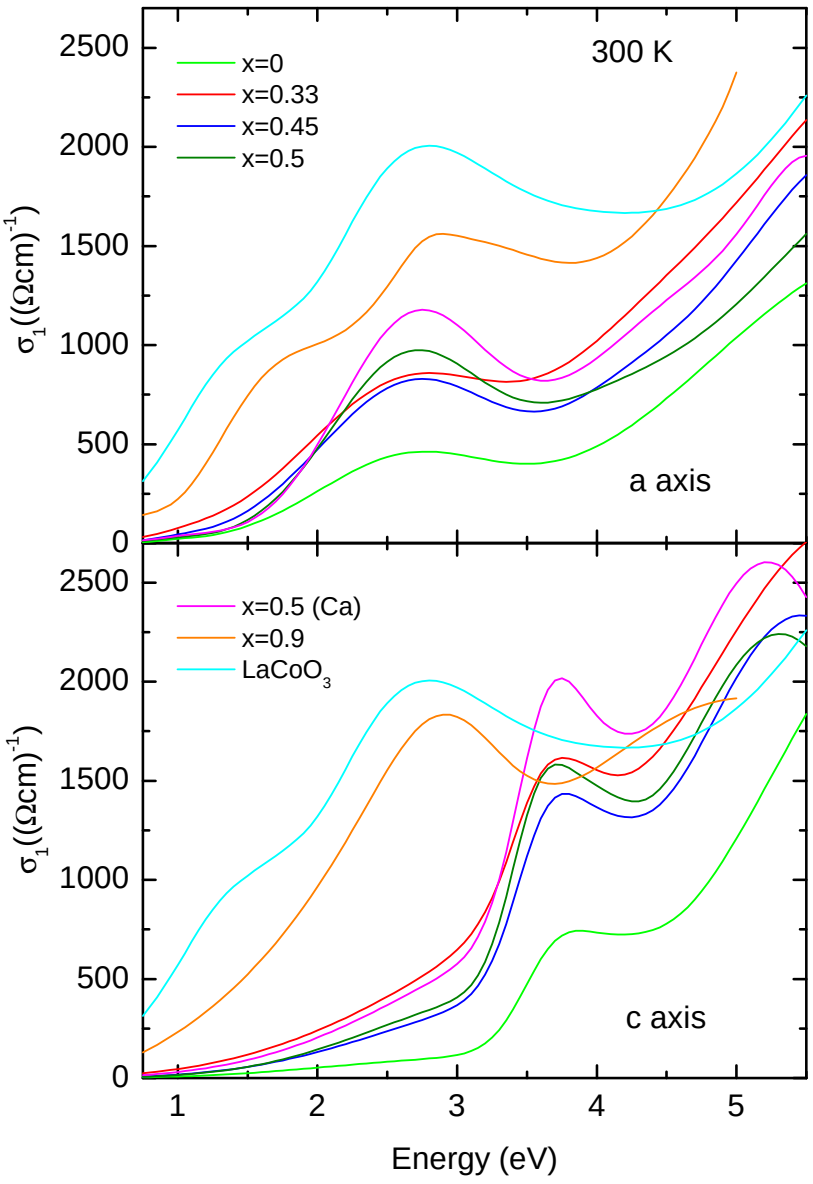

Figure 7.58: Optical conductivity $\sigma_1(\omega)$ of $La_{2-x}Sr_xCoO_4$ (x =0, 0.33, 0.45, 0.5, 0.9), $La_{1.5}Ca_{0.5}CoO_4$, and $LaCoO_3$ for $T = 300\,\mathrm{K}$.

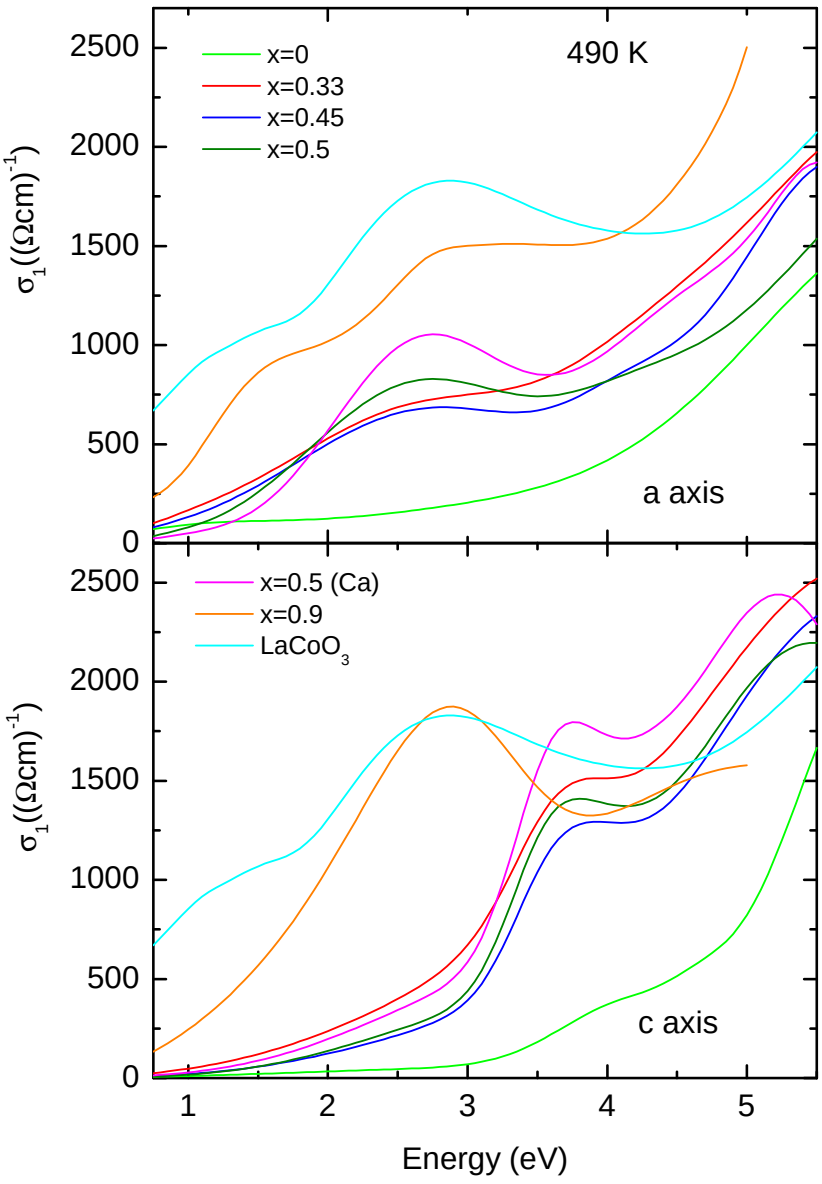

Figure 7.59: Optical conductivity $\sigma_1(\omega)$ of $La_{2-x}Sr_xCoO_4$ ($x = 0$, 0.33, 0.45, 0.5, 0.9), $La_{1.5}Ca_{0.5}CoO_4$, and $LaCoO_3$ for $T = 490\,\mathrm{K}$.

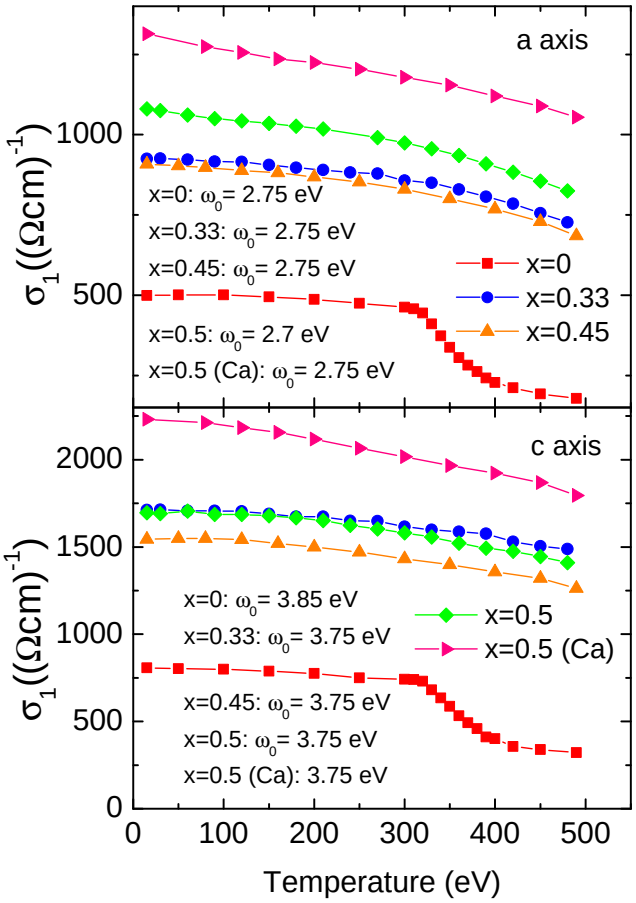

Figure 7.60: Upper panel: Maximum value of the optical conductivity $\sigma_1^{ab}(\omega)$ at the broad peak around 2.5 eV in $\sigma_1^{ab}(\omega)$ of $La_{2-x}Sr_xCoO_4$ ($x = 0, 0.33, 0.45, 0.5$) and $La_{1.5}Ca_{0.5}CoO_4$. Lower panel: Maximum value of the optical conductivity $\sigma_1^{c}(\omega)$ at the pronounced peak around 3.5 eV − 4 eV in $\sigma_1^{c}(\omega)$ of $La_{2-x}Sr_xCoO_4$ ($x = 0, 0.33, 0.45, 0.5$) and $La_{1.5}Ca_{0.5}CoO_4$.

Temperature dependence

As already discussed, temperature-dependent optical data of $La_{1.5}Sr_{0.5}CoO_4$ and $La_{1.5}Ca_{0.5}CoO_4$ have already been published by Lee *et al.* [32], see Fig. 7.52. Lee *et al.* [32] find that the optical gap decreases significantly with increasing temperature for $T \gtrsim 400\,\mathrm{K}$. It vanishes completely at $\sim 850\,\mathrm{K}$. They observe an isobestic point at $\sim 2\,\mathrm{eV}$. A low-energy excitation develops at $\sim 1\,\mathrm{eV}$ with increasing temperature, whereas the pronounced peak at $\sim 2.5\,\mathrm{eV}$ is significantly suppressed for $T > 700\,\mathrm{K}$. The increase of the spectral weight at around 1 eV sets in at lower temperatures in the Sr-doped compound ($\sim 400\,\mathrm{K}$) than in the Ca-doped counterpart ($\sim 600\,\mathrm{K}$). As the changes of the optical spectra appear at temperatures significantly lower than the charge-ordering temperature of approx. 850 K in $La_{1.5}Sr_{0.5}CoO_4$ and $La_{1.5}Ca_{0.5}CoO_4$, Lee *et al.* [32] attribute them to a spin-state transition from a Co^{3+} LS state at lower temperatures to a Co^{3+} HS or IS state at higher temperatures. They argue that the spin-blockade mechanism is lost as a consequence of the spin-state transition and the electronic system gains kinetic energy. According to Lee *et al.* [32], this scenario is in agreement with the temperature dependence of structural data. The structural data collected by Cwik [42] reveal a huge increase of the *c*-axis lattice constant above 400 K in $La_{1.5}Sr_{0.5}CoO_4$. The phonon spectra of $La_{1.5}Sr_{0.5}CoO_4$ and $La_{1.5}Ca_{0.5}CoO_4$ collected by Lee *et al.* [32] reveal a splitting of the apical oxygen bending mode above 400 K and 600 K for $La_{1.5}Sr_{0.5}CoO_4$ and $La_{1.5}Ca_{0.5}CoO_4$, respectively. As discussed in Sec. 7.1.2, the magnetic susceptibility data collected by Hollmann *et al.* [29] also give evidence for a temperature-induced spin-state transition in $La_{1.5}Sr_{0.5}CoO_4$.
Unfortunately, the pronounced temperature-dependent changes at $T \gtrsim 500\,\mathrm{K}$ of the optical spectra of $La_{1.5}Sr_{0.5}CoO_4$ and $La_{1.5}Ca_{0.5}CoO_4$ cannot be seen in our data, as the highest measured temperature amounts to merely 490 K. However, the findings of Lee *et al.* [32] for $La_{1.5}Sr_{0.5}CoO_4$ and $La_{1.5}Ca_{0.5}CoO_4$ resemble our findings for La_2CoO_4. For La_2CoO_4, we observe the drastic changes of the optical spectra at reduced temperatures starting at $\sim 320\,\mathrm{K}$. The peak at ~ 2.5 eV is completely suppressed at the maximum measured temperature of 490 K and the spectral weight around 1 eV increases significantly. However, in opposition to the findings of Lee *et al.* [32] for $La_{1.5}Sr_{0.5}CoO_4$ and $La_{1.5}Ca_{0.5}CoO_4$, the spectral weight is not conserved in La_2CoO_4, see Fig. 7.61. The loss of spectral weight at around 2.5 eV is not counterbalanced by the gain of spectral weight around 1 eV. The temperature-dependent optical data of La_2CoO_4 indicate an increased carrier mobility at higher temperatures. As the pure HS Co^{2+} compound La_2CoO_4 does neither show charge ordering, nor is the spin-blockade mechanism at work, these changes cannot be attributed to a melting of one of these phenomena. The magnetic ordering temperature of La_2CoO_4 amounts to 275 K. Although the pronounced changes in our optical spectra set in a higher temperature of $\sim 320\,\mathrm{K}$, one might speculate, that the temperature dependence of the data of La_2CoO_4 is as-

sociated with the melting of the magnetic order. However, this is only speculation and the exact origin is still unclear.

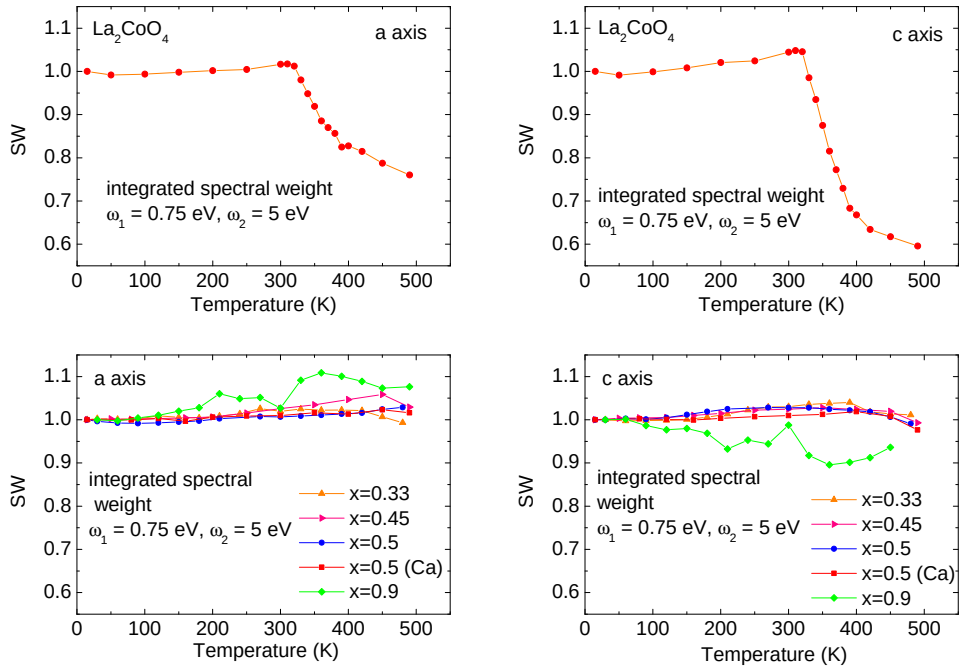

Figure 7.61: Integrated spectral weight $\int_{\omega_1}^{\omega_2} \sigma_1(\omega) d\omega$ of La_2CoO_4 (upper panels), and $La_{2-x}Sr_xCoO_4$ ($x = 0, 0.33, 0.45, 0.5, 0.9$) and $La_{1.5}Ca_{0.5}CoO_4$ (lower panels) for the *ab* plane and the *c* axis, normalized to one for the lowest measured temperature.

7.4 Conclusion

We perform a very detailed doping, temperature, and polarization dependent ellipsometric analysis on the pseudocubic perovskites $LaCoO_3$ and $EuCoO_3$ and the single-layered cobaltates $La_{1.5}Ca_{0.5}CoO_4$ and $La_{2-x}Sr_xCoO_4$ (x=0, 0.33, 0.45, 0.5, 0.9) in the energy range from 0.75 eV to 5.5 eV for temperatures ranging from 15 K to 490 K.

For the single-layered cobaltates with mixed Co^{2+} $3d^7$ and Co^{3+} $3d^6$ sites, we succeed in a consistent peak assignment. $La_{2-x}Sr_xCoO_4$ and $La_{1.5}Ca_{0.5}CoO_4$ belong to the group of charge-transfer systems. The observed absorption bands are assigned to charge-transfer excitations from the O $2p$ level to the different Co^{3+} and Co^{2+} $3d$ orbitals. According to our interpretation, the polarization dependence of the optical spectra is mostly due to the different energetic positions of the O_{basal} $2p$ and O_{apical} $2p$ bands. While the optical spectra of the compounds with doping concentrations $x \leq 0.5$ show strong similarities, the optical spectra of $La_{1.1}Sr_{0.9}CoO_4$ differ significantly, both in σ_1^{ab} and σ_1^c. Whereas it is well established that the $3d^7$ Co^{2+} ions realize the HS state ($t_{2g}^5 e_g^2$, $S = 3/2$), the spin state of the Co^{3+} ions with $3d^6$ electron configuration has been widely disputed for a long time. However, recently evidence accumulated that the Co^{3+} ions are in the LS state (t_{2g}^6, $S = 0$) for doping concentrations $0.4 \lesssim x \lesssim 0.8$, while a mixed spin-state system of Co^{3+} HS ($t_{2g}^4 e_g^2$, $S = 2$) and LS sites is realized for $x \gtrsim 0.8$. We can therefore conclude from our results on layered cobaltates that the optical spectra differ significantly for a Co^{3+} HS and a Co^{3+} LS electron configuration.

The ground state of the pure Co^{3+} systems $LaCoO_3$ and $EuCoO_3$ is the LS state. A thermal population of the HS state takes place in $LaCoO_3$ at $T \gtrsim 25$ K, the spin-state transition is shifted to much higher temperatures in $EuCoO_3$. We do observe remarkable changes in the optical conductivity of $LaCoO_3$ across the spin-state transition temperature, that are absent in the data of $EuCoO_3$. However, these changes are much smaller than expected from our results on layered cobaltates. The spectra of $LaCoO_3$ resemble the spectra of the mixed Co^{3+} HS/LS system $La_{1.1}Sr_{0.9}CoO_4$ already at lowest temperatures.

8 Conclusion

Within the framework of this thesis the optical spectra of different transition-metal oxides with open $3d$ shells are studied by means of spectroscopic ellipsometry. The investigated compounds belong to the group of Mott-Hubbard or charge-transfer insulators. The main concern lies on the interband transitions from the lower to the upper Hubbard band and their interrelation with low-energy spin and orbital degrees of freedom. The optical excitations from the lower to the upper Hubbard band are a sensitive probe of orbital and spin correlations. A change of nearest-neighbor spin-spin or orbital-orbital correlations greatly affects the optical spectral weights, leading to a pronounced dependence on both, temperature and polarization. Our spectra show distinct multi-peak structures which reflect the complex multiplet structure of the excited states. The assignment of the distinct absorption bands can be verified by taking the temperature and polarization dependence into account.

Ellipsometry

The optical investigations are performed by the use of a rotating-analyzer ellipsometer (VASE, J. A. Wollam), which is equipped with a retarder between polarizer and sample. It works in the energy range from 0.75 eV to 5.5 eV. Measurements at temperatures ranging from 15 K to 490 K are performed at an angle of incidence of 70° inside a UHV cryostat with a pressure below 10^{-9} mbar. To obtain the dielectric tensor of the anisotropic single crystals, measurements are carried out on different polished surfaces. The different data sets are analyzed simultaneously. Since ellipsometry is a surface-sensitive technique, a finite surface roughness is taken into account in the analysis of the ellipsometric data.

Probing orbital fluctuations in $R\mathrm{VO}_3$ ($R =$ Y, rare earth ion)

We apply spectroscopic ellipsometry to perform an elaborate temperature-dependent analysis of the optical conductivity of the pseudocubic perovskites YVO_3, GdVO_3, and CeVO_3 for temperatures ranging from 15 K to 490 K. Undoped $R\mathrm{VO}_3$ ($R =$ Y, rare earth ion) can be characterized as a Mott-Hubbard insulator which exhibits a $3d^2$ electron configuration on the V^{3+} sites. We assign the observed absorption bands to Mott-Hubbard excitations, $|d_i^2 d_j^2\rangle \rightarrow |d_i^1 d_j^3\rangle$, and charge-transfer excitations, $|p^6 d^2\rangle \rightarrow |p^5 d^3\rangle$. The complex multi-peak structure observed in the

optical spectra reflects the multiplet splitting of the $3d^3$ final states. The coupling of the orbitals to the lattice is only weak in the t_{2g} systems $R\mathrm{VO}_3$. As a consequence, a competition between spin and orbital degrees of freedom arises which is reflected in a complex spin and orbital ordering phase diagram. We arrive at a consistent peak assignment and understand the temperature dependence of the optical spectra on the basis of nearest-neighbor spin-spin and orbital-orbital correlations.
The lowest absorption band in $\sigma_1^c(\omega)$ shows a pronounced double-peak structure and its spectral weight changes by a factor of 2 to 3 due to the ordering of spins and orbitals. We compare our result with a theory which calculates the temperature dependence of the optical spectral weight based on a low-energy spin-orbital superexchange Hamiltonian [8,10]. The temperature dependence is expected to be different for rigid orbital order or strong orbital fluctuations. Our results clearly rule out that orbital fluctuations are strong in $R\mathrm{VO}_3$. We attribute the double-peak structure to an excitonic resonance, i.e. not a truly bound state below the gap but a resonance within the absorption band. The spectral weight of this excitonic resonance is greatly enhanced when entering the orbitally ordered phase. This clearly indicates that the so-called Mott-Hubbard exciton becomes energetically favorable not only due to the attractive interaction between a $3d^3$ state in the upper Hubbard band and a $3d^1$ state in the lower Hubbard band, but also due to a gain of kinetic energy. Recent pump-probe measurements on YVO_3 substantiate this interpretation [115].

Ellipsometry on $\mathrm{LaSrFeO}_4$

We acquire ellipsometric data on the correlated insulator $\mathrm{LaSrFeO}_4$ with single-layered perovskite structure for temperatures between 15 K and 250 K. The ellipsometric data is analyzed in combination with transmittance data from 0.5 eV to 2.5 eV. The character of $\mathrm{LaSrFeO}_4$, being either a charge-transfer or a Mott-Hubbard system, is still debated. We succeed in identifying Mott-Hubbard and charge-transfer excitations by exploiting the strong anisotropy between the in-plane and out-of-plane optical selection rules of the layered structure. We attribute the lowest interband transition, which is visible in $\sigma_1^a(\omega)$ only, to a Mott-Hubbard excitation and thus conclude that $\mathrm{LaSrFeO}_4$ belongs effectively to the group of Mott-Hubbard insulators. We point out that this result is rather unexpected, as the $3d^5$ electron configuration of Fe^{3+} is particularly stable due to the intra-atomic Hund exchange J_H. Accordingly, recent optical measurements on non-layered ferrites are interpreted in terms of charge-transfer systems [125]. We justify our interpretation by taking the large splitting of the e_g orbitals in the tetragonal structure into account. The strong hybridization between the Fe $3d$ and the ligand O $2p$ bands further contributes to the positioning of the lowest Mott-Hubbard

excitation below the onset of charge-transfer excitations.
In agreement with the fact that nearest-neighbor spin-spin and orbital-orbital correlations hardly change below room temperature in this high-spin $3d^5$ compound with a Néel temperature of $T_N = 366\,\mathrm{K}$, the Mott-Hubbard excitations show only a weak dependence on temperature. However, the overlap of the Mott-Hubbard excitations with the much stronger charge-transfer excitations makes a detailed analysis of the temperature dependence of the former unfeasible.

Ellipsometry on cobaltates

We present a detailed temperature-dependent ellipsometric analysis of the optical spectra of the pseudocubic perovskites $LaCoO_3$ and $EuCoO_3$ and the doped single-layered perovskites $La_{1-x}Sr_xCoO_4$ with doping concentrations x =0.0, 0.33, 0.45, 0.5, and 0.9, and the half-doped Ca compound $La_{1.5}Ca_{0.5}CoO_4$.
While the compounds $LaCoO_3$ and $EuCoO_3$ exhibit a $3d^6$ electron configuration on the Co^{3+} sites, the single-layered perovskites are mixed Co^{3+} $3d^6$ and Co^{2+} $3d^7$ systems. The $3d^6$ electron configuration is particularly interesting as a competition arises between the crystal-field splitting and the Hund exchange. As a consequence, different $3d^6$ multiplets lie energetically close. These are (in cubic symmetry) the ${}^1A_{1g}$ multiplet, the so-called low-spin (LS) state with $S = 0$ ($t_{2g}^6 e_g^0$ electron configuration), the ${}^3T_{1g}$ multiplet, referred to as the intermediate-spin (IS) state with $S = 1$ ($t_{2g}^5 e_g^1$ electron configuration), and the ${}^5T_{2g}$ multiplet, which is the so-called high-spin (HS) state with $S = 2$ ($t_{2g}^4 e_g^2$ electron configuration).
$LaCoO_3$ and $EuCoO_3$ are paramagnetic insulators at low temperatures, the ground state of Co^{3+} is the LS state. Whereas a thermal population of Co^{3+} HS states takes place in $LaCoO_3$ above $T \gtrsim 25\,\mathrm{K}$, the so-called spin-state transition is shifted to much higher temperatures in $EuCoO_3$ [25, 26]. While it is well established that the Co^{2+} sites of the layered cobaltates with $3d^7$ electron configuration realize the HS state ($S = 3/2$, $t_{2g}^5 e_g^2$), doping- and temperature-induced spin-state transitions have been discussed to take place on the Co^{3+} sites [28–32]. Recently evidence accumulated that the Co^{3+} ions are in the LS state for doping concentrations $x \lesssim 0.8$, while a mixed spin-state system of Co^{3+} HS and LS sites is realized for $x \gtrsim 0.8$.
The studied cobaltates are characterized as charge-transfer systems. Due to the strikingly different electron configurations realized in the LS and the HS state, we expect a spin-state transition to be well visible in the optical spectra. Accordingly, we find that the optical spectra of the mixed Co^{3+} HS/LS compound $La_{1.1}Sr_{0.9}CoO_4$ differ significantly from the spectra of the pure Co^{3+} LS compounds $La_{1-x}Sr_xCoO_4$ with doping concentrations $x \leq 0.5$ and $La_{1.5}Ca_{0.5}CoO_4$. This clearly indicates that Co^{3+} LS and Co^{3+} HS electron configurations lead to very different optical spectra. We achieve a consistent peak assignment in terms of charge-transfer excitations from the O $2p$ bands to the different Co^{3+}

and Co^{2+} 3*d* orbitals. The polarization dependence of our data indicates that the density of states of the O 2*p* bands plays a significant role for the determination of the optical conductivity. Interestingly, temperature-dependent optical data on $LaCoO_3$ published by Tokura *et al.* [27] hardly vary across the spin-state transition temperature. The data have been acquired by reflectivity measurements with a subsequent Kramers-Kronig analysis. Our elaborate temperature-dependent ellipsometric analysis of the optical conductivity of $LaCoO_3$ reveals some remarkable changes across the spin-state transition temperature, that are absent in the data of $EuCoO_3$. However, these changes are much smaller than expected. The spectra of $LaCoO_3$ resemble the spectra of $La_{1.1}Sr_{0.9}CoO_4$ already at low temperatures. This might be due to the fact that the optical spectra of the cobaltates are dominated by the O 2*p* bands.

List of Figures

2.1 Valence band splitting into upper and lower Hubbard band 6
2.2 Crystal structure of the cubic and single-layered perovskite 9
2.3 Orthorhombic crystal structure of the distorted perovskite 10
2.4 Sketch of the t_{2g} and e_g orbitals 10
2.5 Simple example for FM and AFM correlations due to superexchange 13
2.6 Simple sketch of the collective Jahn-Teller effect 14
2.7 Sketch of a MH excitation 15
2.8 Optical data of Ref. [11] on $LaMnO_3$ 17
2.9 Sketch of PES and IPES spectra of a MH and a CT insulator . . 18
2.10 Sketch of a MH excitation and a CT excitation 18

3.1 Definition of the ellipsometer coordinate system 25
3.2 Example for the dependence of $|r_{pp}/r_{ss}|$ and $(\Delta_{pp} - \Delta_{ss})$ on the angle of incidence 25
3.3 Example for a Lorentz, Gaussian, and Tauc-Lorentz oscillator . . 27
3.4 Sketch of an ellipsometric experiment 29

4.1 Picture of the ellipsometer 44
4.2 Sketch of the setup of the ellipsometric measurements 45
4.3 Picture of the ellipsometer including the control unit 45
4.4 Exemplary Laue pattern of $GdVO_3$ 47
4.5 Picture of the polishing machine 47
4.6 Picture of the brass cone which serves as a sample holder 48
4.7 Calibration curve for low-temperature measurements 49
4.8 Picture of the input unit without and equipped with the alignment detector 49
4.9 Result for ε_2^a of $LaSrFeO_4$ following from physical models assuming different surface roughnesses 52

5.1 Orthorhombic crystal structure of $R\mathrm{VO}_3$ 57
5.2 Orthorhombic splitting $\varepsilon = 2|b-a|/(b+a)$ of the compounds $R\mathrm{VO}_3$ 57
5.3 Spin and orbital ordering phase diagram of $R\mathrm{VO}_3$ 60
5.4 Visualization of C/G type orbital/spin order 61
5.5 Result of Ref. [48] for the spin and orbital ordering temperatures in $R\mathrm{VO}_3$ 61

5.6 Phonon spectrum of $GdVO_3$ 67
5.7 Oscillator strength of the phonon modes of $GdVO_3$ 68
5.8 Optical conductivity of $GdVO_3$ between $8000\,cm^{-1}$ and $10500\,cm^{-1}$ 69
5.9 Sketch of different t_{2g}^2 and t_{2g}^3 multiplets 71
5.10 Energy separation between the t_{2g}^3 multiplets 71
5.11 Theoretically obtained optical spectral weights of the MH excitations in RVO_3 74
5.12 Raw experimental data of YVO_3 with fit 78
5.13 Dielectric function $\varepsilon(\omega)$ of YVO_3 79
5.14 Optical conductivity $\sigma_1(\omega)$ of YVO_3 80
5.15 Gaussian and Tauc-Lorentz oscillators that constitute $\varepsilon_2(\omega)$ in the fit to the data of YVO_3 80
5.16 Comparison between two data sets of YVO_3 81
5.17 Dielectric function $\varepsilon(\omega)$ of YVO_3 81
5.18 Optical conductivity $\sigma_1(\omega)$ of YVO_3 82
5.19 Gaussian oscillators that constitute $\varepsilon_2(\omega)$ in the fit to the data of $GdVO_3$ 85
5.20 Raw experimental data of $GdVO_3$ with fit 86
5.21 Dielectric function $\varepsilon(\omega)$ of $GdVO_3$ 86
5.22 Optical conductivity $\sigma_1(\omega)$ of $GdVO_3$ 87
5.23 Close-up view of the optical conductivity $\sigma_1(\omega)$ of $GdVO_3$ 88
5.24 Gaussian oscillators that constitute $\varepsilon_2(\omega)$ in the fit to the data of $CeVO_3$ 90
5.25 Raw experimental data of $CeVO_3$ with fit 91
5.26 Dielectric function $\varepsilon(\omega)$ of $CeVO_3$ 91
5.27 Optical conductivity $\sigma_1(\omega)$ of $CeVO_3$ 92
5.28 Close-up view of the optical conductivity $\sigma_1(\omega)$ of $CeVO_3$ 93
5.29 Optical conductivity $\sigma_1(\omega)$ of YVO_3, $GdVO_3$, and $CeVO_3$ 98
5.30 Sketch of MH excitations to final t_{2g}^3 multiplets 99
5.31 Result of Ref. [21] for the optical conductivity of $LaVO_3$ and YVO_3 101
5.32 Result of Ref. [23] for the dielectric function of YVO_3 101
5.33 Fit with Tauc-Lorentz/Gaussian and Lorentz oscillators to the data of YVO_3 103
5.34 Drude-Lorentz fit to the data of YVO_3, $GdVO_3$, and $CeVO_3$, and sum of $N_{eff}(T)$ of peaks A and B in σ_1^c 104
5.35 Experimental and theoretical result for $N_{eff}(T)$ of the lowest MH excitation along c in RVO_3 105
5.36 Result of Ref. [13] for the optical conductivity of $YTiO_3$ 106
5.37 LDA+U results of Fang *et al.* [99] for the optical conductivity of YVO_3 and $LaVO_3$ 107
5.38 LDA+U results of Solovyev *et al.* [100] for the optical conductivity of $LaVO_3$ 108

5.39 LDA+DMFT results of De Raychaudhury *et al.* [20] for the spectral matrix $A_{m,m'}$ of $LaVO_3$ and YVO_3 109
5.40 Photoemmision results of Mossanek *et al.* [102] on $SrVO_3$, $CaVO_3$, and $LaVO_3$ 110
5.41 Ultraviolet photoemission and bremsstrahlung spectra of $LaVO_3$ of Ref. [101] 110
5.42 Mechanism of exciton formation as proposed by Zhang and Ng [105] 112
5.43 Simple sketch of the formation and propagation of Hubbard excitons as suggested in Ref. [13] 114
5.44 Ratio of the spectral weights of peaks A and B in $\sigma_1^c(\omega)$ of YVO_3, $GdVO_3$, and $CeVO_3$ 115
5.45 Time-domain spectroscopy data on YVO_3 of Ref. [115] 115

6.1 Sketch of a Mott-Hubbard and a charge-transfer insulator 118
6.2 Crystal and magnetic structure of $LaSrFeO_4$ 121
6.3 Dielectric function $\varepsilon_2(\omega)$ of $LaSrFeO_4$ below the charge gap 122
6.4 Comparison between the pseudo-dielectric function and the dielectric function of $LaSrFeO_4$ 123
6.5 Dielectric function $\varepsilon(\omega)$ of $LaSrFeO_4$ 124
6.6 Optical conductivity $\sigma_1(\omega)$ of $LaSrFeO_4$ 125
6.7 Fit with Gaussian oscillators to the data of $LaSrFeO_4$ 126
6.8 Sketch of MH excitations in $LaSrFeO_4$ 128
6.9 Temperature dependence of the normalized spectral weight of MH1 and MH2 in $LaSrFeO_4$ 133
6.10 Fit with a Gaussian oscillator and an exponential function to $\varepsilon_2^a(\omega)$ of $LaSrFeO_4$ 134

7.1 Rhombohedral unit cell of $LaCoO_3$ 141
7.2 Electrical resistivity of $La_{1-x}Eu_xCoO_3$ 142
7.3 Magnetic susceptibility of $La_{1-x}Eu_xCoO_3$ 144
7.4 Tanabe-Sugano-Kamimura diagram of a d^6 system 145
7.5 Sketch of the LS, IS, and HS $3d^6$ electron configuration in a cubic crystal field 146
7.6 Energy of the LS, IS, and HS $3d^6$ electron configuration as a function of Δ_{CF} 146
7.7 Kriener's [167] result for the occupation number of the LS and IS state in $LaCoO_3$ and $EuCoO_3$ 149
7.8 Orthorhombic unit cell of La_2CoO_4 152
7.9 Spin-ordering and charge-ordering pattern of $La_{1-x}Sr_xCoO_4$ (x = 0, 0.5) 153
7.10 Phase diagram of $La_{2-x}Sr_xCoO_4$ as proposed by Cwik *et al.* [174] 155
7.11 Arrhenius plot of the DC electrical resistivity of $La_{2-x}Sr_xCoO_4$ . . 156

7.12 The spin-blockade mechanism 159
7.13 Raw experimental data of $La_{1.55}Sr_{0.45}CoO_4$ with fit 160
7.14 Gaussian oscillators that constitute $\varepsilon_2(\omega)$ in the fit to the data of $LaCoO_3$ and $EuCoO_3$ 162
7.15 Dielectric function $\varepsilon(\omega)$ of $LaCoO_3$ 162
7.16 Optical conductivity $\sigma_1(\omega)$ of $LaCoO_3$ 163
7.17 Dielectric function $\varepsilon_2(\omega)$ of $LaCoO_3$ resulting from two different measurement series 163
7.18 MIR data for $\varepsilon(\omega)$ of $LaCoO_3$ 164
7.19 MIR data for $\sigma_1(\omega)$ of $LaCoO_3$ 164
7.20 Fit parameters of the Gauss fit to the data of $LaCoO_3$ 165
7.21 Fit parameters of the Gauss fit to the data of $LaCoO_3$ 166
7.22 Dielectric function $\varepsilon(\omega)$ of $EuCoO_3$ 167
7.23 Optical conductivity $\sigma_1(\omega)$ of $EuCoO_3$ 167
7.24 Fit parameters of the Gauss fit to the data of $EuCoO_3$ 168
7.25 Fit parameters of the Gauss fit to the data of $EuCoO_3$ 169
7.26 Dielectric function $\varepsilon(\omega)$ of La_2CoO_4 171
7.27 Optical conductivity $\sigma_1(\omega)$ of La_2CoO_4 172
7.28 Gaussian oscillators that constitute $\varepsilon_2(\omega)$ in the fit to the data of $La_{1.55}Sr_{0.45}CoO_4$ 173
7.29 Dielectric function $\varepsilon(\omega)$ of $La_{1.67}Sr_{0.33}CoO_4$ 173
7.30 Optical conductivity $\sigma_1(\omega)$ of $La_{1.67}Sr_{0.33}CoO_4$ 174
7.31 Dielectric function $\varepsilon(\omega)$ of $La_{1.55}Sr_{0.45}CoO_4$ 175
7.32 Optical conductivity $\sigma_1(\omega)$ of $La_{1.55}Sr_{0.45}CoO_4$ 176
7.33 Dielectric function $\varepsilon(\omega)$ of $La_{1.5}Sr_{0.5}CoO_4$ 177
7.34 Optical conductivity $\sigma_1(\omega)$ of $La_{1.5}Sr_{0.5}CoO_4$ 178
7.35 Dielectric function $\varepsilon(\omega)$ of $La_{1.5}Ca_{0.5}CoO_4$ 179
7.36 Optical conductivity $\sigma_1(\omega)$ of $La_{1.5}Ca_{0.5}CoO_4$ 180
7.37 Fit parameters of the Gauss fit to the data of $La_{1-x}Sr_xCoO_4$ ($x =$ 0, 0.33, 0.45, 0.5) and $La_{1.5}Ca_{0.5}CoO_4$ (*ab* plane) 181
7.38 Fit parameters of the Gauss fit to the data of $La_{1-x}Sr_xCoO_4$ ($x =$ 0, 0.33, 0.45, 0.5) and $La_{1.5}Ca_{0.5}CoO_4$ (*c* axis) 182
7.39 Gaussian oscillators that constitute $\varepsilon_2(\omega)$ in the fit to the data of $La_{1.1}Sr_{0.9}CoO_4$ 183
7.40 Dielectric function $\varepsilon(\omega)$ of $La_{1.1}Sr_{0.9}CoO_4$ 184
7.41 Optical conductivity $\sigma_1(\omega)$ of $La_{1.1}Sr_{0.9}CoO_4$ 185
7.42 Fit parameters of the Gauss fit to the data of $La_{1.1}Sr_{0.9}CoO_4$ (*ab* plane) 186
7.43 Fit parameters of the Gauss fit to the data of $La_{1.1}Sr_{0.9}CoO_4$ (*ab* plane) 187
7.44 Fit parameters of the Gauss fit to the data of $La_{1.1}Sr_{0.9}CoO_4$ (*c* axis) 188
7.45 Optical conductivity of $LaCoO_3$ as obtained by Tokura *et al.* [27] 190

7.46 Optical conductivity $\sigma_1(\omega)$ of $LaCoO_3$ and $EuCoO_3$ 192
7.47 Tanabe-Sugano-Kamimura diagram of a d^7 system 193
7.48 Optical conductivity $\sigma_1(\omega)$ of $LaCoO_3$ between 40 K and 80 K . . 194
7.49 Value of the optical conductivity of $LaCoO_3$ at 2 eV and 3.2 eV . . 195
7.50 Value of the optical conductivity of $EuCoO_3$ at 1.85 eV and 3.5 eV 195
7.51 Optical conductivity of $La_{2-x}Sr_xCoO_4$ (x = 0.0, 0.5, and 0.8) as obtained by Uchida *et al.* [195] 196
7.52 Optical data of Lee *et al.* [32] of $La_{1.5}Ca_{0.5}CoO_4$ and $La_{1.5}Sr_{0.5}CoO_4$ 197
7.53 Sketch of the HS Co^{2+} $3d^7$ electron configuration in a tetragonally distorted crystal field 198
7.54 Sketch of the LS, IS, and HS Co^{3+} $3d^6$ electron configuration in a tetragonally distorted crystal field 199
7.55 Result of Wu and Burnus [139] for the density of states of the Co^{2+} HS / Co^{3+} LS ground state of $La_{1.5}Sr_{0.5}CoO_4$ 204
7.56 Result of Wu [138] for the density of states of the Co^{3+} HS / Co^{3+} LS mixed ground state of $LaSrCoO_4$ 205
7.57 Optical conductivity $\sigma_1(\omega)$ of $La_{2-x}Sr_x(Ca_x)CoO_4$, $La_{1.5}Ca_{0.5}CoO_4$, and $LaCoO_3$ at $T = 15$ K 206
7.58 Optical conductivity $\sigma_1(\omega)$ of $La_{2-x}Sr_xCoO_4$, $La_{1.5}Ca_{0.5}CoO_4$, and $LaCoO_3$ at $T = 300$ K 207
7.59 Optical conductivity $\sigma_1(\omega)$ of $La_{2-x}Sr_xCoO_4$, $La_{1.5}Ca_{0.5}CoO_4$, and $LaCoO_3$ at $T = 490$ K 208
7.60 Maximum values of $\sigma_1(\omega)$ of $La_{2-x}Sr_xCoO_4$ and $La_{1.5}Ca_{0.5}CoO_4$. 209
7.61 Integrated spectral weight of $La_{2-x}Sr_xCoO_4$ and $La_{1.5}Ca_{0.5}CoO_4$. 211

List of Tables

5.1 Lattice parameters of YVO_3 64
5.2 Lattice parameters of $CeVO_3$ 65
5.3 Theoretically obtained optical spectral weights of the MH excitations in RVO_3 73
5.4 Parameters of the fit to the measured data of YVO_3 with Gaussian and Tauc-Lorentz oscillators (a and b axis) 83
5.5 Parameters of the fit to the measured data of YVO_3 with Gaussian and Tauc-Lorentz oscillators (c axis) 84
5.6 Parameters of the fit to the measured data of $GdVO_3$ with Gaussian oscillators (a axis) 89
5.7 Parameters of the fit to the measured data of $GdVO_3$ with Gaussian oscillators (c axis) 89
5.8 Parameters of the fit to the measured data of $CeVO_3$ with Gaussian oscillators (a axis) 94
5.9 Parameters of the fit to the measured data of $CeVO_3$ with Gaussian oscillators (c axis) 94
5.10 Peak assignment for the data of RVO_3 99

6.1 Matrix elements for MH excitations in $LaSrFeO_4$ 129
6.2 Parameters of the fit to the measured data of $LaSrFeO_4$ with Gaussian oscillators (a axis) 135
6.3 Parameters of the fit to the measured data of $LaSrFeO_4$ with Gaussian oscillators (c axis) 136

7.1 Lattice parameters of $La_{2-x}Sr_xCoO_4$ and $La_{1.5}Ca_{0.5}CoO_4$ at room temperature 152
7.2 Information on the data acquisition and analysis of the cobaltate samples 189

Bibliography

[1] M. Imada, A. Fujimori, and Y. Tokura, Reviews of Modern Physics **70**(4), 1039–1263 (1998).

[2] S. Jin, T. H. Tiefel, M. McCormack, R. A. Fastnacht, R. Ramesh, and L. H. Chen, Science (New York, N.Y.) **264**(5157), 413–5 (1994).

[3] P. Schiffer, A. Ramirez, W. Bao, and S.-W. Cheong, Physical Review Letters **75**(18), 3336–3339 (1995).

[4] P. W. Anderson, Science (New York, N.Y.) **235**(4793), 1196–8 (1987).

[5] N. Mott, Proc. Phys. Soc. **62**, 416 (1949).

[6] J. Hubbard, Proc. roy. Soc. A **276**, 238 (1963).

[7] Y. Tokura and N. Nagaosa, Science **288**(5465), 462–468 (2000).

[8] A. M. Oleś, G. Khaliullin, P. Horsch, and L. F. Feiner, Physical Review B **72**(21), 214431 (2005).

[9] J. S. Lee, M. W. Kim, and T. W. Noh, New Journal of Physics **7**(05), 147–147 (2005).

[10] G. Khaliullin, P. Horsch, and A. M. Oleś, Physical Review B **70**(19), 195103 (2004).

[11] N. Kovaleva, A. V. Boris, C. Bernhard, A. Kulakov, A. Pimenov, A. M. Balbashov, G. Khaliullin, and B. Keimer, Physical Review Letters **93**(14), 147204 (2004).

[12] A. Gössling, M. W. Haverkort, M. Benomar, H. Wu, D. Senff, T. Möller, M. Braden, J. A. Mydosh, and M. Grüninger, Physical Review B **77**(3), 035109 (2008).

[13] A. Gössling, R. Schmitz, H. Roth, M. W. Haverkort, T. Lorenz, J. A. Mydosh, E. Müller-Hartmann, and M. Grüninger, Physical Review B **78**(7), 075122 (2008).

[14] G. Khaliullin, P. Horsch, and A. M. Oleś, Physical Review Letters **86**(17), 3879–3882 (2001).

[15] C. Ulrich, G. Khaliullin, J. Sirker, M. Reehuis, M. Ohl, S. Miyasaka, Y. Tokura, and B. Keimer, Physical Review Letters **91**(25), 257202 (2003).

[16] P. Horsch, G. Khaliullin, and A. M. Oleś, Physical Review Letters **91**(25), 257203 (2003).

[17] A. M. Oleś, P. Horsch, and G. Khaliullin, Physical Review B **75**(18), 184434 (2007).

[18] E. Benckiser, R. Rückamp, T. Möller, T. Taetz, A. Möller, A. A. Nugroho, T. T. M. Palstra, G. S. Uhrig, and M. Grüninger, New Journal of Physics **10**(5), 053027 (2008).

[19] Z. Fang and N. Nagaosa, Physical Review Letters **93**(17), 176404 (2004).

[20] M. De Raychaudhury, E. Pavarini, and O. K. Andersen, Physical Review Letters **99**(12), 126402 (2007).

[21] S. Miyasaka, Y. Okimoto, and Y. Tokura, Journal of the Physical Society of Japan **71**(9), 2086–2089 (2002).

[22] J. Fujioka, S. Miyasaka, and Y. Tokura, Physical Review B **77**(14), 144402 (2008).

[23] A. A. Tsvetkov, F. P. Mena, P. H. M. van Loosdrecht, D. van der Marel, Y. Ren, A. A. Nugroho, A. A. Menovsky, I. S. Elfimov, and G. A. Sawatzky, Physical Review B **69**(7), 075110 (2004).

[24] M. A. Korotin, S. Y. Ezhov, I. V. Solovyev, V. I. Anisimov, D. I. Khomskii, and G. A. Sawatzky, Physical Review B **54**(8), 5309–5316 (1996).

[25] J. Baier, S. Jodlauk, M. Kriener, A. Reichl, C. Zobel, H. Kierspel, A. Freimuth, and T. Lorenz, Physical Review B **71**(1), 1–10 (2005).

[26] M. W. Haverkort, Z. Hu, J. C. Cezar, T. Burnus, H. Hartmann, M. Reuther, C. Zobel, T. Lorenz, A. Tanaka, N. B. Brookes, H. H. Hsieh, H. Lin, C. T. Chen, and L. H. Tjeng, Physical Review Letters **97**, 176405 (2006).

[27] Y. Tokura, Y. Okimoto, S. Yamaguchi, H. Taniguchi, T. Kimura, and H. Takagi, Physical Review B **58**(4), 1699–1702 (1998).

[28] Y. Moritomo, K. Higashi, K. Matsuda, and A. Nakamura, Physical Review B **55**(22), 725–728 (1997).

[29] N. Hollmann, M. W. Haverkort, M. Benomar, M. Cwik, M. Braden, and T. Lorenz, Physical Review B **83**(17), 174435 (2011).

[30] M. Merz, D. Fuchs, A. Assmann, S. Uebe, H. v. Löhneysen, P. Nagel, and S. Schuppler, Physical Review B **84**(1), 014436 (2011).

[31] J. Wang, Y. C. Tao, W. Zhang, and D. Y. Xing, Journal of Physics: Condensed Matter **12**, 7425 (2000).

[32] J. S. Lee, H. Q. Yamamoto, M. Uchida, and Y. Tokura, Physical Review B **86**(4), 045133 (2012).

[33] P. Fazekas, *Lecture Notes on Electron Correlation and Magnetism, Series in Modern Condensed Matter Physics - Vol. 5*, World Scientific, Singapore, 1999.

[34] A. Altland and B. D. Simons, *Condensed Matter Field Theory*, Cambridge University Press, 2 edition, 2010.

[35] S. Sugano, Y. Tanabe, and H. Kamimura, *Multiplets of Transition-Metal Ions in Crystals, volume 33 in Pure and Applied Physics*, Academic Press, New York and London, 1970.

[36] C. Ballhausen, *Introcuction to Ligand Field Theory*, McGraw-Hill, 1962.

[37] E. Benckiser, *Optical Spectroscopy of Orbital and Magnetic Excitations in Vanadates and Cuprates*, PhD thesis, University of Cologne, 2007.

[38] Y. S. Lee, J. S. Lee, T. W. Noh, D. Y. Byun, K. S. Yoo, K. Yamaura, and E. Takayama-Muromachi, Physical Review B **67**(11), 113101 (2003).

[39] T. Higuchi, T. Tsukamoto, M. Watanabe, M. M. Grush, T. A. Callcott, R. C. Perera, D. L. Ederer, Y. Tokura, Y. Harada, Y. Tezuka, and S. Shin, Physical Review B **60**(11), 7711–7714 (1999).

[40] H. A. Jahn and E. Teller, Proc. roy. Soc. **161**, 220 (1937).

[41] Y. Jean, *Molecular Orbitals of Transition Metal Complexes*, Oxford University Press, New York, 1 edition, 2005.

[42] M. Cwik, *The Interplay of Lattice, Spin, and Charge Degrees of Freedom in Layered Cobaltates*, PhD thesis, University of Cologne, 2007.

[43] A. Gössling, *Electronic structure of Titanates and layered Manganites probed by optical spectroscopy*, PhD thesis, University of Cologne, 2007.

[44] Y. Tanabe and S. Sugano, Journal of the Physical Society of Japan **9**, 766 (1954).

[45] J. van den Brink, W. Stekelenburg, D. I. Khomskii, G. A. Sawatzky, and K. I. Kugel, Physical Review B **58**(16), 10276–10282 (1998).

[46] P. W. Anderson, Physical Review **115**(1), 2 (1959).

[47] K. I. Kugel and D. I. Khomskii, Sov. Phys. Usp. **25**, 231 (1982).

[48] P. Horsch, A. M. Oleś, L. F. Feiner, and G. Khaliullin, Physical Review Letters **100**(16), 167205 (2008).

[49] G. Khaliullin, Progress of Theoretical Physics Supplement **160**(160), 155–202 (2005).

[50] B. Henderson and G. F. Imbusch, *Optical Spectroscopy of Inorganic Solids*, Oxford University Press, 1989.

[51] P. Y. Yu and M. Cardona, *Fundamentals of Semiconductors*, Springer, 2001.

[52] J. Zaanen, A. G. Sawatzky, and J. W. Allen, Physical Review Letters **55**(4), 418–421 (1985).

[53] J. Zaanen and G. A. Sawatzky, Journal of Solid State Chemistry **88**, 8 (1990).

[54] T. Mizokawa and A. Fujimori, Physical Review B **54**(8), 5368–5380 (1996).

[55] J. Matsuno, Y. Okimoto, M. Kawasaki, and Y. Tokura, Physical Review Letters **95**(17), 176404 (2005).

[56] P. Olalde-Velasco, J. Jiménez-Mier, J. D. Denlinger, Z. Hussain, and W. L. Yang, Physical Review B **83**(24), 241102 (2011).

[57] T. Arima, Y. Tokura, and J. B. Torrance, Physical Review B **48**(23), 17006 (1993).

[58] Y. Okimoto, T. Katsufuji, Y. Okada, T. Arima, and Y. Tokura, Physical Review B **51**(15), 9581 (1995).

[59] K. Tobe, T. Kimura, Y. Okimoto, and Y. Tokura, Physical Review B **64**(18), 184421 (2001).

[60] H. Kuzmany, *Solid-State Spectroscopy: An Introduction*, Springer, 1 edition, 1998.

[61] F. Wooten, *Optical Properties of Solids*, Academic Press Inc, New York and London, 1972.

[62] C. Kittel, *Einführung in die Festkörperphysik*, Oldenbourg Wissenschaftsverlag GmbH, München, 13 edition, 2002.

[63] H. G. Tompkins and E. A. Irene, *Handbook of Ellipsometry*, William Andrew Publishing, Springer, USA, 2005.

[64] J. Honerkamp and H. Römer, *Klassische Theoretische Physik: Eine Einführung*, Springer, 3 edition, 1993.

[65] *WVASE32 MANUAL: Guide to using WVASE32*, J.A. Woollam Co., Inc.

[66] F. Bréhat and B. Wyncke, J. Phys. D: Appl. Phys. **24**, 2055 (1991).

[67] D. E. Aspnes, Josa Letters **70**(10), 1275–1277 (1980).

[68] G. R. Blake, T. T. M. Palstra, Y. Ren, A. A. Nugroho, and A. A. Menovsky, Physical Review B **65**(17), 174112 (2002).

[69] N. Qureshi, H. Ulbrich, Y. Sidis, A. Cousson, and M. Braden, Physical Review B **87**(5), 054433 (2013).

[70] M. Kriener, C. Zobel, A. Reichl, J. Baier, M. Cwik, K. Berggold, H. Kierspel, O. Zabara, A. Freimuth, and T. Lorenz, Physical Review B **69**(9), 094417 (2004).

[71] J. Küppersbusch, *Ellipsometrische Untersuchungen der Mott-Hubbard-Anregungen in YVO_3 und $GdVO_3$*, Diploma thesis, University of Cologne, 2009.

[72] M. Reehuis, C. Ulrich, P. Pattison, B. Ouladdiaf, M. Rheinstädter, M. Ohl, L. Regnault, M. Miyasaka, Y. Tokura, and B. Keimer, Physical Review B **73**(9), 094440 (2006).

[73] Y. Ren, A. A. Nugroho, A. A. Menovsky, J. Strempfer, U. Rütt, F. Iga, T. Takabatake, and C. W. Kimball, Physical Review B **67**(1), 3–8 (2003).

[74] M. Sage, G. R. Blake, C. Marquina, and T. T. M. Palstra, Physical Review B **76**(19), 195102 (2007).

[75] M. Reehuis, C. Ulrich, P. Pattison, M. Miyasaka, Y. Tokura, and B. Keimer, The European Physical Journal B **64**(1), 27–34 (2008).

[76] A. Muñoz, J. A. Alonso, M. T. Casáis, M. J. Martínez-Lope, J. L. Martínez, and M. T. Fernández-Díaz, Physical Review B **68**(14), 144429 (2003).

[77] P. Bordet, C. Chaillout, M. Marezio, Q. Huang, A. Santoro, S.-W. Cheong, H. Takagi, and B. Oglesby, Journal of Solid State Chemistry **106**(2), 253 (1993).

[78] S. Miyasaka, Y. Okimoto, M. Iwama, and Y. Tokura, Physical Review B **68**(10), 100406 (2003).

[79] F. Wang, J. Zhang, P. Yuan, Q. Yan, and P. Zhang, Journal of Physics: Condensed Matter **12**, 3037–3040 (2000).

[80] J. Pickardt, T. Schendler, and M. Kolm, Z. Allg. Anorg. Chem **560**, 153 (1988).

[81] I. V. Solovyev, Journal of Physics: Condensed Matter **20**(29), 293201 (2008).

[82] Y. Otsuka and M. Imada, Journal of the Physical Society of Japan **75**(12), 124707 (2006).

[83] Y. Ren, T. T. M. Palstra, D. I. Khomskii, A. A. Nugroho, A. A. Menovsky, and G. A. Sawatzky, Physical Review B **62**(10), 6577–6586 (2000).

[84] H. Kawano, H. Yoshizawa, and Y. Ueda, Journal of the Physical Society of Japan **63**(8), 2857–2861 (1994).

[85] A. Muñoz, J. A. Alonso, M. T. Casais, M. J. Martínez-Lope, J. L. Martínez, and M. T. Fernández-Díaz, Journal of Materials Chemistry **13**(5), 1234–1240 (2003).

[86] M. Noguchi, A. Nakazawa, S. Oka, T. Arima, Y. Wakabayashi, H. Nakao, and Y. Murakami, Physical Review B **62**(14), 9271–9274 (2000).

[87] G. R. Blake, T. T. M. Palstra, Y. Ren, A. A. Nugroho, and A. A. Menovsky, Physical Review Letters **87**(24), 245501 (2001).

[88] Y. Ren, T. T. M. Palstra, D. I. Khomskii, E. Pellegrin, A. A. Nugroho, A. A. Menovsky, and G. A. Sawatzky, Nature **396**, 441–444 (1998).

[89] T. Mizokawa, D. I. Khomskii, and G. A. Sawatzky, Physical Review B **60**(10), 7309–7313 (1999).

[90] J. Sirker and G. Khaliullin, Physical Review B **67**(10), 100408 (2003).

[91] S. Miyasaka, S. Onoda, Y. Okimoto, J. Fujioka, M. Iwama, N. Nagaosa, and Y. Tokura, Physical Review Letters **94**(7), 076405 (2005).

[92] S. Miyasaka, J. Fujioka, M. Iwama, Y. Okimoto, and Y. Tokura, Physical Review B **73**(22), 224436 (2006).

[93] S. Sugai and K. Hirota, Physical Review B **73**(2), 020409 (2006).

[94] G. R. Blake, A. A. Nugroho, M. J. Gutmann, and T. T. M. Palstra, Physical Review B **79**(4), 045101 (2009).

[95] J. Fujioka, T. Yasue, S. Miyasaka, Y. Yamasaki, T. Arima, H. Sagayama, T. Inami, K. Ishii, and Y. Tokura, Physical Review B **82**(14), 144425 (2010).

[96] M. Voigt, *Kollektive orbitale Anregungen in* $GdVO_3$, Diploma thesis, University of Cologne, 2012.

[97] J. Mc Carthy, C. A. Sipe, and E. Mc Ilvried, Mater. Res. Bull. (9), 1279 (1974).

[98] A. M. Oleś, Journal of Physics: Condensed Matter **24**(31), 313201 (2012).

[99] Z. Fang, N. Nagaosa, and K. Terakura, Physical Review B **67**(3), 035101 (2003).

[100] I. Solovyev, N. Hamada, and K. Terakura, Physical Review B **53**(11), 7158–7170 (1996).

[101] K. Maiti and D. D. Sarma, Physical Review B **61**(4), 2525–2534 (2000).

[102] R. J. O. Mossanek, M. Abbate, T. Yoshida, A. Fujimori, Y. Yoshida, N. Shirakawa, H. Eisaki, S. Kohno, and F. C. Vicentin, Physical Review B **78**(7), 075103 (2008).

[103] D. G. Clarke, Physical Review B **48**(10), 7520 (1993).

[104] Y. Y. Wang, F. C. Zhang, V. P. Dravid, K. K. Ng, M. V. Klein, S. E. Schnatterly, and L. L. Miller, Physical Review Letters **77**(9), 1809–1812 (1996).

[105] F. C. Zhang and K. K. Ng, Physical Review B **58**(20), 13520–13525 (1998).

[106] P. Wróbel and R. Eder, Physical Review B **66**(3), 035111 (2002).

[107] R. O. Kuzian, R. Hayn, and A. F. Barabanov, Physical Review B **68**(19), 195106 (2003).

[108] M. E. Simón, A. A. Aligia, C. D. Batista, E. R. Gagliano, and F. Lema, Physical Review B **54**(6), R3780–R3783 (1996).

[109] D. Ellis, J. Hill, S. Wakimoto, R. J. Birgeneau, D. Casa, T. Gog, and Y.-J. Kim, Physical Review B **77**(6), 060501 (2008).

[110] A. S. Moskvin, R. Neudert, M. Knupfer, J. Fink, and R. Hayn, Physical Review B **65**(18), 180512 (2002).

[111] E. Collart, A. Shukla, J.-P. Rueff, P. Leininger, H. Ishii, I. Jarrige, Y. Cai, S.-W. Cheong, and G. Dhalenne, Physical Review Letters **96**(15), 157004 (2006).

[112] J. E. Hirsch, Physical Review Letters **59**(2), 228–231 (1987).

[113] J. E. Hirsch, Science (New York, N.Y.) **295**(5563), 2226–7 (2002).

[114] H. J. A. Molegraaf, C. Presura, D. van Der Marel, P. H. Kes, and M. Li, Science (New York, N.Y.) **295**(5563), 2239–41 (2002).

[115] F. Novelli, D. Fausti, J. Reul, F. Cilento, P. H. M. van Loosdrecht, A. A. Nugroho, T. T. M. Palstra, M. Grüninger, and F. Parmigiani, Physical Review B **86**(16), 165135 (2012).

[116] J. Reul, L. Fels, N. Qureshi, K. Shportko, M. Braden, and M. Grüninger, Physical Review B **87**, 205142 (2013).

[117] T. Arima and Y. Tokura, Journal of the Physical Society of Japan **64**(7), 2488 (1995).

[118] Y. Moritomo, T. Arima, and Y. Tokura, Jounal of the Physical Society of Japan **64**(11), 4117 (1995).

[119] Y. S. Lee, T. Arima, S. Onoda, Y. Okimoto, Y. Tokunaga, R. Mathieu, X. Z. Yu, J. P. He, Y. Kaneko, Y. Matsui, N. Nagaosa, and Y. Tokura, Physical Review B **75**(14), 144407 (2007).

[120] J. H. Jung, K. H. Kim, D. J. Eom, T. W. Noh, E. J. Choi, J. Yu, Y. S. Kwon, and Y. Chung, Physical Review B **55**(23), 15489–15493 (1997).

[121] M. A. Quijada, J. R. Simpson, L. Vasiliu-Doloc, J. W. Lynn, H. D. Drew, Y. M. Mukovskii, and S. G. Karabashev, Physical Review B **64**(22), 224426 (2001).

[122] M. W. Kim, P. Murugavel, S. Parashar, J. S. Lee, and T. W. Noh, New Journal of Physics **6**(04), 156–156 (2004).

[123] M. W. Kim, S. J. Moon, J. Jung, J. Yu, S. Parashar, P. Murugavel, J. H. Lee, and T. W. Noh, Physical Review Letters **96**(24), 247205 (2006).

[124] A. S. Moskvin, A. A. Makhnev, L. V. Nomerovannaya, N. N. Loshkareva, and A. M. Balbashov, Physical Review B **82**(3), 035106 (2010).

[125] R. V. Pisarev, A. S. Moskvin, A. M. Kalashnikova, and T. Rasing, Physical Review B **79**(23), 235128 (2009).

[126] Y. Moritomo, Y. Tomioka, A. Asamitsu, and Y. Tokura, Physical Review B **51**(5), 3297–3301 (1995).

[127] T. Omata, K. Ueda, H. Hosono, T. Miyazaki, S. Hasegawa, N. Ueda, and H. Kawazoe, Physical Review B **49**(15), 10200 (1994).

[128] J. L. Soubeyroux, P. Courbin, L. Fournes, D. Fruchart, and G. Le Flem, Journal of Solid State Chemistry **31**, 313–320 (1980).

[129] T. Omata, K. Ueda, H. Hosona, M. Katada, N. Ueda, and H. Kawazoe, Physical Review B **49**(15), 10194–10199 (1994).

[130] T. Omata, H. Ikawa, S. Fijitsu, N. Ueda, H. Hosono, and H. Kawazoe, Solid State Communications **97**(5), 411–415 (1996).

[131] S. Tajima, H. Ishii, T. Nakahashi, T. Takagi, S. Uchida, M. Seki, S. Suga, Y. Hidaka, M. Suzuki, T. Murakami, K. Oka, and H. Unoki, Journal of the Optical Society of America B **6**(3), 475 (1989).

[132] A. I. Galuza, A. B. Beznosov, and V. V. Eremenko, Low Temperature Physics **24**(10), 726–729 (1998).

[133] R. Rückamp, E. Benckiser, M. W. Haverkort, H. Roth, T. Lorenz, A. Freimuth, L. Jongen, A. Möller, G. Meyer, P. Reutler, B. Büchner, A. Revcolevschi, S.-W. Cheong, C. Sekar, G. Krabbes, and M. Grüninger, New Journal of Physics **7**(05), 144–144 (2005).

[134] B. N. Figgis and M. A. Hichman, *Ligand Field Theory and Its Applications*, Wiley-VCH, 2000.

[135] W. Harrison, *Elementary Electronic Structure, revised edition*, World Scientific, Singapore, 2011.

[136] K. Takada, H. Sakurai, E. Takayama-Muromachi, F. Izumi, R. A. Dilanian, and T. Sasaki, Nature **422**(March), 53–55 (2003).

[137] J. Pérez, J. GarcÄś, J. Blasco, and J. Stankiewicz, Physical Review Letters **80**(11), 2401–2404 (1998).

[138] H. Wu, Physical Review B **81**(11), 115127 (2010).

[139] H. Wu and T. Burnus, Physical Review B **80**(8), 081105 (2009).

[140] R. Eder, Physical Review B **81**(3), 035101 (2010).

[141] P. Radaelli and S.-W. Cheong, Physical Review B **66**(9), 094408 (2002).

[142] M. Kriener, M. Braden, H. Kierspel, D. Senff, O. Zabara, C. Zobel, and T. Lorenz, Physical Review B **79**(22), 224104 (2009).

[143] M. Zhuang, W. Zhang, C. Hu, and N. Ming, Physical Review B **57**(17), 710–715 (1998).

[144] M. Abbate, R. Potze, G. A. Sawatzky, and A. Fujimori, Physical Review B **49**(11), 7210–7218 (1994).

[145] H. Takahashi, F. Munakata, and M. Yamanaka, Physical Review B **53**(7), 3731–3740 (1996).

[146] P. M. Raccah and J. B. Goodenough, Physical Review **155**, 932 (1967).

[147] S. Xu, Y. Moritomo, K. Mori, T. Kamiyama, T. Saitoh, and A. Nakamura, Jounal of the Physical Society of Japan **70**(11), 3296–3299 (2001).

[148] Y. Kobayashi, T. Mitsunaga, G. Fujinawa, A. Tadashi, M. Suetake, K. Asai, and J. Harada, Journal of the Physical Society of Japan **69**(10), 3468–3469 (2000).

[149] G. Maris, Y. Ren, V. Volotchaev, C. Zobel, T. Lorenz, and T. T. M. Palstra, Physical Review B **67**(22), 224423 (2003).

[150] G. Thornton, B. C. Tofield, and A. W. Hewat, Journal of Solid State Chemistry **61**, 301 (1986).

[151] S. Yamaguchi, Y. Okimoto, H. Taniguchi, and Y. Tokura, Physical Review B **53**(6), R2926–R2929 (1996).

[152] S. Amaguchi, Y. Okimoto, and Y. Tokura, Physical Review B **54**(16), R11022–R11025 (1996).

[153] S. R. English, J. Wu, and C. Leighton, Physical Review B **65**(22), 220407 (2002).

[154] R. Mahendiran and A. K. Raychaudhuri, Physical Review B **54**(22), 16044–16052 (1996).

[155] S. Stolen, F. Gronvold, H. Brinks, T. Atake, and H. Mori, Physical Review B **55**(21), 103–106 (1997).

[156] K. Berggold, M. Kriener, P. Becker, M. Benomar, M. Reuther, C. Zobel, and T. Lorenz, Physical Review B **78**(13), 134402 (2008).

[157] S. Yamaguchi, Y. Okimoto, and Y. Tokura, Physical Review B **55**(14), 8666–8669 (1997).

[158] C. Zobel, M. Kriener, D. Bruns, J. Baier, M. Grüninger, T. Lorenz, P. Reutler, and A. Revcolevschi, Physical Review B **66**(2), 020402 (2002).

[159] G. H. Jonker and J. H. Van Santen, Physica (Amsterdam) **19**, 120 (1953).

[160] V. Bhide, Physical Review B **6**, 1021 (1972).

[161] K. Asai, O. Yokokura, N. Nishimori, H. Chou, J. M. Tranquada, G. Shirane, S. Higuchi, Y. Okajima, and K. Kohn, Physical Review B **50**(5), 3025 (1994).

[162] M. Itoh, I. Natori, S. Kubota, and K. Motoya, Journal of the Physical Society of Japan **63**(4), 1486–1493 (1994).

[163] M. Senaris-Rodriguez and J. Goodenough, Journal of Solid State Chemistry **116**, 224 (1995).

[164] A. Ishikawa, J. Nohara, and S. Sugai, Physical Review Letters **93**(13), 136401 (2004).

[165] G. H. Kwei, D. Louca, J. L. Sarrao, J. D. Thompson, and H. Ro, Physical Review B **60**(14), 378–382 (1999).

[166] T. Saitoh, T. Mizokawa, A. Fujimori, M. Abbate, Y. Takeda, and M. Takano, Physical Review B **55**(7), 4257–4266 (1997).

[167] M. Kriener, *Spinzustandsänderung, magntische Ordnung und Metall-Isolator-Übergang in Kobaltaten*, PhD thesis, University of Cologne, 2005.

[168] S. Noguchi, S. Kawamata, K. Okuda, H. Nojiri, and M. Motokawa, Physical Review B **66**(9), 094404 (2002).

[169] Z. Ropka and R. J. Radwanski, Physical Review B **67**(17), 172401 (2003).

[170] A. Podlesnyak, S. Streule, J. Mesot, M. Medarde, E. Pomjakushina, K. Conder, A. Tanaka, M. W. Haverkort, and D. I. Khomskii, Physical Review Letters **97**(24), 247208 (2006).

[171] N. Sundaram, Y. Jiang, I. E. Anderson, D. P. Belanger, C. H. Booth, F. Bridges, J. F. Mitchell, T. Proffen, and H. Zheng, Physical Review Letters **102**(2), 026401 (2009).

[172] K. Asai, A. Yoneda, O. Yokokura, J. M. Tranquada, G. Shirane, and K. Kohn, Journal of the Physical Society of Japan **67**(1), 290–296 (1998).

[173] G. Thornton, F. C. Morrison, S. Partington, B. C. Tofield, and D. E. Williams, J. Phys.C - Solid State Phys. **21**, 2871–2880 (1988).

[174] M. Cwik, M. Benomar, T. Finger, Y. Sidis, D. Senff, M. Reuther, T. Lorenz, and M. Braden, Physical Review Letters **102**(5), 057201 (2009).

[175] I. A. Zaliznyak, J. M. Tranquada, R. Erwin, and Y. Moritomo, Physical Review B **64**(19), 195117 (2001).

[176] K. Yamada, M. Matsuda, Y. Endoh, B. Keimer, R. J. Birgeneau, S. Onoder, J. Mizusaki, T. Matruura, and G. Shirane, Physical Review B **39**(4), 2336–2343 (1989).

[177] S. Wakimoto, R. J. Birgeneau, M. A. Kastner, Y. S. Lee, R. Erwin, P. M. Gehring, S. H. Lee, M. Fujita, K. Yamada, Y. Endoh, K. Hirota, and G. Shirane, Physical Review B **61**(5), 3699–3706 (2000).

[178] K. Yamada, C. H. Lee, K. Kurahashi, J. Wada, S. Wakimoto, S. Ueki, H. Kimura, Y. Endoh, S. Hosoya, G. Shirane, R. J. Birgeneau, M. Greven, M. A. Kastner, and Y. J. Kim, Physical Review B **57**(10), 6165–6172 (1998).

[179] H. Yoshizawa, T. Kakeshita, R. Kajimoto, T. Tanabe, T. Katsufuji, and Y. Tokura, Physical Review B **61**(2), 854–857 (2000).

[180] R. Kajimoto, K. Ishizaka, H. Yoshizawa, and Y. Tokura, Physical Review B **67**(1), 014511 (2003).

[181] I. A. Zaliznyak, J. P. Hill, J. M. Tranquada, R. Erwin, and Y. Moritomo, Physical Review Letters **85**(20), 4353–6 (2000).

[182] B. J. Sternlieb, J. P. Hill, U. C. Wildgruber, G. M. Luke, B. Nachumi, Y. Moritomo, and Y. Tokura, Physical Review Letters **76**(12), 2169–2172 (1996).

[183] K. Horigane, H. Nakao, Y. Kousaka, T. Murata, Y. Noda, Y. Murakami, and J. Akimitsu, Journal of the Physical Society of Japan **77**(4), 044601 (2008).

[184] K. Horigane, H. Hiraka, T. Uchida, K. Yamada, and J. Akimitsu, Journal of the Physical Society of Japan **76**(11), 114715 (2007).

[185] M. Benomar, *Einkristall-Präparation und Charakterisierung von dotiertem La_2MO_4 mit M=Co, Mn, und Ni*, PhD thesis, University of Cologne, 2007.

[186] T. Matsuura, J. Tabwchi, J. Mizusaki, and S. Yamauchi, J. Phys. Chem. Solids **49**(12), 1403–1408 (1988).

[187] M. Itoh, M. Mori, Y. Moritomo, and A. Nakamura, Physica B: Condensed Matter **261**, 997–998 (1999).

[188] N. Hollmann, M. W. Haverkort, M. Cwik, M. Benomar, M. Reuther, A. Tanaka, and T. Lorenz, New Journal of Physics **10**(2), 023018 (2008).

[189] C. F. Chang, Z. Hu, H. Wu, T. Burnus, N. Hollmann, M. Benomar, T. Lorenz, A. Tanaka, H.-J. Lin, H. Hsieh, C. T. Chen, and L. H. Tjeng, Physical Review Letters **102**(11), 116401 (2009).

[190] T. Jia, H. Wu, G. Zhang, X. Zhang, Y. Guo, Z. Zeng, and H. Q. Lin, Physical Review B **82**(20), 205107 (2010).

[191] L. Helme, A. T. Boothroyd, R. Coldea, D. Prabhakaran, C. D. Frost, D. A. Keen, L. P. Regnault, P. G. Freeman, M. Enderle, and J. Kulda, Physical Review B **80**(13), 134414 (2009).

[192] A. Chichev, M. Dlouhá, S. Vratislav, K. Knížek, J. Hejtmánek, M. Maryško, M. Veverka, Z. Jirák, N. O. Golosova, D. P. Kozlenko, and B. N. Savenko, Physical Review B **74**(13), 134414 (2006).

[193] Y. Shimada, S. Miyasaka, R. Kumai, and Y. Tokura, Physical Review B **73**, 134424 (2006).

[194] R. Ang, Y. P. Sun, X. Luo, C. Y. Hao, and W. H. Song, Journal of Physics D: Applied Physics **41**(4), 045404 (2008).

[195] S. Uchida, H. Eisaki, and S. Tajima, Physica B: Condensed Matter **188**, 975–980 (1993).

Acknowledgements

Last but not least I would like to thank all people who contributed to the successful completion of this thesis.

Special thanks go to my supervisor Prof. Dr. Markus Grüninger. Thank you for many valuable suggestions and fruitful discussions and finally for giving me the opportunity to perform this PhD study. I really enjoyed working with you!

I would like to thank Prof. Dr. ir. Paul H. M. van Loosdrecht for co-assessing this thesis.

My best thanks go to all current and former members of the optics group, Christina Hilgers, Luis Mäder, Eva Benckiser, Konstantin Shportko, Holger Schmitz, Malte Langenbach, Ignacio Vergara, Michael Voigt, and Komalavalli Thirunavukkuarasu for always lending a helping hand and the excellent team work.

Special thanks go to the colleagues of my office Jens Rohrkamp, Daniel Niermann, and Christoph Grams for the excellent atmosphere in our office and the extraordinary helpfulness with all kinds of (computer) problems.

My best thanks go to the crystal growers A. A. Nugroho, T. T. M. Palstra, N. Qureshi, A. C. Komarek, and M. Reuter for providing the high-quality singly crystals, which are the basis of this PhD work.

I would like to thank D. Basov for giving me the opportunity to spend four excellent month working with his group at the University of California San Diego.

Special thanks go to the Bonn-Cologne Graduate School of Physics and Astronomy for the great support throughout this PhD project and the DFG for funding this PhD project through the SFB 608.

I would like to thank all members of the II. Physical Institute for the outstanding working atmosphere. It was a wonderful time.

Last but not least I would like to thank my family Philipp and Lila and my parents for the outstanding support throughout this PhD project.

Publications

Probing orbital fluctuations in $R\mathrm{VO}_3$ ($R =$ Y, Gd, or Ce) by ellipsometry
J. Reul, A. A. Nugroho, T. T. M. Palstra, and M. Grüninger
Physical Review B **86**, 125128 (2012)

Temperature-dependent optical conductivity of layered $\mathrm{LaSrFeO}_4$
J. Reul, L. Fels, N. Qureshi, K. Shportko, M. Braden, and M. Grüninger
Physical Review B **87**, 205142 (2013)

Ultrafast optical spectroscopy of the lowest energy excitations in the Mott insulator compound YVO_3: Evidence for Hubbard-type excitons
F. Novelli, D. Fausti, J. Reul, F. Cilento, P. H. M. van Loosdrecht, A. A. Nugroho, T. T. M. Palstra, M. Grüninger, and F. Parmigiani
Physical Review B **86**, 165135 (2012)

Abstract

Within the scope of this thesis different transition-metal oxides with open d shells are investigated by means of spectroscopic ellipsometry in the energy range from 0.75 eV to 5.5 eV for temperatures ranging from 15 K to 490 K. The focus is on spin and orbital degrees of freedom and their impact on the optical spectra. The multipeak structures observed in the optical conductivity show a pronounced dependence on both temperature and polarization. We analyze the spectra in terms of multiplets which form the upper Hubbard band.

Our optical analysis of the multi-orbital Mott-Hubbard insulators YVO_3, $GdVO_3$, and $CeVO_3$ yields a consistent description of the observed absorption bands in terms of $3d^3$ excited states which constitute the upper Hubbard band and thereby solves the discrepancies of the optical spectra of YVO_3 reported in the literature. The temperature and polarization dependence of the optical spectra reflects the complex spin and orbital ordering phase diagram of RVO_3 ($R = $ Y, rare earth ion). A comparison of our data with theoretical predictions based on either rigid orbital order or strong orbital fluctuations leads us to the conclusion that orbital fluctuations cannot be strong in RVO_3. The line shape and temperature dependence of a feature observed in the optical conductivity at around 2 eV gives evidence for an excitonic Mott-Hubbard resonance, i.e. not a truly bound state below the gap but a resonance within the absorption band, and demonstrates the important role played by the kinetic energy for exciton formation in orbitally ordered Mott-Hubbard insulators.

Due to the layered structure of the correlated insulator $LaSrFeO_4$ the optical spectra strongly depend on polarization. This anisotropy in combination with their different spectral weights offers an efficient tool to disentangle Mott-Hubbard excitations, corresponding to an electron transfer between neighboring Fe^{3+} sites, and charge-transfer excitations, corresponding to an electron transfer from the oxygen $2p$ band to the Fe $3d$ band. We arrive at a consistent peak assignment and find that the lowest dipole-allowed excitation, which contributes to the in-plane optical conductivity only, is of Mott-Hubbard type. This result is rather unexpected at first sight as the $3d^5$ electron configuration of Fe^{3+} is particularly stable due to the intra-atomic Hund exchange. We argue that the Fe $3d-$O $2p$ hybridization and particularly the large splitting of the e_g level originating from the tetragonal structure justify our result. The temperature dependence of the Mott-Hubbard excitations is only weak. This finding is in accordance with the fact that variations of nearest-neighbor spin-spin and orbital-orbital correlations are not strong below room temperature in $LaSrFeO_4$ with a Néel temperature of 366 K.

A further concern of this work lies on the correlated insulators $LaCoO_3$ and $EuCoO_3$ with Co^{3+} $3d^6$ electron configuration, which have attracted a lot of interest because of the spin-state degree of freedom. The low-spin state ($S = 0,\ t_{2g}^6 e_g^0$), the intermediate-spin state ($S = 1,\ t_{2g}^5 e_g^1$), and the high-spin state ($S = 2,\ t_{2g}^4 e_g^2$)

lie energetically close in these pseudocubic perovskites. It is well established that a thermal population of the high-spin state takes place from the low-spin ground state at $T \gtrsim 25\,\mathrm{K}$ in $LaCoO_3$. This so-called spin-state transition is shifted to much higher temperatures in the sister compound $EuCoO_3$. In addition, we present optical data of the single-layered perovskites $La_{2-x}Sr_xCoO_4$ ($x = 0, 0.33, 0.45, 0.5, 0.9$) and $La_{1.5}Ca_{0.5}CoO_4$, which contain both Co^{3+} $3d^6$ and Co^{2+} $3d^7$ ions. In agreement with claims of the literature for a doping-induced spin-state transition from a Co^{3+} low-spin state being realized in $La_{2-x}Sr_xCoO_4$ for doping concentrations $x \lesssim 0.8$ to a state of mixed Co^{3+} low-spin and high-spin ions in $LaSrCoO_4$, our optical spectra of $La_{1.1}Sr_{0.9}CoO_4$ differ considerably from the spectra of the compounds with $x \leqslant 0.5$. We assign the observed absorption bands to charge-transfer excitations from the oxygen $2p$ bands to the upper Hubbard bands. Surprisingly, we observe only small changes in the optical spectra of $LaCoO_3$ across the spin-state transition temperature, our spectra of $LaCoO_3$ resemble the spectra of $La_{1.1}Sr_{0.9}CoO_4$ already at low temperatures.

Kurzzusammenfassung

Im Rahmen dieser Arbeit werden die temperaturabhängigen optischen Spektren verschiedener Übergangsmetalloxide mit offenen d Schalen mit der Methode der spektroskopischen Ellipsometrie im Energiebereich von 0.75 eV bis 5.5 eV für Temperaturen von 15 K bis 490 K bestimmt und analysiert. Der Schwerpunkt liegt auf den Spin- und orbitalen Freiheitsgraden und deren Auswirkung auf die optischen Spektren. In der optischen Leitfähigkeit werden Multipeakstrukturen beobachtet, welche eine starke Temperatur- und Polarisationsabhängigkeit zeigen. Die Spektren werden im Sinne von Multiplettanregungen in das obere Hubbard-Band analysiert.
Unsere Analyse der optischen Daten an den multiorbitalen Mott-Hubbard-Isolatoren YVO_3, $GdVO_3$ und $CeVO_3$ mit $3d^2$-Elektronenkonfiguration liefert eine konsistente Beschreibung der beobachteten Absorptionsbänder in Form von Mott-Hubbard-Anregungen, einem Elektronentransfer zwischen benachbarten V^{3+}-Ionen, in die verschiedenen $3d^3$-Multipletts, welche das obere Hubbard-Band bilden. Die existierenden Widersprüche in der Literatur, welche sowohl die experimentellen optischen Daten an YVO_3 als auch deren Interpretation betreffen, können somit gelöst werden. Die starken Temperatur- und Polarisationsabhängigkeiten der optischen Spektren spiegeln das komplexe Phasendiagramm der Spin- und orbitalen Ordnung von RVO_3 ($R = $ Y, seltene Erde) wider. Der Vergleich unserer experimentellen Daten mit theoretischen Vorhersagen, welche entweder klassische orbitale Ordnung voraussetzen oder aber fluktuierende Orbitale zulassen, führt uns zu dem Ergebnis, dass orbitale Fluktuationen in RVO_3 nicht stark sein können. Die Linienform eines Absorptionsbandes, welches bei ca. 2 eV in der optischen Leitfähigkeit beobachtet wird, deutet auf das Vorliegen einer exzitonischen Resonanz hin. Damit ist nicht ein wirklich gebundener Zustand unterhalb der Bandlücke gemeint sondern vielmehr eine Resonanz innerhalb des Absorptionsbandes. Die beobachtete Temperaturabhängigkeit stellt die Wichtigkeit der kinetischen Energie für Exzitonenbildung in Mott-Hubbard-Isolatoren heraus.
Aufgrund der geschichteten Struktur des korrelierten Isolators $LaSrFeO_4$ zeigen dessen optische Spektren eine ausgeprägte Polarisationsabhängigkeit. Die beobachteten Absorptionsbänder werden Mott-Hubbard-Anregungen und Ladungstransferanregungen zugeordnet. Sowohl deren unterschiedliche spektralen Gewichte als auch die Anisotropie der Spektren können dazu genutzt werden, beide Typen von Anregungen in den Spektren zu identifizieren. Uns gelingt eine konsistente Peakzuordnung und wir kommen zu dem Resultat, dass die niedrigste dipolerlaubte Anregung eine Mott-Hubbard-Anregung ist. Dieses Ergebnis ist recht unerwartet, da die $3d^5$-Elektronenkonfiguration der Fe^{3+}-Ionen durch die Hundsche Kopplung besonders stabil ist. Das Resultat kann jedoch durch Fe-$3d$ O-$2p$-Hybridisierung und vor allem durch die recht große Aufspaltung des e_g-Levels, welche durch die tetragonale Struktur hervorgerufen wird, begründet werden.

Ein weiterer Schwerpunkt dieser Arbeit liegt auf der Analyse der korrelierten Isolatoren $LaCoO_3$ und $EuCoO_3$ mit Co^{3+} $3d^6$-Elektronenkonfiguration. Diese Verbindungen sind von besonderem Interesse aufgrund ihres Spinfreiheitsgrades. Der LS-Zustand mit $S = 0$, der IS-Zustand mit $S = 1$, und der HS-Zustand mit $S = 2$ liegen energetisch dicht beieinander. Es ist wohl bekannt, dass in dem pseudokubischen Perowskiten $LaCoO_3$ eine thermische Besetzung höherer Spinzustände vom LS-Grundzustand ab $T \gtrsim 25\,\mathrm{K}$ stattfindet. In der Verbindung $EuCoO_3$ ist dieser thermisch induzierte Spinübergang zu viel höheren Temperaturen verschoben. Außerdem werden optische Daten an den einfach geschichteten Perowskiten $La_{1.5}Ca_{0.5}CoO_4$ und $La_{2-x}Sr_xCoO_4$ ($x = 0$, 0.33, 0.45, 0.5, 0.9) vorgestellt, sie beinhalten sowohl Co^{3+} $3d^6$- als auch Co^{2+} $3d^7$-Ionen. In Übereinstimmung mit Behauptungen der Literatur eines dotierungsinduzierten Spinübergangs von einem Co^{3+} LS-Zustand für Dotierungen $x \lesssim 0.8$ in einen gemischten Zustand bestehend aus LS-Co^{3+}- und HS-Co^{3+}-Ionen in $LaSrCoO_4$, unterscheiden sich unsere optischen Spektren an $La_{1.1}Sr_{0.9}CoO_4$ signifikant von den Spektren an $La_{2-x}Sr_xCoO_4$ mit $x \leqslant 0.5$. Die beobachteten Absorptionsbänder werden Ladungstransferanregungen vom Sauerstoff-$2p$-Band in das obere Hubbard-Band zugeordnet. Erstaunlicherweise sind die Änderungen der Spektren an $LaCoO_3$ bei Überqueren der Spinübergangstemperatur nur klein. Die Spektren an $LaCoO_3$ ähneln denen an $La_{1.1}Sr_{0.9}CoO_4$ schon bei tiefen Temperaturen.

Offizielle Erklärung

Ich versichere, dass ich die von mir vorgelegte Dissertation selbständig angefertigt, die benutzten Quellen und Hilfsmittel vollständig angegeben und die Stellen der Arbeit - einschließlich Tabellen, Karten und Abbildungen -, die anderen Werken im Wortlaut oder dem Sinn nach entnommen sind, in jedem Einzelfall als Entlehnung kenntlich gemacht habe; dass diese Dissertation noch keiner anderen Fakultät oder Universität zur Prüfung vorgelegen hat; dass sie - abgesehen von unten angegebenen Teilpublikationen - noch nicht veröffentlicht worden ist, sowie, dass ich eine solche Veröffentlichung vor Abschluss des Promotionsverfahrens nicht vornehmen werde. Die Bestimmungen der Promotionsordnung sind mir bekannt. Die von mir vorgelegte Dissertation ist von Prof. Dr. Markus Grüninger betreut worden.

Köln, den 12. August 2013

Julia Reul